Autonomous Radar-based Gait Monitoring System

by

Hajar Abedifirouzjaei

A thesis

presented to the University of Waterloo

in fulfillment of the

thesis requirement for the degree of

Doctor of Philosophy

in

Systems Design Engineering

Waterloo, Ontario, Canada, 2023

Examining Committee Membership

The following served on the Examining Committee for this thesis. The decision of the Examining Committee is by majority vote.

External Examiner	Dr. Goutam Chattopadhyay Adjunct Professor, Physics, Mathematics, and Astronomy California Institute of Technology Senior Scientist, NASA-Jet Propulsion Lab
Supervisor(s)	Dr. Plinio Morita Associate Professor, Public Health and Health Systems University of Waterloo
	Dr. George Shaker Adjunct Professor, Electrical & Computer Engineering University of Waterloo
Internal Member	Dr. Jennifer Boger Adjunct Professor, Systems Design Engineering University of Waterloo
Internal Member	Dr. Eihab Abdel-Rahman Professor, Systems Design Engineering University of Waterloo
Internal-external Member	Dr. Steven Fischer Associate Professor, Kinesiology and Health Sciences University of Waterloo

Author's Declaration

This thesis consists of material, all of which I authored or co-authored: see Statement of Contributions included in the thesis. This is a true copy of the thesis, including any required final revisions, as accepted by my examiners.

I understand that my thesis may be made electronically available to the public.

Statement of Contributions

Papers included in this thesis:

Hajar Abedi, Clara Magnier, Kavini Rabel, Divya Kamath, Kashish Grover, Shenbei Fan, Shyan Mascarenhas, Plinio P. Morita, Jennifer Boger, Alexander Wong, and George Shaker, "A Comprehensive Review of Gait: Exploring Existing Technologies, Methods, and Analyses" (under preparation).

A part of this monograph is incorporated in Chapter 3 of this thesis.

Contributor	*Statement of contribution*
Hajar Abedi (candidate)	*Conceptual design (50%)* *Literature review (30%)* *Writing and editing (30%)*
Clara Magnier	*Conceptual design (20%)* *Literature review (40%)* *Writing and editing (40%)*
Kavini Rabel	*Literature review (10%)* *Writing and editing (10%)*
Divya Kamath	*Literature review (5%)* *Writing and editing (5%)*
Kashish Grover	*Literature review (5%)* *Writing and editing (5%)*
Shenbei Fan	*Literature review (5%)* *Writing and editing (5%)*
Shyan Mascarenhas	*Literature review (5%)* *Writing and editing (5%)*
Plinio. P Morita	*Conceptual design (5%)* *Supervision*
Jennifer Boger	*Conceptual design (5%)* *Supervision*
Alexander Wong	*Supervision*
George Shaker	*Conceptual design (20%)* *Supervision*

Hajar Abedi, Ala Eldin Omer, John Hanna, Steven Ding, Ahmad Ansariyan, Andrei Felipe Perez, Tom Paraschuk, Plinio P. Morita, Jennifer Boger, Alexander Wong, Safieddin Safavi-Naeini, and

George Shaker, “In-Package Integrated 3D-Printed Dielectric Lens for a Millimeter-Wave Radar,” *IEEE Transactions on Components, Packaging and Manufacturing Technology* (under review).

This paper is incorporated in Chapter 5 of this thesis.

Contributor	*Statement of contribution*
Hajar Abedi (candidate)	*Conceptual design (70%)* *Measurement (60%)* *Fabrication (10%)* *Simulation (85%)* *Writing and editing (70%)*
Ala Eldin Omer	*Measurement (20%)* *Writing and editing (5%)*
John Hanna	*Fabrication (35%)* *Simulation (5%)*
Steven Ding	*Fabrication (30%)* *Writing and editing (5%)*
Ahmad Ansariyan	*Measurement (10%)*
Andrei Felipe Perez	*Fabrication (25%)*
Tom Paraschuk	*Measurement (5%)*
Plinio P. Morita	*Supervision*
Jennifer Boger	*Supervision*
Alexander Wong	*Supervision*
Safieddin Safavi-Naeini	*Conceptual design (5%)*
George Shaker	*Conceptual design (25%)* *Simulation (10%)* *Measurement (5%)* *Writing and editing (20%)* *Supervision*

Hajar Abedi, Jennifer Boger, Plinio P. Morita, Alexander Wong, and George Shaker, “Hallway Gait Monitoring System Using an In-Package Integrated Dielectric Lens Paired with a mm-Wave Radar*,”* *Sensors–MDPI*, 2023, 23,71.

This paper is incorporated in Chapter 4 and Chapter 5 of this thesis.

Contributor	*Statement of contribution*
Hajar Abedi (candidate)	*Conceptual design (70%)* *Measurement (100%)* *Data collection (100%)* *Data analysis (80%)* *Writing and editing (60%)*
Jennifer Boger	*Conceptual design (5%)* *Writing and editing (15%)* *Supervision*
Plinio P. Morita	*Conceptual design (5%)* *Supervision*
Alexander Wong	*Supervision*
George Shaker	*Conceptual design (20%)* *Data analysis (20%)* *Writing and editing (25%)* *Supervision*

Hajar Abedi, Jennifer Boger, Plinio P. Morita, Alexander Wong, and George Shaker, "Hallway Gait Monitoring Using Novel Radar Signal Processing and Unsupervised Learning," *IEEE Sensors Journal*, 2022.

This paper is incorporated in Chapter 4 and Chapter 5 of this thesis.

Contributor	*Statement of contribution*
Hajar Abedi (candidate)	*Conceptual design (70%)* *Data collection (100%)* *Data analysis (80%)* *Writing and editing (60%)*
Jennifer Boger	*Conceptual design (5%)* *Writing and editing (20%)* *Supervision*
Plinio P. Morita	*Conceptual design (5%)* *Supervision*
Alexander Wong	*Supervision*
George Shaker	*Conceptual design (20%)* *Data analysis (20%)* *Writing and editing (20%)* *Supervision*

Hajar Abedi, Eric Hedge, Carmelo Mastrandrea, Ahmad Ansariyan, Plinio P. Morita, Jennifer Boger, Alex Wong, Richard Hughson, and George Shaker “Non-Visual Contactless RF Sensor Shows 14-Day Head-Down Bedrest Promotes Reductions in Walking Speed,” (under preparation).

This paper is incorporated in Chapter 5 of this thesis.

Contributor	*Statement of contribution*

Hajar Abedi (candidate)	*Conceptual design (40%)* *Data collection (50%)* *Data analysis (60%)* *Writing and editing (50%)*
Eric Hedge	*Conceptual design (20%)* *Data analysis (20%)* *Data collection (10%)* *Writing and editing (20%)*
Carmelo Mastrandrea	*Conceptual design (20%)* *Data analysis (15%)* *Data collection (10%)* *Writing and editing (15%)*
Ahmad Ansariyan	*Data collection (30%)* *Data analysis (5%)* *Writing and editing (5%)*
Plinio P. Morita	*Conceptual design (2.5%)* *Supervision*
Jennifer Boger	*Conceptual design (2.5%)* *Supervision*
Alexander Wong	*Supervision*
Richard Hughson	*Conceptual design (5%)*
George Shaker	*Conceptual design (10%)* *Writing and editing (10%)* *Supervision*

Hajar Abedi, Ahmad Ansariyan, Plinio P. Morita, Jennifer Boger, Alex Wong, and George Shaker "Contactless In-Home Cluttered-Environment Gait Analysis," (under preparation).

This paper is incorporated in Chapter 6 of this thesis.

Contributor	*Statement of contribution*
Hajar Abedi (candidate)	*Conceptual design (80%)* *Data analysis (90%)*

	Data collection (80%) *Writing and editing (80%)*
Ahmad Ansariyan	*Data collection (20%)* *Data analysis (20%)* *Writing and editing (5%)*
Plinio P. Morita	*Conceptual design (5%)* *Supervision*
Jennifer Boger	*Conceptual design (5%)* *Supervision*
Alexander Wong	*Supervision*
George Shaker	*Conceptual design (10%)* *Writing and editing (10%)* *Supervision*

Hajar Abedi, Ahmad Ansariyan, Plinio P. Morita, Jennifer Boger, Alex Wong, and George Shaker,” AI-Powered Non-Contact In-Home Gait Monitoring and Activity Recognition System Based on mm-Wave FMCW Radar and Cloud Computing,” *IEEE Internet of Things Journal*, 2023.

This paper is incorporated in Chapter 6 of this thesis.

Contributor	*Statement of contribution*
Hajar Abedi (candidate)	*Conceptual design (50%)* *Data analysis (70%)* *Data collection (60%)* *Writing and editing (50%)*
Ahmad Ansariyan	*Conceptual design (30%)*

	Data analysis (30%) *Data collection (40%)* *Writing and editing (15%)*
Plinio P. Morita	*Writing and editing (5%)* *Conceptual design (5%)* *Supervision*
Alexander Wong	*Conceptual design (2.5%)* *Supervision*
Jennifer Boger	*Conceptual design (2.5%)* *Supervision*
George Shaker	*Conceptual design (10%)* *Writing and editing (30%)* *Supervision*

Abstract

Features related to gait are fundamental metrics of human motion [1]. Human gait has been shown to be a valuable and feasible clinical marker to determine the risk of physical and mental functional decline [2], [3]. Technologies that detect changes in people's gait patterns, especially older adults, could support the detection, evaluation, and monitoring of parameters related to changes in mobility, cognition, and frailty. Gait assessment has the potential to be leveraged as a clinical measurement as it is not limited to a specific health care discipline and is a consistent and sensitive test [4].

A wireless technology that uses electromagnetic waves (i.e., radar) to continually measure gait parameters at home or in a hospital without a clinician's participation has been proposed as a suitable solution [3], [5]. This approach is based on the interaction between electromagnetic waves with humans and how their bodies impact the surrounding and scattered wireless signals. Since this approach uses wireless waves, people do not need to wear or carry a device on their bodies. Additionally, an electromagnetic wave wireless sensor has no privacy issues because there is no video-based camera.

This thesis presents the design and testing of a radar-based contactless system that can monitor people's gait patterns and recognize their activities in a range of indoor environments frequently and accurately. In this thesis, the use of commercially available radars for gait monitoring is investigated, which offers opportunities to implement unobtrusive and contactless gait monitoring and activity recognition. A novel fast and easy-to-implement gait extraction algorithm that enables an individual's spatiotemporal gait parameter extraction at each gait cycle using a single FMCW (Frequency Modulated Continuous Wave) radar is proposed. The proposed system detects changes in gait that may be the signs of changes in mobility, cognition, and frailty, particularly for older adults in individual's homes, retirement homes and long-term care facilities retirement homes. One of the straightforward applications for gait monitoring using radars is in corridors and hallways, which are commonly available in most residential homes, retirement, and long-term care homes. However, walls in the hallway have a strong "clutter" impact, creating multipath due to the wide beam of commercially available radar antennas. The multipath reflections could result in an inaccurate gait measurement because gait extraction algorithms employ the assumption that the maximum reflected signals come from the torso of the walking person (rather than indirect reflections or multipath) [6].

To address the challenges of hallway gait monitoring, two approaches were used: (1) a novel signal processing method and (2) modifying the radar antenna using a hyperbolic lens. For the first approach, a novel algorithm based on radar signal processing, unsupervised learning, and a subject detection,

association and tracking method is proposed. This proposed algorithm could be paired with any type of multiple-input multiple-output (MIMO) or single-input multiple-output (SIMO) FMCW radar to capture human gait in a highly cluttered environment without needing radar antenna alteration. The algorithm functionality was validated by capturing spatiotemporal gait values (e.g., speed, step points, step time, step length, and step count) of people walking in a hallway. The preliminary results demonstrate the promising potential of the algorithm to accurately monitor gait in hallways, which increases opportunities for its applications in institutional and home environments. For the second approach, an in-package hyperbola-based lens antenna was designed that can be integrated with a radar module package empowered by the fast and easy-to-implement gait extraction method. The system functionality was successfully validated by capturing the spatiotemporal gait values of people walking in a hallway filled with metallic cabinets. The results achieved in this work pave the way to explore the use of stand-alone radar-based sensors in long hallways for day-to-day long-term monitoring of gait parameters of older adults or other populations.

The possibility of the coexistence of multiple walking subjects is high, especially in long-term care facilities where other people, including older adults, might need assistance during walking. GaitRite and wearables are not able to assess multiple people's gait at the same time using only one device [7], [8]. In this thesis, a novel radar-based algorithm is proposed that is capable of tracking multiple people or extracting walking speed of a participant with the coexistence of other people. To address the problem of tracking and monitoring multiple walking people in a cluttered environment, a novel iterative framework based on unsupervised learning and advanced signal processing was developed and tested to analyze the reflected radio signals and extract walking movements and trajectories in a hallway environment. Advanced algorithms were developed to remove multipath effects or ghosts created due to the interaction between walking subjects and stationary objects, to identify and separate reflected signals of two participants walking at a close distance, and to track multiple subjects over time. This method allows the extraction of walking speed in multiple closely-spaced subjects simultaneously, which is distinct from previous approaches where the speed of only one subject was obtained. The proposed multiple-people gait monitoring was assessed with 22 participants who participated in a bedrest (BR) study conducted at McGill University Health Centre (MUHC).

The system functionality also was assessed for in-home applications. In this regard, a cloud-based system is proposed for non-contact, real-time recognition and monitoring of physical activities and walking periods within a domestic environment. The proposed system employs standalone Internet of Things (IoT)-based millimeter wave radar devices and deep learning models to enable autonomous,

free-living activity recognition and gait analysis. Range-Doppler maps generated from a dataset of real-life in-home activities are used to train deep learning models. The performance of several deep learning models was evaluated based on accuracy and prediction time, with the gated recurrent network (GRU) model selected for real-time deployment due to its balance of speed and accuracy compared to 2D Convolutional Neural Network Long Short-Term Memory (2D-CNNLSTM) and Long Short-Term Memory (LSTM) models. In addition to recognizing and differentiating various activities and walking periods, the system also records the subject's activity level over time, washroom use frequency, sleep/sedentary/active/out-of-home durations, current state, and gait parameters. Importantly, the system maintains privacy by not requiring the subject to wear or carry any additional devices.

Acknowledgements

I would like to extend my deepest appreciation to my supervisors, Professor George Shaker and Professor Plinio P. Morita, for their exceptional guidance, invaluable advice, and unwavering support throughout my Ph.D. studies. Their expertise and wisdom in the field have been instrumental in shaping my research and academic pursuits. I am truly fortunate to have had the opportunity to work under their supervision, and I will forever be grateful for their mentorship and encouragement.

I would like to express my sincere gratitude to Professor Alexander Wong and Professor Richard Hughson for their invaluable contributions to my research. Their insightful comments, constructive feedback, and expert guidance have greatly enhanced the quality and rigor of my work.

I wish to thank my doctoral committee members, Professor Jennifer Boger, Professor Eihab Abdel-Rahman, Professor Steve Fischer and Professor Goutam Chattopadhyay, for their valuable comments and suggestions.

I wish to acknowledge the University of Waterloo Faculty of Engineering, Microsoft Corporation, MITACS, TandemLaunch Inc and Gold Sentintel for financial support of my research.

I would also like to thank my friends and colleagues in Wireless Sensors and Devices Lab (WSDL), Ubiquitous Health Technology Lab (UbiLab), Vision and Image Processing (VIP) lab, Intelligent Technologies for Wellness and Independent Living (ITWIL) Lab, and Vascular Aging and Brain Health Lab.

I would like to express my heartfelt appreciation to Christopher Lehman, the COO of Gold Sentintel, for his invaluable support and feedback throughout the completion of my thesis. I am deeply grateful for his time and effort to read my thesis and provide me with his valuable insights.

I would like to thank all my friends who have provided me with support, encouragement, and inspiration throughout my academic journey. Their companionship, laughter, and kindness have helped me maintain a healthy work-life balance and have made my time at the university more enjoyable.

Finally, I would like to express my deepest gratitude and love to my family in Iran for their unconditional love and support. My special gratitude and love go to my loving husband, Ahmad Ansariyan, who has accompanied me in my amazing journey through my Ph.D. in Canada. He has always provided me with a safe haven during the most challenging times, cheering me on and celebrating the successful ones. I have only gotten where I am because I had him by my side, always encouraging me to reach higher and to never stop. Thank you for your love and patience over these amazing years.

Dedication

To those who dedicated their lives to a better world, freedom, equity, and humanity.

Table of Contents

List of Figures

List of Tables

Chapter 1

Introduction

Human gait and activity monitoring play important roles in many applications that can significantly improve the ability to be as independent, secure, and healthy as possible [2], [9]. Notably, gait qualities are increasingly being recognized as a measure of a person's health status; changes in normal walking patterns, such as gait speed reduction or lack of balance, can signify a change in cognition and an increase in the probability of a fall occurring, especially for older adults [10]. Extensive research and multiple longitudinal studies conducted on gait analysis [9], [11]–[13] have shown that accurate, reliable knowledge of general gait characteristics at a given time, and even more importantly, over a period of time can enable detection and diagnosis of changes in mobility and cognition [10]. Tracking gait can also support finding the best treatment options and ongoing management [10]. However, variations in gait characteristics as a result of cognitive or other conditions may go undetected as the effect can be gradual and often goes unnoticed by the individual and/or during clinical visits [1], [14]. Technologies that can detect changes in people's gait patterns could be used to support the detection, evaluation, and monitoring of parameters related to changes in mobility, cognition, and frailty [1]. Early detection of such changes results in a higher probability they can be better supported, which in turn can increase the probability of independence and quality of life of the person being monitored [1]. This approach is especially relevant to the growing population of older adults, most of whom wish to remain in their own homes.

Numerous studies have been conducted to identify the relative association between walking and functional decline in people, especially older adults [9], [13], [15], [16]. While gait parameters have been assessed and used as a clinical indicator for health status in various studies, there is no consensus on a standard measurement methodology for the walking test [4]. Moreover, most measurements are conducted during clinical visits [9]. Another issue related to assessing gait is that the unfamiliar setting of a clinic often causes people to (intentionally or unintentionally) change their gait patterns during clinical assessments.

In many studies (e.g., [12], [17]), a habitual or usual gait speed (i.e., walking at a normal speed on level ground) was considered a reliable and consistent clinical indicator. A person's walking speed in a clinical setting may not be an accurate and reliable representation of their day-to-day gait because of their focus on walking and awareness of the importance of their gait. It may negatively impact medical conclusions and recommendations, thus, diagnosis, follow-up, and treatment of pathologies from gait obtained in clinical settings may be based on inaccurate data. A quantification method of gait parameters in a naturalistic setting (e.g., one's home) is required to obtain a more accurate representation of day-to-day gait patterns. Gold standard systems such as the GaitRite mat system [18] and Vicon [19] can be expensive, difficult to operate, have limited coverage, and present challenges for deployment in real-world settings.

Therefore, there is a pressing need for affordable, ubiquitous, and unobtrusive technology that can measure human gait parameters continuously and reliably to get a better understanding of an individual's true gait and how their gait may change over time. A comprehensive system is needed that can measure and analyze people's gait in their living environment, namely, at home, in hospitals or long-term care facilities.

A wearable device could be a possible solution for frequent in-home gait assessments, but using them requires people to want and remember to use and recharge them. Wearable sensors such as the Opal sensor [20] and Physilog [21] could be used for day-to-day gait assessments; however, many people do not like using wearables or may not remember to wear them. Moreover, wearable devices might cause feelings of burden and discomfort. On the other hand, optics-based systems, such as computer vision and infrared, have the problem of line-of-sight detection; they cannot detect people behind obstacles. There can also be concerns regarding privacy and overhead costs.

A radar-based sensor is a promising alternative to capture gait information during people's daily activities in their living environments over long periods as it is a relatively affordable, easy-to-use, non-invasive, and zero-effort system [14], [22]–[29]. The use of a radar system is appealing due to its reliable functionality in different lighting levels, protection of privacy, penetration through obstacles, and long-range detection capabilities [29]. Radar sensors could make it possible to monitor and analyze gait outside the laboratory and capture information about human gait and activity levels during the person's everyday activities [30]. It should be mentioned that there is little research on radar's accuracy and applicability for in-home applications such as gait monitoring, and people may not feel comfortable installing radars in their homes (since it is new and not a common technology used at homes). However, there is a growing interest in the use of radar systems in everyday life [30].

The purpose of this thesis is to perform gait monitoring using radar technology to monitor gait during daily life activities. The focus of this thesis is to integrate machine learning algorithms with radar signal processing to identify the type of in-home activity performed by a subject and to detect in-home walking periods to distinguish them from other in-home activities and capture gait parameters.

1.1 Motivation

Clinicians typically evaluate patients/subjects by testing their motor skills during clinic visits. These semi-subjective measurements are often skewed by outside factors, such as patients' awareness of their gait quality or fatigue from travelling to the appointment. Additionally, numerous people (especially older adults) may never be treated by a specialist (especially those with Parkinson's disease), often because they live too far from an urban center or have difficulty travelling.

As mentioned above, most existing technologies rely on cameras and wearable sensors to monitor, record, and analyze people's daily activities and health-related signals. However, wearable technologies and computer vision suffer from many drawbacks hindering them from being used for day-to-day frequent gait assessment. Wireless ambient sensors capable of sensing any environment dynamics without the need for wearable devices could be a promising solution for monitoring human health-related signals.

Most previously proposed human gait analysis and activity recognition systems based on wireless ambient sensors have been done in a simple, clutter-free, or low-clutter environment with a constrained range and limited activity. The implementation of radar-based in-home cluttered environment gait monitoring and activity recognition system can be beneficial for the following reasons:

- The in-home monitoring system could pave the way to explore the use of radar-based sensors in retirement apartment buildings or individual's homes for use in day-to-day long-term monitoring of gait parameters, especially for older adults.
- The in-home monitoring system could record activity levels, daily variations, and changes over time and could provide this information remotely to a professional caregiver in a timely manner.
- The in-home monitoring system could open new possibilities that could improve clinical practice across all people in addition to older adults.

- The capabilities of the in-home monitoring system mean that it also has the potential to be used for other in-home applications, including people counting and fall detection and offer excellent long-term care benefits.

Chapter 2

Objective, Research Questions and Approaches

2.1 Objectives

The aim of this Ph.D. thesis is to create a state-of-the-art, zero-effort wireless sensor system that leverages wireless millimeter-wave signals to monitor and extract gait parameters. The objective is to create a system that can autonomously recognize the activity performed by a subject and extract crucial spatiotemporal gait parameters without the need for explicit interaction from the subject being monitored. This autonomous gait monitoring system combines radar technology with advanced signal processing and machine learning algorithms to classify various activities, identify walking periods, and extract gait parameters with a high degree of accuracy.

To achieve this objective, in the following subsections, research questions defined to guide this thesis, along with the approaches followed to address these questions, are outlined. The research will delve into the technical aspects of using millimeter-wave signals for gait analysis, the development of machine learning algorithms for activity classification and advanced signal processing methods for gait parameter extraction. The ultimate objective of this research is to provide a novel, non-invasive solution for gait analysis that can be used in a variety of settings, including individual's homes, retirement homes and long-term care facilities, to improve the quality of life for individuals.

2.2 Research Questions

The following key research questions (RQ) and sub-questions will be used to guide this research:

RQ 1. How can radar sensors be used for the ambient detection of gait?

This research question guided this thesis to explore the use of radar sensors in gait analysis. Since several key factors should be considered, including but not limited to the type of radar sensor, a proper algorithm for gait parameter extractions, and gait analysis in a familiar environment (such as one's home), these sub-questions were identified.

RQ. 1.1 What are the appropriate radar sensors needed for a gait monitoring system?

One of the key elements in radar-based gait monitoring systems is the radar sensor. A proper radar sensor should be selected to extract gait parameters accurately. Therefore, this sub-question was defined to guide this research to find a proper radar sensor in this thesis.

RQ. 1.2 What signal processing techniques can be used to quantify gait parameters?

Since gait values should be extracted based on the radar received data, the proper signal processing method would be the second need. This sub-question was defined to guide this research to propose a gait extraction algorithm based on the selected radar sensor.

RQ. 1.3 How can the dependency of the micro-Doppler signature on the direction of motion be overcome?

One of the common features used in gait analysis was the micro-Doppler signature of walking, but this signature depends on the angle of motion. This sub-question was defined to guide this research toward finding a method to overcome this dependency. This would pave the way for gait analysis to be used in people's in-home environments where they walk at different relative angles with the radar sensor.

RQ. 1.4 How can the effects of noise/ multipath from a highly cluttered environment be overcome?

One of the primary purposes of the use of radar sensors for gait analysis is for frequent day-to-day in-home monitoring. To achieve this goal, it is of paramount importance to explore the radar performance in an in-home or cluttered environment where walking processes create noise or multipath. This sub-question was defined to guide this research to explore in-home gait monitoring and multipath mitigation methods.

RQ. 1.5 How can gait be monitored in multiple-person scenarios?

Most of the current gait monitoring methods were focused on a single subject, while the probability of having more than one subject walking together is high. This research question was defined to guide this research to explore the use of radar for multiple-people gait monitoring.

RQ 2. How can machine learning algorithms be used to identify the type of activity being performed by the subject who is being monitored?

As mentioned, this radar-based technology is intended to be used in an individual's home for frequent day-to-day measurement. The radar sensor should identify walking periods first and distinguish them from other in-home activities to extract gait parameters. To achieve this, this research question was defined to guide this research in using artificial intelligence (AI) for in-home activity recognition and gait monitoring.

RQ. 2.1 What features should be used for machine learning algorithms to classify activity types?

Features or inputs are key elements in machine learning. Proper inputs could lead to finding an appropriate and accurate model. This sub-question was defined to guide this research to find sufficient and suitable features to be fed to machine learning models.

RQ. 2.2 What machine learning algorithm should be used to distinguish gait from other activities?

A proper machine learning model should be selected to apply to the radar data. This sub-question was defined to explore different machine learning models and find an accurate one for in-home gait monitoring and activity recognition systems.

2.3 Approaches and Contributions

In this subsection, approaches followed to address the research questions are summarized. Seven primary phases were defined and divided into four chapters in this thesis. In this subsection, each phase, the corresponding chapter linked to each phase, and the outcomes, contributions and publications related to each phase are explained.

Phase 1: Literature review –the first phase performed for this thesis was a literature review on the history of gait, the definition of gait parameters, studies on gait analysis, common devices used for gait analysis and radar sensors utilized for gait analysis. This phase is detailed in Chapter 3. This phase helped the researcher to recognize the gaps in gait analysis using radar sensors and define the research questions to guide this Ph.D. research. Phase 1 is associated with the following monograph:

- Hajar Abedi, Clara Magnier, Kavini Rabel, Divya Kamath, Kashish Grover, Shenbei Fan, Shyan Mascarenhas, Plinio P. Morita, Jennifer Boger, Alexander Wong, and George Shaker, "A Comprehensive Review of Gait: Exploring Existing Technologies, Methods, and Analyses" (under preparation).

Phase 2: Sensor selection – literature review and experimental tests were conducted to select a proper radar sensor for autonomous gait monitoring and activity recognition. Availability, cost, performance, the radar type, output power, etc., were some key factors in selecting a radar sensor. Various types of off-the-shelf radar sensors, such as those available from Infineon [31], Vayyar [32] and Texas Instruments [33], were used. One radar sensor was used throughout this thesis to provide a reliable and reasonable comparison (in terms of operation frequency, range resolution, angular resolution, etc.) and for conciseness. A millimeter-wave MIMO FMCW (AWR1443) radar sensor was used to conduct all the experiments since it has better angular resolution and longer range detection compared with the Infineon radar [34] and is cheaper and easy to use compared with the Vayyar radar [32]. All radar parameters could be configured through the provided software MMWAVE_STUDIO.

Phase 3: Gait parameter extraction algorithm – various signal processing methods were investigated, and a novel method was proposed to extract spatiotemporal gait parameters at each single gait cycle. The outcome of phase 3 was a fast and easy-to-implement signal processing technique to extract and quantify gait parameters at each single gait cycle. Phase 3 addressed RQ. 1.2 detailed in Chapter 4. The outcome of phase 3 was a method used to address other RQs explained in Chapter 4, Chapter 5 and Chapter 6. Hence, this method was a core technique described and used in almost all publications of this thesis to quantify gait parameters.

Phase 4: Gait monitoring independent of the angle of motion – this phase required in-depth research on how to compensate for the angle effects on the micro-Doppler patterns (RQ. 1. 3). One of the quick and straightforward solutions was to monitor human gait in a corridor or hallway as this is something that is in virtually every place people live and requires a relatively straight line of walking several times a day. However, walls in the hallway have a strong "clutter" impact, creating multipath due to the wide beam of commercially available radar antennas. To eliminate the multipath reflections, two viable solutions were proposed: 1. Novel signal processing and 2. Radar antenna modification. Outcomes of phase 4 were: (1) a novel unsupervised learning-based method for tracking and association of the subject walking across a hallway, and (2) an in-package hyperbola-based dielectric antenna designed, fabricated, and integrated with the available radar chipset for hallway gait monitoring. Phase 4 is presented in detail in Chapter 5, which addresses two research questions (RQ. 1.3 and RQ. 1.4). Phase 3 and Phase 4 are associated with the following journal papers:

- Hajar Abedi, Ala Eldin Omer, John Hanna, Steven Ding, Ahmad Ansariyan, Andrei Felipe Perez, Tom Paraschuk, Plinio P. Morita, Jennifer Boger, Alexander Wong, Safieddin Safavi-Naeini, and George Shaker, "In-Package Integrated 3D-Printed Dielectric Lens for a

Millimeter-Wave Radar," *IEEE Transactions on Components, Packaging and Manufacturing Technology* (under review).

- Hajar Abedi, Jennifer Boger, Plinio P. Morita, Alexander Wong, and George Shaker, "Hallway Gait Monitoring System Using an In-Package Integrated Dielectric Lens Paired with a mm-Wave Radar*,"* *Sensors–MDPI*, 2023, 23,71.
- Hajar Abedi, Jennifer Boger, Plinio P. Morita, Alexander Wong, and George Shaker, "Hallway Gait Monitoring Using Novel Radar Signal Processing and Unsupervised Learning," *IEEE Sensors Journal*, 2022.

Phase 5: Multiple people gait monitoring – this phase required in-depth research on how to track walking subjects when multiple people are walking simultaneously (RQ. 1. 5). To monitor multiple people, in collaboration with other groups, datasets were collected from several older adults participated in a first-of-its-kind study conducted in Canada at MUHC. The outcome of phase 5 was a multiple-people hallway gait monitoring algorithm developed to monitor two subjects walking simultaneously across a hallway in MUHC. In this phase, the radar sensor was demonstrated to be able to detect any variation in participants walking speed before and after bed rest. Phase 5 addressed RQ. 1.5, which is detailed in Chapter 5 (Section 5.3). Phase 5 is associated with the following journal paper:

- Hajar Abedi, Eric Hedge, Carmelo Mastrandrea, Ahmad Ansariyan, Plinio P. Morita, Jennifer Boger, Alex Wong, Richard Hughson, and George Shaker "Non-Visual Contactless RF Sensor Shows 14-Day Head-Down Bedrest Promotes Reductions in Walking Speed*,* (under preparation).

Phase 6: In-home gait monitoring – since all walking tests were conducted in a straight line, this research required more work while a subject walks in a non-straight line. To monitor people in a highly cluttered living environment, independent of the angle of motion (RQ.1.3 and RQ. 1.4), in addition to the hallway gait analysis, there was a need to implement algorithms to mitigate multipath signals in a home. Several subjects were invited to perform an in-home walk in the research area of the Schlegel-University of Waterloo Research Institute for Aging (Schlegel-UW RIA) and a small apartment. The output of phase 6 was a novel signal processing method proposed to track and monitor a subject walking in a cluttered environment such as one's home. Phase 6 addressed RQ.1.3 and RQ. 1.4, which is detailed in Chapter 6 (Section 6.5). Phase 6 is associated with the following journal paper:

- Hajar Abedi, Ahmad Ansariyan, Plinio P. Morita, Jennifer Boger, Alex Wong, and George Shaker "Contactless In-Home Cluttered-Environment Gait Analysis," (under preparation).

Phase 7: Deployment of machine learning algorithm – after performing in-home gait extraction, one of the remaining challenges was that other in-home activities could be detected as walking periods. It is shown that this type of error in gait assessment is preventable by implementing machine learning. A critical step for autonomous classification was using suitable inputs for the machine learning algorithm and a proper machine learning model. Note that the research conducted to address the first research questions (RQ. 1.1 - RQ. 1.4) was needed to tackle the second question (RQ. 2.1 and RQ. 2.2). Therefore, phase 7 was an iterative process between producing features and testing the machine learning algorithm. The outcomes of phase 7 were proper features to be fed to machine learning algorithms and a proper model to identify gait/activity among several explored models such as GRU (Gated recurrent unit), LSTM (Long short-term memory), and CNN (Convolutional Neural Network). Phase 7 addressed RQ. 2.1 and RQ. 2.2, which is detailed in Chapter 6.

Phase 7 is associated with the following journal paper:

- Hajar Abedi, Ahmad Ansariyan, Plinio P. Morita, Jennifer Boger, Alex Wong, and George Shaker," AI-Powered Non-Contact In-Home Gait Monitoring and Activity Recognition System Based on mm-Wave FMCW Radar and Cloud Computing*," IEEE Internet of Things Journal*, 2023.

A flowchart of the defined phases and the corresponding chapters is provided in Figure **2.1**. As shown, all defined phases are highly correlated, and the outcome of one phase/ chapter is used in the next phase/chapter. NOTE: Each specified phase corresponds to a sub-question of the defined research questions listed in Section 2.2.

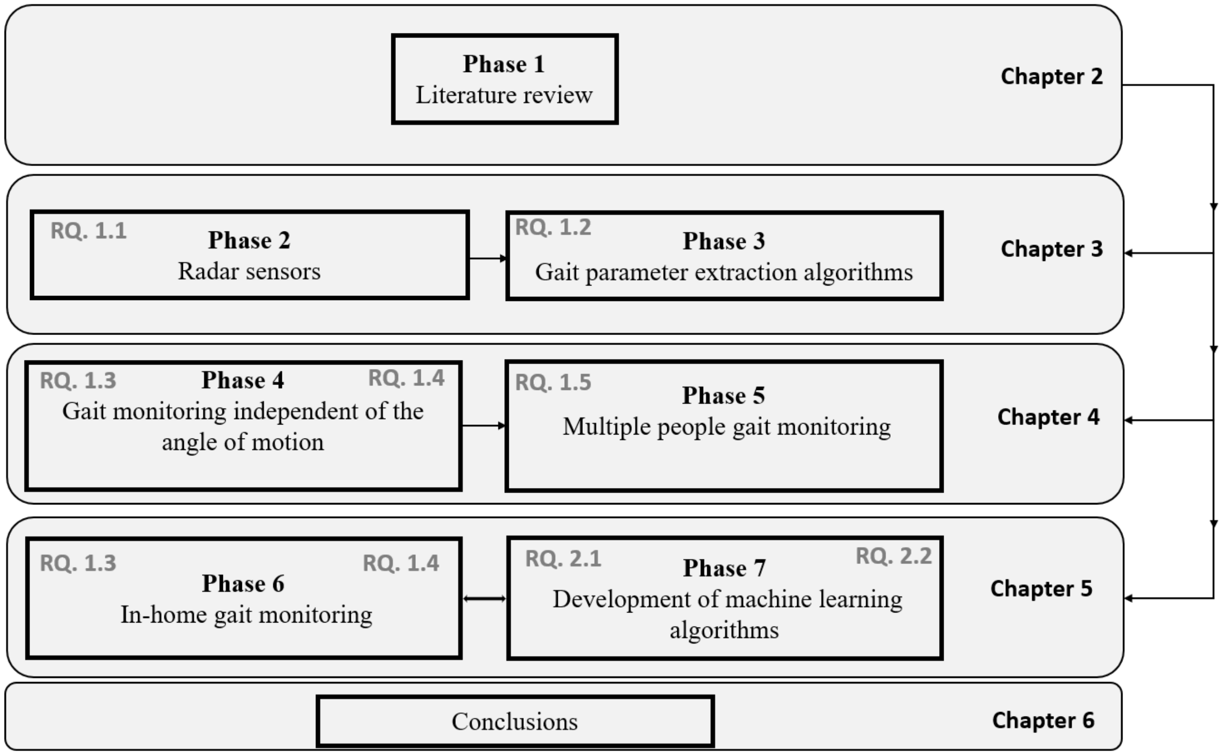

Figure 2.1. Flowchart of research phases done for this thesis (RQ: research question).

Chapter 3

Background

3.1 Background to Gait Parameters

“Gait” is defined as the pattern of moving the body from one place to another over a solid substrate by alternately and repetitively changing the location of feet [2]. Gait is an important activity of daily living that is an excellent functional test of several human systems involving the interaction of many joint movements. It is a highly coordinated process involving the peripheral nervous system, perceptual system, central nervous system, muscles, energy production and/or delivery and bone and/or joints [1]. When these systems are not functioning correctly, they will impact our gait parameters. For instance, a slower walking speed than normal or a variation in normal/usual gait parameters can alert clinicians that something is going wrong in the human body. Gait can provide insight into surgical decision-making, prosthetic design, orthopedic design, rehabilitation strategies, accurate tracking of progress, and biometric and milestone profiles [1], [9].

The research described in this thesis, however, is mainly centered on achieving a quantitative measurement of gait parameters to be used as a health indicator. The most basic description of the gait is the gait cycle [35]. As shown in Figure **3.1**, from a temporal perspective, the gait cycle is composed of two phases: (1) the stance phase (when the foot remains in contact with the ground) and (2) the swing phase (when the foot is not in touch with the ground).

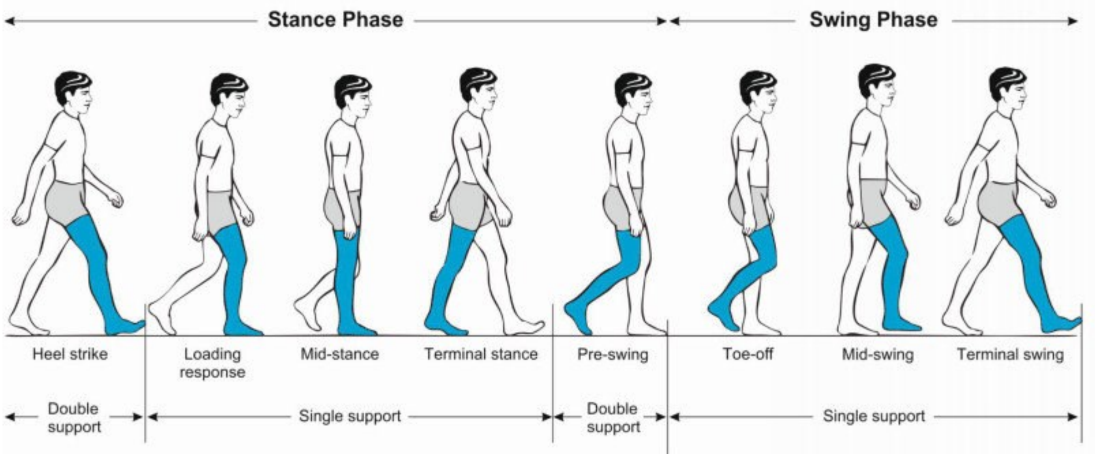

Figure 3.1. Gait cycle during walking, reproduced from [1].

Each phase can be broken into different subparts, such as the initial contact or the terminal swing. There are also critical support phases such as the single support phase (only one limb is in touch with the ground), initial double support phase (the sub-phase between heel contact of the phase to contralateral foot-off), and terminal double support phase (sub-phase from contralateral foot-on to the toe-off) [35]. Figure **3.2** shows the temporal parameters of a gait cycle where a low signal represents a foot touching the ground, and a high signal means it is not in contact with the ground.

From a spatial perspective, Figure **3.3** shows typical spatial gait parameters used in gait assessments, such as step length, stride length, and step width. The general gait parameters are defined and listed in Table **3.1**. In the following discussion, gait assessment, analysis, and measurement refer to the capture and analysis of spatiotemporal gait parameters.

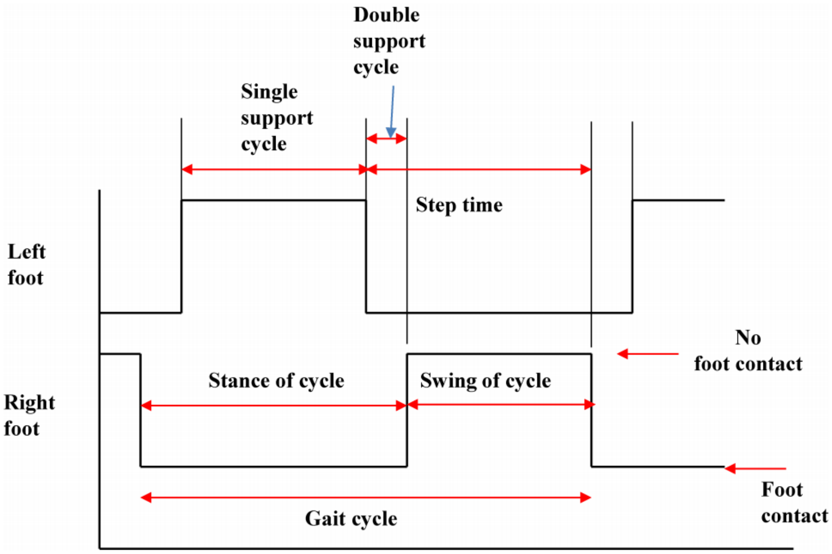

Figure 3.2. Temporal parameters describing the gait cycle, reproduced from [1].

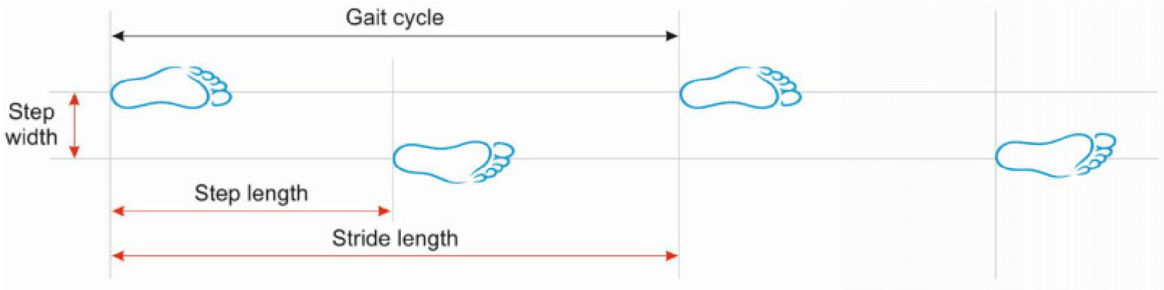

Figure 3.3. Spatial gait terminology describing the gait cycle, reproduced from [1].

Table 3.1. Definition of gait parameters.

Parameters	Definition
Gait speed (m/s)	The distance walked divided by the walking time
Step length (cm)	The length measured parallel to the line followed by the body while walking, from the contact of the heel of the previous footfall to the contact of the heel from the opposite footfall. It can be calculated as the distance covered divided by the number of steps completed
Step width (cm)	The distance measured between lines of progression of the right and left foot. Medio-lateral distance between the heels in the double support phase
Stride length (cm)	The distance measured parallel to the line followed by the body between the heel points of the same foot for two consecutive footprints
Cadence (number of steps/minute)	The number of steps by minutes
Step time (s)	The time between the initial contact of one foot and the initial contact of the opposite foot
Stance time (s)	The duration between the initial contact and final contact of the same foot.
Swing time (s)	The duration between the last contact of a footfall and the initial contact of the following footfall
Single support time (s)	The duration of the swing phase where only one limb is in contact with the ground
Double support time (s)	The duration of the phase of support on both feet

3.2 History of Gait Analysis

Throughout history, people have been thinking about the way they walk. The first recorded experiment in gait analysis was performed by Borelli [36]. Borelli's ideas played a pivotal role in Weber brothers' achievements resulting in the second breakthrough in gait assessment, using only a stopwatch, measuring tape, and a telescope [37]. Their method was a new milestone in the history of gait assessment, which quantitatively analyzed human locomotion using observations of the stance and swing phases of the gait cycle. Marey and Muybridge adopted the Weber brothers' method and introduced a technique known as chronophotography. They demonstrated the sequence of motion of a horse running using several stationary cameras [15].

As progress on kinematic measurements continued to evolve, the forces exerted by the foot on the floor were recorded by a shoe developed by Carlet to enable kinetic measurements [38]. A breakthrough in the evolution of instrumental gait analysis was the introduction of three-dimensional (3-D) analysis of human movement. The method overcame the limitation of the time-consuming process of chronophotography. Electromyography (EMG) became a valuable part of clinical gait analysis in 1970 [39]. EMG is an electrodiagnostic technique used to identify an abnormality in muscle contractions to an injury, nerve damage, or muscular or neurological disorder that causes motor dysfunction [40].

Studies on kinematics, kinetics, and EMG measurement tools were carried out separately until it was recognized that a complete gait analysis needs the integration of various types of measurement technologies. Kinesiological electromyography (KEMG), 3D forces, and energy measurements were added to gait analysis by Vern Inman [41]. Methodological approaches to observational gait analysis were developed to complement EMG [1] as well as instrumented methods for measuring simple temporal-spatial parameters [38]. Technological progress has led to the development of various efficient and effective measurement instruments integrated into a gait analysis system providing reliable information. Currently, clinical gait analysis usually consists of measurement of EMG, kinetic measurement, kinematic analysis, and general gait parameters. The primary kinetic measurement concentrates on the cause of motion (i.e., the force beneath each foot while walking) using various sophisticated devices such as spectrophotometers, spectrofluorometer, and potentiometers [42]. Kinematic measurements, on the other hand, are the measurements of the range of motion without dealing with the forces controlling the movements [43]. General gait parameter measurement assesses spatiotemporal gait parameters and is a powerful complement to EMG. Unlike other types of gait analysis requiring more advanced equipment to be measured, the spatiotemporal gait parameters can now be collected without expensive tools [44].

3.3 Clinical Values of General Gait Parameters

Based on extensive research and multiple longitudinal studies conducted on the gait analysis [9], [11]–[13], [17], it has been shown that accurate, reliable knowledge of general gait characteristics at a given time, and even more importantly, monitoring and evaluating them over time, can enable early diagnosis of disease and track their progression to help with finding the best treatment and ongoing management. For example, gait can be used to detect and even predict brain-related pathologies without using MRI or other invasive detection systems [45].

Hispanic Established Population for the Epidemiological study (H-EPESE) with 2070 noninstitutionalized Mexican-American men and women aged 65 and older showed that a slower walking speed over an 8-foot course could be an early indicator of cognitive decline. Furthermore, it was stated that those who walked over 8 feet at a faster speed were at fewer risk of cognitive function decline [12]. In [46], it was shown that acceleration of the decline in walking speed precedes approximately 12 years earlier than Mild Cognitive Impairment (MCI) onset. The walking speed was shown to be an early indicator of MCI, while most of the existing tests, X-Ray, for instance, can only detect the symptom after it is too late to take preventative measures. Beyond brain-related pathology, gait has been shown to be related to cardiovascular diseases since the cardiovascular system is involved during physical efforts. [47].

Gait speed has also been shown to be a discriminating factor in identifying the potential for rehabilitation and future fall risks or the fear of falling [15]. In [16], gait speed, step length, step time, cadence, double-support phase, and step width were measured and collected at a usual walking speed to investigate the relationship between falls and gait characteristics. They used a 4.6 m computerized walkway system (GaitRite) to assess people's gait parameters. Note that GaitRite is expensive (a 6.096 m GaitRite system is $34,725 USD) but is currently considered a gold standard measure of gait analysis as it provides accurate spatial and temporal gait parameters in addition to pressure distribution under the feet. Data about the fall rate was obtained with a fall questionnaire every two months. In this population-based study, greater intra-individual variability in step length and double-support phase were linearly associated with an increased risk of multiple falls ($P = 0.04$). Non-linear associations with multiple falls were found for gait speed ($P = 0.002$), cadence ($P = 0.004$) and step time variability ($P = 0.03$). However, one of the main limitations of this study [16] was that the results were based on self-reported fall rates, which may not be reliable; participants may forget how many times they fell or not report their fall rate intentionally (for fear of being considered too frail or unstable to live at home safely). Moreover, 12 months may not be enough time to generalize the relationship between gait and fall risks, especially as a decline in walking speed may not be detected during that time. To reliably monitor balance and gait, there is a clear need for an affordable technology that can autonomously detect falls and monitor gait in living environments for a long period of time.

For the older adult population, walking speed has been demonstrated to be correlated with a higher risk of mortality. In many studies, gait has been expressed as a valuable indicator of health and well-being [48]. In [48], 3047 older adults participated in a study to identify and validate cut-points (threshold) for usual (normal) gait speed. In this study, gait speeds of 2031 participants were used for identification, and gait speeds of the other 1016 older adults were used for validation. One of the main strengths of the study reported in [48] was the definition of cutpoints for a normal walking speed that could facilitate the use of walking speed in clinical settings. Those with a walking speed of more than 1m/s were considered to be in a low-risk group, while participants with a walking speed <1m/s were in a high-risk group. Participants in the high-risk group had a higher risk of persistent lower extremity limitation, persistent severe lower extremity limitation, death, and hospitalization than those in the low-risk group. A complete analysis led by two consortiums (Biomathics and Canadian Gait Consortium) published in 2017 provides consensus guidance for clinical and spatiotemporal gait analysis and reference values for spatiotemporal gait analysis [49]. Researchers used two different databases obtained by GaitRite for individuals older than 65 years. The guidance for clinical gait analysis was defined with either a minimal or full dataset. The minimal dataset was composed of four gait parameters (walking speed, value and variation of stride time, swing time and stride width) evaluated in normal walking conditions. Parameters added to the full dataset were the value and variation of stride length, stance time, single and double support, and stride time velocity. This study indicated the importance of the different gait parameters in addition to the walking speed. Researchers suggested all adults older than 65 be examined each year for gait disorders, and everyone with a history of falls or acute treatment should also be examined.

In general, one of the main issues related to the gait assessment studies is that the methodology of gait measurement, protocols for walking tests, measurement devices and cutpoints distinguishing the normal gait from abnormal one varied widely from one study to another. Without any normative value and a standard measurement methodology, it is impossible to consider gait parameters as comparable vital signs or clinical indicators in clinical assessments.

The following discusses methods for quantifying gait parameters. While a thorough evaluation of gait can be conducted in specialized medical settings, there is a pressing need for a cost-effective, user-friendly, non-invasive, and effortless system that can provide gait information gathered during daily activities in a person's natural environment over an extended period.

3.4 Gait Assessment Tools

Technological devices used to study human gait can be classified into wearable, non-wearable sensors, and hybrid systems using a combination of both methods.

3.4.1 Floor Sensors

The most commonly used devices are non-wearable sensors based on floor sensors—force platforms where gait information is measured through pressure sensors and ground reaction force sensors. Force plates and the GaitRite mat system are commonly used floor systems to assess gait clinically [50].

3.4.2 Image Processing Sensors

Another type of non-wearable sensor is an image processing system that obtains data from the human's gait using optic sensors such as digital cameras, laser range scanners, infrared sensors, and Time-of-Flight cameras. Commercially available systems being used for gait analysis are Vero Vicon, Vantage camera, and Microsoft Kinect [19]. However, optics-based systems have issues related to line-of-sight detection; they do not detect the target behind obstacles. Finally, the use of cameras for motion capture raises the question of the patient's privacy, particularly for in-home applications.

3.4.3 Hybrid Systems

Some studies have chosen to integrate motion capture with other systems for gait analysis. In [20], video cameras from Sony were used along with APDM Opal sensors. In [51], a motion capture system was used along with AMTI force plates for gait analysis. Not surprisingly, integrating two systems increases the precision of the measurement, decreases the ease of use, and increases costs.

3.4.4 Wearable Systems

Wearable systems use sensors located on one or more parts of human bodies, such as feet, knees, thighs, waist, or wrist. Various types of sensors are being used to capture the various signals that characterize human gait, including accelerometers, gyroscopic, magnetometers, force sensors, extensometers, goniometers, active markers, and electromyography. Commercially available sensors such as Opal sensor, BTS G-WALK, Physilog and smartwatches [44] could be used as an in-home gait monitoring system. However, wearable devices have several disadvantages that make them not suitable for in-home monitoring, such as short battery life, the need to download the data, and the need for additional hardware for wireless data collection. Additionally, people may not consistently wear them; they may forget or choose not to wear the device every day. The same limitations apply to several models of shoes with embedded sensors developed for gait assessments. For example, FootMoov shoes are designed with a 3D accelerometer, 3D gyroscope and 3D magnetometer, microprocessors, and wireless modules. However, this is not robustly reliable for long-term, in-home gait monitoring for the same reasons mentioned above.

3.4.5 Radar Sensors

As discussed above, neither optic nor wearable sensors are suitable for monitoring people in their daily life; they can be too cumbersome, inconvenient, and intrusive. In contrast, radar sensors using electromagnetic waves have been proposed as a potential solution for frequent in-home gait monitoring [3], [5], [30], [52], [53]. The use of a radar system is appealing due to its reliable functionality during different illumination levels, protection of privacy, ability to penetrate through obstacles and long-range detection capabilities. Radar sensors could make it possible to monitor and analyze gait outside the laboratory and capture information about the human gait during the subject's everyday activities.

Studies on the application of radar technologies in gait analysis have been conducted to obtain gait parameters. In 2001, a bi-static continuous-wave (CW) radar operating near 10.5 GHz was introduced to be used as a sensor for a human gait assessment system at Georgia Tech Research [54]. However, the system enables Doppler measurement but prevents range estimates. In [55], a motion capture system was used to model the Doppler effects of a walking subject and then compared with the spectrogram of the walking cycles obtained by the radar sensor. The comparison with the spectrogram results with a motion capture system represented the radar gait signature due to legs and body motion [56]. Although this paper used a motion capture system to visualize the Doppler effects of each segment of the human body during walking, the results were not quantitatively analyzed and compared. In 2005, a simple, binary classifier was developed to identify the presence of a subject based on the short-time Fourier transform (STFT) of signals from a CW radar [57]; the STFT performed on received signals from motion provides information on the signal in both time and frequency domain (spectrogram) [58]. A Fourier transform was performed on each bin of the STFT results to extract the cadence frequency. While results were promising, all results (from the spectrogram) were only visualized; more sophisticated techniques are needed to resolve the contributions to gait motion from body parts such as the arms, upper leg, lower leg, and foot.

In [59], human gait was characterized based on a CW radar operating at 24 GHz. Unlike the reference reported in [57], which claimed that the velocity of the torso is constant, this paper demonstrated that the velocity of the torso varies with a sinusoidal shape during walking. Moreover, the radar system showed that human legs produce the highest velocity during walking; while one leg has the highest speed, the other one reaches its minimum value.

In [58], a multiple-frequency CW radar was used to extract micro-Doppler signatures from a vehicle, animals (dog, goat, and deer) and a person performing different activities such as walking, running, jogging, crawling, and transitioning from walking to crawling. The effects of the approach angles of motion on the micro-Doppler patterns were also investigated. It was shown that the micro-Doppler signature of a person walking towards the radar at a relatively 90º angle is different from that at 0º angle. The dependency of the micro-Doppler on the direction of the motion was also investigated in [60]. Although the research in [61] visualized the difference between the motion patterns of humans and other animals, there was no quantification method to compare them nor a method to distinguish those patterns from each other. Furthermore, the dependency of the Doppler signatures on the direction of motions was explained, but no solution was reported to tackle the problem.

Other studies have been conducted to extract other gait characteristics, such as cadence and stride length [62]. In [58], the reflected signals from the torso in the spectrogram were obtained based on the assumption that the maximum signals are related to the torso's return; this assumption is conditionally correct and explained in more detail in Chapter 5. Information-theoretic (IT) techniques [63] were applied to analyze the spectrogram obtained from STFT, as IT can identify the difference between the spectrogram images with the content from all body contributions without analyzing particular body parts. However, most of the works visualized the results without quantifying and showing the exact values of parameters.

Previous researchers [64] used a CW radar operating at 10.525 GHz to conduct tests on ten young men and ten young women (there was no information about their exact ages). Common and different features among men and women were shown. For common features, first, the torso's movement is relatively stationary in the swing phase and has a small speed change during the double supporting time; second, there are regular swing phases with the legs accelerating and decelerating; third, the two legs swing in an almost symmetric state. For differences, first, women have longer double supporting time than men do. Second, women have a more rapid deceleration process in the terminal phase than men. Third, women walk in a more symmetric motion of two legs than men do since normally women walk more smoothly. The results demonstrated the radar capability of obtaining gait data in a human instinctive walking state. The difference between gait patterns of healthy people and a person with Parkinson's syndrome and a man with hemiplegics disease were illustrated in [45]. This research included the quantification of the velocity of the torso, the acceleration of leg in the initial swing, and the deceleration of leg in the terminal swing based on an envelope detection method. However, there was no explanation for obtaining the envelope of the frequency of each part of the body from the spectrogram leading to the quantification of gait parameters. This part is the main challenge in gait assessment; if we can find a way to extract the frequency of each segment of the body from the spectrogram, we can then quantify spatiotemporal gait parameters. Moreover, the paper did not provide a measure of accuracy or other systematic evaluation of the proposed methods.

The overreaching purpose of the research outlined in this thesis is to perform gait monitoring using radar technology to monitor gait during daily life activities. Therefore, it is important to perform gait studies in a familiar and commonly used environment, such as one's home. In contrast, most works reported above were conducted in a low-clutter environment. In [65], it was shown that because of the multipath signals in an indoor environment and the human non-rigid body parts comprising different Radar Cross-Section (RCS) [66] and velocity profiles, the Doppler-frequency pattern in an indoor environment is complex. Two joint time-frequency estimation methods, STFT and the Multiple Signal Classification (MUSIC) [67], have been applied to the received signals from a CW radar to extract the Doppler frequency signature of a human body. Although the accuracy and reliability of their methods were not cited, one of the main strengths of this paper was the proposed methods to quantify the velocity profile from the spectrogram.

As discussed above, CW radars have been explored through various studies to extract gait characteristics as well as to identify the types of walking and distinguish a normal gait from a pathological one. However, one of the significant limitations of CW radars is that the position of the subjects cannot be obtained. As mentioned, the dependency of the micro-Doppler signature on the direction of the motion is a downside of gait detection based on CW radars. Knowing the position of the subject during walking can help a radar-based system obtain the speed of walking through a change in the subject's position regarding its taken time (i.e., velocity = position/time). In [67], two pulse-Doppler range control radars (one for the foot and the other one for the torso) operating at 5.8 GHz were used for gait assessments. This work was different from other studies because of the type of radars they used, in addition to the extraction of the step instances and validation of the methods. Cameras and a Vicon system were used to compare the results of the radar to ground truth data. Moreover, they implemented their proposed approach in real scenarios in 13 older adults' apartments [68], [69]. However, their proposed method was not designed to distinguish walking from other movements, which is the main issue in in-home gait monitoring. Their study also used two radars for gait monitoring, which increases the cost of the implementation. In addition, the proposed method (similar to other works using micro-Doppler signatures) is dependent on the direction of the motion.

One possible solution to overcome the dependency on the relative angle between the radar and a walking subject is to obtain walking speed through the changes in the subject's position over time. FMCW (frequency modulated continuous wave) radars [3], [70]–[73] can provide range information in addition to the Doppler information, which makes it a good candidate for the application outlined in this thesis. Moreover, to obtain a subject's exact position, azimuth information is also required. A MIMO FMCW radar system can provide 2D (x-y) or 3D (x-y-z) point cloud information of a subject in addition to the velocity [30], [72]. More details about MIMO FMCW radar systems are provided in Appendix D.

As mentioned above, the micro-Doppler signature directly depends on the direction of motions. None of the papers discussed above provided a solution to address the dependency of the micro-Doppler pattern on the direction of motions for in-home monitoring. A WiGait system was proposed in [14] that extracts the walking speed through the change in the subject's position. Based on the proposed algorithm, the system identifies walking periods where the user is walking from one point to another and differentiates gait from other activities. After this, the stable phase of each walking period is separated from the acceleration and the time-series data, which are then used to compute gait velocity and stride length. The estimation of the stride length starts with the estimation of the stride frequency by observing how the velocity and location change over time and calculating the Fast Fourier Transform (FFT) of both the velocity and the elevation values. The accuracy of the measures from WiGait was assessed by comparing the values obtained from the radar with values from a Vicon system. Among the eighteen subjects who participated in this experiment, the average error rates were 1.9% and 4.2% for the gait velocity and stride length, respectively. Although [14] obtained the overall velocity from the change in the position, which is independent of the direction, all obtained parameters were the average values. For instance, the stride length was extracted by the division of gait velocity by the stride frequency; this is an approximation rather than a true measured value. It is important to know gait parameters for each cycle because the variation and instability of gait parameters during walking cycles can be obtained through the comparison between parameters extracted at each cycle. Moreover, their heuristic method to identify gait cycles and discriminate them from other activities will fail in the case of other periodic motions, for instance, vacuuming or workouts. Furthermore, like other papers reported above, there was a single subject (mover) in the monitored environment; however, for a long-term, in-home monitoring system, there is a need for tracking multiple people, often simultaneously.

Regarding the problem with one-person gait monitoring, almost all the methods mentioned above are based on the maximum amplitude, which was assumed to be related to the scattered signals from the walking subject. However, this assumption is correct only if the radar is located at a proper height while its main beam illuminates the subject's torso. In other words, if the radar has a narrow beamwidth while located in a way that its main beam illuminates the feet, the maximum signal is not necessarily coming from the torso. In a cluttered environment, multipath effects might create signals stronger than those related to the torso's reflections. Therefore, the assumption is conditionally correct but needs to be addressed in a different radar setup and a highly cluttered environment.

To be used in a home environment, a gait monitoring algorithm must distinguish a subject's walking periods from other activities and be able to handle the clutter that is to be expected in a typical home setting.

3.4.5.1 Integration of AI and Radar Technology

Artificial intelligence (AI) is a method that can be used to tackle the problem of identifying gait periods from other in-home activities. The use of AI leads to extensive research on human activity recognition to determine the type of activity each subject performs. In [74], STFT was applied to the received data of 12 people performing different activities, including running, walking, walking while holding a stick, crawling, boxing while moving forward, and boxing while standing in place and sitting still. A support vector machine (SVM) was used to identify the seven activities fed by the STFT results. In [75], Logistic Regression, Naïve Bayes, K-nearest neighbour (KNN), SVM and Random Forest [76] classifiers were performed on the signals received by a Walabot Pro RF-radar sensor. The comparison of the performance of these classifiers performed on the data from a wrist-worn sensor (Microsoft Band 2), from the radar, and the combination with the radar and the wearable sensor were also provided. Results showed that classification accuracy using the Walabot Pro RF-radar sensor alone was higher than that from the wrist-worn sensor. In [77], the empirical mode decomposition was performed on the signals collected from an S-band radar and a W-band millimeter-wave (mm-wave) radar to produce features to be fed to the SVM classifier. The classifier's results showed that the S-band radar was 75% accurate in identifying human motions through the wall, while the mm-wave had an accuracy of 90% in identifying different types of movements from long distances (91 m). In [74], an SVM classifier was used to categorize different activities such as running, walking, walking while holding a stick, crawling, boxing while moving forward, boxing while standing in place, and sitting still. The resulting classification accuracy was about 85%.

One of the main steps in machine learning is feature extraction, which can be difficult. In [78], Deep Convolutional Neural Networks (DCNN) were applied to the spectrogram of different targets, including a human, a dog, a horse, and a car. One of the main advantages of DCNN is its capability of automatic feature extraction, although it is time-consuming. A comprehensive review of the integration of deep learning with radar technologies in human activity recognition, including deep learning techniques, radar systems, and deep learning for radar-based applications in human activity recognition using radar technologies, can be found in [79].

3.5 Gaps and Challenges

Through the review of the literature presented above, several gaps and challenges remain with using radars for gait monitoring. In the following, some of the identified gaps in the field are listed and linked with the phases conducted in this thesis to fulfill these gaps (Section 2.3).

Most of the studies conducted for gait parameter extraction were based on micro-Doppler patterns of the gait spectrogram. However, this requires research on how to identify frequencies in the spectrogram column bins and how to match those with the corresponding velocity of each segment of human bodies. It has been shown that STFT and other methods mentioned above can visualize the joint time-frequency of human motions, while more sophisticated techniques are required to turn those frequencies into numbers according to each segment of moving parts [3]. Therefore, extracting the speed and other gait values from STFT requires very sophisticated methods or remains an unsolved problem and a significant gap in the radar application of gait detection. Phase 3 and RQ. 1.2 attempt to address this gap.

While FMCW radars can provide the subject's position in addition to the velocity, they have been less explored in gait monitoring (since most studies have focused on extracting the overall velocity by Doppler signatures). Range-azimuth maps of subjects could be useful features in identifying the type of activities, distinguishing gait from other movements as well as extracting gait values. Moreover, the position of the torso can be obtained so that other spatial information of subjects during walking, such as step length, can be extracted. Phase 2 and Phase 3, as well as RQ. 1.1 and RQ. 1.2 attempt to address this gap.

Almost all studies on gait monitoring used off-the-shelf radar sensors without considering the hardware modification for gait analysis. Since radar antennas play a key role in interacting the signals with human bodies and objects around, there is a lack of research showing the impact of radar antenna modification for gait analysis. Phase 4, as well as RQ. 1.3 and RQ. 1.4 attempt to address this gap.

Although the speed of random walking could be extracted using a MIMO FMCW radar, the position of a subject performing other in-home non-walking activities, such as vacuuming, change over time. Therefore, for an in-home gait monitoring and activity recognition system, we need an algorithm to distinguish walking periods from other activities and movements. Machine learning and deep learning have been widely implemented for activity recognition; however, they are not integrated as a basis for in-home gait monitoring and recognition. Most of the research on human gait analysis and activity recognition has been done in a simple, clutter-free, or low-clutter environment with a constrained range and limited activity [26], [29], [52], [80], [81]. However, when someone walks randomly in a cluttered environment such as a usual home, his walking patterns are entirely different from that of straight-line walking in a large area [30]. Identifying walking periods and recognizing the type of activity a person performs is a complicated phase in such an environment using radar signal processing methods. Phase 4, phase 5, phase 6 and Phase 7, as well as RQ. 1.3, RQ. 1.4, RQ. 2.1, RQ. 2.2 attempt to address this gap.

Although gait monitoring was investigated in many studies, there is no report on multiple-people gait monitoring. However, for a long-term monitoring system, there is a need for tracking multiple people, often simultaneously. Phase 5, as well as RQ. 1.5 attempt to address this gap.

Although radar sensors were introduced to be used for frequent daily gait monitoring, there is a lack of a stand-alone IoT and cloud-based sensor to capture the received data without needing an extra desktop/ laptop system to store the data over time. Phase 6 and Phase 7 aim to address this gap.

Chapter 4
Clutter-Free Gait Monitoring

4.1 Relevance

Although radar sensors have been widely used for gait analysis, in many studies, only average gait speed was extracted [52], [55], [68], [82]. There are a few existing studies that employ radar systems and extract several average gait parameters over the entire walking period [6], [14], [26], [69]. For example, in [6], two radar sensors and a treadmill were used to extract average spatiotemporal gait parameters. However, none have developed an automated approach and system that can extract gait parameters at each single gait cycle.

This chapter mainly focuses on how to extract gait parameters (e.g., speed, step length, stride length, step time, step point, step count, etc.) at each single gait cycle using only one single radar sensor. In this chapter, data was collected while a subject was walking in a large clutter-free environment. In this thesis, clutter is defined as stationary/unanimated objects in an environment without considering humans; a clutter-free or low-cluttered environment means an environment with only ground and roof, not other objects. Note that subjects or participants would interchangeably be used throughout the thesis to represent a person (s) walking or performing other activities in data collection periods. Throughout this thesis, all radar data with a subject (s) is captured when subjects only performed walking tests except in Chapter 6, as other activities were also captured for machine learning models for in-home activity recognition.

Since all data for this chapter were collected in a clutter-free environment, it is acceptable to assume that all reflected signals come from a walking subject's body [26], [52], [80], [81]. The second condition is that the subject walks in a straight line in all walking tests. In this chapter, the radar sensor used for this thesis and its proper installation for gait monitoring is detailed first.

Disclaimer: A major part of this section was reported in two journal papers:

- Hajar Abedi, Plinio P. Morita, Jennifer Boger, Alexander Wong, and George Shaker, "Hallway Gait Monitoring System Using an In-Package Integrated Dielectric Lens Paired with a mm-Wave Radar*," Sensors–MDPI*, 2023, 23,71.

- **Hajar Abedi**, Plinio P. Morita, Jennifer Boger, Alexander Wong, and George Shaker, “Hallway Gait Monitoring Using Novel Radar Signal Processing and Unsupervised Learning,” *IEEE Sensors Journal*, 2022.

4.2 Radar Sensor

To collect data, Texas Instrument (TI) mm-wave MIMO FMCW radar sensor (AWR1443Boost) [83] was used for all experiments conducted in this thesis, which operates at 77 GHz81 GHz. This is an mm-wave MIMO FMCW radar that provides range-azimuth-elevation information of subjects in addition to the velocity, so this radar is a perfect fit for this application [72]. As shown in Figure **4.1**, AWR1443 has three transmitters (Tx) and four receivers (RX) capable of estimating both azimuth and elevation angles.

The criteria for selecting the proper radar sensor were as follows:

1. The type of radar: the MIMO FMCW radars have unique advantages that differentiate them from other radar systems, including simultaneous detection of range, angle, and micro-Doppler shifts, which make these types of radars suitable for a variety of applications.
2. Cost: the significant advantages of the new generation of these radars are low-cost, affordable, and scalable.
3. Power: The radar sensor is low power which would have less or no negative health impacts. Its transmitted signals have less than 10 dBm of power. In comparison, Wifi is more than 20 dBm, and cellphones are in the order of 30 dBm. Power-wise, this system is much lower in power than other wireless devices; thus, it could be used for the long term.
4. Availability: the radar sensor is available and can be purchased online, whereas many other commercial radar sensors are not sold to individuals easily.
5. Easy access to raw data: a data-capture adapter, DCA1000 EVM board [84], was developed by TI to transfer binary data of chirp samples over the UART interface to a PC. MATLAB could be easily used to process the raw data from the radar.
6. Performance of the radar sensor: the performance of the radar sensor was proven in other studies conducted in Wireless Sensors and Devices Lab (WSDL) for automotive applications [72], [73], [85]–[88].

7. Frequency of operation: this mm-wave radar operates at 79 GHz; mm-waves are non-ionizing, unlike x-rays which do sort ionize body molecules. Mm-wave is absorbed by water and does not penetrate the body; electromagnetic absorption at these frequencies is more than 10 times less than those used for cellular bands and Wifi.

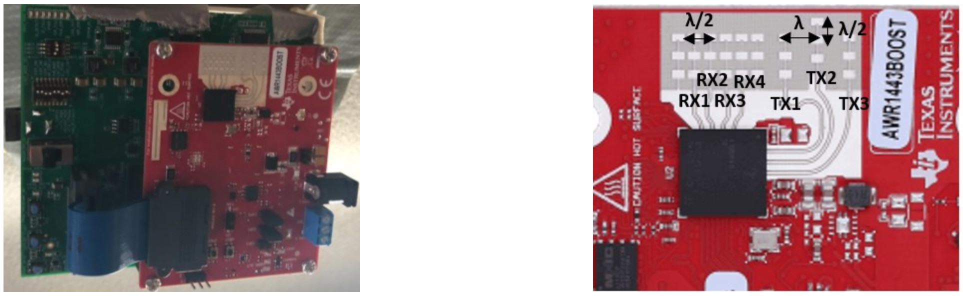

(a) (b)

Figure 4.1. AWR 1443 radar integrated with the DCA1000 board (a) front view of the sensor and (b) PCB antennas.

4.2.1 Radar Installation

Human locomotion (which includes the gait cycle) is a complex scenario. The velocity of each segment of the human body varies over time, leading to different Doppler shifts (micro-Doppler) in scattered signals [59]. As discussed in the literature review, using a CW radar, micro-Doppler signatures have been extracted as a superposition of Doppler shifts in received signals [6], [89]. However, the position of signals coming from subjects' different body segments has not been distinguishable; micro-Doppler signatures show complex patterns requiring very advanced algorithms to extract each velocity accordingly. In previous studies, the speed of a walking subject was obtained based on the assumption that the maximum signal in the spectrogram is associated with the torso. However, this type of extraction can be extremely noisy and inaccurate as the signal-to-noise of the radar may not be sufficient [3]. This is because the returned signals are often not isolated to the torso line, but knee and arm motions can also be picked up as the strongest signal depending on the angles and RCS of each body part [3]. The radar should be located where its main beam illuminates the torso to associate the maximum of the reflected signals to the torso. From the Lund & Browder chart [90], the torso contributes approximately 13% of the total body surface area, which is more than the surface area of other parts. Therefore, with an appropriate radar setup, an individual's torso constitutes a major part of the reflected signals. Two factors play a crucial role in finding the best position to place the radar sensor: (1) radar antenna radiation pattern and (2) the height of the radar.

For the first factor, the radar antenna patterns could be found online (if the radar is an off-the-shelf one), or they could be simulated and measured. To install the radar and find an appropriate location, we first analyzed the radar antenna radiation pattern. Although the radar radiation pattern is available online [33], we simulated the radar antennas in HFSS (High-Frequency Structure Simulator) [91] and measured the radiation patterns. In this chapter, for simplicity, we just provided the simulated 3D radiation patterns of the radar antenna while transmitting with the Tx_1 in Figure **4.2** (a) to show the wide beam of the radar antennas. Figure **4.2** (a) shows that the radar antennas provide a wide beamwidth with more than 10 dBi gain. This wide beamwidth ensures wide coverage of the environment. As Figure **4.2** (a) shows, the antenna's main beam occurs at azimuth and elevation angle of $\theta= \varphi =0$ °. Figure **4.2** (b) shows the orientation of the radiation pattern and the antenna structure on the radar board, simulated in HFSS. More details about the radar sensor and simulation/measurement results can be found in Section 5.2.2

Figure **4.3** depicts the proper radar setup (radar position) at the height of "h", showing the main beam illuminates the subject's torso. To obtain the best value for "h", we referred to some facts about the average value of human height, lower body length and torso length. Based on the average human height of about 164.5 cm, the mean lower body length of about 98 cm (1.4 of the height) and a mean torso length of about 48 cm [92], the radar was located at a height of 120 cm to illuminate the walking subject s' torso with its main beam. With this measurement setup, the chance to pick up strong returned signals

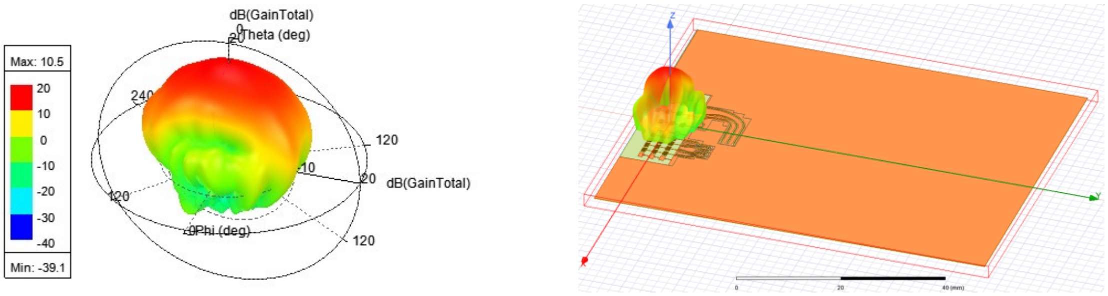

(a) (b)

Figure 4.2. Antenna Pattern (a) simulated 3D radiation pattern of AWR1443 radar antenna (transmitting with Tx_1) (b) orientation of the radiation pattern and the antenna structure on the radar board.

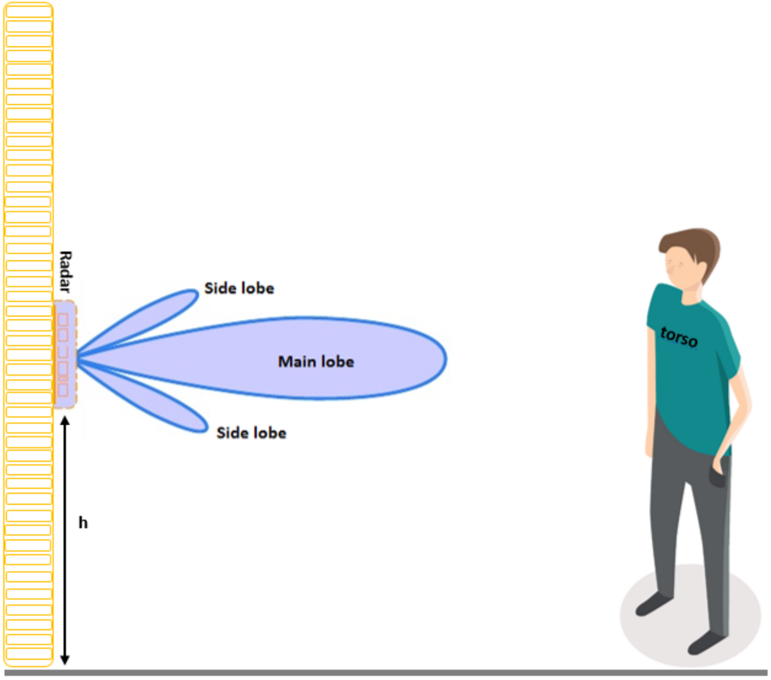

Figure 4.3. Proper radar position for gait monitoring (the main beam illuminates the torso).

from knee and arm motions is very low, and then the torso line can be selected from the occupied range bins by isolating the maximum signal. Unlike many studies [93]–[98], we suggest that both antenna patterns and signal processing techniques should be considered in radar-based gait monitoring systems. As discussed, the height of h=120 cm was selected based on the average height of human beings [92], so with this setup, the maximum signals come from the torso line (for the case of walking in a clutter-free environment). This height is the proper position where, regarding the average human height and the length of the torso, the main beam of the radar will illuminate the walking subject's torso.

In addition to the position of the radar sensor and its antenna pattern, a suitable radar sensor can make the gait monitoring algorithm easier and faster. As stated above, since CW radars cannot provide the position information of subjects, and micro-Doppler of each body part cannot be obtained using the range bin, sophisticated methods are required to extract the velocity of the torso [54], [59], [64], [99]. However, due to some distinctive features of FMCW radar sensors [28], [72], [73], [87], [88], FMCW radars are promising alternatives as range and micro-Doppler could be provided simultaneously. Moreover, as shown in the following chapters, a MIMO is chosen because the subjects' angle information is also needed for several gait monitoring scenarios. Therefore, for this thesis and for the sake of consistency throughout the whole experiments conducted in this thesis, an mm-wave FMCW radar operating at 76 GHz—81 GHz was used. This range of operation has many advantages, such as large bandwidth, higher resolution, small component size (for example, smaller antenna dimensions), and cost-efficacy.

More details of FMCW radars are provided in Appendix A, but generally, as a subject walks, his body occupies multiple cells of range bins calculated from FMCW radars. Although the RCS of various body parts (the amplitude of each occupied cell bin in FMCW radar's data) is a function of aspect angle and operating frequency, a proper radar setup could align the main beam of the radar with the torso; without a proper setup, every algorithm is prone to failing.

4.3 Measurement Setup

To assess the effectiveness of this thesis' proposed gait monitoring algorithm for gait parameters, such as step length and step counts, the true/ reference values were extracted by asking volunteers to follow a traced line with marks on which the volunteers had to step. These scenarios helped to know the number of steps each subject takes (the cadence) in addition to the step length. Using a stopwatch and knowing the total distances each subject walked as a rough estimate of accuracy, the ground truth velocity was calculated and compared with the result obtained from the proposed algorithm performed on the received signals. It should be mentioned that due to the COVID-19 restriction, we did not have access to a GaitRite Mat or a Vicon system during these experiments.

As shown in Figure **4.4**, for all experiments conducted in a clutter-free large environment (in a local industrial partner's garage located in Waterloo), a participant walked 420 cm in 6 steps toward and away from the radar three times. The distance between each marker (step length) was 70 cm for men, and 60 cm for women participants, as this was cited as the average step length for men and women [100]. The reason for the selected distance of 420 cm for walking was that the active area of the GaitRite (14' model) is 4.27 m, and this is analogous to a typical hallway length in a conventional home environment (e.g., house or apartment). The GaitRite was referred to because it was aimed to be used as a ground truth before COVID-19 restrictions. It should be noted that the setup shown in Figure **4.4** is designed to calculate cadence and step length and may not fully represent the gait patterns observed in a home environment. However, this setup was chosen to provide a controlled environment to validate the accuracy of our proposed algorithm for calculating cadence and step length. Moreover, the current

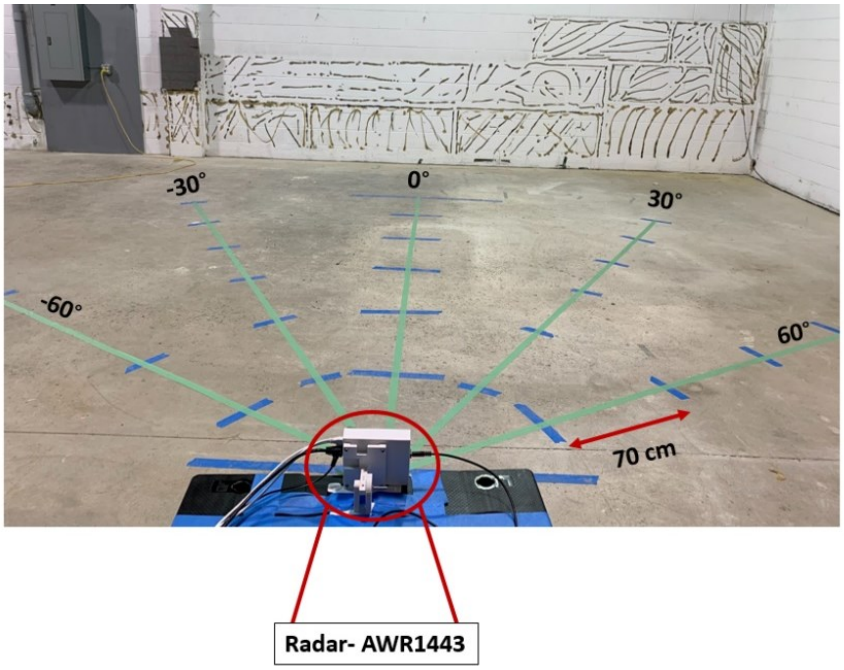

Figure 4.4. Experimental setup for gait assessment in a large clutter-free environment.

experimental setup does not consider the natural variability in stride lengths that occurs in a home environment, especially during acceleration/deceleration and at the ends of a hallway. This variability might potentially affect the accuracy of gait measurements, walking speed, and activity recognition. Future work is needed to focus on validating the algorithm using data collected from home environments to ensure that it can accurately capture the full range of gait patterns.

According to the walking distance, the radar configuration parameters used for experiments in this chapter are defined and listed in Table **4.1**

4.4 Gait Extraction Algorithm

The block diagram of the proposed gait extraction algorithm is depicted in Figure **4.5**. To obtain range information of a walking subject, the range FFT is applied to the received chirp samples from the FMCW radar [72], [73]. Since the array of antennas is not entirely isolated in the MIMO system, the leakage between two antenna elements (especially between receivers and transmitters) is removed [28], [72], [73]. To remove signals reflected from stationary targets (clutters) in signal processing, a stationary clutter removal algorithm is performed on each channel to remove all stationary targets. To

Table 4.1. Radar parameters, definition and values used for radar configuration.

Characteristic name	Characteristic description	Specification	Units
Start Frequency	The frequency the radar signal will start at	77	GHz
Frequency Slope	The slope at which the frequency of the radar is increasing.	60	MHz/μs
Idle Time	The time between the previous chirp finishing and the frequency ramp starting	250	μs
Transmit Start Time	The time within the chirp where the transmitter is turned on	98	ms
ADC Start Time	The time when the ADC starts sampling	10	μs
ADC Samples	The number of samples the ADC takes	64	
ADC Sample Rate	The rate at which the ADC takes samples	2200	Ksps
Ramp End Time	The time when the frequency ramps finished	60	μs
Bandwidth	The total frequencies spanned by the chirp	3600	GHz
Chirps/ frame	The number of chirps per frame	256	

do so, the average value of the signal is computed and subtracted from the aggregated signals [28], [72], [73]. Therefore, the range profile of a walking subject is obtained. Note that since we considered only one walking subject to be monitored in this chapter, we used only one transmitter and one receiver, meaning that there is no need for a MIMO radar sensor for single-person gait monitoring. However, the MIMO channels should be used for multiple-person scenarios and in-home gait monitoring, as shown in the following chapters.

The whole body of a human being could be regarded as a single point to extract and quantify gait parameters [14]. Since an individual's torso constitutes a significant part of the reflected signals, the torso line can be selected from the occupied radar range bins by isolating the maximum signal [14], [52]. As discussed above, this is true only if the main beam of the radar antenna illuminates the torso. For instance, if the radar is on the ground and directed at the walking subject’s legs, the torso’s reflected signal might not create the maximum value in the FMCW radar range bins. However, as shown in Figure **4.3**, a proper installation setup was considered, thus, it ensures that the main beam is directed at the torso of the walking subject. As shown in Figure **4.5**, obtaining the torso’s range bin by taking the maximum value in the range bins, the position of the walking subject is approximated. Having the

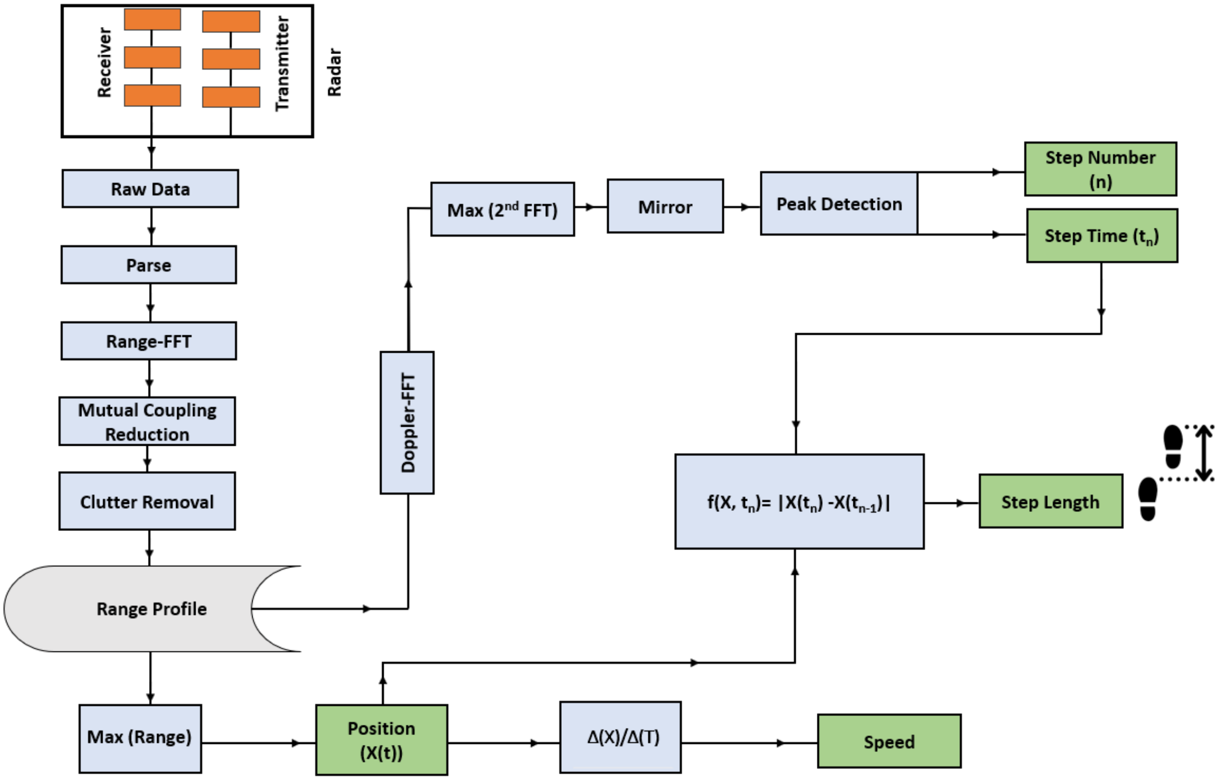

Figure 4.5. Gait parameter extraction algorithm.

position of the subject over time, the overall velocity of walking (i.e., the distance a walking subject travels over a second (velocity=position/time)) can be calculated.

The velocity of the torso is calculated by performing a second FFT (Doppler-FFT) over the torso's range bin. Since the maximum velocity of the torso is achieved when the foot touches the ground (step time) [59], applying a peak detection algorithm to the results of the absolute value of Doppler-FFT over the torso's range bin, the torso's maximum speed is obtained. To extract the torso's maximum speed, a peak detection algorithm is applied to the Doppler-FFT. Based on the peak detection algorithm [101], a local peak is defined as a data sample which is either larger than the two neighbouring samples or is equal to infinity. We defined two variables for the peak detection algorithm, 'Min Peak Height' as MPH and 'Min Peak Distance' as MPD. MPH finds only those peaks that are greater than the minimum peak height, and MPD finds peaks separated by more than the minimum peak distance. MPD is specified to ignore smaller peaks that may occur in close proximity to a large local peak. In this work, MPH is the minimum acceptable value of the maximum velocity of the torso. To find a proper value for the MPH, we assumed that the subject walks more than 0.5 m/s. Moreover, MPD is the minimum time interval between two consecutive step points. MPD is set to 0.1 s because we assumed that our subject could not take a step for less than 0.1 s. These two variables are selected based on the fact that our subjects are walking but not running. Moreover, several studies have shown that the cut-point for speed is 1 m/s [9], [17], meaning that any value less than this threshold might notify an unhealthy status of the subject. In this regard, in this chapter, we set MPH to 0.5 m/s to cover almost all types of subjects and even the worst-case scenarios when subjects walk very slowly. The corresponding time of the torso's maximum speed shows the time when the foot touches the ground (contact position time/step time). Then, the contact position time can be obtained, which can be used to determine the number of steps or step counts.

Consequently, as shown in Figure **4.5**, knowing the step time of every single step (t_n) along with the position of the subject ($X(t_n)$), the step point of each step is acquired. The step length at each cycle is then obtained by subtracting two consecutive step points. Finally, a count of the number of occurrences of these maximum values over time results in the overall step count. It is worth mentioning that we take advantage of the distinctive feature of FMCW radars, providing the range and Doppler information of a subject simultaneously, enabling us to provide spatiotemporal gait parameters using only one radar sensor. While other methods reported in the literature have extracted the average value of cadence and other parameters by applying FFT on the spectrogram [6], [67], [102]–[104], our proposed method can show the instance gait values (spatiotemporal gait parameters at every single gait cycle) of each metric. Note that the instance values of each gait cycle could be used for balance detection and other gait analysis in future works [3]. A full gait cycle is defined from one heel strike to the next [6].

4.5 Gait Values Obtained in a Clutter-Free Environment

The results presented here are from the measurement setup conducted in the garage (Figure **4.4**) because of less clutter in the surrounding environment. To show the extracted gait parameters at each stage of the proposed algorithm, obtained results from one participant walking at a relative angle of 0^{o} with the radar are detailed here.

The results of the range-FFT at two different positions of this subject, at the range (radial distance between the radar and the subject) of R=5.82 m and R=3.44 m away from the radar, are plotted in Figure **4.6** (a) and (b), respectively, after running the clutter removal algorithm. As mentioned above, stationary clutter removal is done on each channel to remove all stationary targets by computing the average value of the signals and subtracting them from the aggregated signals. Since there is only one moving subject (the walking subject), the FFT results, performed on chirp samples, show only one peak at the target position for each frame. The range-azimuth map of the subject at R=3 .44 m away from the radar is also illustrated in Figure **4**.**7**. The details on how to provide a range-azimuth map of the subject are provided in Appendix C. The same process was applied to all frames of walking periods. The trajectory of the walking subject (three times toward and away from the radar) is plotted in Figure **4**.**8**. As seen in Figure **4**.**8**. (a), the subject started moving toward the radar at a distance of R=5.8 m from the radar to a range of R=1.6 m near the radar.

These results show the three times back-and-forth movements. Additionally, applying the second FFT on the maximum range bins of the selected range bin, the velocity of the torso was obtained and shown in Figure **4**.**8**. (b). As seen, the velocity of the torso is negative when the subject is getting close to the radar and is positive during moving away from the radar. In addition, it is evident from the results that the velocity of the torso is not constant during walking, but it is a saw-tooth shape, showing the stance and swing phases [53]. Figure **4**.**8**. (b) also shows the transition between positive and negative velocities that are turning cycles. To the best of the author's knowledge, this research was the first time that the velocity of torso's component at each cycle was obtained using torso's range bin. Previous methods obtained the average velocity of the torso by performing FFT on the maximum value of the spectrogram using CW radars, which might not be accurate since the spectrogram is a superposition of all components of our body [89].

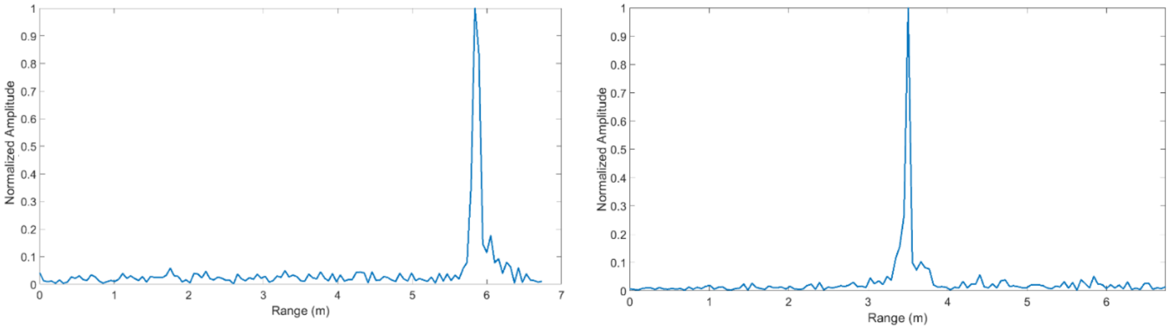

(a) (b)

Figure 4.6. Range- FFT of a walking subject in the clutter-free environment for the case when the radar was installed at the height of h=120 cm (a) R=5.82 m and (b) R=3.44 m.

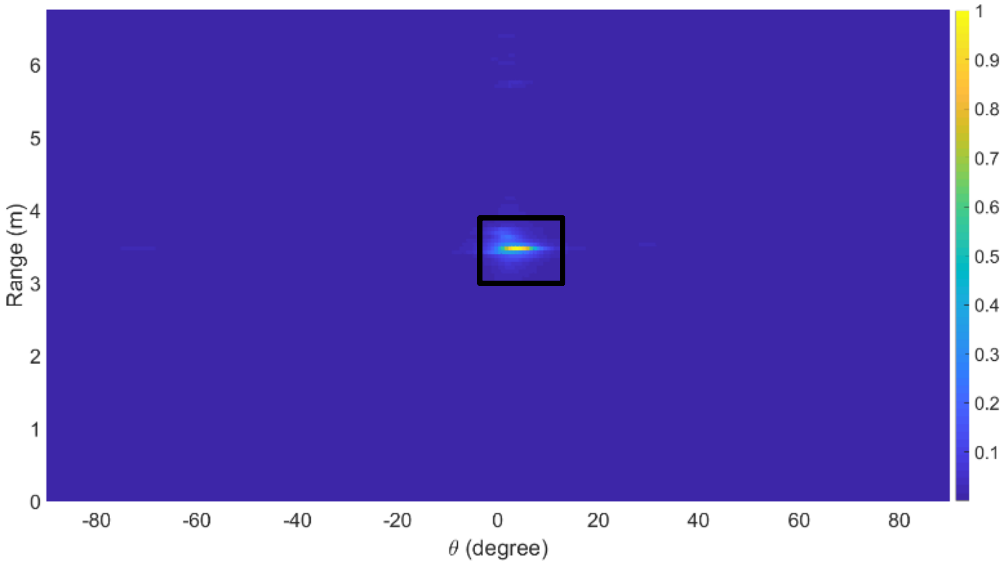

Figure 4.7. Position (R=3.44 m) of the walking subject in the clutter-free space (heat-map obtained by the Capon beamformer [72].

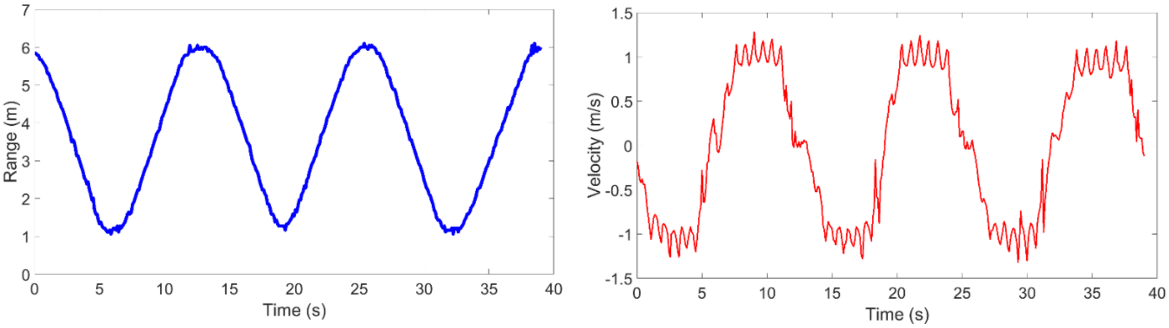

(a) (b)

Figure 4.8. Trajectory of a walking subject in a clutter-free environment for the case when radar was installed at h=120 cm. (a) range of the target over time (b) the velocity of the torso over time (the variation of the peak velocity is due to the bipedal motion of the human body).

A walking cycle is a complex motion where all segments of our body create various frequency shifts in the returned signals. To show shifts in frequencies, the range-Doppler (Doppler is transformed in velocity) map of the subject at R=3.44 m away from the radar is illustrated in Figure **4.9**. As shown in [59], although a small portion of the reflected signals comes from the leg, the velocity of the leg is higher than that of the torso. The maximum amplitude of the range-Doppler map is associated with the torso signals.

The spectrogram showing a typical micro-Doppler signature of the motion is illustrated in Figure **4.10**. More details on how to provide the spectrogram are provided in Appendix B. The speed is displayed on the vertical axis, and the time on the horizontal. The amplitude of the reflected signals is color-coded in this thesis, with yellow being the highest intensity and blue being the lowest. Forming these short-time FFTs is the first step in processing because it visualizes the velocities and the amplitudes of the moving body components. The dominant contribution to the micro-Doppler signature appears to be the motion of the torso and the legs, but since it is not rigid, there is no distinct line but a spectral spread, and the contribution of the arms is not as dominant. The body motion, which is the stronger component underneath the leg swings, tends to have a slightly saw-tooth shape because the body speeds up and slows down during the swing phase [105].

As shown in Figure **4.10**, the spectrogram visualizes the time-frequency created by human motion while quantitatively understanding the radar return characteristics of these typical motion classes is considerably needed for gait assessment. It is necessary to extract the value of gait parameters for each walking cycle. As shown in Figure **4.8** (b), the velocity of the torso, showing a saw-tooth signature, was obtained by applying FFT on the torso's range bins. Since the torso's speed goes ups and down during the stance and swing phases, extracting the maximum and minimum of these saw-tooth signatures can be used to obtain the stance and swing time. Further, by applying a peak detection algorithm to the torso's velocity plot, stance and phase time can be obtained.

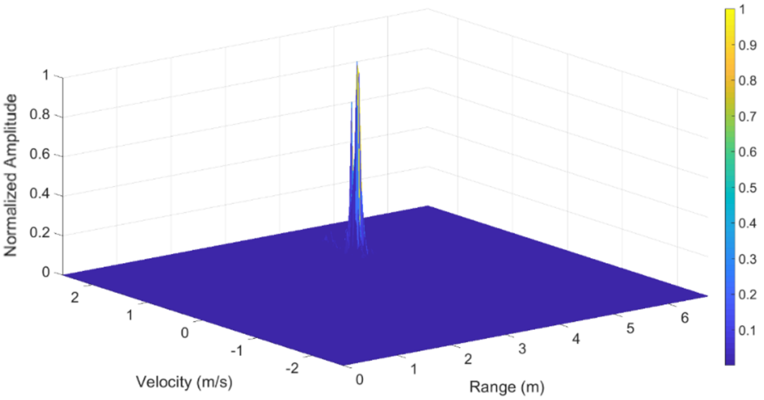

Figure 4.9. Range-velocity map of a walking subject in a clutter-free environment (R=3.44 m).

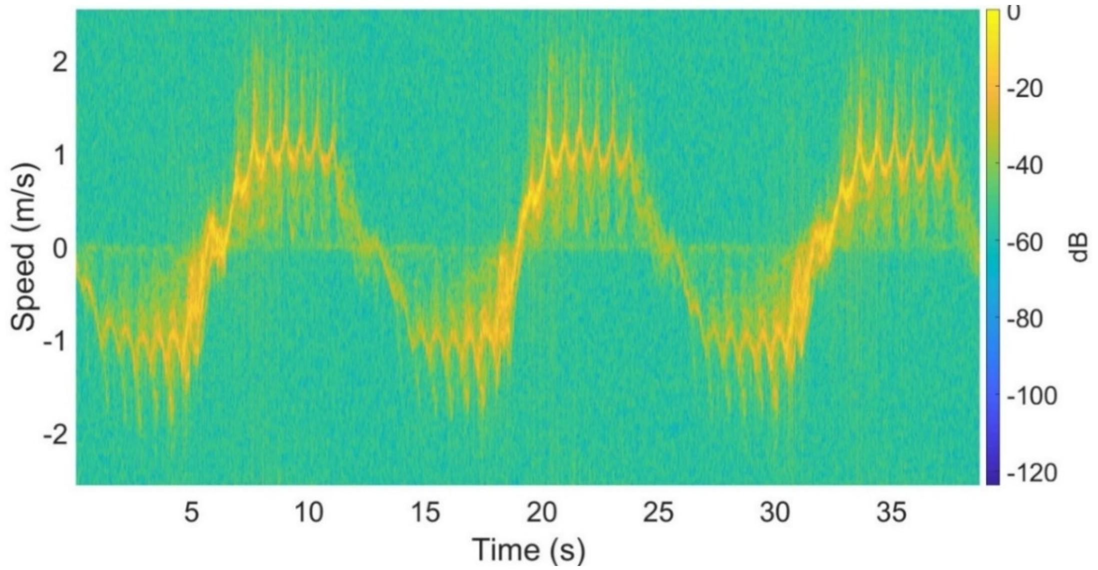

Figure 4.10. Joint time-velocity representation of a walking subject in the clutter-free environment for the case when radar was installed at h=120 cm.

Figure **4.11** shows the result of the peak detection performed on the absolute values of the torso's speed. As shown, the number of steps is equal to the number of peaks in the plot, corresponding to the time when the participant took one step. As seen in Figure **4.11**, the proposed algorithm accurately detects all six steps taken by the walking subject in addition to the steps taken during turning cycles (steps #19, #32 and #39). In Figure **4.11**, gait parameters were extracted, including step time, stance and swing time, and the number of steps/time (cadence). Additionally, by extracting the corresponding time of each step and having the position of the subject during walking, step length at each cycle can be obtained from the range of the subjects over time. Figure **4.12** shows the step points over range during walking where step length and stride length are shown that the distance between two successive points is the step length.

As described above, by applying the proposed gait monitoring technique using the FMCW radar, spatiotemporal gait parameters such as step length, stride length, step time, and overall speed could be extracted at each cycle. To the best of the author's knowledge, during this thesis, the stride length, contact position, and contact time for each cycle were extracted using an mm-wave FMCW radar for the first time. As mentioned, the proposed method is based on the condition that the radar antenna's main beam illuminates the human's torso, leading to the maximum amplitude of range bins being related to the torso's range bin; otherwise, the maximum value may not be associated with the torso's

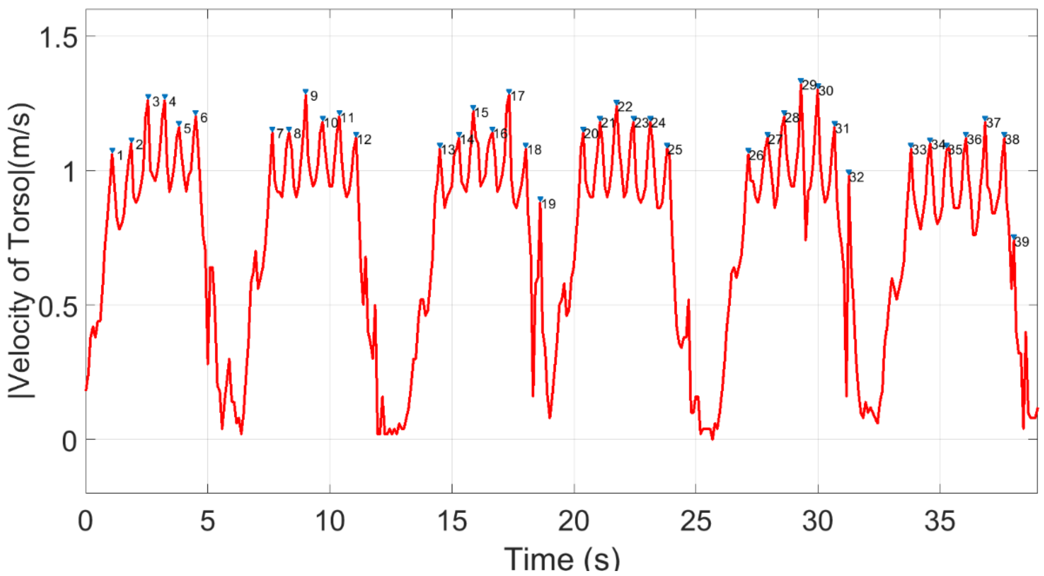

Figure 4.11. Peak detection algorithm applied to the absolute value of the torso velocity showing the steps time and the number of steps.

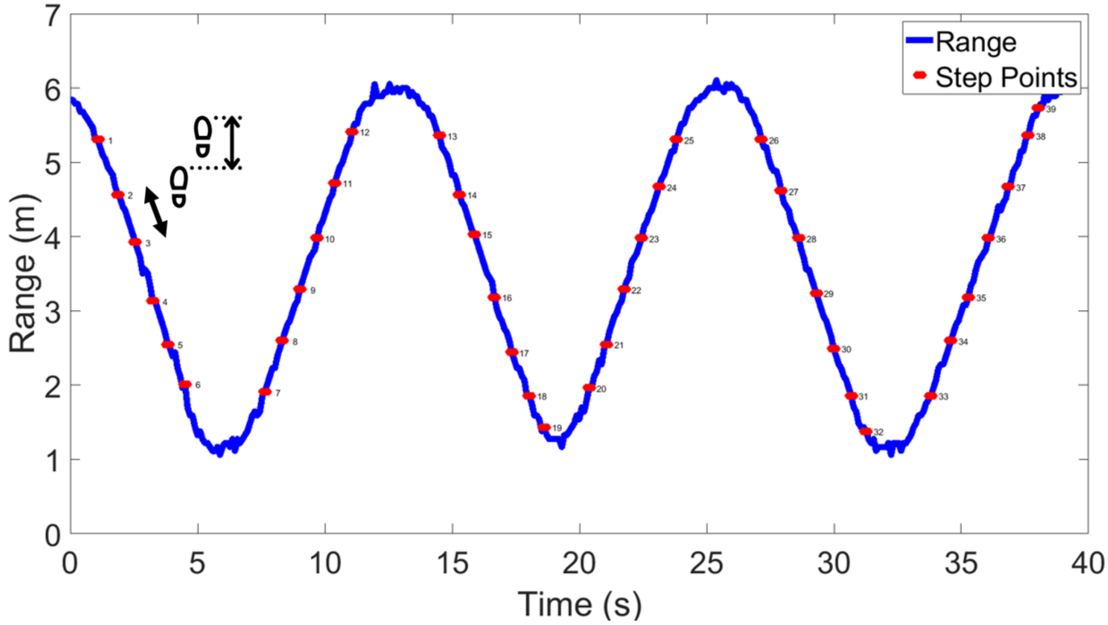

Figure 4.12. Range of the subject walking in a clutter-free environment for the case when the radar was installed at h=120 cm. Step points (dots) and step counts (numbers) detected by the algorithm are indicated on the plot line.

reflections. The radar was placed at a low height (15 cm above the ground), and gait parameters were extracted to show the importance of a proper height ("h=120" for my radar setup). The same protocol used for the previous tests was also used here.

The joint time-velocity representation (STFT performed on the radar data received from the walking subject) in Figure **4.13** shows that when the radar was located at "h=15", the torso's returns were not the dominant signals. Therefore, the maximum amplitude is not associated with the torso's reflections but from the leg's signals at various periods as the radar is located close to the ground, the algorithm fails in extracting the stance/swing phases. In this regard, Figure **4.14** shows the result of the FFT applied to the maximum signals of the range bins, which are not necessarily the velocity of the torso; in many cycles, instead of extracting the velocity of the torso, the velocity of legs is derived. Therefore, applying peak detection to the absolute value of the velocity, various points were selected, while the actual number of steps was six for each round. As seen in the case where the radar was not located at the proper height, the proposed algorithm does not function correctly. These results confirm that all signal processing techniques for gait monitoring should be associated with adequate hardware setup and performance. It should be noted that for real-world environments, our system can also be

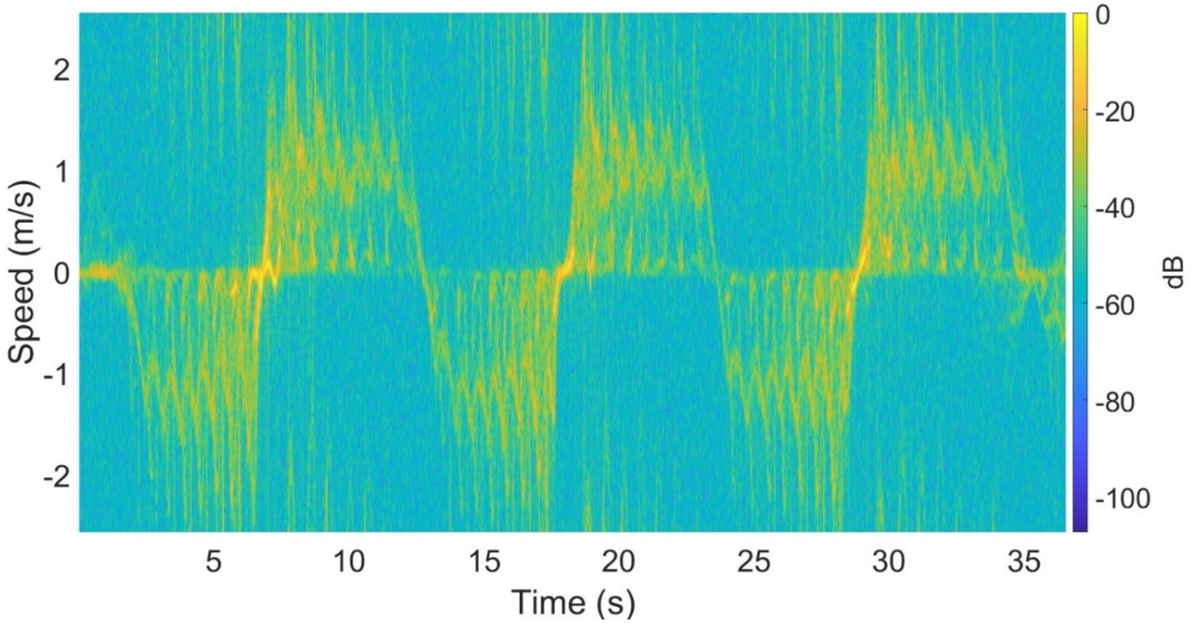

Figure 4.13. Joint time-velocity representation of a walking subject in a low cluttered environment from the case when radar was located at h=15 cm.

customized to accommodate multiple occupants. 5.3, this setup is tested with a larger group of 22 participants to increase the validity of our results.

A summary of the extracted values of walking at different angles is provided in Table **4.2**. As seen, the proposed gait extraction algorithm is very accurate in calculating the walking speed, which is independent of the direction of walking. This is because walking speed is obtained based on the change in the subject's position over time, not the micro-Doppler pattern. For other gait values, although the algorithm uses the Doppler patterns to find the step time, the accuracy is not significantly impacted by the direction of walking. The reason is that our proposed algorithm is based on the variation of the torso’s velocity during the stance and swing phases (it speeds up and slows down, creating a sawtooth shape) but not the actual value of the Doppler.

In Chapter 4, the criteria for radar sensor selection to be used to carry out experiments in this thesis were outlined. A proper installation option and consideration were also detailed. Additionally, a gait extraction algorithm was proposed to extract spatiotemporal gait values at each single gait cycle.

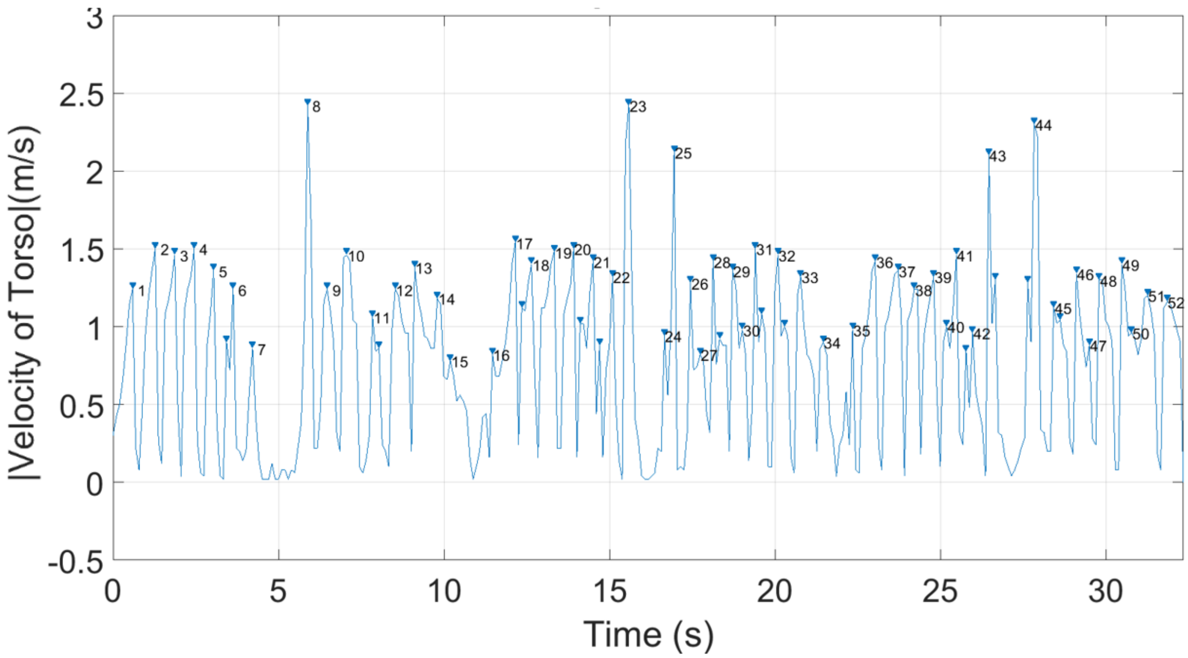

Figure 4.14. Peak detection applied to the absolute value of the velocity of a walking subject in a low cluttered environment for the case when radar was located at h=15 cm.

Table 4.2. Extracted gait values in a large area in various directions.

Direction of walking	Step count	Error in Step Count	Step length (cm)	Error in step length (cm)	Speed (Radar) (m/s)	Speed (Stopwatch) (m/s)	Error in speed (m/s)
-60 °	35	1	65.7974	-4.20	0.95	0.91	0.04
-30 °	36	0	68.0146	-1.98	0.86	0.90	-0.04
0 °	36	0	69.1098	-0.89	0.95	0.97	-0.02
30 °	36	0	68.5695	-1.43	0.94	0.98	-0.04
60 °	33	3	65.0564	-4.94	0.94	0.98	-0.03

Differences between this proposed gait extraction algorithm and those found in the literature are as follows:

1) Extract the velocity of the torso from the torso's range bin, while previous works obtained the average walking speed by extracting the maximum value of the STFT signature of walking.
2) Apply a peak detection algorithm on the velocity of the torso to extract several gait parameters for each cycle; previous methods applied FFT on the spectrogram (SFTF patterns) to get the average value of stride length without extracting other parameters at each cycle.
3) Find the proper position of the radar to be used for gait monitoring according to its radiation pattern.
4) Fast and easy-to-implement gait extraction method, independent of the direction of movements.

In contrast to the existing published research, we employed only one single FMCW radar and developed autonomous algorithms for gait analysis. The novelty in this chapter is the spatiotemporal gait features extracted at each gait cycle. Although the results obtained in this chapter should be validated by a ground truth such as a GaitRite mat or a Vicon system, in addition to the inclusion of more participants, the FMCW radar was shown to be able to extract spatiotemporal gait parameters at each single gait cycle. As detailed in the following chapters, the proposed gait extraction method was implemented in a more challenging environment, such as a hallway.

It should be noted that due to radar's resolution limitations, it cannot provide detailed information about specific body parts, angles, joints, and pressures during the walking activity. The radar signal reflects from the entire body, making it difficult to distinguish between different body parts. However, this limitation does not affect the main purpose of this thesis, which is to develop a system for high-level detection of walking activity and gait analysis. Future research could explore the use of higher resolution radars, and complementary sensor modalities, such as wearable or pressure sensors, to provide more detailed information about specific body parts and angles. However, the use of multiple sensors also increases the complexity of the system and requires careful calibration and synchronization. Overall, while the radar system used in this thesis has some limitations, it still offers a promising approach for non-invasive and remote monitoring of walking activity and gait analysis in home environments.

Chapter 5
Hallway Gait Monitoring

5.1 Relevance

As stated in Chapter 3, the most currently available methods for gait values extraction were based on Doppler information, which depends on the relative angle between the radar and a walking subject [3], [53]. Additionally, most of them were conducted in large clutter-free environments [26], [52], [80], [81]. However, there is a pressing need to develop gait assessment solutions for naturalistic settings (e.g., individual's homes, long-term care, and hospitals). We proposed hallway gait monitoring as a simple and practical solution for continuous gait assessment in long-term care facilities. Hallways are commonly found in various living environments and provide a predictable location where individuals frequently walk, making them suitable for gait analysis [106]. One of the main challenges in such environments is the existence of stationary objects (i.e., clutter), creating multipath signals or ghosts [107]. Walls in the hallway have a strong "clutter" impact, creating multipath signals due to the wide beam of commercially available radar antennas [3], [106]. Multipath occurs when a signal takes two or more paths from the transmitting antenna to the receiving antenna. The multipath reflections can interfere with the accuracy of gait measurement algorithms that rely on the assumption that the maximum reflected signals come from the torso of the walking subject rather than indirect reflections or multipath [6]. For instance, reflected signals from the torso in the spectrogram were obtained in [6] to extract stride rate based on the assumption that the maximum signals are the torso's returns. However, this assumption is correct only if the subject is walking in a large clutter-free environment [3]. The number and particular behaviour of the multiple paths depends on the room structure and the presence of objects [107]. The multipath issue is more significant when people walk since moving even a small object in an environment causes changes in multipath reflections [107]. Radar technologies must be able to work in practical settings where day-to-day gait assessments will be made to be broadly applicable. [3].

This thesis proposes two viable solutions to eliminate the multipath reflections: (1) Novel signal processing and (2) Radar antenna modification. This chapter details these two methods in two separate subsections for single-person hallway gait monitoring. Moreover, Section 5.3 covers proposed multiple-people hallway gait monitoring methods.

Disclaimer: A major part of this section was reported in four journal papers:

- **Hajar Abedi**, Ala Eldin Omer, John Hanna, Steven Ding, Ahmad Ansariyan, Andrei Felipe Perez, Tom Paraschuk, Plinio P. Morita, Jennifer Boger, Alexander Wong, Safieddin Safavi-Naeini, and George Shaker, "In-Package Integrated 3D-Printed Dielectric Lens for a Millimeter-Wave Radar," *IEEE Transactions on Components, Packaging and Manufacturing Technology* (under review).
- **Hajar Abedi**, Plinio P. Morita, Jennifer Boger, Alexander Wong, and George Shaker, "Hallway Gait Monitoring System Using an In-Package Integrated Dielectric Lens Paired with a mm-Wave Radar*, " Sensors–MDPI*, 2023, 23,71.
- **Hajar Abedi**, Plinio P. Morita, Jennifer Boger, Alexander Wong, and George Shaker, "Hallway Gait Monitoring Using Novel Radar Signal Processing and Unsupervised Learning," *IEEE Sensors Journal*, 2022.
- **Hajar Abedi**, Eric Hedge, Carmelo Mastrandrea, Ahmad Ansariyan, Plinio P. Morita, Jennifer Boger, Alex Wong, Richard Hughson, and George Shaker "Non-Visual Contactless RF Sensor Shows 14-Day Head-Down Bedrest Promotes Reductions in Walking Speed," (under preparation).

5.2 Single-Person Hallway Gait Monitoring Methods

5.2.1 Signal Processing

A novel hallway gait monitoring algorithm was proposed to address the multipath problem that could be deployed for any radar type without the need for radar sensor alteration or modification. The proposed method uses the MIMO features of an FMCW radar to find the range and azimuth heatmap of the environment along with the Doppler information of a walking subject.

The block diagram of the proposed hallway gait monitoring algorithm is illustrated in Figure **5.1**. To show the detail of our proposed system and the corresponding result of each section of the algorithm, the results of the proposed system deployed in a long hallway, as pictured in Figure **5.2**. It should be noted that in the hallway alcove, there was a hospital transport stretcher, a wheelchair, a medical cart, a metal cabinet, and some other wooden objects, causing too many multipath effects. The same commercially available mm-wave FMCW radar (Figure **4.1**) was used for this experiment. All the

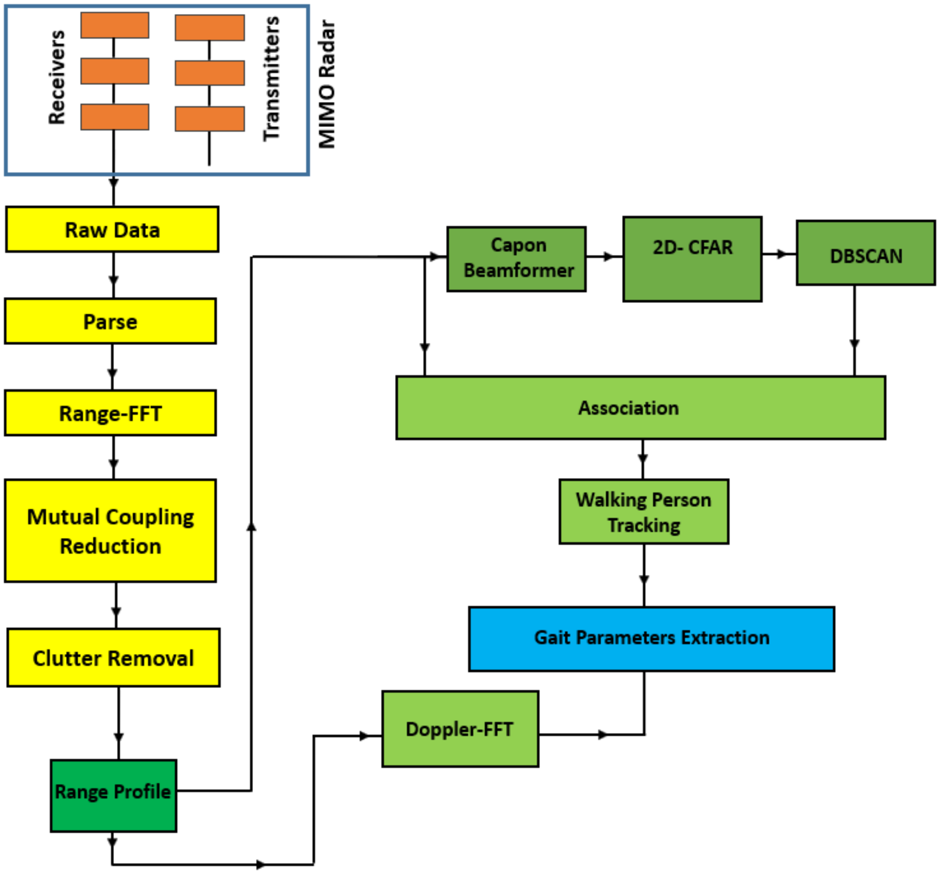

Figure 5.1. Proposed single-person hallway gait monitoring algorithm.

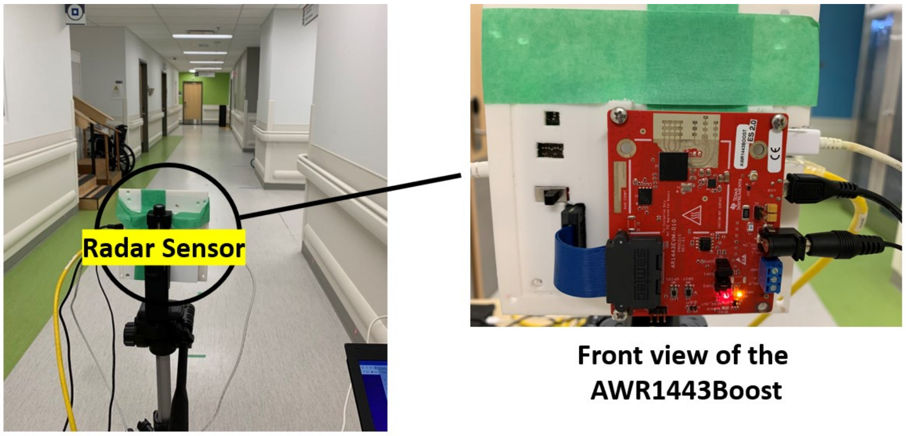

Figure 5.2. Experimental setup for 14 m- hallway walk at MUHC.

results provided in this chapter are radar-agnostic, and the proposed algorithm could be paired with any other type of MIMO FMCW radar. The radar configuration for this experiment is listed in Table **5.1**. Since the goal was to cover 14 m walking segments, the radar was configured for a maximum range of 16.4986 m. The radar was placed 1.5 m away from the walking subject's starting point. The schematic of the hallway walking test setup is provided in Figure **5.3**. The maximum and minimum relative angles between the radar position and the hallway walls are 38.19° and 4.02°, respectively.

5.2.1.1 Clutter Removal

As stated in previous chapters, the received signal includes not only the desired walking subject itself but also unwanted detections, known as clutter, which come from the reflections of, e.g., walls, floor, or objects around (i.e., stationary clutter). Same as in Chapter 4, the average value of the signal is computed and subtracted from the aggregated signals to remove the reflections from the passive clutter.

Table 5.1. Radar sensor parameters for MUHC hallway gait monitoring.

Start Frequency (GHz)	Frequency Slope (MHz/µs)	Idle time (µs)	ADC Start Time (µs)	ADC Samples	ADC Sample Rate (Ksps)	Ramp End Time (µs)	Chirps/ Frame	Bandwidth (MHz)
77	20	100	10	256	4400	105	256	2070

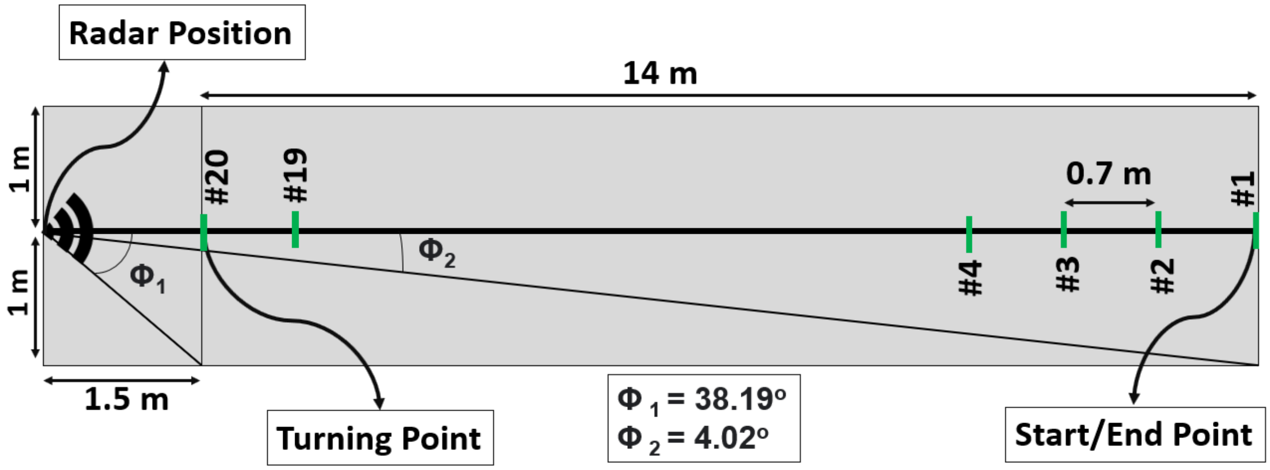

Figure 5.3. Schematic of the hallway walking test setup. The green rectangles show the step points. The minimum and the maximum relative angle between the radar position and the hallway walls are Φ_1 and Φ_2, respectively.

Since the signal variation reflected by clutter is small, removing the average is equivalent to eliminating the stationary scatter [73]. Compared with stationary clutter, humans have a much higher variation through their breathing, heartbeat, and small movements even when standing still, and this variation is more significant during walking.

The range-time map of the environment for the case when a subject was walking across the hallway is provided in Figure **5**.**4** after performing clutter removal. As shown, there are various reflections other than the direct reflections from the subject, created due to multipath reflections in such a cluttered environment. As mentioned above, in most gait monitoring algorithms, it is assumed that the maximum value of the range profile or the STFT pattern represents the torso's bin [26], [80]. However, as shown in Figure **5**.**4** and Figure **5**.**5**, due to the multipath effects, isolating the maximum values of the range bin would not result in obtaining the torso's correct position. Therefore, the torso's range bin cannot accurately be obtained by extracting the maximum amplitude from the range profile. The same limitation also applies to isolating maximum values from the STFT patterns [6].

After generating a range profile of the subject, we performed a Capon beamformer algorithm to create a range-azimuth heatmap of the environment. The Capon beamformer algorithm is detailed in Appendix C. This method not only paves the way for future versions of the algorithm that can track multiple subjects but provides more information on the environment to distinguish between the reflections from the walking subject (direct signal) and their multipath effects.

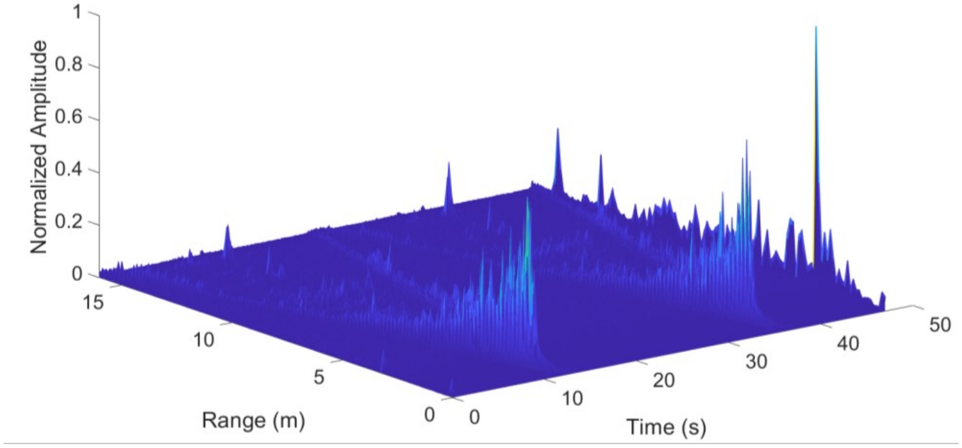

Figure 5.4. Range- time map of the environment after performing clutter removal algorithm when the subject was walking across the hallway.

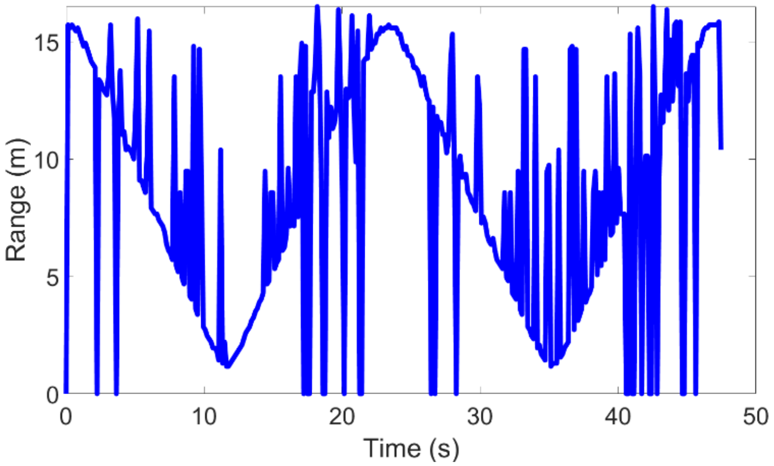

Figure 5.5. Range of the walking subject over time obtained from the common gait extraction algorithm.

5.2.1.2 2D-CFAR

As shown in Figure **5.6** (a), the range-azimuth heatmap represents the density of reflected signals in the environment. If a walking subject is at a specific range and azimuth, that location has more reflections in comparison with other non-occupied positions. This phenomenon is true if no multipath effects exist or the heatmap is obtained in a clutter-free environment (Figure **4.7**). However, as shown in Figure **5**.**6**, in addition to the walking subject's position (the black circle), the heatmap also shows other strong reflections (the red circles). The amplitude of the multipath signals is more than the subject's direct reflected signals.

Therefore, the position of the walking signals could not be isolated by taking the maximum values of the range-azimuth heatmap. Because the reflections from the hallway cause too much noise/anomalies, the common gait monitoring algorithm [6], [14], [108] could not accurately extract gait values in a highly cluttered environment, as shown in Figure **5.5**. Hence, an algorithm is required to find the exact position of the walking subject over time (to track the walking subject) before performing a gait extraction algorithm. To do so, we first perform 2D-CFAR (2D Constant False Alarm Rate) [109] to detect signals of the range-azimuth heatmap. Figure **5.6** (b) shows the 2D-CFAR output of the subject's detected points and ghosts.

5.2.1.3 Unsupervised Machine Learning: DBSCAN

An unsupervised machine learning algorithm was applied to cluster detected points to remove ghost clusters and track the subject walking across the hallway. This allows for separating and identifying the true signal (subject's direct signals) from the ghosting ones. Since the multipath effects in our application vary from one frame to the other, sufficient information about the number of ghosting clusters is not known. As density-based clustering does not require one to specify the number of clusters in the data a priori, the density-based spatial clustering of applications with noise (DBSCAN) algorithm was applied to group the detected points [3]. The DBSCAN approach was selected based on several factors. Firstly, it is a density-based clustering method that is robust to noise and can handle irregularly shaped clusters, which is important for our gait monitoring application. Secondly, it does not require the number of clusters to be specified in advance, which is useful in cases where the number of clusters is unknown. Finally, it has been widely used in the literature for several applications and has shown promising results.

For a point to be assigned to a cluster, it must satisfy the condition that its epsilon neighbourhood (ε) contains at least a minimum number of neighbours (*min_points*). Based on the performance of the different variables set for the DBSCAN parameters, ε=2 and *min_points*=5 were selected as optimized values. However, to reliably group the detected points from the walking subject to a correct cluster, it was realized that data from one frame is not sufficient. As shown in Figure **5**.**7** (a), the purple points (subjects detected points) are estimated as noise points or "No-Cluster" — an outlier that does not belong to any cluster. Note that each range sample represents 12.99 cm and each θ sample is 0.6990^{o}. To prevent missed detection and avoid having empty detected points as input for the clustering algorithm, the clustering algorithm should be applied to the aggregated data over time. It has been shown in previous radar-based human monitoring application research that adding time as an extra variable or having an observation time in the signal processing chain increases the accuracy of detection significantly (e.g., [73]). In other words, the subject being tracked might not appear in every single frame. Therefore, integrating multiple successive frames or detecting the subject over time can significantly improve detection accuracy. We, therefore, selected several frames (*N_frame*=3) of range-azimuth heatmaps, aggregated their CFAR detected points, and then applied DBSCAN to the result. *N_frame*=3 is selected to ensure the target cluster has enough detected points to satisfy the minimum clustering criteria. Additionally, it is chosen not to add too much complexity as the ghosting clusters would also be more if we aggregate more frames. As shown in Figure **5**.**7** (b), the subject's detected points could be clustered correctly by integrating the detected points over N_frame or equivalently adding time as an extra variable to the processing chain.

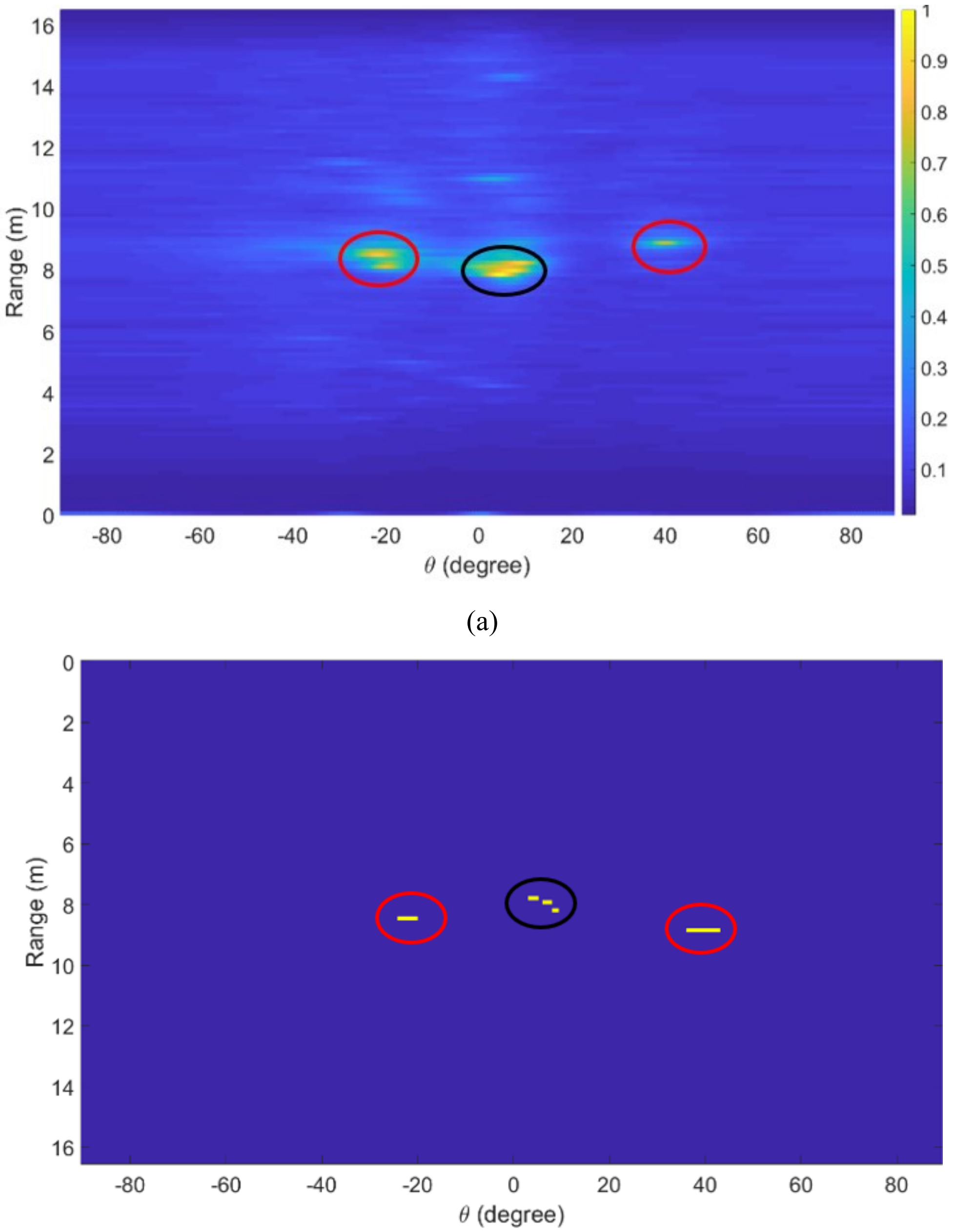

(a)

(b)

Figure 5.6. A single frame example of the range-azimuth of a walking subject at frame #122 (a) the Capon beamformer results (b) CFAR outputs. The black circle represents the subject being tracked, and the red circles represent multipath reflections.

In order to remove ghosting clusters, associate the subject's cluster to its previous cluster and track the subject over time, we propose a tracking and association algorithm that identifies the subject's cluster (target cluster) during walking and associates it with the target cluster of the previous frame. Figure **5**.**7** (c) demonstrates the target cluster obtained from our proposed tracking algorithms, detailed in the following subsection. Note that frame #122 in Figure **5**.**7** helps to illustrate the detail, while the same results could be obtained in other frames. A screenshot of the video of the subject's walking process in frame #122 is provided in Figure **5**.**7** (d). It should be mentioned that in this hallway location, there was a hospital transport stretcher and a medical cart on the right side of the subject in the hallway alcove.

Our proposed tracking algorithm is shown in Algorithm 4.1. To initiate the tracking and association process, we need to find the initial position of the subject that we wish to track. The initial position of the walking subject could be selected manually so that we can select the correct cluster that represents the subject from the DBSCAN outcome. For example, in Figure **5**.**8** (a), since the start position of the

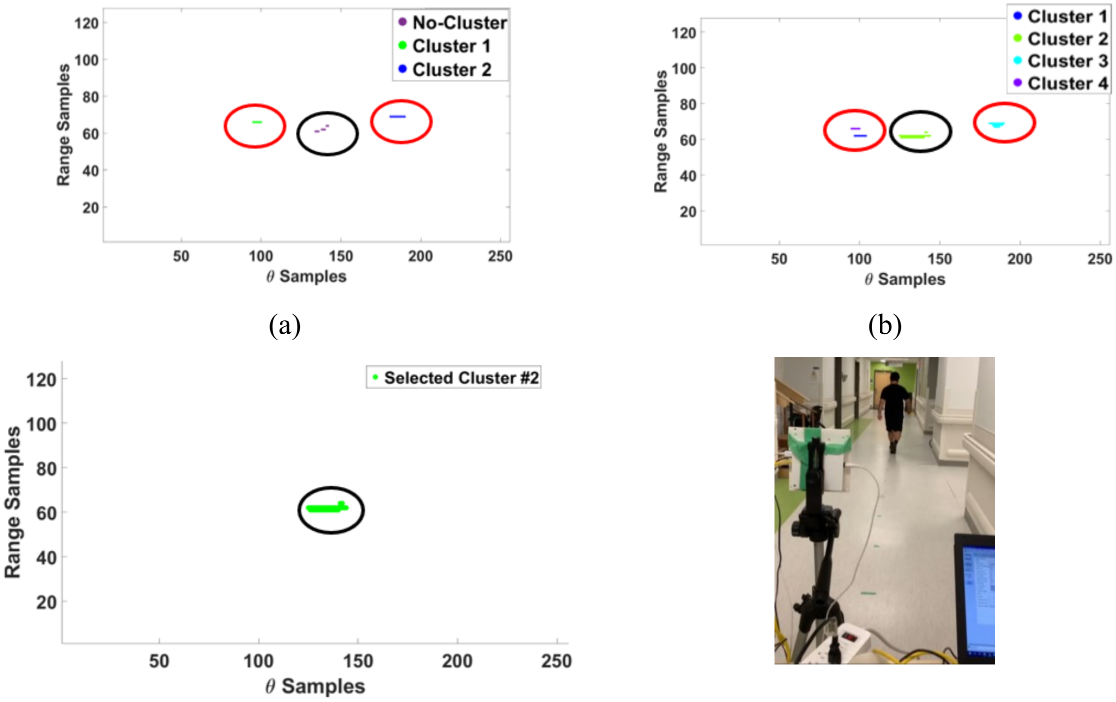

(a)

(b)

(c)

(d)

Figure 5.7. Output of the DBSCAN algorithm at frame #122 (a) applied to the data from one frame, (b) applied to the aggregated frames, (c) target cluster among other ghosting clusters based on the tracking method and (d) the corresponding snapshot of the video. The black circle represents the subject being tracked, and the red circles represent ghost clusters.

subject is known, we know that cluster 3 is the target cluster. However, as our goal is to have an autonomous system, it must be able to initiate the process accurately and automatically. We realized that for all initial points, the cluster with the maximum number of detected points is the subject's cluster. This is true only for the initial points when the subject is about to start walking as they were standing still and thus in the same position for more than one frame. Therefore, the signal aggregation of almost the same position has more detected points than other positions. Additionally, as the subject is about to start walking and has less movement, the multipath reflections are comparatively less, while during the walking cycles, as will be shown, ghosting clusters could have more detected points. Thus, to get the initial position of the subject, the cluster with the maximum number of detected points was selected as the target cluster, as shown in Figure **5.8** (b).

Various radar tracking algorithms have been proposed and extensively used in different studies, such as extended Kalman filters, unscented Kalman filters (UKF), multiple hypothesis testing, particle filters and alpha-beta filter [110]–[113]. In a state-of-art processing pipeline, the radar detections from CFAR are passed into a tracking, for example, UKF, where the track-to-detect association is done through detection gating, and the target state parameters (position and velocity) are updated by the tracker [114]. The subject's speed is a crucial decisive element in the aforementioned tracking methods. However,

Algorithm 4.1: Association **&** Tracking Algorithm

```
Input: range-azimuth heatmaps, CFAR outputs, initial_center
Output: Center points of the walking subject
center_old= initial_center
For i= N_frame+1: number of frames:
CF_Sum=0
   For n=i- N_frame:i
    CF_Sum= CFAR outputs (n)+ CF_Sum
  CFAR outputs (i)= CF_Sum
  If ~isempty
   detect_clusters=DBSCAN (CFAR outputs(i))
      For j=1: length (detect_clusters):
      center= max (range_azimuth_map (detect_clusters)))
      dist (j)= Euclidean_distance (cluster_center, center_old)
     center=min (dist)
     center_points (i)= center
    else
  center_points (i)=center_old
```

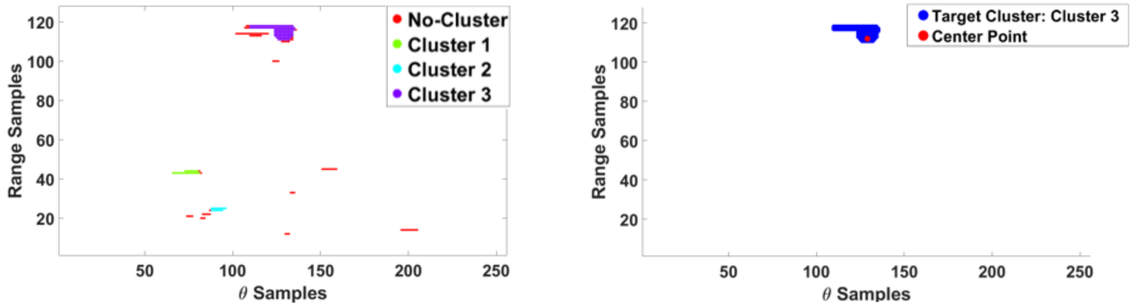

(a) (b)

Figure 5.8. Subject's initial position (a) detected clusters (b) target cluster (subject's cluster) and its center point to be tracked over time.

prediction based on the subject's velocity might lead to inaccurate results. For example, if the subject is missed for a frame or due to the multipath effects, the target cluster is not selected correctly and thus, the velocity of the subject would be obtained incorrectly for some frames, and the prediction leads to inaccurate results. Moreover, the velocity of the subjects obtained from the Doppler highly depends on the relative angles between the subject and the radar, leading to an inaccurate outcome. Our goal is to find the subject's position and walking speed based on his position but not his Doppler/velocity. Therefore, we base our tracking method on the current and previous positions of the subject, a point with the maximum amplitude of each cluster from the range-azimuth heat map, and some facts about walking cycles. We propose our tracking and association method based on the Euclidean distance between two consecutive center points of the subject's cluster.

To associate each identified cluster with the previous one and to track the subject over time, we first calculated the center point of each cluster. Our criteria to find the center point of each cluster was to find the point with the maximum amplitude. As each cluster has a *range_index* and *azimuth_index* – (range samples and θ samples in plots), these can be used to obtain the corresponding cluster's amplitude from the range-azimuth heatmap. For our method, we considered the whole body of a human being to be a single point [14]. This assumption holds because an individual's torso constitutes a significant part of the reflected signals, which means the torso line can be selected from the occupied radar range bins by isolating the maximum signal from his cluster [52]. The center point of the initial subject position is shown in Figure **5.8** (b) as an example. Therefore, if we select the torso's range bin from the subject's cluster, we can reliably extract distinctive and informative features of gait parameters from the velocity of the torso speeding up and slowing down during the swing phase of each leg [59].

As detailed in Algorithm 4.1, to find the subject's cluster among other ghosting clusters, our criterion is to find the nearest point to the previous center point of the target cluster (*center_old*). For each frame, the algorithm takes the center position of the last target cluster and the aggregated output of the detected points from CFAR. The DBSCAN algorithm is then applied to cluster the detected points. In the next step, the center of each cluster is calculated by obtaining the maximum amplitude of the cluster in the range-azimuth heatmaps. The Euclidean distance between the center point of the current cluster (*cluster_center*) to *center_old* is then calculated. The cluster with the closest center point to *center_old* is associated with the subject's cluster, which indicates the subject's torso's position. Consequently, the successive center points of the subject's cluster over time show the subject's position during walking. Tracking the subject over time provides the trajectory of walking (range, azimuth, and Doppler information). Based on the trajectory of walking, gait parameters can be extracted by performing our proposed gait extraction algorithm. As an example, the tracking algorithm's output of frames #124 and #126 are shown in Figure **5.9** (a) and (b), respectively. As seen, the algorithm correctly identifies the subject's clusters and associates them with the previous corresponding frame.

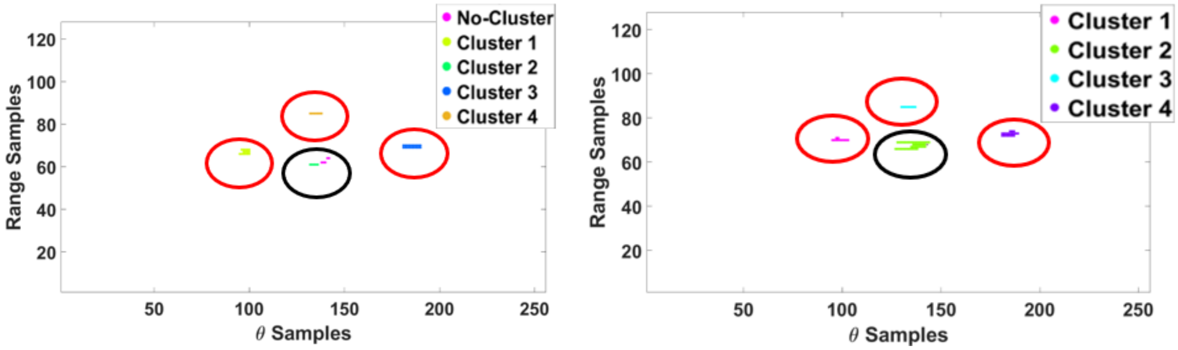

(a) (b)

Figure 5.9. Output of the DBSCAN and the tracking algorithm at (a) frame #124 and (b) frame #126. The black circle shows that the tracking algorithm correctly identified the cluster of data that corresponds to the true location of the subject.

5.2.1.4 EXPERIMENTAL RESULTS

The performance of the proposed method was evaluated in a long hallway pictured in Figure **5.2**. Gait parameters were extracted by asking five volunteers to walk back and forth along the hallway twice by following a straight line with marks showing the step points the volunteers were asked to step on. The total number of step points was 80 for the two full-lap walks. Although this setup might not properly represent normal gait, it gives a good estimate of the true gait without needing GaitRite or Vicon systems.

For all tests, comparison time values were recorded using a stopwatch and asking volunteers to follow a traced line, as depicted in Figure **5.3**. We have used the stopwatch method as a simple and easy-to-implement approach for validation purposes. However, we also acknowledge its limitations and potential sources of error, such as human reaction time and stopwatch accuracy. Hence, future works are needed to perform additional validation experiments using a more accurate motion capture system as a gold standard for comparison.

As shown in Figure **5.10**, the position and the time duration for the first 2 m-walk (T_1, R_1), the first 10 m-walk (|(T_2, R_2) -(T_1, R_1)|), the first turn (|(T_3, R_3) -(T_2, R_2)|), the second 10 m-walk (|(T_4, R_4) -(T_3, R_3)|), the second turn (|(T_5, R_5) -(T_4, R_4)|), the third 10 m-walk (|(T_6, R_6) -(T_5, R_5)|), the third turn (|(T_6, R_6) -(T_7, R_7)|), the fourth 10 m-walk (|(T_8, R_8) -(T_7, R_7)|), the last 2 m-walk (|(T_{end}, R_{end}) -(T_8, R_8)|) are calculated. Table **5.2** summarizes the gait values obtained using our proposed method along with the measured values.

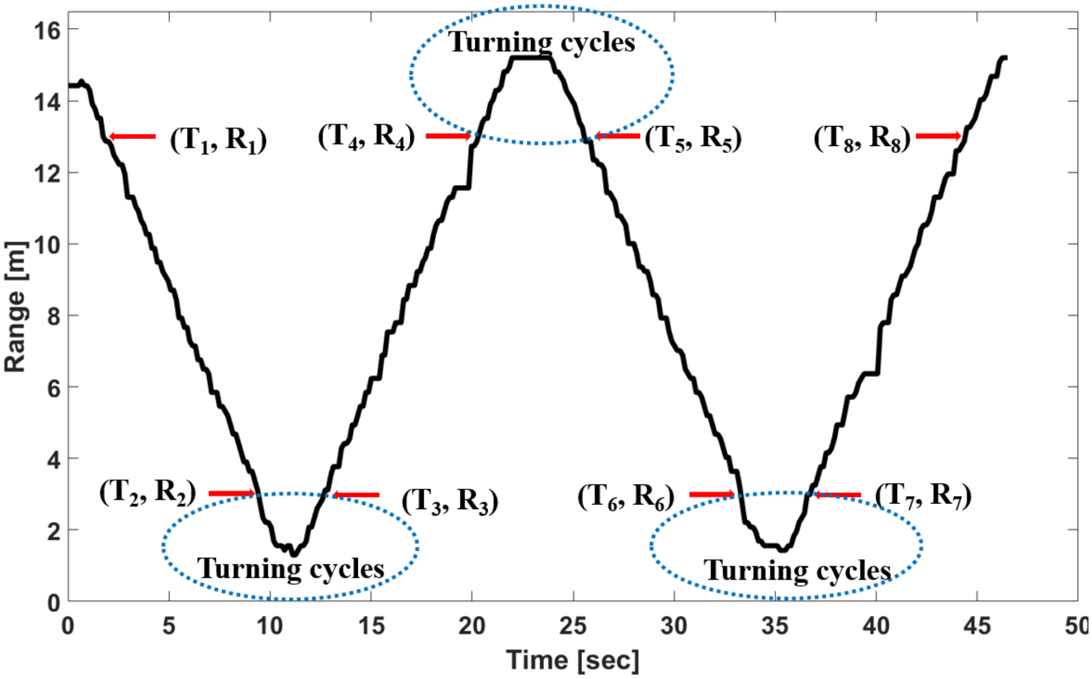

Figure 5.10. Range of the subject over time to capture walking speed with points used for calculations indicated.

Note that the time it took for turning cycles (2 m-walk) is excluded in walking speed and step length calculation processes; therefore, 10 m-walk cycles were used for calculations. The “estimated values” in Table **5.2** are the number of steps the volunteers were asked to follow; thus, we assume our subjects followed the protocol perfectly. It should be noted that gait parameters were extracted using the method proposed in Figure **4.5**. To demonstrate the performance of our proposed algorithm and show the result of our gait extraction algorithm, we presented a case study of results from one of the volunteers. Having the position (range) of the subject while walking toward and away from the radar (Figure **5.10**) and corresponding time according to the protocol mentioned above, the average walking speed of 1.3618 m/s is calculated, while the measured (stopwatch) value was 1.3699 m/s. Applying the Doppler-FFT to the torso’s range bin, the velocity of the torso is obtained, as shown in Figure **5**.**11**.

Applying the peak detection algorithm to the absolute values of the velocity of the torso results in the identification of the step time of each gait cycle, step number, and step counts, as shown in Figure **5**.**12**. As the time of each step is known from Figure **5**.**12**, and the position of the subject is obtained from Figure **5.10**, step points at each gait cycle can be obtained, as shown in Figure **5**.**13**. Step length can then be acquired by subtracting two successive step points, as shown in Figure **5**.**13**, by the red

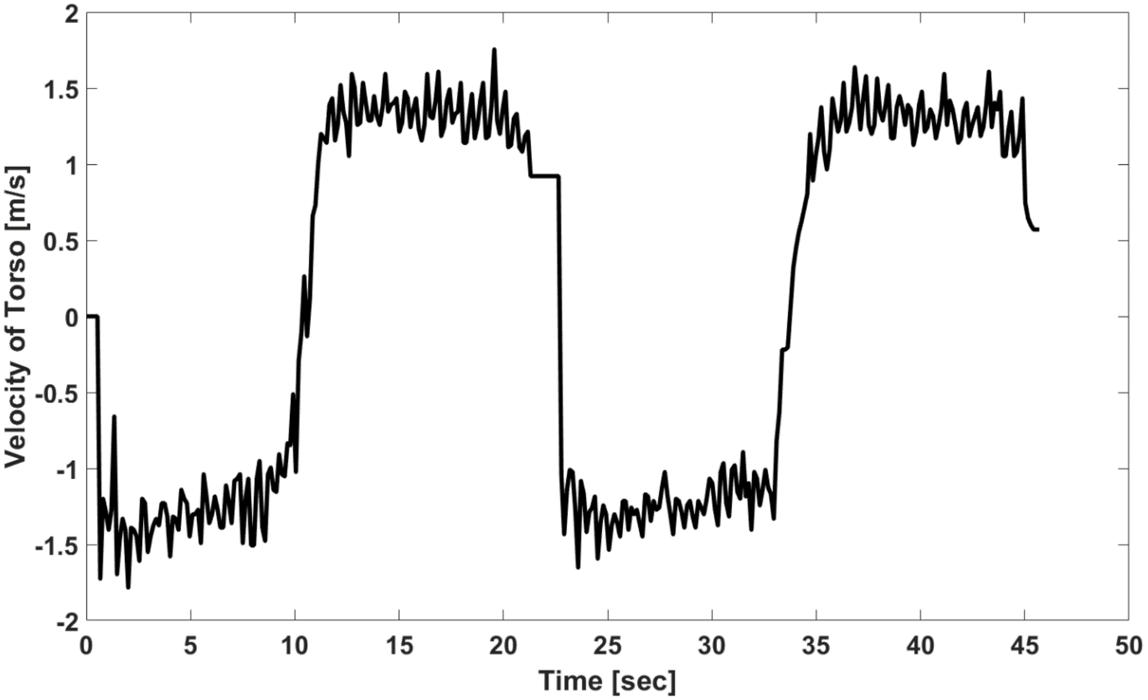

Figure 5.11. Example of torso velocity during walking calculated by the radar system.

arrow and a photo of the step. This means that spatiotemporal gait parameters at each cycle, such as step points, step time, speed of torso, and step length, can be extracted in a long hallway using only one FMCW radar sensor. As shown in Figure **5.12**, the total number of steps calculated by the system for the overall walk in our case study is 84, while the actual step number was 80. As summarized in Table **5.2**, the average step length calculated by the system was 67.64 cm, while the distance marked on the floor was 70 cm.

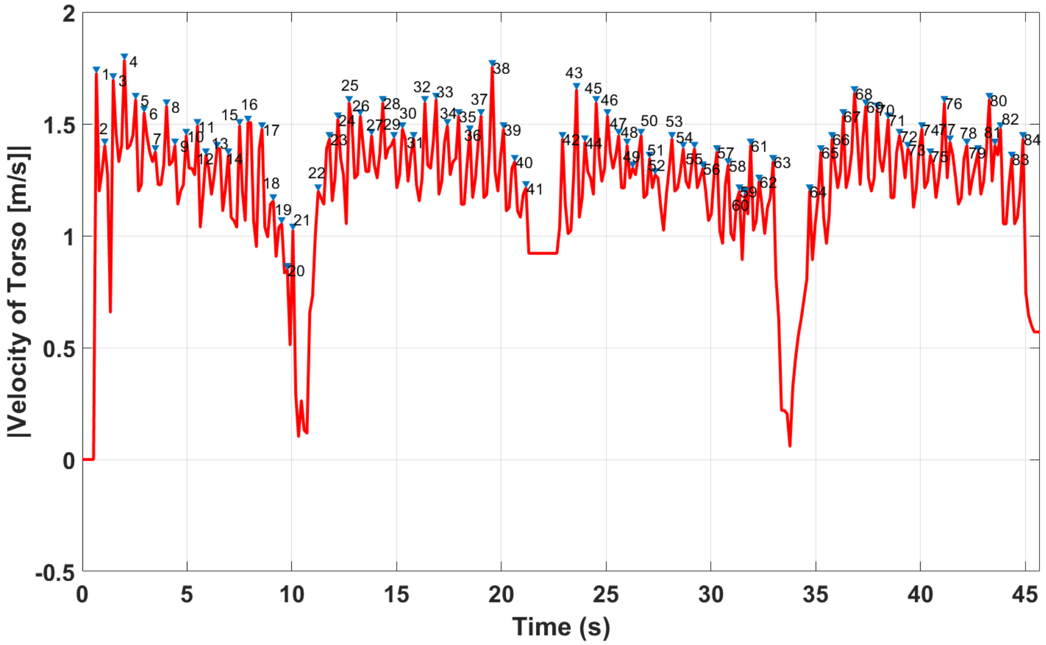

Figure 5.12. Peak detection algorithm applied to the absolute value of the velocity of the torso. Step counts are shown by the small arrows and numbers above the velocity plot line.

Table 5.2. Extracted gait parameters in a large hallway.

Participant	Number of total steps (Estimated value: 80)	Number of 10 m-walk steps (Estimated value: 60)	Step length (cm) (Estimated value: 70 cm)	Speed Measured by our System (m/s)	Speed Measured by Stopwatch (m/s)
A	85	56	69.83	1.37	1.38
B	80	59	65.18	1.28	1.29
C	82	56	67.04	1.37	1.41
D	84	58	67.64	1.36	1.36
E	87	58	67.20	1.32	1.32
Average error for five participants	+3.6	-2.6	-2.622	0.01 m/s	

The five subjects in this validation experiment have gait velocities that range from 1.2811 m/s to 1.3765 m/s, while the system's average absolute error for speed estimation ranged between 0.0040 m/s to 0.0435 m/s. The absolute error was obtained by comparing the speed results obtained from the radar sensor and a stopwatch. Although these results come from a small sample size in a constrained condition, and the 'ground truth' may have been flawed as it was recorded using a stopwatch, these results suggest our radar system may be accurate enough to detect clinically meaningful changes (i.e., changes on a scale of 0.05 m/s [115]). The step length of the individual subjects ranges from 65.18 cm to 69.83 cm, with an error of 0.17 cm to 4.82 cm, respectively. Additionally, the system had an average absolute error between 1 step to 4 steps in measuring step counts for 10 m-walk and 0 steps to 7 steps for the whole walking process. As shown, our proposed work can extract spatiotemporal gait values at each gait cycle using a single FMCW radar. It is also worth mentioning that, as shown in Figure **5.12**, step time, stride time, and stance time could be extracted at each single gait cycle; however, as we did not have access to a GaitRite mat or a Vicon system, we did not report them in this work.

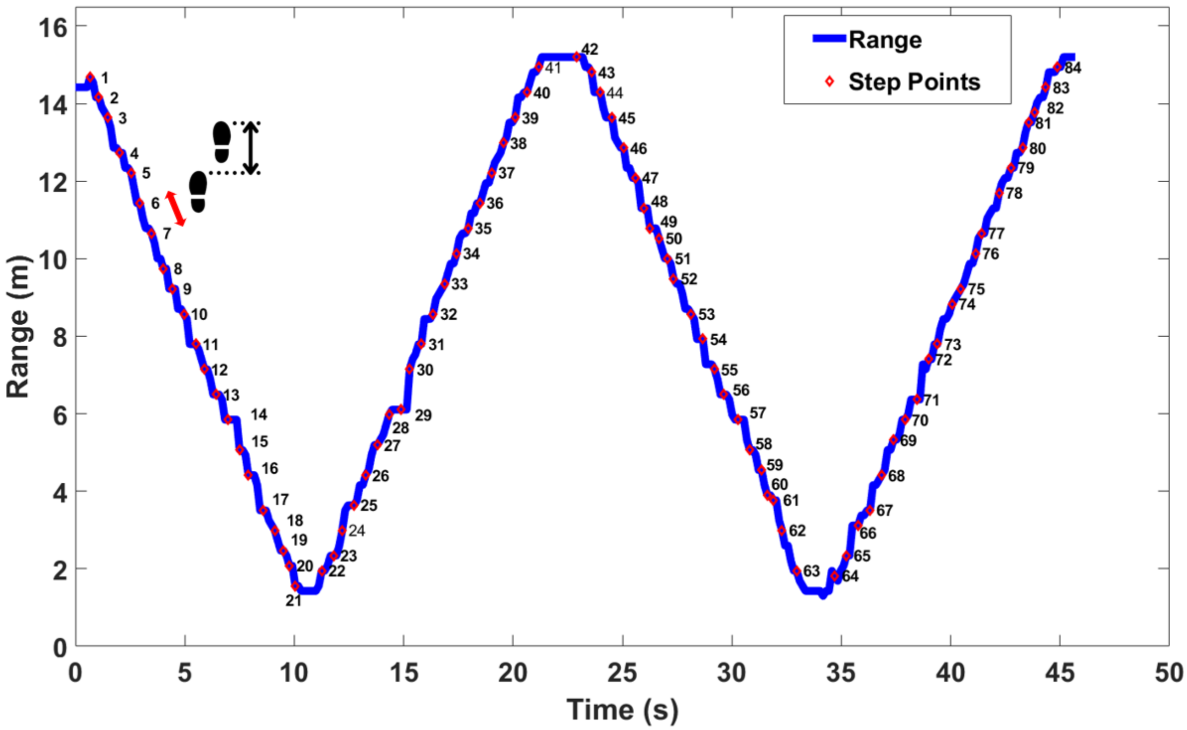

Figure 5.13. Range of the subject walking. Step points (dots) and step counts (numbers) detected by the algorithm are indicated on the plot line.

To compare the outcomes of this work with previous works, we listed a number of references in Table **5.3** with the reported error range, extracted gait parameters, the type of radar and the number of radars used for their experiment. Differences between this proposed gait monitoring algorithm and those found in the literature are as follows:

As shown, the error reported in our work is very low compared with other reported works. Moreover, we used only one FMCW radar that provided both spatiotemporal gait parameters at each gait cycle, while other works either used two radars to provide some detailed gait parameters or added an extra device, such as a treadmill, to provide these parameters. Additionally, we provided spatiotemporal gait parameters at every single cycle; for instance, step time, step lengths, step points, etc., are extracted at

Table 5.3. Comparison of the outcomes of this work with other previous works.

Reference	Reported error in speed	Number of radars	Type of environment	Extracted parameters	Radar type and other required devices
[26]	Not reported	1	Low clutter	mean walking speed, maximum leg velocity, maximum leg velocity, mean leg velocity in the swing and stance phase, degree of variation of leg velocity in the swing and stance phase,	Micro-Doppler
[6]	For 1.1. m/s walk (foot velocity error): 0.06 m/s to 0.17 m/s	2	Low clutter	Stride time, stance time, flight time, step time, cadence, stride length, step length, maximal foot velocity, maximal ankle velocity, maximal knee velocity, and time instant of maximal knee velocity:	Continuous waves and treadmill
[69]	0.144 m/s	2	Low clutter	Foot velocity, torso velocity, step time	pulse-doppler
[116]	For 10 GHz: slow walk: 0.4 m/s and normal walk: 0.14 m/s For 24 GHz: 0.5 m/s and normal walk: 0.06 m/s	1	Low clutter	Walking speed	10 GHz pulse-doppler 24 GHz FMCW
This work	0.0040 m/s to 0.0435 m/s	1	High clutter	At each gait cycle: walking speed, maximum velocity of the torso, step length, number of steps, step points, step time, step count	FMCW radar

each cycle for the first time in this work. Therefore, while future work with a greater range of test conditions and more participants must be done to ascertain the accuracy of our algorithm, these preliminary results demonstrate the promising potential of our algorithm to monitor several aspects of gait in hallways accurately.

As people in their natural environments might not start walking down hallways from standing still, for this approach to translate to real-world applications, we need to add machine learning to the proposed signal processing chain to identify walking cycles and distinguish them from other activities. In this, we based our algorithm on the assumption that we know the subject is walking. However, in a real-world application, we should first identify the walking cycles and then apply a gait monitoring algorithm (detailed in Chapter 6).

5.2.2 Radar Antenna Modification

In the previous section, we put forward a novel radar signal processing and unsupervised learning algorithm to track a subject walking in the hallway and distinguish the direct signals from multipath reflections. The results above showed that the proposed association and tracking method could reliably track the walking subject combined with our proposed gait extraction algorithm to extract spatiotemporal parameters accurately. However, multiple transmitters and receivers are required to obtain a range-azimuth heatmap of the environment for single-person monitoring.

This section aims to showcase the effectiveness of radar antenna modification in mitigating multipath reflections in hallway gait monitoring without the need for advanced signal processing methods. As stated in previous sections, we have been using commercially available low-cost radars that typically have wide beamwidth and suffer from low gain and short-range coverage. High-directive antennas could mitigate reflections from surrounding environments. As such, there is a need for an array of antennas with a higher gain and sharper beam, i.e., a pencil beam. Rather than building a printed circuit board for the radar system with different antenna designs, a dielectric lens antenna is a promising low-cost solution [117], [118]. One advantage of lens antennas compared to array antennas [119] is the simplicity of the design, which features a small feeder, usually a single element such as a patch or a slot, at the focal point of a dielectric lens [120]. Lens antennas have been widely used to direct waves in a prescribed direction and prevent signals from propagating into undesired directions [121]. Moreover, lenses have been used to enhance antenna gain leading to an increased SNR at the receiver [122]–[125], to steer the beam [126]–[129], to shape the beam [130], and to enable ultra-wideband usage [131]. This could address issues related to the limited range due to the higher path loss and the wide beamwidth of the available mm-wave radar antennas.

5.2.2.1 Dielectric Lens Antenna

Based on the principle of refraction [121], lens antennas come in various shapes that translate into different performance, usability, and manufacturing cost [132], [133]. High manufacturing costs, excessive weight, and costly fabrication are among the drawbacks of most lens technologies reported in these works. Moreover, most of these lenses are integrated with the primary feeds, called an integrated lens antenna (ILA) [134]. ILAs have a considerable profile and volume, making them incompatible with some on-board applications. For instance, since there is not sufficient real estate on the AWR1443Boost radar board [83], it is not possible to place a lens directly on top of the radar board. Therefore, the ILA design for AWR1443Boost fabrication and integration would be greatly confined, resulting in poor lens performance. However, due to the ease of integration and packaging, an off-body lens antenna (i.e., a lens antenna that has no contact with the antenna board) [135]–[138] is a promising solution in our radar system. Extensive research has been conducted on hemispherical, elliptical, and hyperbolic lenses[121]. Due to their unconventional forms, hemispherical and elliptical lenses are challenging structures to manufacture and integrate into radar systems. On the other hand, the hyperbolic lens is appealing due to its aesthetic packaging (because it presents an outer planar surface), ease-of-integration, and ease-of-fabrication.

5.2.2.2 Hyperbolic Lens Antenna Fed by a Single Source

To collimate waves from a feeder (assuming a point source), all rays at the outer surface of the lens should have the same phase. Hence, the electrical path length of every ray needs to be the same at the exiting wavefront to transform all waves into plane waves [121]. As shown in Figure **5.14** (a), in a hyperbolic lens, the refraction occurs in the hyperbolic surface where the waves enter. In this configuration, the other side, where waves exit, is planer and does not refract the rays. The shape of the outer surface of the hyperbolic lens in the polar coordinates can be obtained by imposing the path length collimation condition [121]:

$$r(\eta) + nt = F + nt + nt_1 \tag{1}$$

where F is the focal length of the hyperbolic or the distance to the feed, $n=\sqrt{(\varepsilon_r)}$, $0<r<R$, and R is the radius of the hyperbola, t is the thickness of the hyperbola, and $t_1 = T - t$ where T is the maximum

thickness of the hyperbola. Furthermore, because of the actual physical length condition, it could be written as:

$$r(\eta)\cos(\eta) = F + t_1 \tag{2}$$

By subtracting (2) from (1),

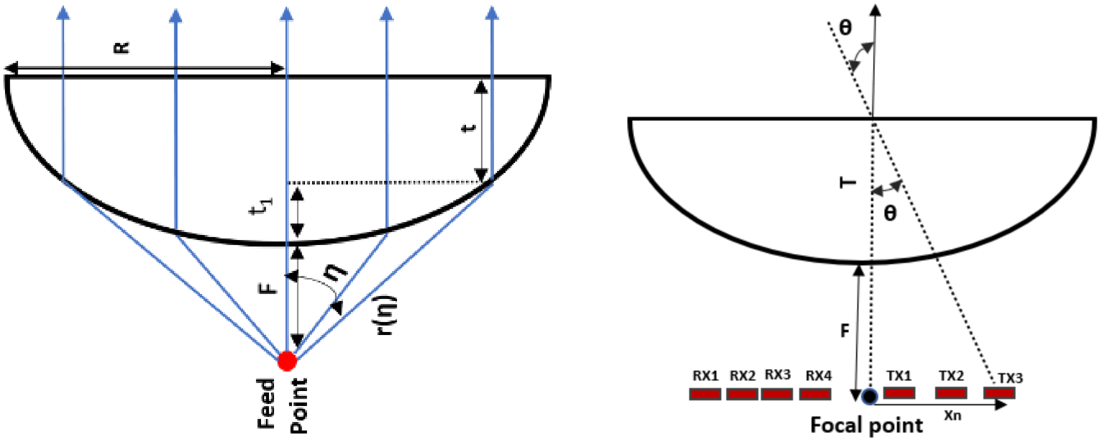

(a) (b)

Figure 5.14. Geometry of a hyperbolic lens antenna fed by (a) a single point source and (b) fed by multiple sources in a MIMO system. TXs: transmitters, RXs: receivers.

$$r\left(1-\cos(\eta)\right) = t_1\left(n-1\right) \tag{3}$$

Hence,

$$t_1 = \frac{r\left(1-\cos(\eta)\right)}{n-1} \tag{4}$$

and by replacing (4) with (2),

$$r\left[\cos(\eta)(n-1)-\left(1-\cos(\eta)\right)\right] = F(n-1) \tag{5}$$

meaning the relationship between the focal length and its radius could be written as

$$r = \frac{F(n-1)}{n\cos(\eta)-1} \tag{6}$$

where the thickness of the lens (t_r) in cartesian coordinates, in terms of F, r and n, is written as [131]

$$t(r) = \frac{F}{n+1}\left(\sqrt{1+\frac{n+1}{n-1}\left(\frac{r}{F}\right)^2}-1\right) \tag{7}$$

In this work, we base our design of the in-package lens on our previously used radar sensor (Figure **4.1**) [3], although the same design procedure should be applicable to other types of radar sensors. We point out that while one transmitter and one receiver are enough for single-person gait monitoring proposed in this work using our proposed gait extraction algorithm (explained in Chapter 4), we designed the lens for the same radar (Figure **4.1**) used in our previous work [3]. This would help provide a reliable and reasonable comparison (in terms of operation frequency, range resolution, etc.) between the outcome of this work and our previous work presented in Section 5.2.1.

Since the lens should be paired with the radar antennas, the AWR1443Boost antennas are used as primary feeds for a hyperbolic lens. As shown in Figure **4.1**, the AWR1443Boost has four receivers (Rxs) and three transmitters (Txs). However, the design steps of a hyperbolic lens explained in (1)–(7) are based on one point source placed at the center of the lens. Therefore, the impact of the multiple sources positioned at different relative distances to the lens focal point should be investigated. In the AWR1443Boost system, an active source is switched from one element of the transmitters to the other while all receivers receive reflected signals simultaneously [83].

As shown in Figure **4.1** (b), each source has a different relative distance to the center of the lens (apex) in the MIMO system, causing collimated waves directed at different angles. Note that the direction of the main beam can be changed by either moving the position of the feeder of the lens or by switching the active source of the lens in an array of transmitters. In other words, the effect of a change in the position of an active source point is similar to the lens rotation [139]. Thus, the direction of the collimated beams depends on the focal point and the relative distance between the radar antennas and the lens center in the x-y plane. The beam tilt angle along azimuth and elevation direction could be given by

$$\theta = \tan^{-1}\left(-\frac{x_n}{F}\right) \tag{8}$$

$$\varphi = \tan^{-1}\left(-\frac{y_n}{F}\right) \tag{9}$$

where (x_n, y_n) is the position of each element in the x-y plane.

Note that $(x_n, y_n) = (0, 0)$ is considered the origin. Displacements in the x-axis and y-axis lead to beam steering in azimuth and elevation directions, respectively. In this work, it is assumed that a change in position occurs in one dimension (only x or only y direction) because of the geometry of the AWR1443Boost radar antennas shown in Figure **4.1**.

5.2.2.3 Hyperbolic Lens Design

Various simulations and measurements were carried out to design a proper lens antenna and achieve a good level of performance. Two sets of simulations were performed to identify the optimum lens parameters and to realize the effect of multiple sources on the lens antenna. In all simulations, Rogers RO4350 was the substrate of the antenna. The size and shape of the AWR1443Boost antennas are detailed in Figure **5.15**. In the following, the pattern called Tx_1 is the radiation pattern of the AWR1443Boost antenna when the antenna Tx_1 is the only active element while the other two are not transmitting. The same process is applied for other antennas: Tx_2, Tx_3, Rx_1, Rx_2, Rx_3, and Rx_4. Note that in all simulations, the lens dielectric constant is set to ε_r= 2.74 to match the polylactic acid (PLA) building material. We used PLA due to its proven performance, cost, availability, and ease of fabrication [136].

HFSS simulations were started by simulating the AWR 443Boost transmitter antenna without the lens. Since the radar was designed to operate from 76 GHz—81 GHz, results are shown for 76 GHz, 77 GHz, 78 GHz, 79 GHz, 80 GHz and 81 GHz frequencies. Figure 5.**16** shows the antenna's simulated 3D gain radiation pattern when the Tx_1 was excited. As shown, the radar antenna without the lens has a very wide beamwidth with a gain of 10 dBi, 10.5 dBi, 10.3 dBi, 9.5 dBi, 9.5dBi and 9.46 dBi at frequencies of 76 GHz, 77GHz, 78 GHz, 79 GHz, 80 GHz and 81 GHz, respectively. The results show that the patterns of the transmitter antennas are not identical over the frequency bands but have minor gain variations over the frequency bands. The wide beamwidth is the main issue in addition to the low gain in our application. So, there is an excellent need for substantially improving the gain and sharpening of the beam for hallway gait monitoring.

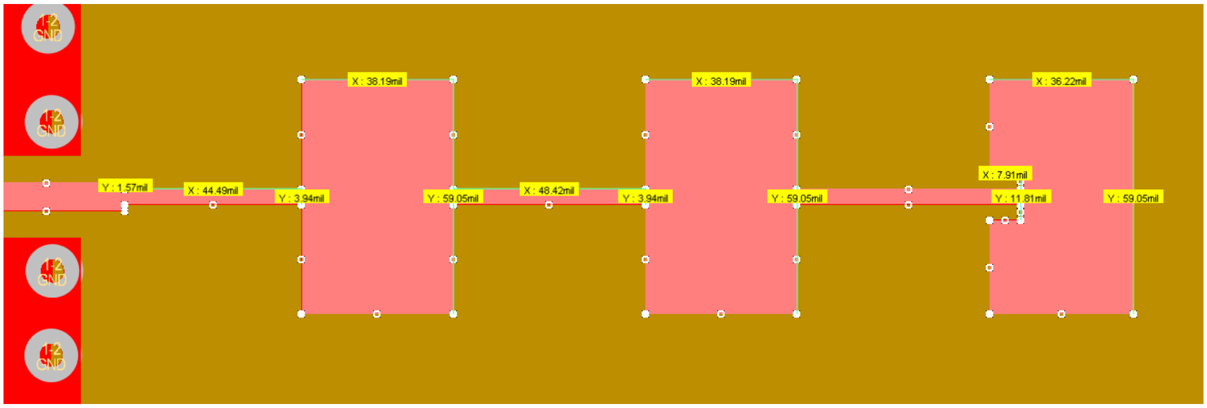

Figure 5.15. Design and parameters of the AWR1443Boost antenna sub-module simulated in HFSS.

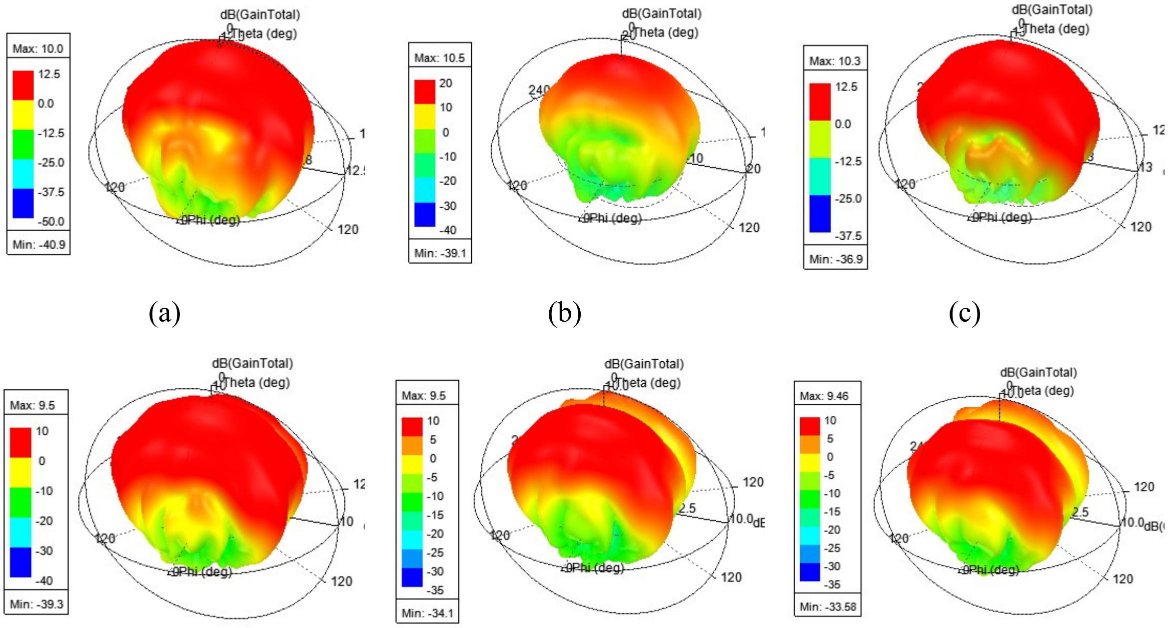

(a) (b) (c)

(d) (e) (f)

Figure 5.16. Simulated 3D gain radiation pattern of the AWR1443Boost transmitter antennas without the lens transmitting with Tx_1 operating at a frequency of (a) f=76 GHz, (b) f=77 GHz, (c) f=78 GHz, (d) f=79 GHz, (e) f=80 GHz, and (f) f=81 GHz.

5.2.2.3.1 Parametric Analyses

As shown in (7), the design of the hyperbolic lens antenna involves two main variables: the focal point (F) and the lens radius (R). The purpose of this subsection is to find the optimum parameters for the lens profile with the highest gain while providing lower sidelobe levels [140]. The center of the hyperbola is fixed at (0, 0) in the x-y plane, and the positions of the Tx_1, Tx_2, and Tx_3 are set to (–λ, 0), (+λ, 0), and (0, -λ/2), respectively.

For the parametric analyses of the focal lens and the radius, one parameter remains fixed while the other ranges from 2 λ to 20 λ. The focal length is fixed at F=10 λ to realize the effect of the radius on the lens performance. The same step is taken to show the impact of the focal length. The lens radius is set to R=10 λ, while F varies from 2 λ to 20 λ. All simulation results from the parametric analysis of the AWR1443Boost transmitter antennas shown below are the results of the Tx_1 antenna (Tx_1: on, Tx_2: off, Tx_3: off) at a frequency of f=77 GHz since the same results are obtained with other transmitters.

To simulate the AWR1443Boost antenna integrated with the lens, a hybrid electromagnetic computer simulation in HFSS is performed, using the integral equation-based method of moments (IE-MoM) for the lens and the finite element method (FEM) for the AWR1443Boost antennas [141]. As a preliminary result, Figure **5.17** shows the lens's radius and focal length effect on the gain. As shown, there is a saturation point at which very little further gain enhancement is achieved by increasing both the focal length and the radius of the lens. Specifically, it is observed that with a value of around R=F=10 λ, the gain would no longer increase in line with an increase in the size or the focal length. This is an intuitive observation due to the lens' limited capability of collimating all waves from the primary feeds represented as sidelobes.

Furthermore, Figure **5.18** demonstrates that both *F* and *R* directly change the SLL values. An increase in *F* increases the SLL, whereas a larger *R* reduces the SLL value. Moving the lens further above the feeder increases the spillover loss [134], which in turn significantly increases the SLL. On the other hand, a lens with a particular focal length but a larger radius could cover wider angles of waves coming from the source. However, a lens antenna with a very large radius would be bulky and, therefore, might be impractical to pair with a small radar sensor. Thus, in the lens design, it is crucial to find the saturated point of the gain and recognize the trade-off between parameters. Improving one parameter may negatively influence another.

To show the details of the impact of the focal length on the AWR1443Boost antenna performance, in Figure **5.19**, the radiation patterns of the antenna at φ=0 for the case of R= 10 λ, F=2.5 λ, with the gain of 18.09 dBi and SLL=3.1 dB is compared with the case with the lens of R= 10 λ, F=20 λ, of the gain of 24.3 dBi and SLL=6.67 dB. The results confirm that the lens at a further distance above the patch has a higher SLL and a sharper beam compared with the closer one.

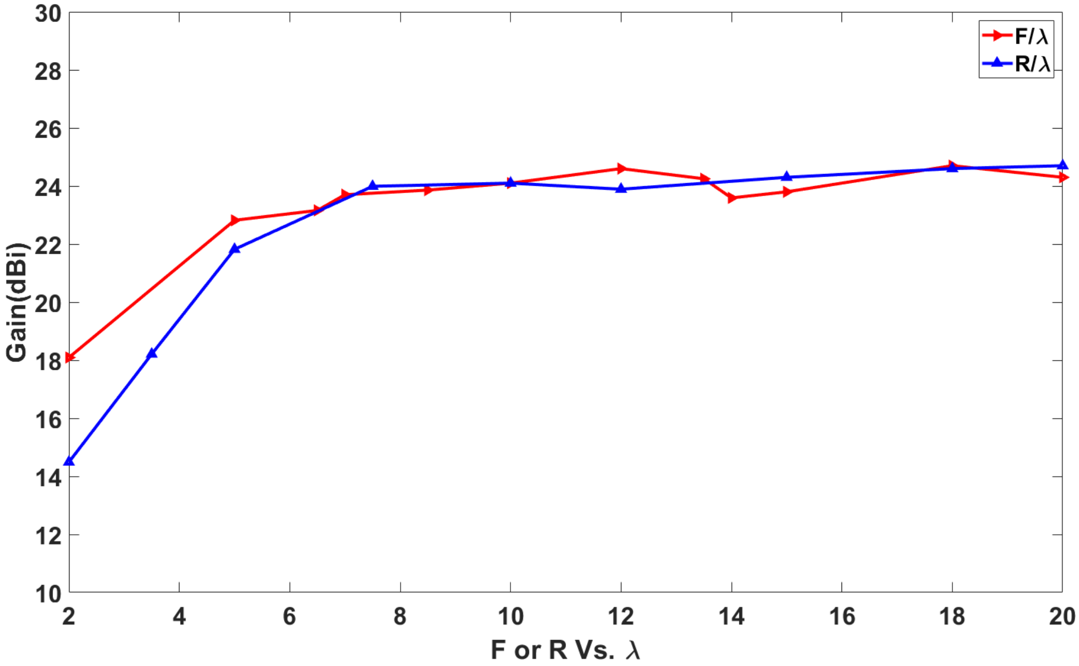

Figure 5.17. Gain variation of the antenna integrated with the lens versus the focal length and the radius.

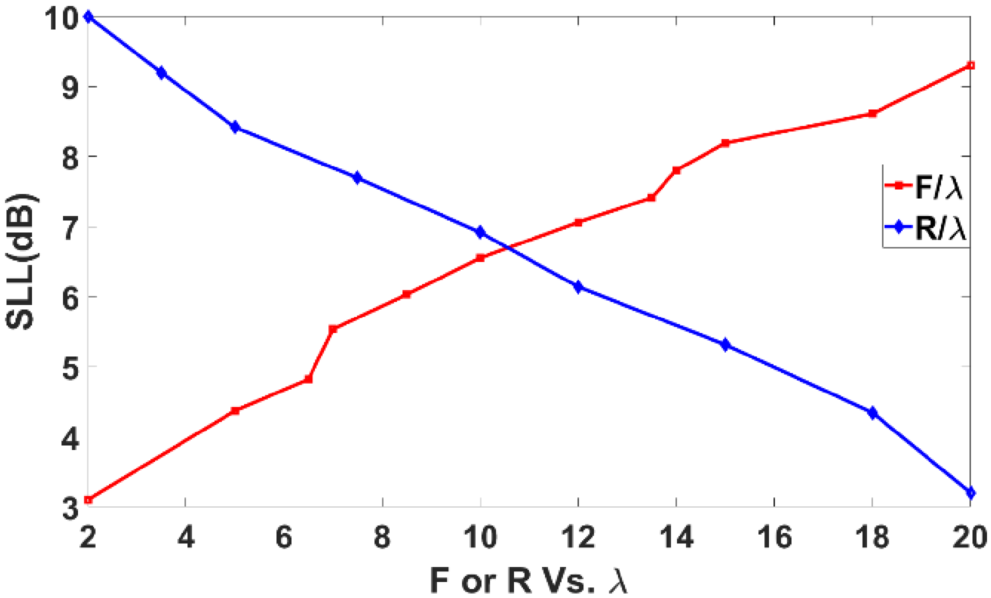

Figure 5.18. Sidelobe level variation of the antenna integrated with the lens versus the focal length and radius.

Figure **5.20** illustrates the reason why the lens closer to the feed has a lower SLL value closer to the feed. As illustrated, a lens closer to the feed can cover more rays coming from the primary feed and, thus, collimate them effectively; however, the lens far away from the feed is less efficient in fully covering rays coming from the feed to be collimated. Therefore, some parts of the uncovered rays diffract near the edge, and other portions tend to follow the original directions leading to a higher SLL. If the primary feed has a radiation pattern of ψ beamwidth, the lens with the radius of R, the thickness of T and the focal length of F_1 could cover $\psi_1=tan^{-1}\ (R/F_1)$, so ψ-ψ_1 would be remained uncovered by the lens. The uncovered rays for the lens further away from the feed would be more than in the other case. For instance, the lens with the radius of R, the thickness of T and the focal length of F_2 could cover $\psi_2=tan^{-1}\ (R/F_2)$, so ψ-ψ_2<ψ-ψ_1. Therefore, moving the lens further on top of the feed would increase the spillover loss, which significantly increases the sidelobe level. On the other hand, a particular focal length but with a larger radius could cover wider angles of waves coming from the source. The lens with a larger radius has a lower SLL compared with the lens with the same focal length but a smaller size. As shown, the increase in the lens dimension and the focal length would increase the

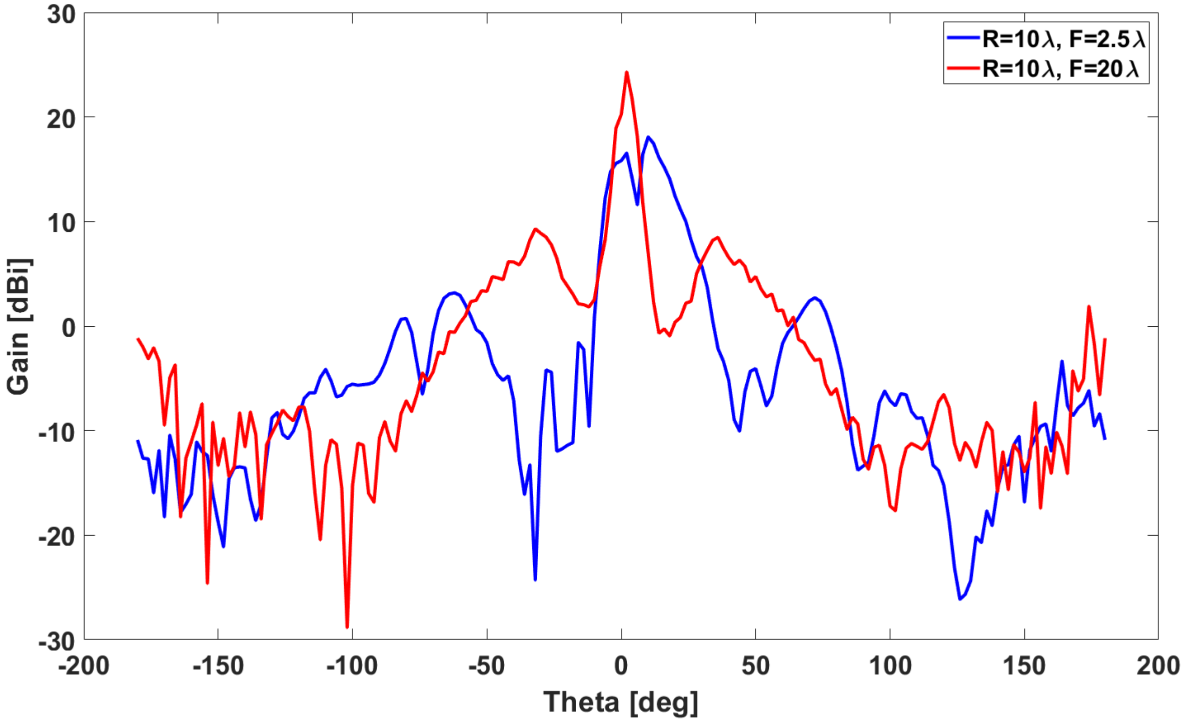

Figure 5.19. Simulated 2D gain at φ=0 of the antenna integrated with the lens with two different values of F.

antenna gain to a specific level. It was shown that the lens has a saturated point where no more gain enhancement would be acquired. The lens aperture has a maximum gain that depends on the feeders' type and dimension in addition to its size and focal length. To find the lens aperture maximum gain and its interaction with other types of antennas, we simulated a half-wave dipole and a horn antenna in HFSS. Then, the same parametric analyses were performed to realize the impacts of the radius and the focal point of the lens on the antenna performance. The same results were obtained for SLL, where increasing the lens dimension reduces the SLL. The total gain of the antennas with and without the lens is plotted in Figure **5.21**.

As shown, without the lens, the dipole, the horn, and the patch (AWR1443Boost-Tx$_1$) have a total gain of 2.5 dBi, 15 dBi and 10 dBi, respectively. The results also illustrate that the lens has the maximum gain around *R= 10 λ* at *F=10 λ* integrated with all types of antennas. It is evident that the lens has a saturated point around R=F=10 λ, where no longer gain improvement was obtained. Additionally, the results show that for the lens integrated with the horn (green curve) and the patch (red curve), around

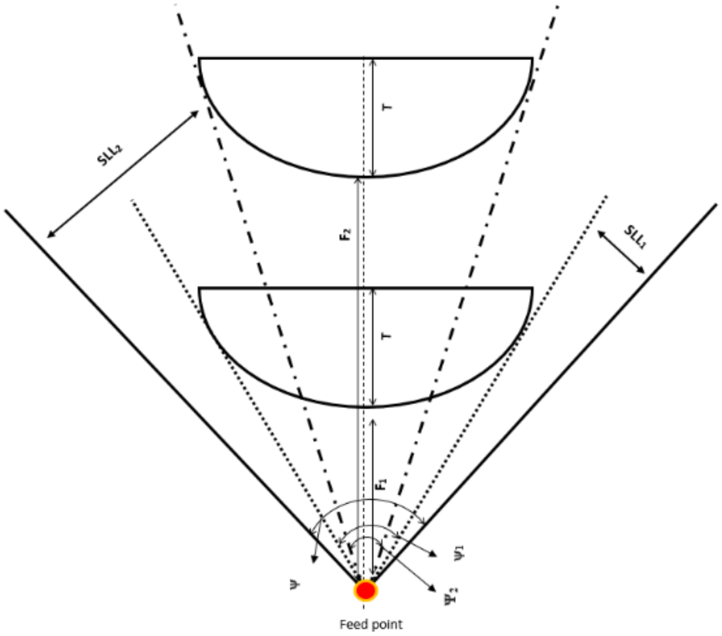

Figure 5.20. Geometry of the lens design, showing the effects of the focal length on the sidelobe level (spillover loss).

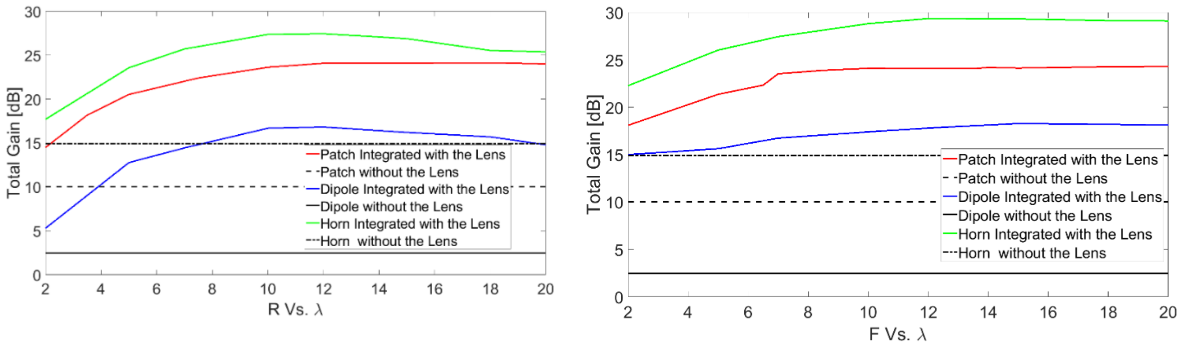

(a) (b)

Figure 5.21. Gain variation of different types of antennas integrated with the lens versus (a) the radius and (b) the focal length of the lens.

14 dBi gain enhancement was achieved. Besides, for the lens integrated with the dipole (blue curve), the gain was improved by around 15.5 dBi.

Consequently, the results above clearly show that in the lens design, it is crucial to find the saturated point of the gain and recognize the trade-off between parameters; improving one parameter may negatively influence other features. It is worth mentioning that spillover loss depends on the radiation pattern of the primary feeds. With the same dimension, the wider radiation pattern of the primary feed element would have more spillover radiation loss, increasing the antenna pattern's side lobes. On the other hand, the narrower radiation pattern of the primary feed element would create less loss and so less sidelobe level [134]. Therefore, in the lens design, not only are the shape, size, and distance relative to the feeders important, but the radiation pattern of the primary feed impacts the lens performance. Ultimately, regarding all the simulations provided above and the trade-off between different parameters, we realized that the best performance of the radar with a sufficient gain is a PLA hyperbola with R=F=10 λ while maintaining the low sidelobe level and the sharp beam. Additionally, the system with R=F=10 λ would be easier to fabricate and commercialize in addition to the affordable cost.

Since the AWR1443Boost radar is a wideband system, the lens should work properly across the whole frequency band. To assess the effectiveness of the lens integrated with the AWR1443Boost antennas over the entire frequency bands (76 GHz—81 GHz), Figure **5.22** shows the gain of AWR1443Boost antennas integrated with and without the hyperbolic lens with *R=F=10 λ* (for the case of active Tx_1 and Tx_3). Note that the results of the Tx_1 and Tx_3 are provided as an example, while other antennas perform similarly. To assess the frequency effects on the lens performance, we fixed other affecting variables on gain, such as the relative distance between the feeder and the lens apex, radius, focal length, etc. To do so, for each feeder, the apex of the lens with *R=F=10* was positioned precisely on top of the specific antenna. The results confirm that the radar antennas with and without the lens provide a minor gain variation over the entire frequency bands (less than 1.5 dB and less than 3 dB gain variation without and with the lens, respectively). These results confirm that the lens inherits its primary feed bandwidth [121].

Furthermore, to investigate the lens effects on the input reflections and mutual coupling between transmitters, S-parameters of the primary antennas integrated with and without the lens are provided in Figure **5.23** and Figure **5.24**, respectively. Note that S_{11} and S_{33} are the magnitudes of the input reflection coefficients at the input of Tx_1 and Tx_3, respectively. As illustrated, the input reflection coefficients of the antenna with and without the lens bear a strong similarity. The lens has no significant effect on the reflection coefficients since it is an off-body lens. However, the lens slightly increases the mutual coupling over the frequency bands.

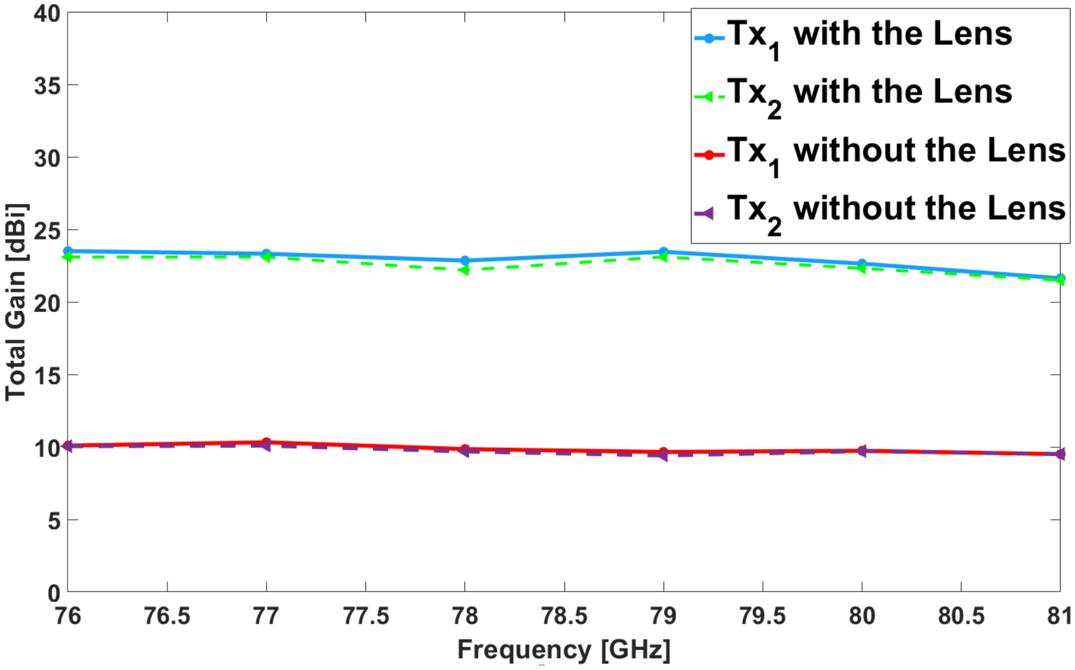

Figure 5.22. Simulated gain variation of AWR1443Boost with and without the lens over the frequency bands.

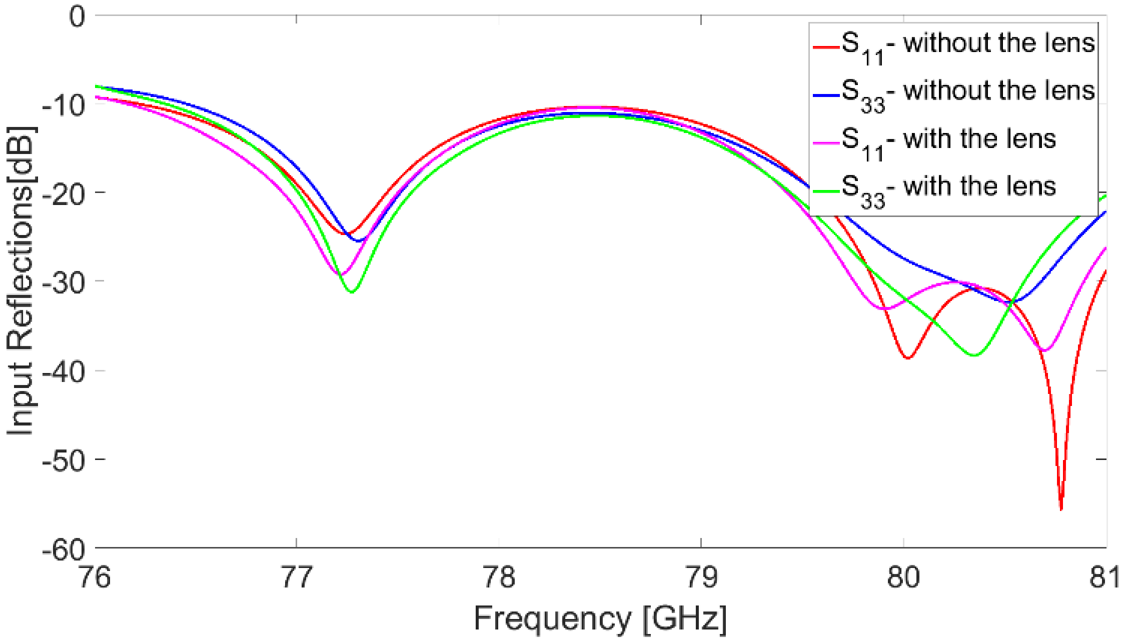

Figure 5.23. Simulated magnitude of the input reflection coefficient of the AWR1443Boost radar antenna with and without the lens with R=F=10 λ.

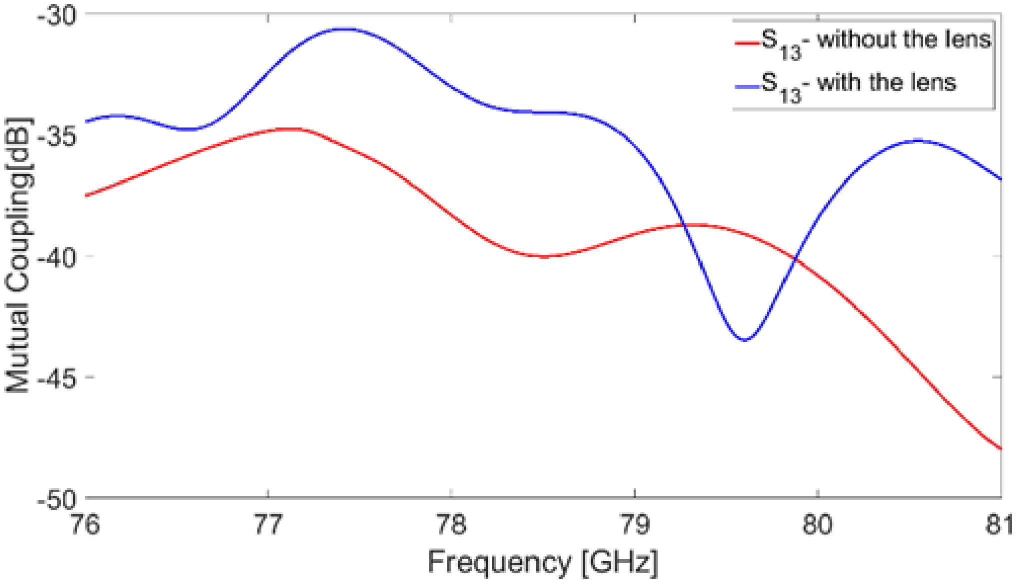

Figure 5.24. Simulated magnitude of mutual coupling between Tx_1 and Tx_3 with and without the lens of R=F=10 λ.

Due to the fabrication error and instability of the dielectric constant of 3D-printed material against filling ratio and varying temperature, sensitivity analysis should be performed to determine their effects on the lens performance. To analyze the impact of changing dielectric properties, the lens with the parameters of $F=R=10\ \lambda$, and $(x_1, y_1) = (-\lambda, 0)$, with varying permittivity between $1.87< \varepsilon_r <3.8$ (in the range of ±%30 of the PLA permittivity), is simulated. Figure **5.25** illustrates the total gain according to the different permittivity values. Since the gain variation is small over the whole band, the result of the Tx_1 operating at f=77 GHz is provided. As shown, with the smallest value of $\varepsilon_r= 1.87$, the gain of the lens fell to 21 dBi while it rose to more than 28 dBi with $\varepsilon_r=3.6$. The results show that varying dielectric properties produce a gain variation of approximately 6 dB over ±30 % of the PLA permittivity. As shown, the dielectric constant of the lens affects the gain of the lens significantly. Therefore, there is a strong need for 3D- printed material characterization to find the electrical properties of the printed materials to assess the performance of the fabricated system. In the previous sets of simulations, the purpose was to realize the relationship between the lens dimension and the focal length with the antenna parameters, namely, gain and sidelobe level. Now, the purpose is to investigate the off-focal point effects of the multiple sources. As stated above, depending on the source position and the focal length, the lens antenna can steer the beam to specific angles. In the case of having multiple sources with different relative distances to the center of the lens, the output waves would be directed at different angles by switching the active element of the transmitters. To investigate how a change in a primary

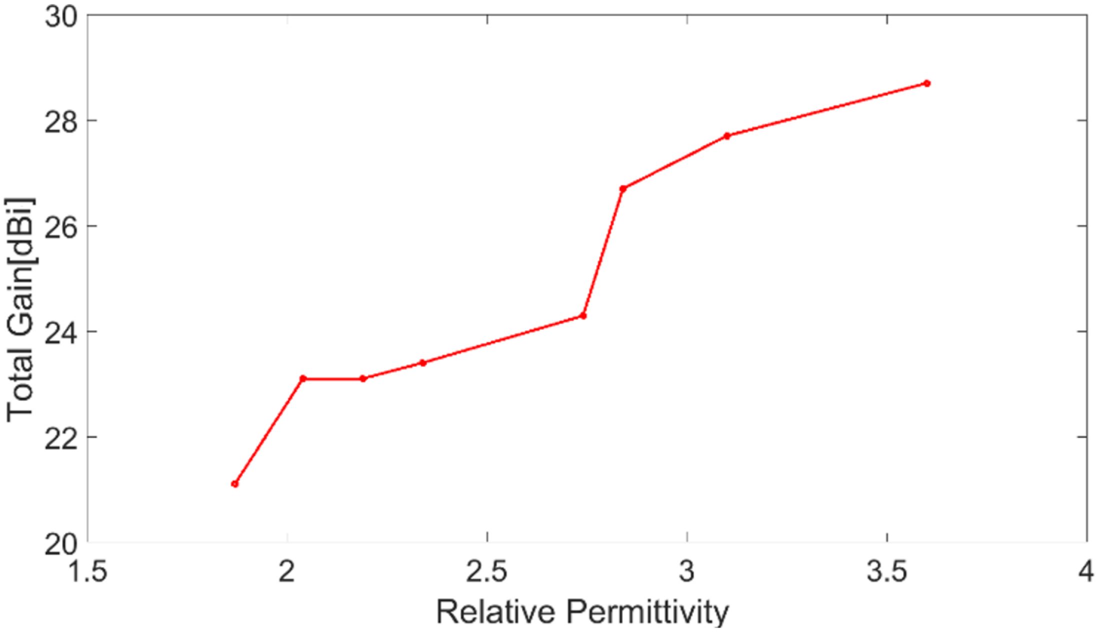

Figure 5.25. Simulated gain of AWR1443Boost integrated with the lens versus the permittivity of the lens.

feed position would change the direction of the beam of the antenna, *R* and *F* were set to 10 λ. Figure **5**.**26** shows the pattern of the AWR1443Boost transmitter antennas integrated with the lens, while the only active transmitter was the Tx_1. The results show that for the case of Tx_1 located at $(x_1, y_1) = 0$, the main beam direct at θ=φ=0°, as shown in equations (8) and (9), $tan^{-1(0/10)}=0$ (magenta curve). In addition, for the case of $(x_1, y_1) = (-0.5\ \lambda, 0)$ (blue curve), $(x_1, y_1) = (-\lambda, 0)$ (green curve) and $(x_1, y_1) = (-1.5\ \lambda, 0)$ (red curve), the main beam steered to φ=0°, θ= 3°, φ=0 °, θ= 5°, and φ=0°, θ= 8°, respectively. The same process was applied for Tx_3 as well. Figure **5**.**27** shows the results of the case when the Tx_3 was the only active element. The results show that for the case of Tx_3 located at $(x_3, y_3) = 0$, the main beam is directed at θ=φ=0° (magenta curve). Additionally, it is shown that we could easily steer the beam to various angles along the azimuth direction by changing the position of Tx_3. For instance, the main beam occurred at φ=0°, θ=-11° (red curve), φ=0°, θ=-5° (green curve), and φ =0°, θ=-3° (blue curve) when the antenna was placed at $(x_3, y_3)= (2\ \lambda, 0)$, $(x_3, y_3)= (\lambda, 0)$ and (x3, y3)= (0.5 λ, 0) respectively. As shown, displacement along the x-axis would change the direction of the main beam along the azimuth direction while the elevation pattern is fixed and vice versa; displacement along the y-axis would change the direction of the main beam along the elevation while the azimuth pattern

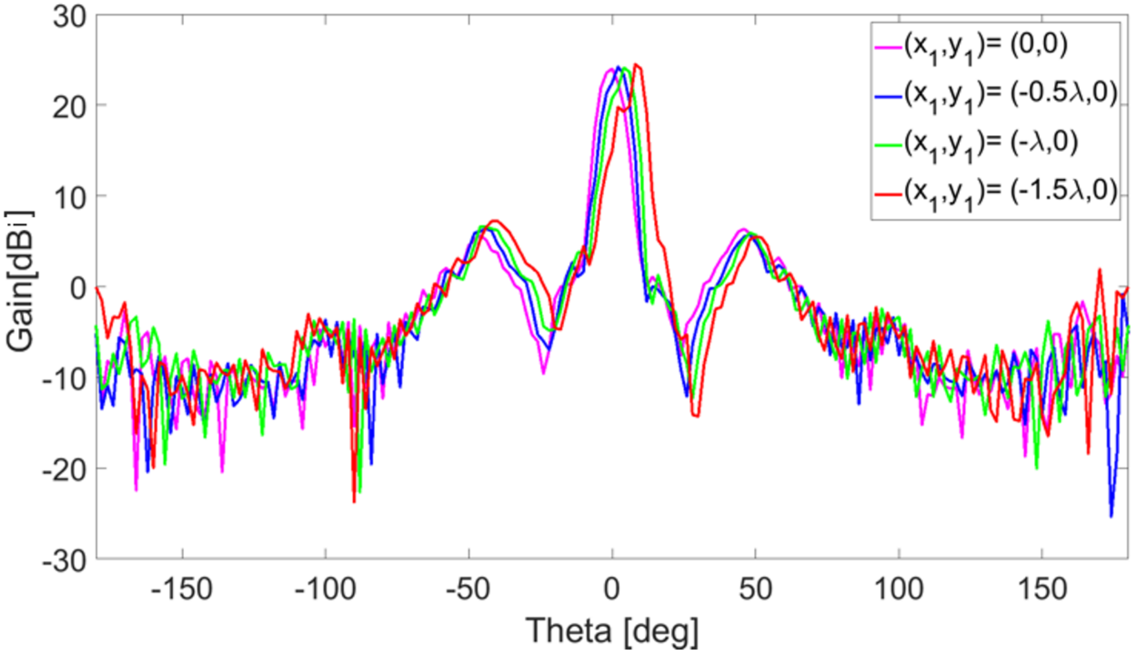

Figure 5.26. Simulated 2D gain of AWR1443Boost integrated with the lens with an active transmitter of Tx_1 located at different positions relative to the apex of the lens.

undergoes no change. Therefore, the variation of the apex position (relative position of Txs) along the x-axis would change the main beam of Tx_1 and Tx_3 in azimuth direction while it has no effect on the beam of Tx_2.

To compare the direction of the beam resulting from Tx_2 along the x-axis and y-axis with other antennas, we located the Tx_1, Tx_2 and Tx_3 antennas at $(x_1, y_1)= (-\lambda, 0)$, $(x_2, y_2)= (0, -\lambda/2)$ and $(x_3, y_3)= (\lambda, 0)$, respectively, where Tx_1 and Tx_3 have relative distance with apex along the x-axis, while Tx_2 has the distance along the y-axis. The elevation and azimuth patterns are provided in Figure **5.28** and Figure **5.29**, respectively. As seen, the main beam of the antenna transmitting by Tx_1 was directed at φ=0°, θ=5° (red curve). Additionally, transmitting with Tx_3, the beam steered at φ=0°, θ=-6° (blue curve) while the main beam was directed at φ=-3° and θ=0° when Tx_2 was transmitting (green curve).

The results validate that for the beam to be steered along the azimuth and elevation direction, the apex should be moved along the x and y-direction, respectively. All results shown above are in good agreement with equations (8) and (9), showing the steered beam of the lens. Note that the positions of the feeders were not very far from the apex. We simulated other types of antennas integrated with the lens to investigate the accuracy of equations (8) and (9) in estimating the steered angle for the lens at

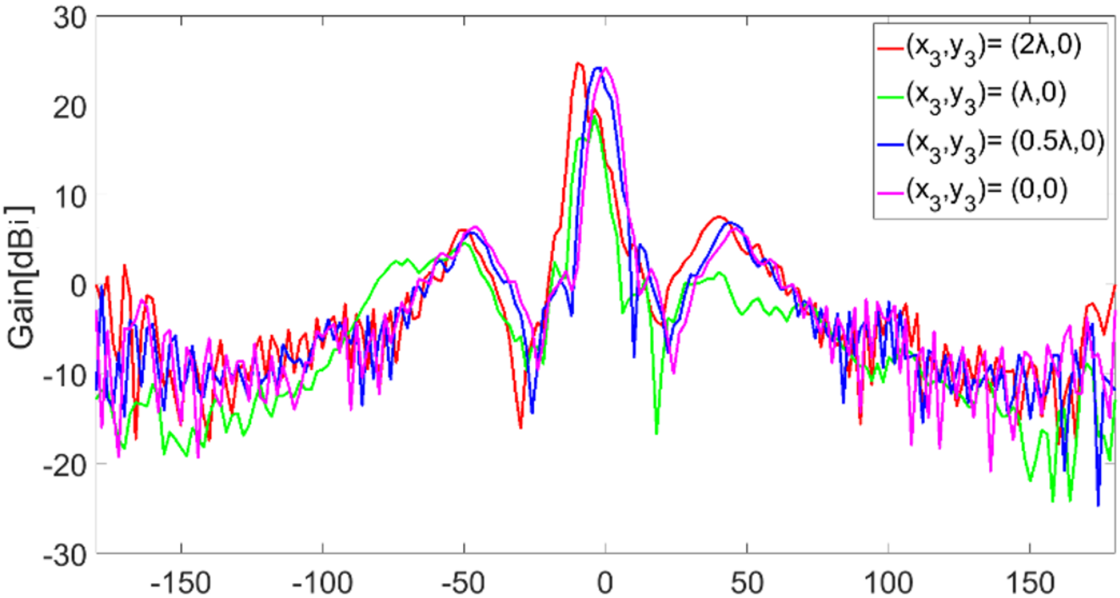

Figure 5.27. Simulated 2D gain AWR1443Boost integrated with the lens with an active transmitter of Tx_3 located at different positions relative to the apex of the lens.

various relative distances. We investigated the beam steering calculated by equations (8) and (9) in other types of antennas with various positions. We considered the half-wave dipole and the horn (with the same performance shown above) and the patch, AWR1443Boost-Tx_1, integrated with the lens of R=F=10 λ. We changed the position of the primary feed from -10 λ to 0 along the x-axis (the apex of the lens was regarded as the origin (0,0)) and provided the simulation results in Figure **5.30**. The magenta curve is the direction of the main beam calculated by (8), while the green, blue and red curves are the angle of the main beam of the horn, the dipole and the patch antennas integrated with the lens, respectively. As seen, the direction of the main beams is very close to the results calculated by (8) when the feeders are located close to the apex of the lens. However, for the larger relative distance, the angle of the main beams of the antennas is slightly different from the estimated angles. The maximum difference between the estimated direction by (8) and the main beam of the patch, the horn and the dipole are about 2.5°, 5.5° and 6°, respectively. The reasons for these differences (although very small) are the dimensions of the feeders that are not a point source, while the lens design is based on the

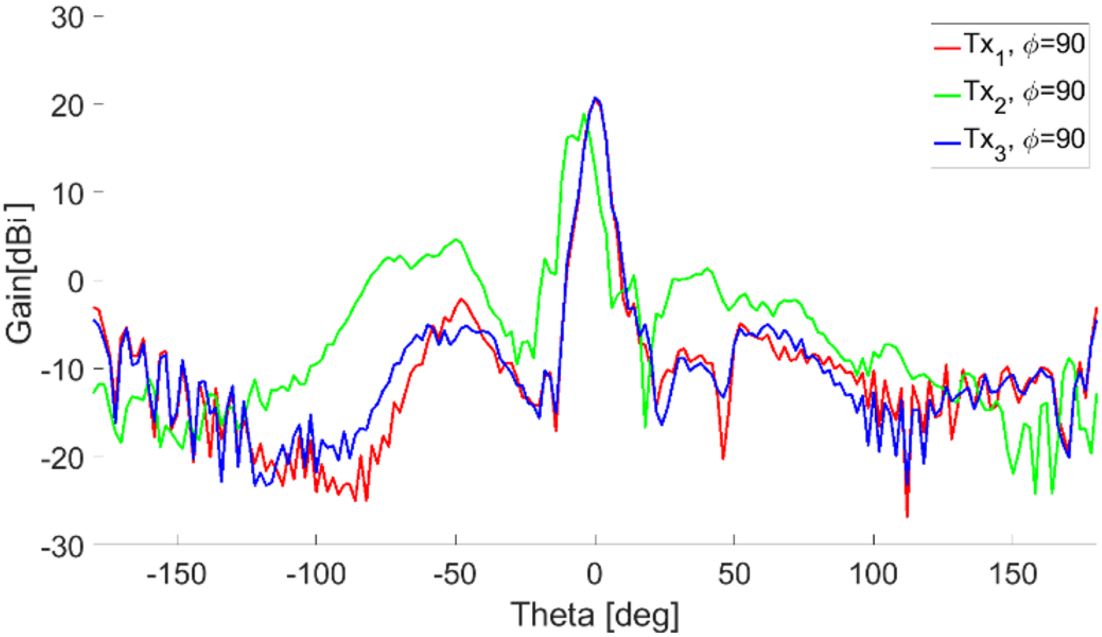

Figure 5.28. Simulated 2D gain of AWR1443Boost integrated with the lens at φ=90°, transmitting with Tx_1, Tx_2 and Tx_3 separately.

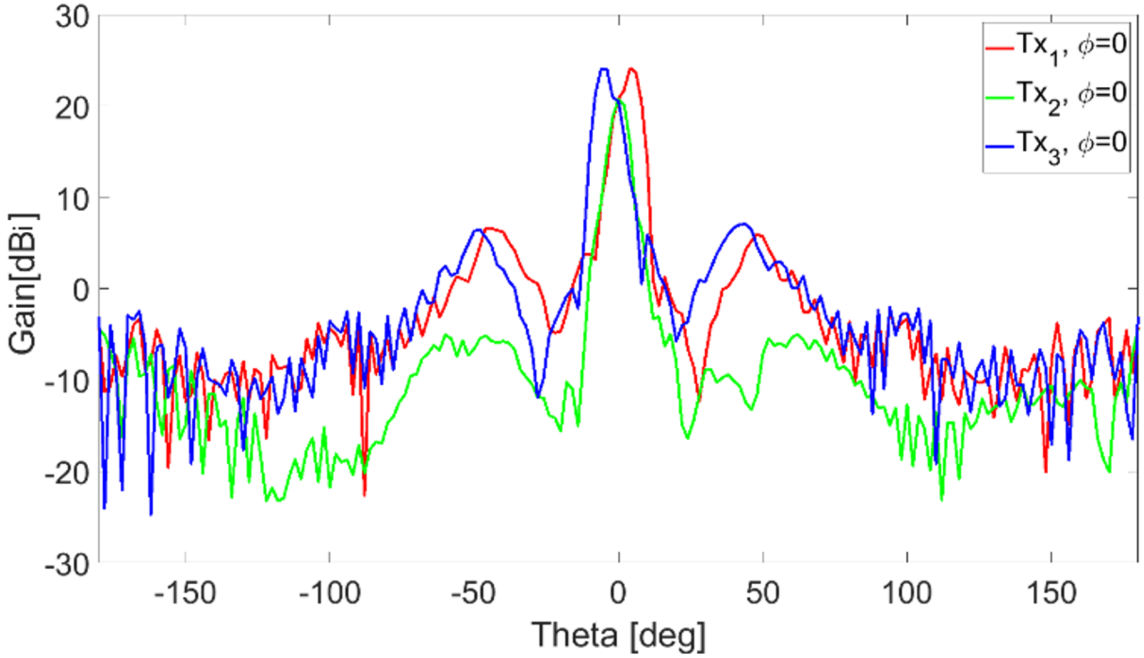

Figure 5.29. Simulated 2D gain of AWR1443Boost integrated with the lens at φ=0 °, transmitting with Tx$_1$, Tx$_2$ and Tx$_3$ separately.

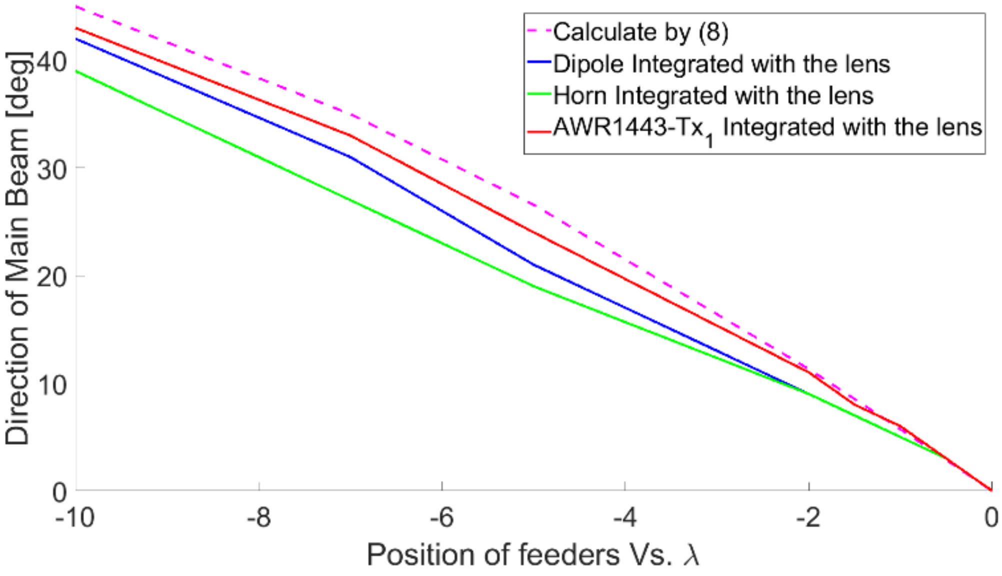

Figure 5.30. Simulated 2D gain of different types of antennas at various relative distances to the apex of the lens.

assumption of the point source. Moreover, the beamwidth of the feeder also plays a crucial role; the antenna with a wider beamwidth would result in more accurate results.

5.2.2.3.2 3D-Printed Sample Characterization

This subsection describes the method carried out for material characterization. The 3D-manufactured lens sample was characterized in the mm-wave range 60 GHz – 67 GHz using the open-ended coaxial probe DAK1.2E-TL [142]. This is done to approximate the electromagnetic behaviour of the lens material when integrating it with the mm-wave radar in HFSS simulations. The measurement setup connects one port of the Keysight Technologies VNA N5227A to the DAK-TL using a coaxial cable, VNA (Vector Network Analyzers) to PC using Ethernet/LAN cable and DAK to PC using a USB cable [142]. To characterize a solid sample in this system, a 50 Ω coaxial probe is pressed against the sample in the sample platform, as shown in Figure **5.31**. The dielectric properties (ϵ' and tanδ) are calculated from the measured reflection coefficient S_{11}, calibrated sample thickness, probe diameter, and bead permittivity. The Keysight VNA settings are set to 0 dBm source power with 100 Hz IF Bandwidth in the system interface.

The force is tuned around 500 N with 3 VNA traces for the averaging reset. Before starting the measurements, the testing fixture was calibrated in the desired frequency range of 60 GHz – 67 GHz at 200 MHz resolution using the standard Open-Short-Load method. The thickness is used as a reference load material at 20^{o} C. Thickness calibration is also performed using the zeroing tool, where a gauge block of the thickness nearest to the 3D-printed sample thickness (~8 mm) was used. Next, the dielectric measurements are performed, where the 3D-printed sample is tested ten times to verify the repeatability of the dielectric measurements. The Eccostock disc (ϵ' = 2.538, tanδ = 0.0005) of about 8 mm average of the extracted ϵ' and tanδ for all trials are plotted in Figure **5.32** (a) and (b), respectively. These plots show that the dielectric constant changes slightly from 2.63 to 2.68 over the 7 GHz measured bandwidth. Smooth fluctuations are also observed in the loss tangent between 0.011 and 0.016. With f=67 GHz set as the upper-frequency limit/bound for this characterizing fixture, the dielectric constant and loss tangent for the tested lens sample is approximated around 2.68 and 0.019, respectively. This would allow us to approximate the EM behaviour of the lens in the numerical simulations when operating in the higher mm-wave range of 77 GHz – 81 GHz of the radar system.

Although the estimated values might not be accurate, this would allow us to approximate the Electromagnetics behaviour of the lens in the numerical simulations when operating in the higher mm-wave range of 77 GHz – 81 GHz of the radar system.

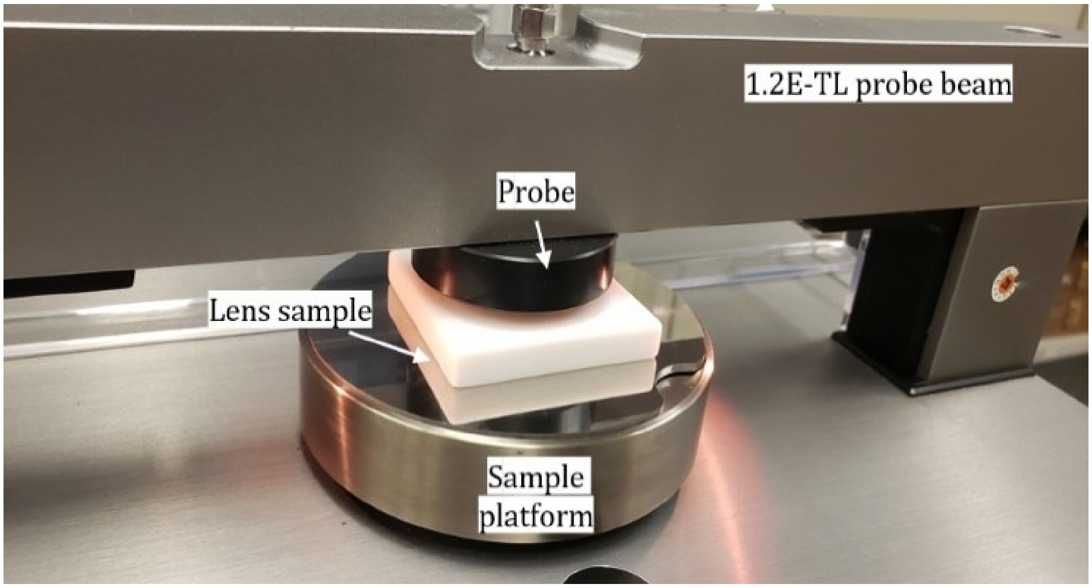

Figure 5.31. Photo of the measurement setup for characterizing the lens sample using the open-ended coaxial probe.

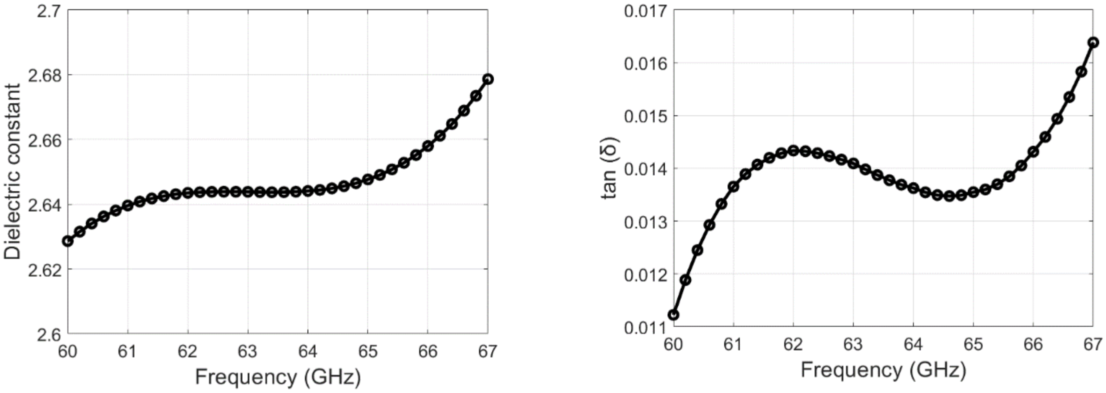

(a) (b)

Figure 5.32. Extracted electrical properties (a) dielectric constant and (b) loss tangent for the lens sample in the mm-wave range.

5.2.2.4 In-Package Integrated Lens Design

In the previous subsections, the purpose was to find the optimum lens parameters and analyze the trade-off between them. However, the main contribution of our antenna design is its entire implementation, including the choice of the type of lens and its inclusion as part of the package design. In previous works [135], [136], only the lens antenna was analyzed without considering the proper packaging.

However, in this work, an in-package hyperbola-based lens antenna with the optimum parameters mentioned above ($F=R=10\,\lambda$) is designed. The schematic of the in-package dielectric hyperbola-based lens antenna integrated with the AWR1443Boost radar is shown in Figure **5.33**. It should be noted that previous works on dielectric lens designs were mainly focused on a single transmitter and a single receiver. However, as shown, our proposed in-package lens covers all transmitters and receivers, thus designed for a MIMO system.

The final component of the design is the radar/lens cover, which encapsulates the AWR1443Boost PCB and serves as a mounting point for the hyperbola-based lens. A cross-view of the 3D model of the designed system in SolidWorks is shown in Figure **5.34** (a), and the whole system is provided in Figure **5.34** (b). As shown, the mount and base are designed to fit any TI data collection adapter (DCA 1000 EVM board [84]). It is used to capture raw data (IQ samples from the receivers) and to transfer it over the Ethernet interface to a PC. The base consists of a plate with a flat bottom that can be mounted to any flat surface, as well as flaps at each corner that can be drilled to mount screws. The DCA cover is an enclosure designed for the DCA 1000 board. The cover is needed to prevent electrostatic damage to the board. A grove is implemented in the DCA enclosure lid to ensure that the radar/lens cover—and, in turn, the lens itself—is always correctly positioned above the AWR1443Boost antennas. The radar/lens cover is designed to fit over all components as closely as possible to avoid unnecessarily increasing the size of the radar. Similarly, the walls are kept relatively thin (at a thickness of 2 mm) to reduce the weight and cost of the cover as well as to minimize any interference it might cause.

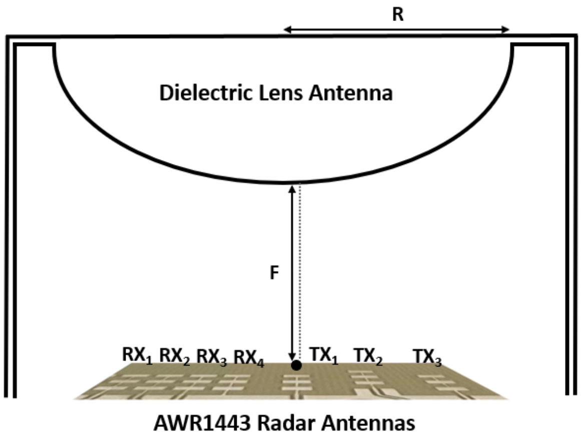

Figure 5.33. Geometry of the in-package lens antenna integrated with the AWR1443Boost radar.

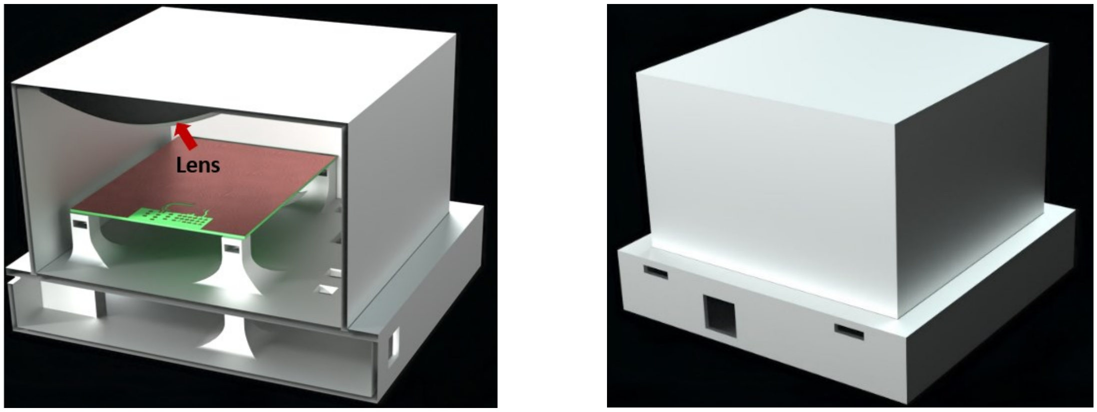

(a) (b)

Figure 5.34. 3D model of the designed system in SolidWorks with the radar/lens cover: (a) cross-view showing the encapsulated lens and (b) the whole system.

To show the impact of the radar/lens cover on lens performance, we simulate the AWR1443Boost radar integrated with the lens with and without the cover in HFSS using the optimum lens parameters in addition to the measured electrical properties of the printed lens sample. Figure **5.35** (a) shows the 2D radiation pattern of the AWR1443Boost radar at φ=0° without the lens (the red curve), with the lens but without the cover (the blue curve) and with the radar/lens cover (the red curve). Figure **5.35** (b) shows the 2D gain radiation pattern of the radar at φ=90° without the lens (the red curve), without the cover (blue curve), and with the cover at φ=90° (red curve), respectively. As seen, the cover does not impact the functioning of the radar but improves the aesthetics of the radar system package. It also enables the lens to be held in place with minimal mechanical interference and protects the AWR1443Boost PCB and the lens from damage. Therefore, with the designed cover, ease-of-

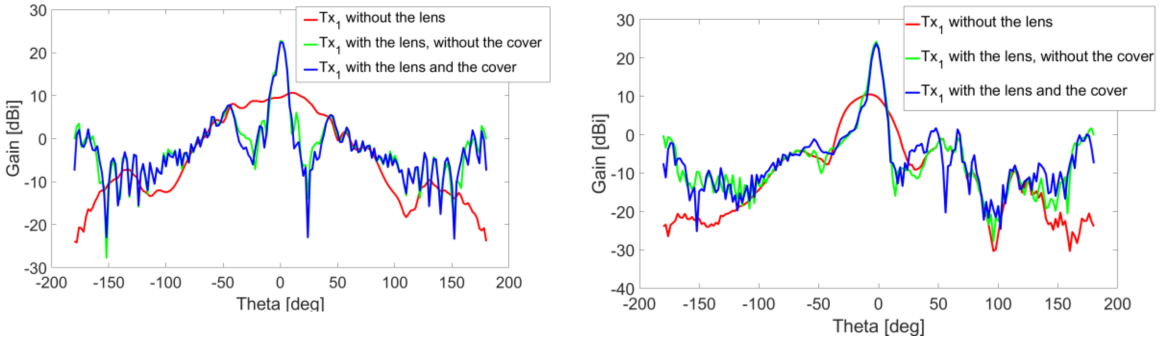

(a) (b)

Figure 5.35. Simulated 2D gain of AWR1443Boost antenna integrated with the lens with and without the radar/lens cover at (a) φ=0° and (b) φ=90°.

packaging and ease-of-fabrication features of the in-package integrated hyperbola-based lens antenna are clearly shown.

Since the proposed in-package lens antenna covers all antennas, it also affects the radiation patterns of receivers. However, the design steps of a hyperbolic lens explained in (1) - (7) are based on a single-point source placed at the center of the lens. Each antenna has a different distance to the center of the lens; thus, the radiation pattern of each of them will be different, and, in turn, the radiation pattern of a transmitter and the corresponding receiver are not identical and fully overlapped. Figure **5**.**36** shows the 3D gain radiation patterns of the radar integrated with the lens. Figure **5**.**36** (a), (b), and (c) show the results of the case when the Tx_1, Tx_2, and Tx_3 antennas are the only active element, respectively. As shown, the maximum beam is directed at $\varphi=2°$ and $\theta=0°$ with the gain of 21.2 dBi with the active Tx_1. The active Tx_2 antenna results in a gain of 18.19 dBi steered to $\varphi=-3°$ and $\theta=-4°$.

The main beam of the active Tx_3 antenna is steered to $\varphi=2°$ and $\theta=-11°$ with a gain of 17.3 dBi. As illustrated, the transmitter with a further relative distance to the lens apex provides lower gain. The gain of the transmitter depends on the relative distance of the antenna to the lens center. The results confirm that a transmitter at the center of the lens provides the best performance. Moreover, Figure **5**.**36** (d)–(g) show the 3D gain radiation pattern of the AWR1443Boost receiver antennas integrated with the lens. Based on the lens position above the radar, Rx_4, Rx_3, Rx_2, and Rx_1 antennas are placed at $(-\lambda, 0)$, $(-1.5\ \lambda, 0)$, $(-2\ \lambda, 0)$, and $(-2.5\ \lambda, 0)$ in the x-y plane, respectively. Figure **5**.**36** (d) is the radiation pattern when Rx_4 is the active element providing the gain of 22.6 dBi steered to $\varphi=2°$ and $\theta=6°$. Additionally, Figure **5**.**36** (e), (f), and (g) are the radiation patterns of the system transmitting by Rx_3, Rx_4, and Rx_1 with the gain of 22.3 dBi, 22.2 dBi, and 21.8 dBi steered to $\varphi=2°$ and $\theta=8°$, $\varphi=2°$ and $\theta=11°$, and $\varphi=4°$ and $\theta=13°$, respectively. As seen, the gain variation between each receiver element is very small because the inter-element spacing between receivers is comparatively small ($\lambda/2$).

As noticed, the relative distance between the feeders and the lens apex impacts the gain and radiation pattern of the antenna. Depending on the application and need, the proper position of the lens apex on top of the feeders could be optimized. As the main application of our lens design is for gait monitoring in a long hallway, it is desired to create the main beam steered around $\varphi=\theta=0°$. Therefore, we selected these parameters for the lens position above the radar antennas: $(x_1, y_1) = (0, 0)$, $(x_2, y_2) = (\lambda, -\lambda/2)$ and $(x_3, y_3) = (2\ \lambda, 0)$.

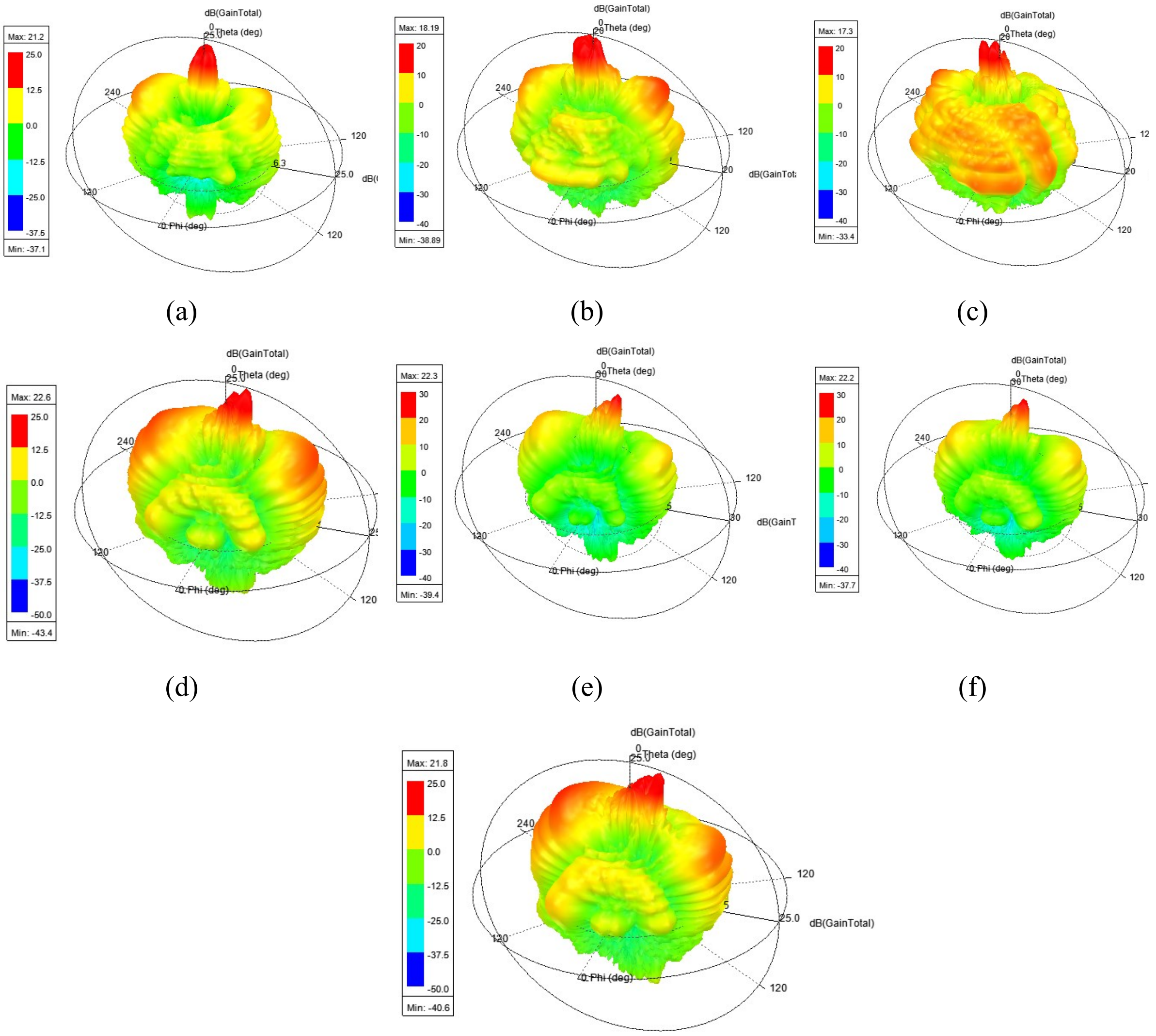

(a) (b) (c)

(d) (e) (f)

(g)

Figure 5.36. Simulated 3D gain radiation pattern of the AWR1443Boost antennas integrated with the lens with the measured electrical properties (a) Tx_1, (b) Tx_2, (c) Tx_3, (d) Rx_4, (e) Rx_3, (f) Rx_2, (g) Rx_1.

5.2.2.5 Measurement Method of Radiation Pattern of Radar Received Power

In a radar system, not only is the radiation pattern of each transmitter and receiver important, but the pattern of radar received power is a key parameter to be analyzed. This is because the primary purpose of a radar system is detection depending on the received power of reflected signals from a target. In this section, we show how the radar received power could be measured and how the measurements could be compared with the simulation results. To realize the pattern of the power of the radar-received signals reflected from a target to the radar receiver, we first formulated the radar-received power. The fundamental relation between the characteristics of a radar, a target, and received signals is called the radar equation [66]. The geometry of scattering from a scatterer (a corner reflector in our test) in our radar is shown in Figure **5.37**. When a signal with the power P_{TXN} is sent by a transmitter T_{XN} with a gain of G_{TXN}, it hits the scatterer at a range of r, and a part of the transmitted signals reflects back to all receivers. At the receiver, R_{XM}, the intensity of the received signal is calculated as

$$P_{RXM} = \frac{\sigma P_{TXN} G_{TXN} G_{RXN} \lambda^2}{(4\pi)^3 r^4} \tag{10}$$

where σ is the target radar cross section (RCS), and G_{RXN} is the gain of the receiver antenna R_{XM}.

We proposed and designed a measurement setup to measure the power of radar-received signals, as shown in Figure **5.37**. Regarding the proposed measurement setup, P_{TXN}, σ, λ, and r are kept constant at all angles in (10). Hence, G_{TXN} and G_{RXN} are two varying parameters in the power of the radar-received signals.

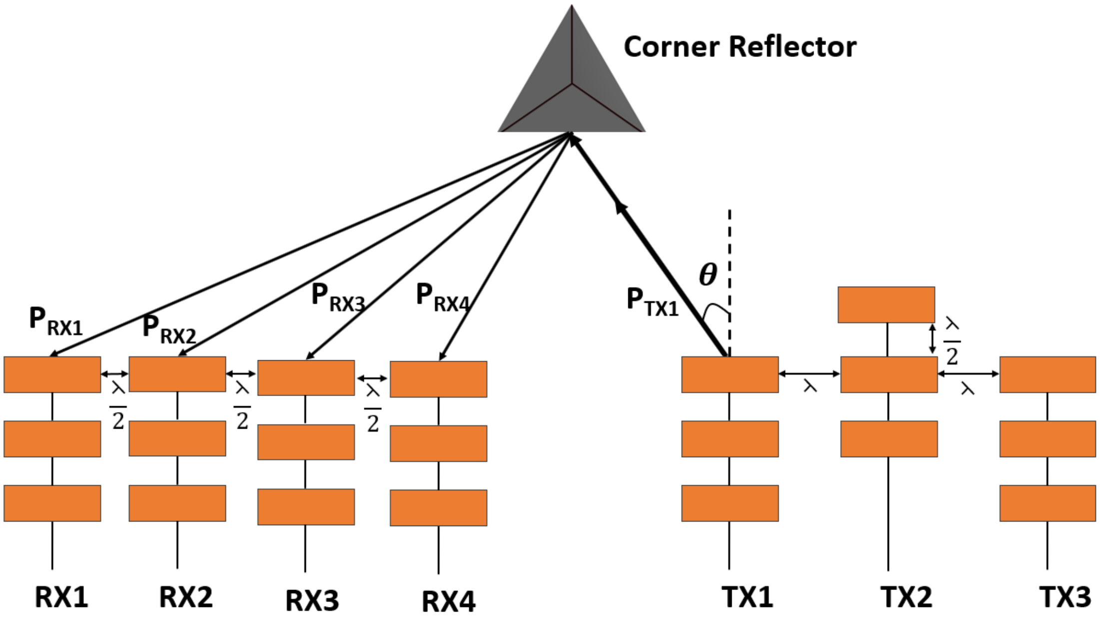

Figure 5.37. Geometry of the radar antennas emitting a corner reflector by one transmitter while receiving the reflected signals by all four receivers. In this case, the Tx_1 antenna is transmitting while all four Rxs are collecting reflected signals simultaneously.

Then, the received power could be calculated as

$$P_{RXM} = KG_{TXN}G_{RXN}, K = \frac{\sigma P_{TXN}\lambda^2}{(4\pi)^3 r^4} \tag{11}$$

K is constant at all angles. Therefore, the pattern of the power of the radar received signals is the multiplication of the gain radiation pattern of the transmitter antenna by the corresponding radiation pattern of the receiver antenna.

In order to compare the measured results using our proposed method (Figure **5.37**) with the simulated results, the radar transmitter and receiver radiation patterns are simulated separately. Then, the result of the multiplication of the two simulation results is the radiation pattern of the power of the radar-received signals.

5.2.2.6 Experimental Results

To evaluate the system performance, we fabricated and printed the in-package hyperbola-based lens antenna (Figure **5.34**). The fabricated system is shown in Figure **5.38**. The lens is inexpensive to manufacture that has a volume of 37 cm3, which takes 47g of PLA filament to print. PLA costs roughly 0.03 CAD/gram on Amazon.ca. Therefore, the total cost works out to approximately \$1.41 CAD (around \$1 USD). Two types of measurements are performed. As the first type, the pattern of the radar-received power is measured according to the proposed measurement method (Figure **5.37**). Moreover, as the second type of measurement, the system performance in multipath mitigation in hallway gait monitoring is evaluated. The amplitude of the received signals collected by the receivers while transmitted by the transmitters is measured for each test. Since the AWR1443Boost is an FMCW radar, FFT is applied to each received signal, thus providing the range information of the scatterer with the corresponding signal intensity [73].

5.2.2.6.1 Pattern of Radar Received Power

To measure the pattern of the radar received power, we designed a measurement method, as shown in Figure **5.37**. As shown, to compare the performance of the radar integrated with the lens, each test is carried out by the radar integrated with and without the lens. The target for all tests is a corner reflector fabricated from stainless steel. It is designed with a side length of 6 cm, as this dimension gives an RCS of approximately 0.025. This RCS is roughly the average range for a human being at f= 77 GHz, making these corner reflectors a reasonable substitute [143]. The corner reflector is placed at all angles (from

0° to 180° with 5° accuracy) to reflect the transmitted signals to receivers, and then all RXs record reflected signals. For the first set of measurements, we collected received signals from the reflector at different angles from the AWR1443Boost receivers without the lens. We activated each of the three transmitters separately while all receivers were collecting reflected signals. Then, the amplitude of the result of the FFT, performed on the received signals at a range of r=1 m, is stored at all angles.

In order to validate our proposed measurement setup, simulated and measured normalized patterns of the received signals transmitted by the Tx_1 while received by all four receivers are provided Figure **5.39**. As shown, the pattern of the received signals without the lens is very wide due to the wide beamwidth of the radar antennas. Figure **5.39** also shows that simulated and measured results are very close, validating our proposed measurement method. The same procedure is used for the case of the active Tx_2, Tx_3 showing the same results. The results show good agreement between measured and simulated patterns. The same procedure is used to analyze and examine the lens performance integrated with the radar system. In a similar vein to the previous tests, the corner reflector is placed at a range of r=1 m and moved along all angles in our measurement setups.

All receivers actively recorded signals reflected from the scatterer emitted by one active transmitter. Figure **5.40** shows the simulated and measured normalized pattern of the received power of the Rx_1

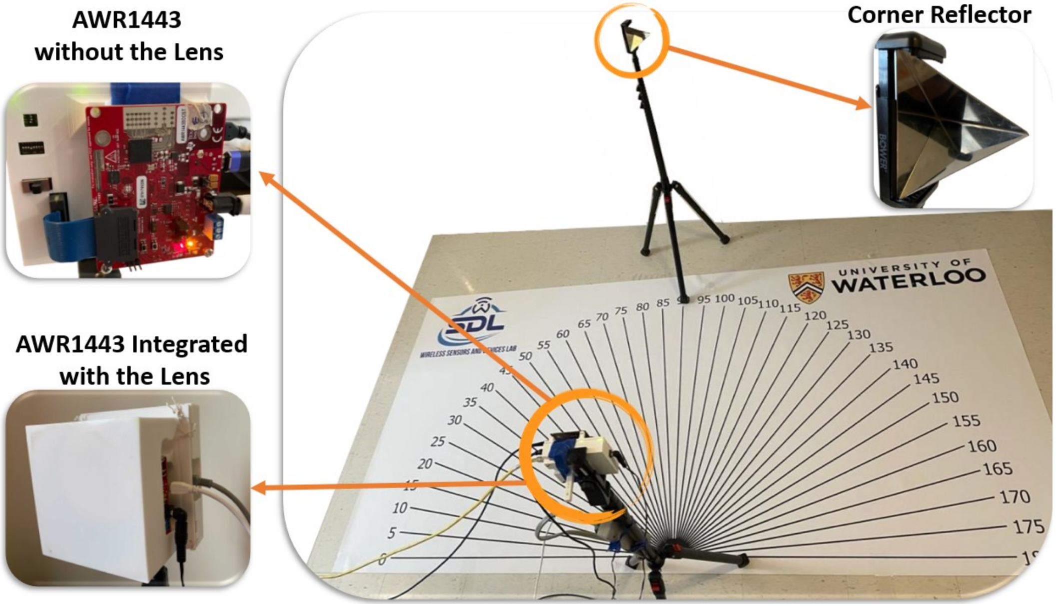

Figure 5.38. Radar receiver power measurement setup. Tests were performed with the radar integrated with and without the lens at all angles from 0° to 180° with 5° accuracy.

while the Tx$_1$ is transmitting without and with the lens. As seen, the measured patterns align with the simulated patterns. The results show that the lens effectively sharpens the beam of the received power compared to the results obtained without the lens. The multiplication of the two patterns is sharp and directed at 0° relative to the radar.

To show the effect of the nonoverlapping pattern of the transmit and the receiver antennas on the pattern of the received power, the received power of all four receivers integrated with and without the lens is provided in Figure **5.41** while transmitted by the Tx$_1$. As observed, the received power from the radar integrated with the lens is sharper and more intensive (more than 14 dB gain improvement). Although the main beam of the transmitter and the receiver antenna integrated with the lens is steered in a different direction, the results of the multiplication of patterns are steered to 0°. These results show that the pattern of received power of the collocated transmitters and receivers in a MIMO system depends on the multiplication of the pattern of transmitter and receiver antennas. To show the lens effect on the other transmitters, Figure **5.42** and Figure **5.43** illustrate the simulated and measured patterns of the received power of Rx$_1$ transmitted by the Tx$_2$ and Tx$_3$, respectively. It should be noted that, as shown in Figure **5.41**, the patterns of the received signals from other receiver antennas are similar to Rx$_1$.

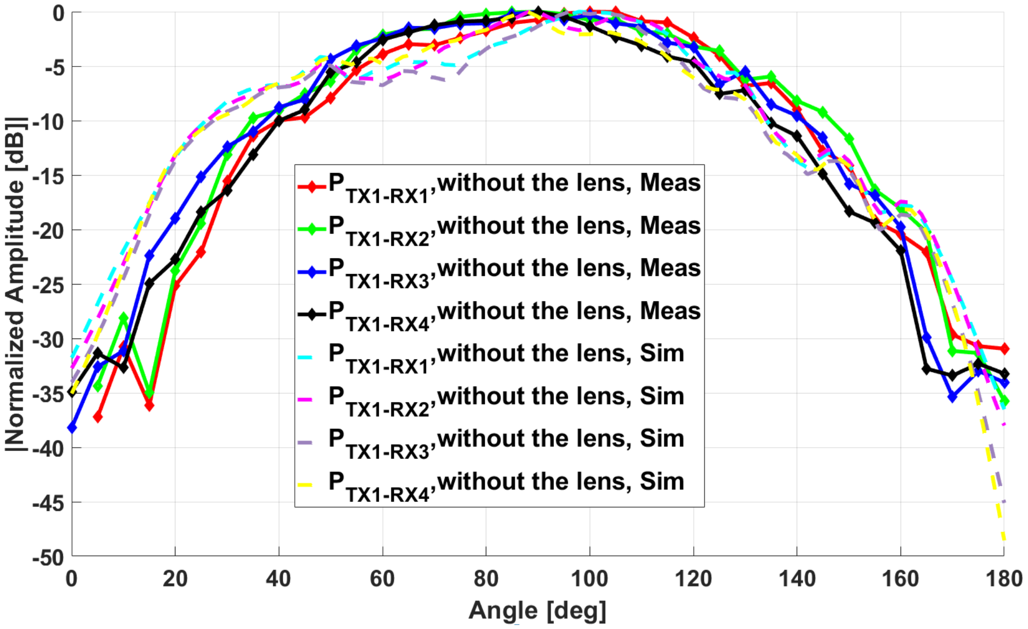

Figure 5.39. Simulated and measured patterns of the radar received power by all receives transmitted by Tx$_1$ without the lens.

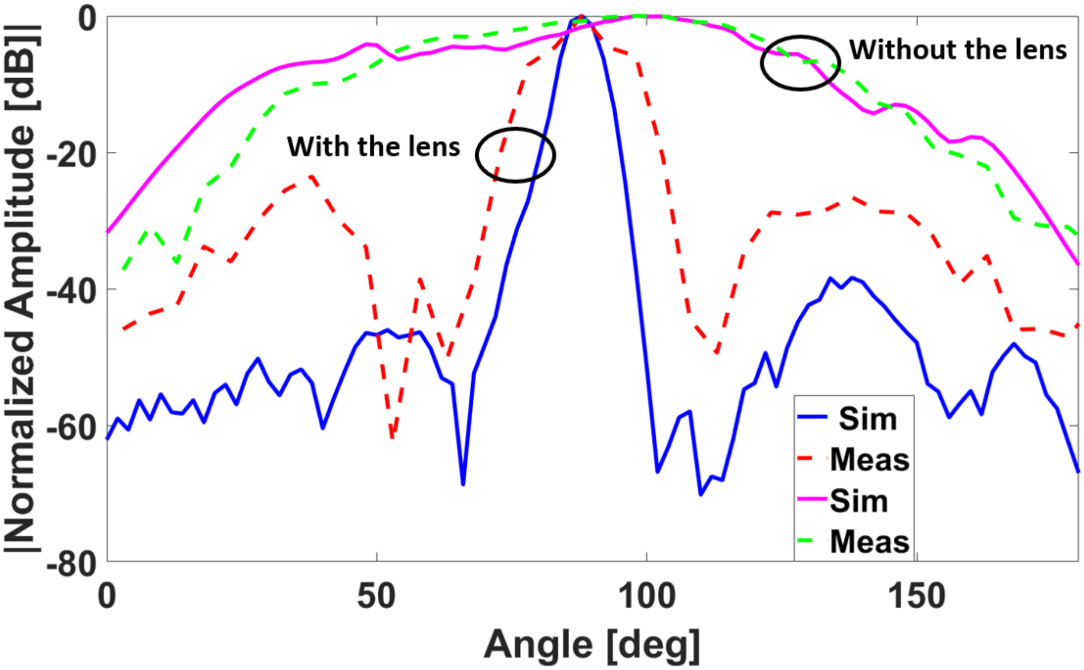

Figure 5.40. Simulated and measured patterns of the radar received power by radar receiver Rx_1 transmitted by Tx_1 integrated with and without the lens.

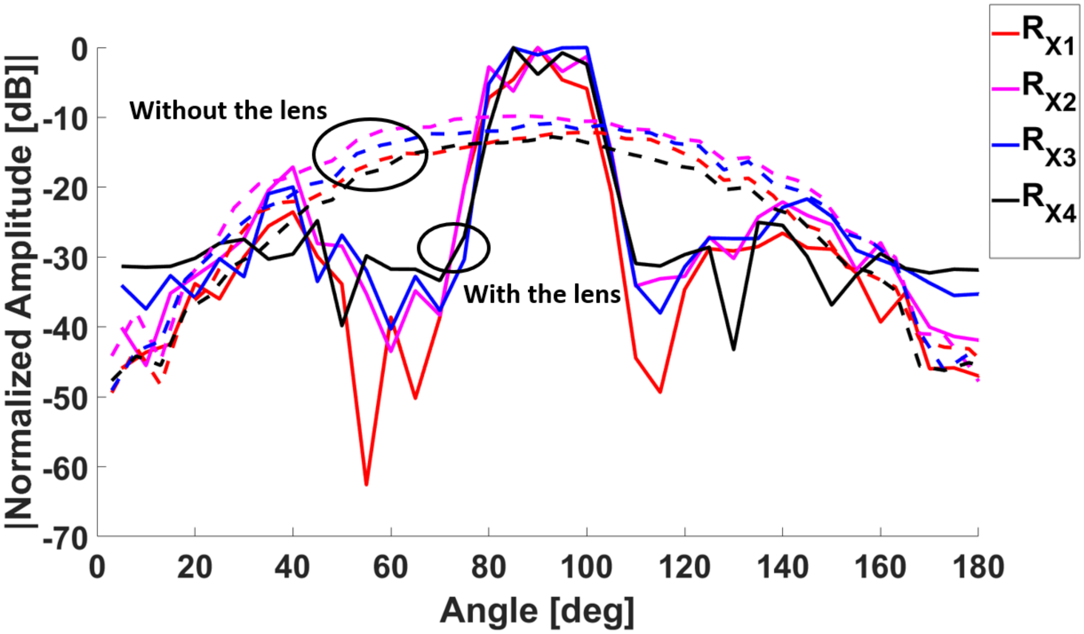

Figure 5.41. Measured patterns of the radar received power by all receivers transmitted by Tx_1 integrated with the lens.

Therefore, in Figure **5.42** and Figure **5.43**, we provide the results from Rx_1 for all transmitters. Note that the Rx_1 is located at the farthest relative distance from the lens apex. Patterns of the worst-case scenarios are plotted in Figure **5.40**, Figure **5.42**, and Figure **5.43**. The results of gain improvement of other pairs of transmitters and receivers are summarized in Table **5.4**. Regarding the results of the gain improvement of the lens in Table **5.4**, it is seen that the maximum gain improvement is obtained with the signals transmitted by Tx_1 and received by Rx_4. This is because both the Tx_1 and the Rx_4 have the minimum relative distance to the lens apex. As mentioned above, the source located at the lens center performs better in terms of collimating the beam and improving gain. Consequently, the results confirm that the lens's effectiveness in gain improvement of received power depends on the relative position of both the transmitter and the receiver. Table **5.4** shows that the minimum gain improvement is 7.2721 dB, while the maximum enhancement is 14.8053 dB.

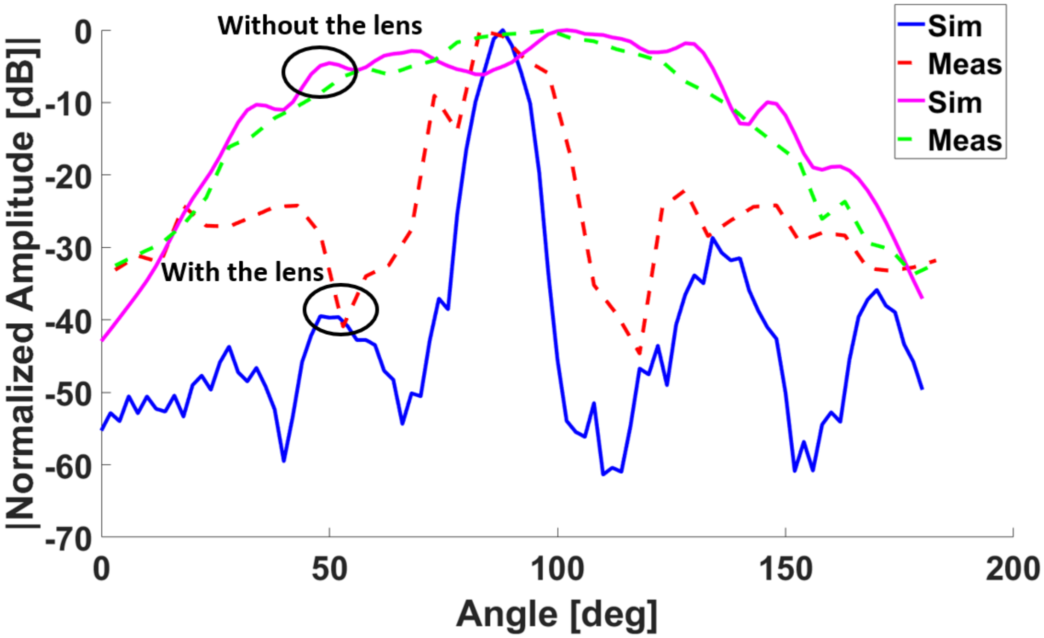

Figure 5.42. Simulated and measured patterns of the radar received power by radar receiver Rx_1 transmitted by Tx_2 integrated with and without the lens.

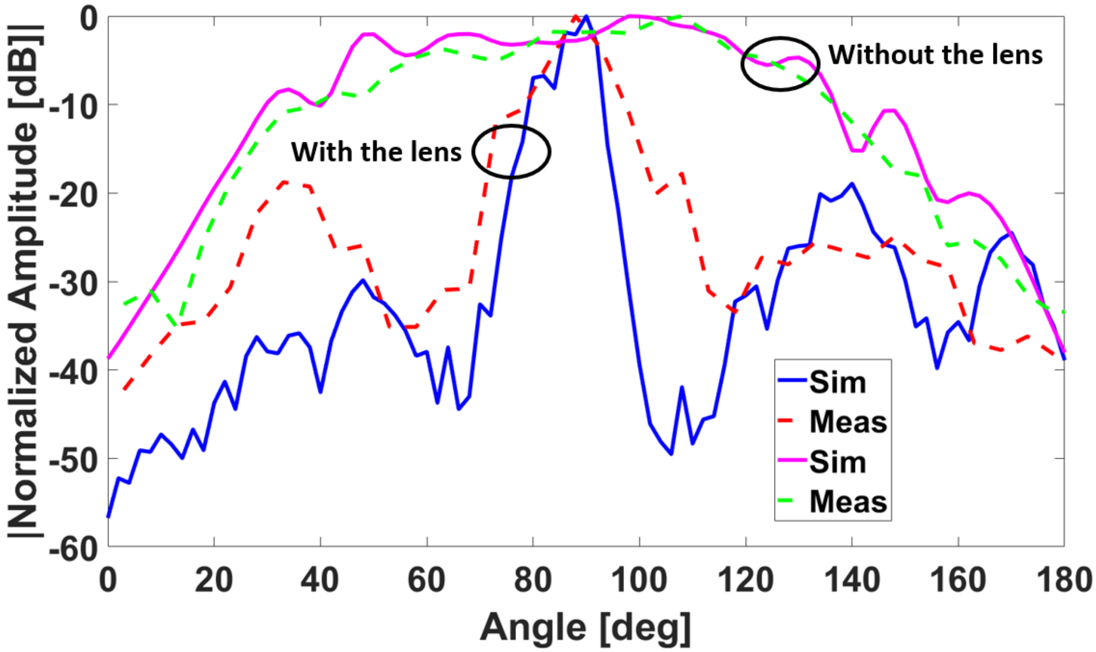

Figure 5.43. Simulated and measured patterns of the radar received power by radar receiver Rx_1 transmitted by Tx_3 with and without the lens.

It should be noted that, as shown in Figure **5.39**–Figure **5.43**, the sidelobe levels in all cases are lower than 20 dB, which is sufficient for radar detection. As will be shown in the next subsubsection, particularly for our hallway gait monitoring application, the system is sufficiently sharp, and the sidelobe level is comparatively low so that the walking subject can be monitored accurately.

Table 5.4. Measurement and simulation results of gain improvement of the radar received power.

	Rx_1		Rx_2		Rx_3		Rx_4	
Gain Improvement	Meas (dB)	Sim (dB)	Meas (dB)	Sim (dB)	Meas (dB)	Sim (dB)	Meas (dB)	Sim (dB)
Tx_1	12.18	13.63	12.80	14.29	13.87	15.92	14.80	16.76
Tx_2	7.27	11.93	9.63	12.59	10.47	13.22	11.70	14.05
Tx_3	7.27	7.76	9.18	8.42	9.19	10.05	10.27	12.88

5.2.2.6.2 Hallway Walking Test Using the In-Package Lens

To show the effectiveness of our proposed radar system paired with our gait extraction algorithm (Figure **4.5**), we evaluated system performance in a hallway filled with metal cabinets, as shown in Figure **5.44**, which is a challenging scenario as the metal cabinets cause a strong reflection that causes significant multipath effects. We also considered this setup to be one of the “worst case” scenarios where gait would plausibly be monitored (i.e., a hospital hallway). Gait cycle parameters were extracted by asking four volunteers to walk back and forth three times by following marked steps (420 cm with six steps, each step is 70 cm for each lap). Same as previous tests, reference values were extracted using a stopwatch and asking volunteers to follow a traced line that had marks the volunteers were asked to step on. To demonstrate radar sensor performance in hallway gait monitoring, we first examined radar results without the lens.

The range of the walking subject at frame #150 is provided in Figure **5.45** to show and compare results. Figure **5.45** (a) shows the range of the subject using the AWR1443Boost without the lens. Note that frame #150 helps to illustrate the detail in this work while the same results could be obtained in other frames. As shown in Figure **5.45**, the amplitude of the multipath reflection is more than the amplitude of the subject’s position (the green circle). Additionally, various multipath reflections can clearly be seen at various range bins (shown by the red circle). However, Figure **5.45** (b) shows that the lens effectively mitigates the multipath reflections. As a result, the range bin of the subject’s torso position (the green circle) corresponds to the maximum amplitude representing the subject’s position. Hence, instead of implementing a potentially time-consuming and computationally expensive signal

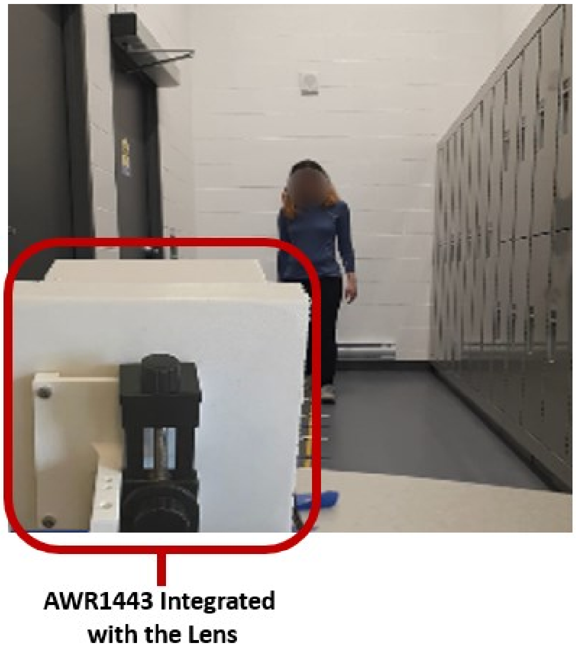

Figure 5.44. Experimental setup for hallway gait assessment using the in-package lens.

processing technique to remove the multipath effects (Figure **5.1**), we could obtain a reliable hallway gait extraction system by using the proposed in-package system and isolating the torso's range bin. Therefore, unlike Figure **5.1**, where the Capon beamformer, 2D-CFAR, DBSCAN clustering and an association and tracking algorithm were proposed to obtain the range of the subject and remove the ghosting effects, the range of the walking subject can be approximated by taking the maximum value in the range bins. Therefore, only one transmitter and one receiver are sufficient for single-person hallway gait monitoring using our in-package lens without the need to generate the 2D heatmap of the environment. Our proposed method in Figure **4.5** could then be applied to the received signals of walking cycles to extract gait spatiotemporal parameters.

As shown summarized in Table **5.5**, the average total number of steps of the whole walking process is N=57 without using the in-package lens, while the actual step count was 36. Moreover, the average walking speed and step length are 2.1 m/s and 90.3 cm, respectively, whereas the true value obtained by using a stopwatch is 0.867 m/s. However, using the system integrated with the lens, an average walking speed of v= 0.831m/s was obtained (true value = 0.867 m/s). The total calculated number of steps is N=36, which is exactly equal to the actual value. The average error of extracted parameters of the four participants is provided in Table **5.5**.

In this work, we addressed the challenges of gait assessment in a cluttered environment, such as a hallway lined with metal cabinets. To overcome the multipath effects, we proposed an easy and low-cost method of radar antenna modification to focus the field of view of a commercially available radar board. Our results suggest that using our add-on hyperbola-based dielectric lens antenna and implementing our gait extraction algorithm, a stand-alone gait assessment system could be developed

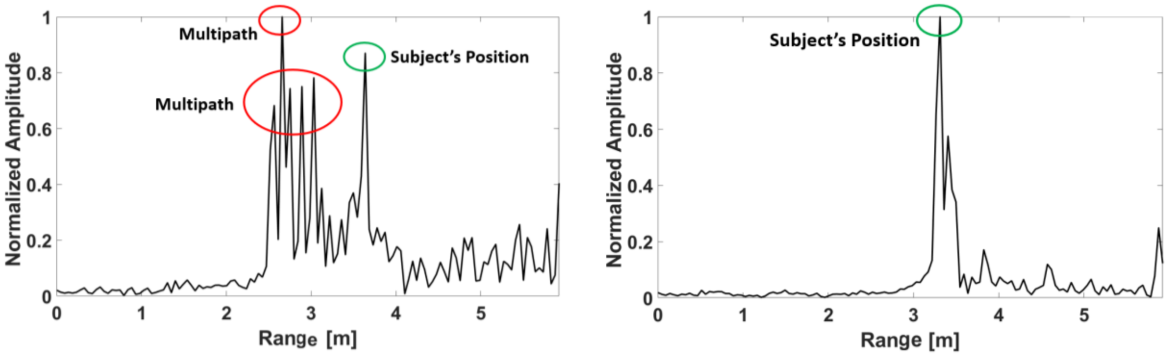

(a) (b)

Figure 5.45. Range of a walking subject at frame #150 (a) without the lens (b) with the lens.

Table 5.5. Extracted gait values in a hallway with/without the lens.

	Speed (m/s)	Step Count	Step Length (cm)
True Value	0.86	36	70.0
W/O the lens	2.10	57	90.3
W/ the lens	0.83	36	68.6
Average error for four participants W/ the lens	0.013	-1.25	-2.33

using any FMCW radar. Our in-package lens antenna design should support relatively easy implementation with commercially available radars. Since the system is portable, easy-to-use, and low-cost, it could be installed in a variety of living environments, including long-term care, hospitals, or individuals' homes for the day-to-day gait of natural gait assessment in a way that requires no effort on the part of the people being monitored.

5.2.3 Summary of Proposed Single-Person Hallway Gait Monitoring Methods

The results provided in Sections 5.2.1.4 and 5.2.2.6.2 indicate that the in-package lens could effectively reduce reflections from walls and produce gait values comparable to those obtained using the proposed novel algorithm. Both methods demonstrated sufficient accuracy for detecting meaningful changes in gait over time (although more participants should be included in the study in more dynamic environments). The modified radar system with the add-on lens antenna was able to extract gait values using fast and easy-to-implement gait extraction algorithms (Figure **4.5**). Thus, one of the main superiorities of the radar antenna modification method is that the processing chain could be implemented in a radar DSP or a Raspberry Pi as a stand-alone hallway gait monitoring system without a need for an extra powerful desktop or a laptop system. Notably, due to the computationally complex and time-consuming processes, the association and tracking method in Figure **5.1** might require an extra powerful system for processing. Moreover, the modified radar system uses only one transmitter and one receiver antenna, whereas the signal processing method requires multiple transmitters and receivers to provide a range-azimuth heatmap of the environment.

One of the significant advantages of the proposed signal processing method is that it could be paired with any radar type capable of generating range-azimuth heatmaps. However, the add-on lens was designed for the specific AWR1443 radar operating at 79 GHz [83]. Therefore, we must repeat the simulations, measurements and fabrication processes separately for the add-on hyperbolic lens method for any new radar sensor. Although the same guideline could be followed to obtain the optimum lens parameters, the design procedure depends on the antenna type, the number of antennas, radiation patterns, frequency of operation, etc. Price-wise, the system modification method might be less expensive for implementation as it could be deployed as a stand-alone system. In contrast, the signal processing method requires a more powerful system. On the other hand, the modification system requires extra work in the design and fabrication process that is time-consuming and requires some sophisticated devices, such as a VNA, a 3D printer, etc., before being implemented in real-life applications. Hence, depending on the available resources, costs, and needs, one of these methods would be useful for single-person hallway gait monitoring. Moreover, the side lobes in the lens antenna can cause reflections and diffraction of the radar signal. This can affect the accuracy of the radar signal, particularly in long hallways. To address this issue, we still need to implement an algorithm that accounts for multipath propagation and extracts useful information from the radar signal. This allowed us to achieve accurate results in our experiments despite the presence of side lobes in the antenna.

The proposed hallway gait monitoring methods were able to track only one single walking subject. In the following section, a multiple-people gait monitoring method will be outlined. Since the radar used for this thesis is a MIMO sensor, it could be suitable for multiple people scenarios.

5.3 Multiple-People Hallway Gait Monitoring

5.3.1 Relevance

As stated in Section 3.4.5, Section 3.5, and Chapter 4, gait analysis applications have so far targeted only gait monitoring under ideal conditions, that is, on a single subject who is relatively walking in a straight line. However, the possibility of the coexistence of multiple walking subjects is high, especially in long-term care facilities where older adults might need assistance during walking. GaitRite and wearables are not able to assess multiple people's gait at the same time using only one device. In this section, a novel radar-based algorithm is proposed to extract walking speed of multiple subjects. In previous chapters, a few participants were involved in evaluating the proposed method, however, in this section, the proposed multiple-people gait monitoring is assessed with 22 participants. In this section, we report walking tests performed by participants who participated in a study to identify how bedrest (BR) gives rise to physical deconditioning.

5.3.2 Bedrest Study

Physical activity is an important lifestyle habit needed to achieve healthy aging, as it promotes autonomy and enhances the quality of life. Conversely, periods of severe inactivity, such as during bedrest (BR) for illnesses or hospitalization, induce dramatic changes to the human body that are often similar in magnitude to those seen over decades of normal aging. Bedrest in otherwise healthy older individuals can lead to a reduction of muscle size and strength, changes in bone strength and function of the heart and blood vessels [144]–[147]. Bedrest can also affect balance, as well as how people process and understand information. All these factors combine to negatively impact the performance of daily living activities, leading to physical function impairment and the development of frailty, a clinical condition associated with an increased risk of disease and death [148].

Six-degree head-down bedrest (HDBR) has been widely used as an experimental model useful for the examination of the rapid physiological deconditioning that occurs during prolonged hospitalization and inactivity [149], [150]. Walking speed is a clear predictor of adverse health-related events [2], [151], and was reported to be slower following BR [150], [152]–[154]. Although these performance measures may not be sensitive enough to detect changes in small groups of volunteers following very short durations of BR, significant changes were identified after 10 days. They were consistent with studies in bed-ridden hospitalized older adults demonstrating a clear negative relationship between the duration of BR and functional capacity [150], [152]–[154]. In this study, we report the negative impact of 14-day HDBR on older adults' walking speed. The purpose of this study is to identify how bedrest gives rise to physical deconditioning. The report provided in this section is the results of walking tests of a first-of-its-kind study conducted in Canada, i.e., Microgravity Research Analogue (MRA): Understanding the Health Impact of Inactivity for the Benefit of older adults and Astronauts' Initiative.

5.3.2.1 Participant Characteristics

Twenty-two healthy 55–65-year-old adults (11 women; age: 59±3 years; mass: 70.1±14.2 kg; height: 1.67±0.09 m) participated in the 14-day BR study. All participants included in the study self-reported regularly performing at least 2.5 hours of moderate-to-vigorous physical activity each week, and all female participants were post-menopausal. Half of the participants were inactive for the 14 days of BR, while the other half completed three exercise sessions per day.

5.3.2.2 Description of the Research Procedures

This research study was conducted at the Center for Innovative Medicine (CIM) within the McGill University Health Centre Research Institute (RI-MUHC). Data collection for this research project lasted around six months (July 2021-January 2022) that included four visits:

Visit 1: 1 full-day screening visit,

Visit 2: 26-day long visit during which participants reside at the CIM,

Visit 3: 1 full-day follow-up visit after four weeks of Visit 2, and

Visit 4: 1 full-day follow-up visit after four months of Visit 2.

The 26-day visit (visit 2) during which participants reside at the CIM is composed of three periods:

- 5 days of adaptation period: During this period, participants underwent various measurements. This work reports the results of walking tests done in 5 days of the adaptation period called baseline (the term “PRE” is being used to show the walking speed).
- 14 days of BR period: During this period, participants spent 24 hours per day in bed. Additionally, the bed was set in a 6° head-down tilt position, and participants were not able to elevate their heads above their shoulders. All activities such as eating, reading, watching TV and all personal hygienic procedures, including showering, teeth brushing, shaving etc., took place in bed for the duration of this period.
- 7 days of recovery period: During this period, participants were able to stand up and walk and do all their activities like during the 5-day adaptation period. Throughout this week, participants had regular physiotherapy and exercise sessions to recover from the bedrest period. They also underwent various measurements, including two walking tests called Recovery 1 and Recovery 3 for day 1 and day 3 after BR (shown as R+1 and R+3), respectively.
- Walking tests were also done in Visit 3, called Recovery +4 weeks (shown as R+4wk).

5.3.2.3 Study Intervention

Participants were randomly assigned to one of the following groups (although it was balanced for the sex, this process is done randomly):

- Exercise Intervention (EX): The exercise intervention was carried out only during the 14-day BR period. All exercises were adjusted to be performed in bed.
- Control (CONT): Participants assigned to the control group underwent daily stretching and passive physiotherapy, as well as massages throughout the bedrest period.

5.3.2.4 Study Tests and Procedures

Since this thesis covers only the results of walking tests of the entire BR study, other tests done within the CIM would not be reported. Participants were instructed to walk as quickly as possible while maintaining safety, without running, and to complete four walks across a 14-meter hallway. The experimental setup was similar to what is pictured in Figure **5.2**. Participants walked toward the radar, which started ~15.5m away from the radar. The time to perform this test was recorded by a research assistant walking beside the participant using a stopwatch to be compared against radar results. The research assistant walked beside participants to ensure their safety because they might be vulnerable after BR. Figure **5.46** (a) shows the experimental setup for this study, while Figure **5.46** (b) shows the corresponding detected clusters by DBSCAN. As shown, due to several detected ghost clusters in addition to the subjects' clusters, an algorithm to analyze multiple-people gait monitoring in a hallway is required for this setup.

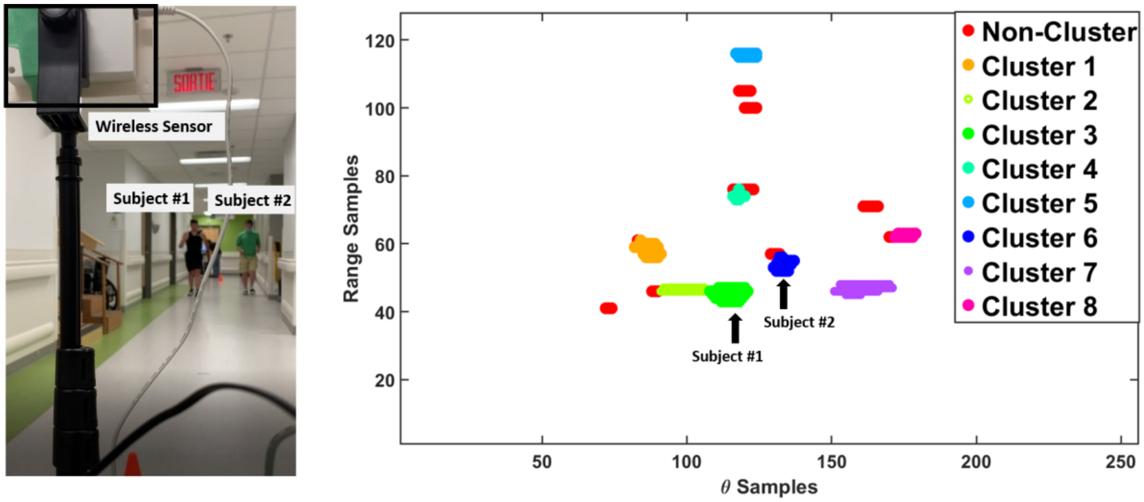

(a) (b)

Figure 5.46. Multiple-people hallway walking tests (a) a snapshot of the video in the middle of walking and (b) corresponding detected subjects' clusters and ghosts.

5.3.3 Proposed Multiple-People Gait Monitoring Algorithm

A block diagram of the proposed algorithm for multiple-people gait monitoring is illustrated in Figure **5.47**. As stated in the previous chapters, after performing the stationary clutter removal algorithm, the remaining signals are direct signals from subjects and their multipath effects (i.e., time-varying clutter or ghosts) [3]. The multipath issue is more significant when there is more than one subject while people are moving around in a space occupied by reflective objects. A novel algorithm called Subjects Tracker and Association (STA) was proposed to track subjects walking in the hallway and remove ghosts. The STA algorithm is a novel approach to tracking subjects based on the spatial information of clusters rather than relying solely on velocity information. This is important because traditional tracking methods that depend on the velocity of the subject often result in inaccurate outcomes due to the dependency of the velocity on the relative angles between the subject and the radar, particularly when multiple subjects are walking in close proximity. The primary objective of the STA algorithm is to find

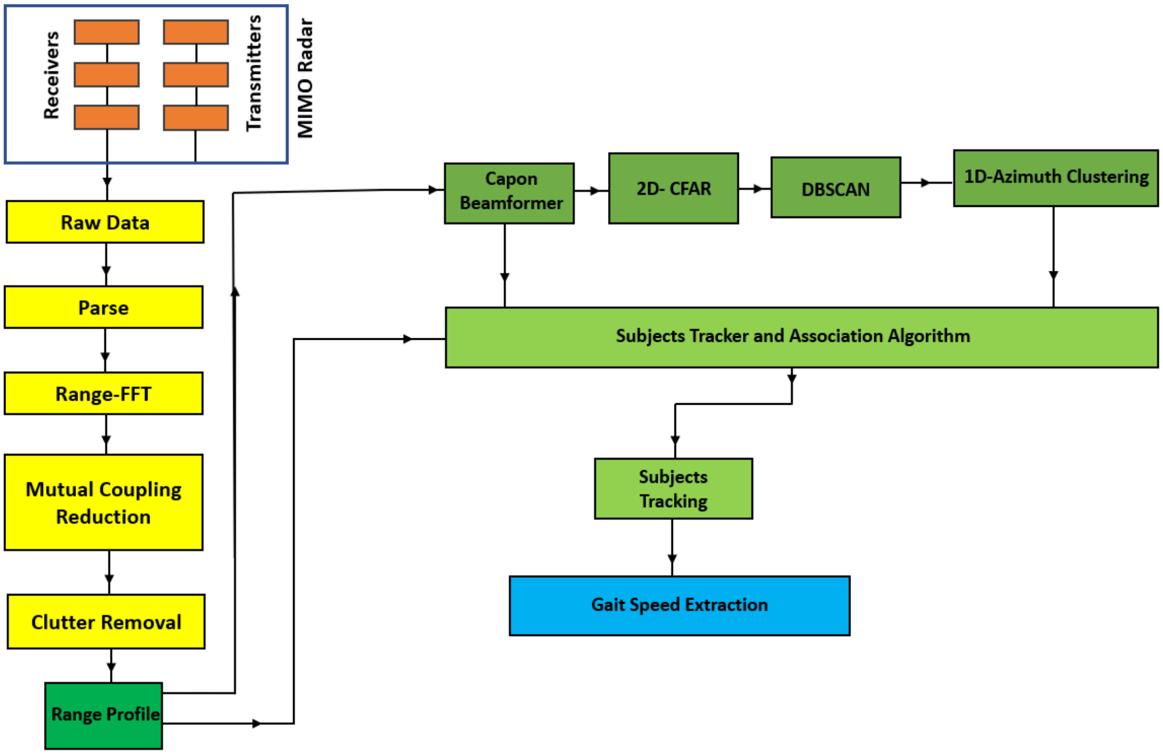

Figure 5.47. Proposed algorithm for multiple-people gait monitoring.

the position of subjects and extract walking speed information accurately. The algorithm operates under three premises:

- Each target cluster (representing a subject) in a new frame is closest to its previous frame's cluster, while ghost or other target clusters will be farther away due to the delay in electromagnetic waves.
- The distance between the target cluster in two consecutive frames should not exceed a defined threshold, which is set based on the maximum expected walking speed of a person (v_{max} = 4 m/s in this work).
- Ghost clusters are not consistent throughout the entire frame and do not have the largest number of sub-clusters, even though they may appear consistently at several consecutive frames.

By utilizing these three principles, the STA algorithm aims to provide a more accurate and robust tracking method for subjects in real-world scenarios. The outcomes of each part of the diagram outlined in Figure **5.47** are presented to provide a detailed understanding of the algorithm.

As illustrated in Figure **5.47**, after removing stationary clutter, similar to previous chapters, the Capon beamformer algorithm is applied to create a range-azimuth heatmap representing the density of reflected signals in the environment. Figure **5.48** (a) shows an example of a range-azimuth heatmap of the environment when two subjects just started to walk across the hallway. A screenshot of the video corresponding to frame #1 is provided in Figure **5.48** (b).

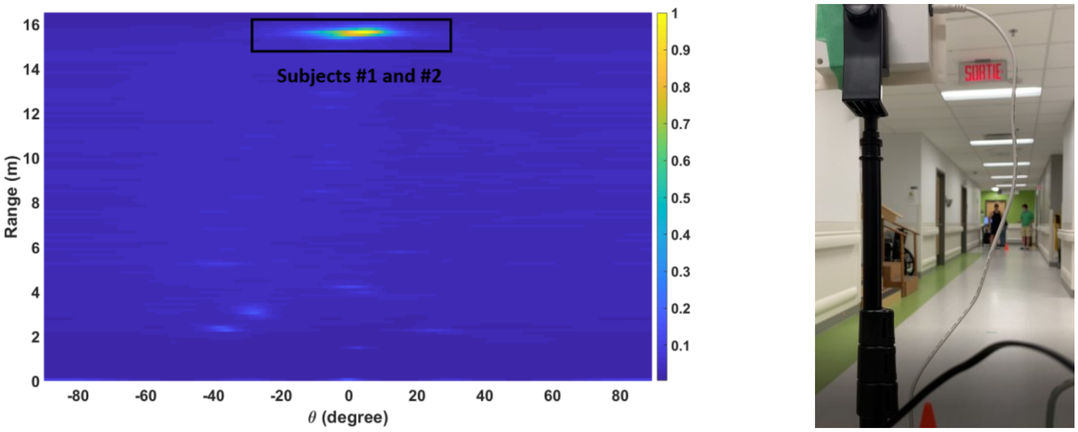

(a) (b)

Figure 5.48. Representation of two walking subjects in a walking environment (a) range-azimuth heatmap of frame #1 obtained by the Capon beamformer, and (b) a snapshot of the video at the beginning of walking tests at frame #1.

The unsupervised machine learning algorithm (DBSCAN) is applied to cluster the output of 2D-CFAR (detect points) to find the exact positions of walking subjects over time (to track multiple subjects) and remove ghosts. Similar to Section 5.2, since sufficient information about the number of ghosting clusters was not known, the DBSCAN clustering algorithm was implemented to group the detected points after performing 2D-CFAR. Based on the performance of the different variables set for the DBSCAN parameters, epsilon neighbourhood, ε=2, and min_points=8 were selected as optimized values. Figure **5.49** (a) shows the detected points after performing 2D-CFAR. Subjects' direct signals are shown in a green rectangle, while other ghosts' points are in red. Figure **5.49** (b) illustrates that the clusters were grouped into four after performing the DBSCAN. Even after examining a range of values to find the optimum values for the DBSCAN variables, the DBSCAN algorithm was unable to reliably group the detected points of multiple subjects walking at a very close distance into separate classes. The results were not satisfactory, as illustrated in Figure **5.49** (b), where both subjects were clustered in one group (shown in purple). This is a particularly challenging scenario when subjects are walking at a very close distance, defined as a case where they are almost at the same range and azimuth.

As outlined in Figure **5.47**, a 1D Azimuth Clustering Algorithm (1D ACA) is proposed to address these limitations and to provide a more effective solution for grouping the close subjects into separate clusters. The algorithm starts by taking the output from DBSCAN, which is an identified cluster, and further divides it into multiple clusters. The division of the cluster is based on the detected points in the azimuth, and the grouping is performed if the epsilon neighbourhood of the detected points (ε=10)

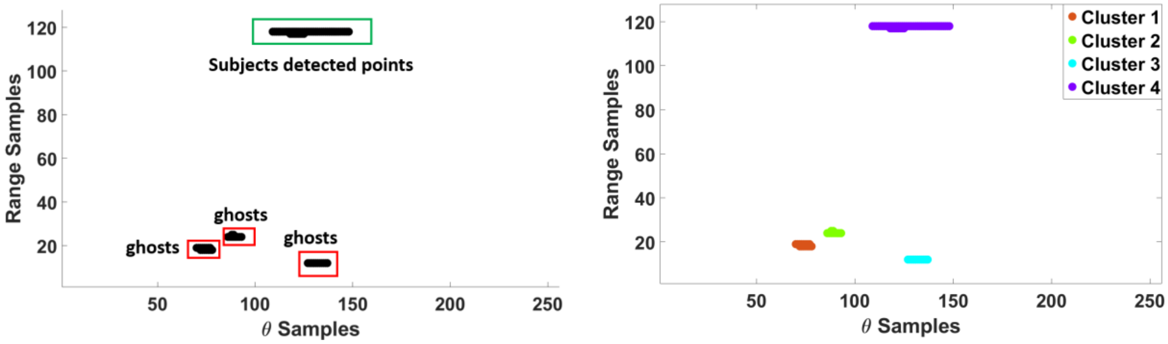

(a) (b)

Figure 5.49. Representation of two walking subjects in the hallway environment (a) detected points by CFAR in frame #1 (b) clusters obtained by DBSCAN in frame #1

contains more than a minimum number of neighbours in azimuth (min_points= 10). The algorithm considers any detected points that do not satisfy the clustering algorithm's conditions as noise points or "No-Cluster", which are outliers that do not belong to any cluster. This 1D ACA algorithm helps to effectively separate close subjects into distinct clusters, making it easier to analyze and process their gait information. A number of clusters are generated at each frame containing subjects' and ghosts' clusters. To show the outcome of the proposed 1D ACA, the detected cluster of frame #1 after performing the 1D ACA is provided in Figure **5.50** (a). As shown, in addition to three ghost clusters that existed, four additional clusters were identified (Cluster 4 to Cluster 7). These clusters are associated with the two close subjects in frame #1. The advanced STA algorithm is then required to track the objects over time and accurately obtain the subjects' positions over time.

As shown in Figure **5.47**, the STA algorithm takes the output of the 1D ACA as input. The STA algorithm manages the identified clusters and organizes them into separate categories. The STA algorithm performs several tasks, including initialization of the detected clusters, confirming their existence, correcting any errors in classification, categorizing the clusters into different classes, and deleting any unnecessary clusters. Each detection is assigned to a specific class. If the detection cannot be assigned to an existing class, the STA algorithm creates a new class for it. This process helps keep track of each subject and organize the detected points into meaningful groups.

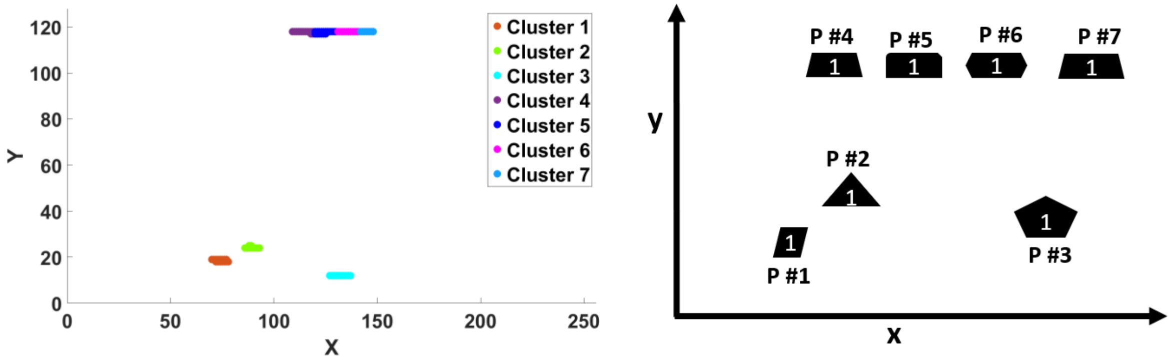

(a) (b)

Figure 5.50. Representation of two walking subjects in a walking environment (a) seven detected clusters after performing the proposed 1D-Azimuth clustering in frame #1 (b) associated seven parents to the seven detected clusters in frame #1.

To initialize the process, as shown in Figure **5.51** (a), the STA algorithm divides all m number of detected clusters into m number of classes at frame #1. All these clusters are the parent of their class, P_m. In the next frame, for every newly identified cluster, the Euclidean distance matrix between this cluster and P_m of all classes is calculated and sorted. As detailed in Figure **5.51** (a), a new cluster will be associated with a previous class if their calculated Euclidean has the minimum values among other sorted distances, which should also be less than the defined threshold (based on the maximum defined v_{max}). For the next frames, each newly added sub-cluster to a class #m is considered P_m of that class, and other old clusters are children of class #m. As detailed in Figure **5.51** (b), if a new cluster does not satisfy these conditions to be categorized to a previous class, it will be a parent of a new class.

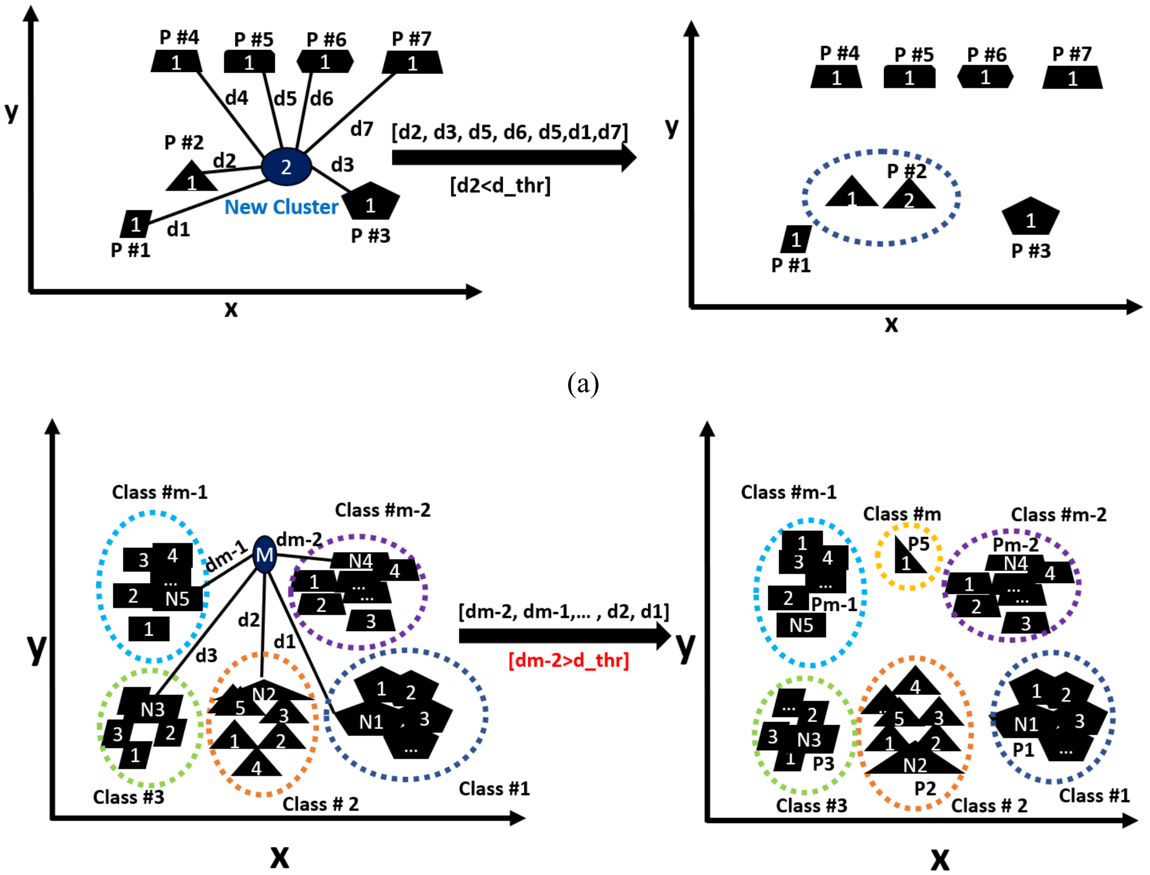

(a)

(b)

Figure 5.51. Details of the proposed STA algorithm (a) the procedure of allocating a new cluster that meets the criteria to previous classes and (b) the procedure of creating a new class for a new cluster that does not meet the condition to be allocated to the previous classes.

This process is iterated through the entire frame. In total, m number of classes with N_m number of children/sub-clusters is created. Figure **5.52** shows all detected clusters throughout the entire walking laps. Two classes with the largest number of children are selected as walking subjects' clusters (target classes). Target classes are constructed with the size of a total number of entire frames. Target classes might have several empty or missed sub-clusters. The algorithm searches in other old classes and checks if any of its children is miscategorized in another class to fill in the missed children. This is done based on the estimated range-azimuth values of the corresponding sub-cluster and the expected speed. If any sub-cluster in other old classes satisfies its conditions, then the detected child from old classes will be identified as a child of the missed frame of the target class. Otherwise, it will remain as a missed child in the target cluster. The missed child is because a subject's reflection is not detected in some frames or concealed under other stronger signals, such as ghosts or direct signals from another walking subject; a subject being tracked might not appear in every single frame. Finally, the target classes, including N_m number of children, represent all points detected from two walking subjects. Based on the detected points over the entire frames (N number of frames) and the corresponding time, a trajectory of subjects

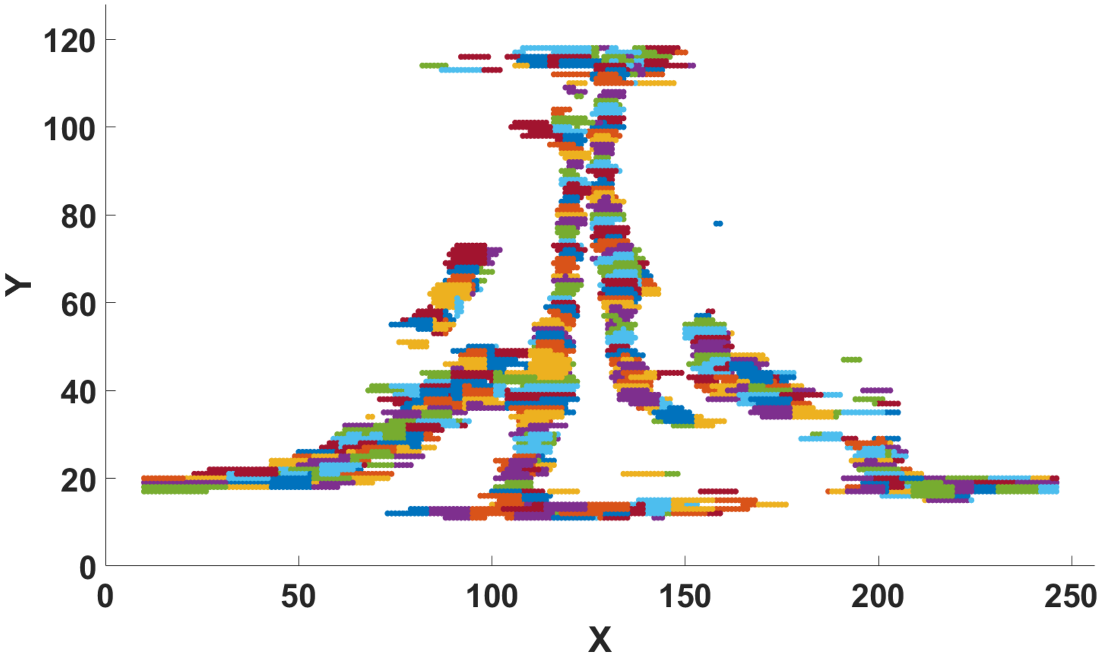

Figure 5.52. All detected clusters throughout the entire walking lap.

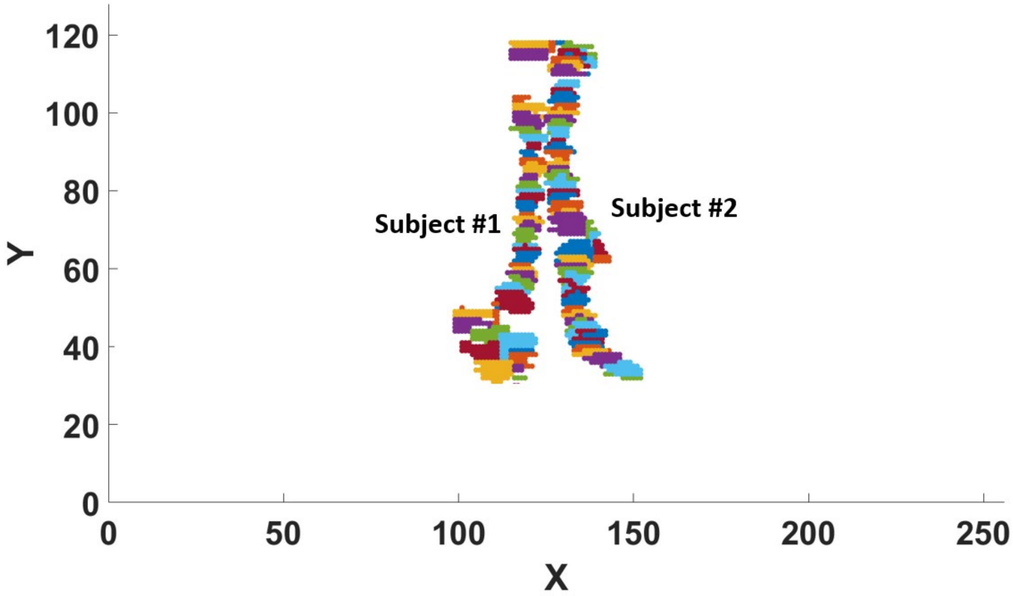

Figure 5.53. Subjects' clusters detected by the proposed STA algorithm.

is acquired (range and azimuth). Figure **5.53** shows the detected clusters of the two subjects walking in the hallway. The movement trajectory is analyzed with respect to time to calculate the participant's gait speed. Having the subject's position over time, the overall velocity of walking (i.e., the distance a walking subject travels over a second (velocity=position/time)) can be calculated.

5.3.4 Results of the Bedrest Study

In this section, we first provide walking speed obtained from the radar and a stopwatch to validate the proposed radar-based system performance in extracting walking speed of multiple people. It should be mentioned that we do not report the walking speeds of the second subject (the research assistant walking beside the participants) because the walking time was not recorded by a stopwatch. But, to show that our algorithms track them both, we provide the trajectory of both walking processes in Figure **5.53**.

We then provide and compare walking speed of PRE, R +1, R+3, and R+ 4wk to show the effect of BR on walking speed. To validate and demonstrate the performance of our proposed system for gait extraction of participants with the coexistence of other people, Figure **5.54** shows speed obtained by the radar empowered by our proposed algorithm (the brown curve) and the stopwatch values in blue. The results provided here are the outcome of 25 different tests done before and after HDBR. As shown, the obtained results are very close, demonstrating the radar performance in extracting walking speed of multiple people.

To show details, a Bland-Altman plot of radar-stopwatch results is provided in Figure **5.55**. It is the pairwise difference between simultaneous measures of radar and stopwatch measures. The solid line at -0.06 m/s is the bias (i.e., average difference). The dashed lines represent the 95% limits of agreement. Each colour represents a unique participant, bias is the solid line, and upper and lower limits of agreements (95% confidence) are the two dashed lines. The limits of agreement are calculated using the repeated measures Bland-Altman analysis, which accounts for within-participant variance. It should be mentioned that the difference here incorporates that there is an error inherent in the stopwatch method (a human pressed a button), and the important thing is that there is no considerable difference between the two devices (0.0644m/s shorter duration with the radar seems trivial). A box plot of the outcome of this BR study is provided in Figure **5.56**. Each individual is represented by a unique colour. The solid line in the boxes represents the median, the dashed line represents the mean, and the top and bottom of the boxes represent the 1st and 3rd quartiles, respectively. Linear mixed models with fixed effects of condition and time and random effect of the participant for the statistical analysis were used. Emmeans with Bonferroni correction was used to evaluate the pairwise comparisons related to the

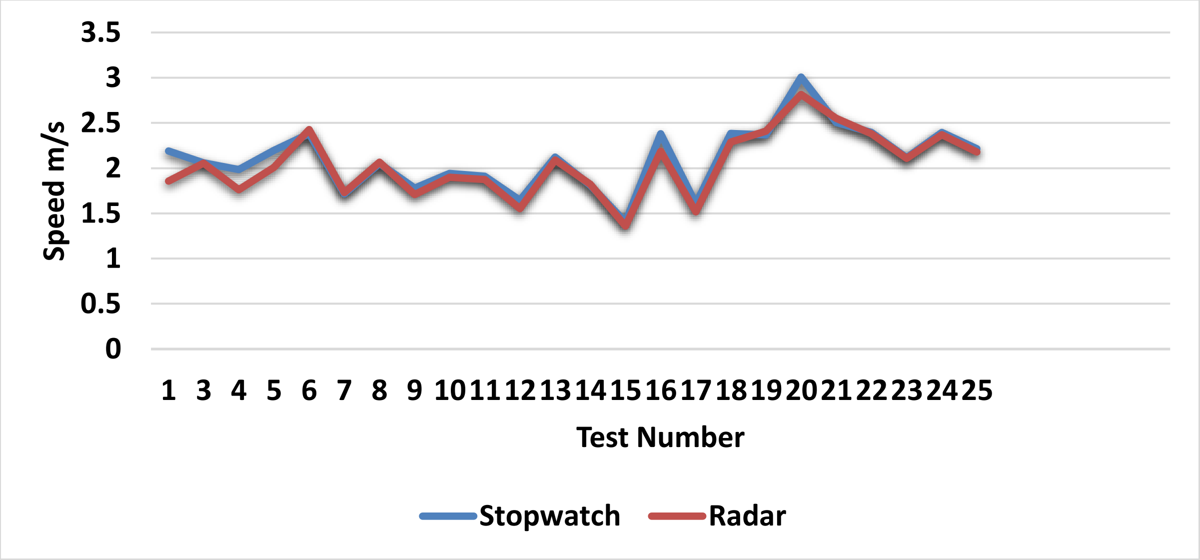

Figure 5.54. Participants' walking speed in the BR study obtained by radar empowered by the proposed STA algorithm and a stopwatch.

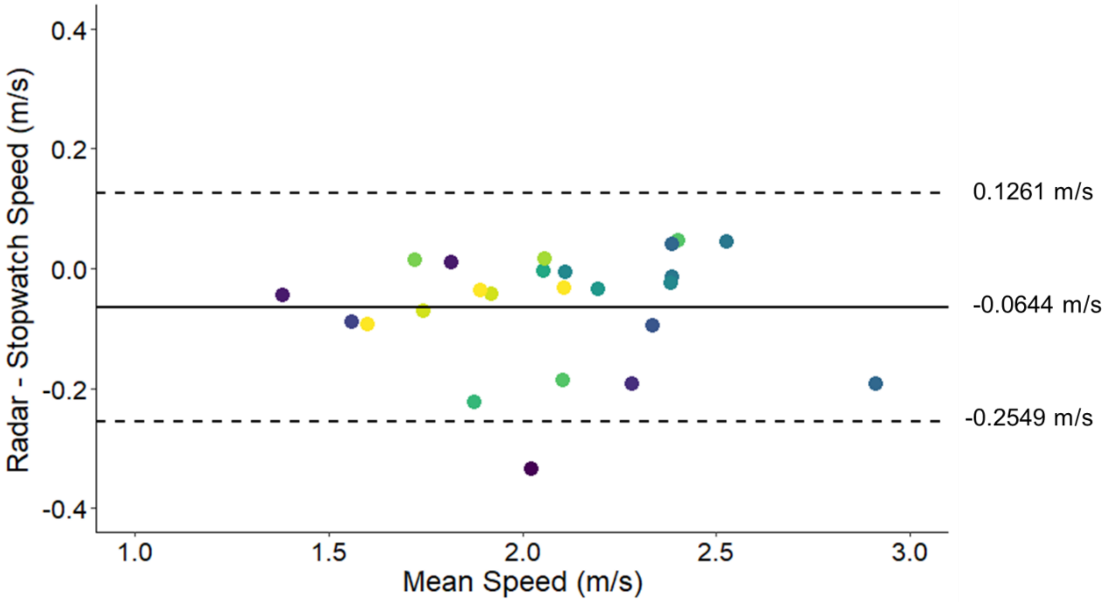

Figure 5.55. Repeated measures Bland-Altman plot comparing the walking speed calculated from the stopwatch and radar data. A given colour represents a unique individual. The solid and dashed horizontal lines represent the bias and 95% limits of agreement.

significant effect of time. All comparisons with R+1 and other time points (PRE, R+3, or R+4wk) were p<0.001. The makers "*" indicates the difference from all other time points when evaluating the main effect of time. Exercise has no impact on the result, as represented in Figure **5.56**. The responses on the left for the control group and the right for the exercise group are not different.

The *p* values for the main effects of time (PRE vs R+1 vs R+3 vs R+4wk), condition (control vs exercise), and their interaction are listed in the top left of Figure **5.56**. Only time has a significant effect on walking speed, so exercise does not have an effect. The significant effect of time was evaluated using post hoc analysis by pairwise comparison of time points with Bonferroni correction for multiple comparisons. Post-hoc analysis revealed that R+1 was different from PRE, R+3, and R+4wk, with no other differences being identified. That is what is being identified with the asterisks above the R+1 time points in the plot. It should be mentioned that more analysis is needed to identify the cause of the decline in walking speed, which is out of the scope of this thesis. Further analysis will be done by other team members involved in this BR study with more background in physiology (a group in Prof. Richard Hughson's lab).

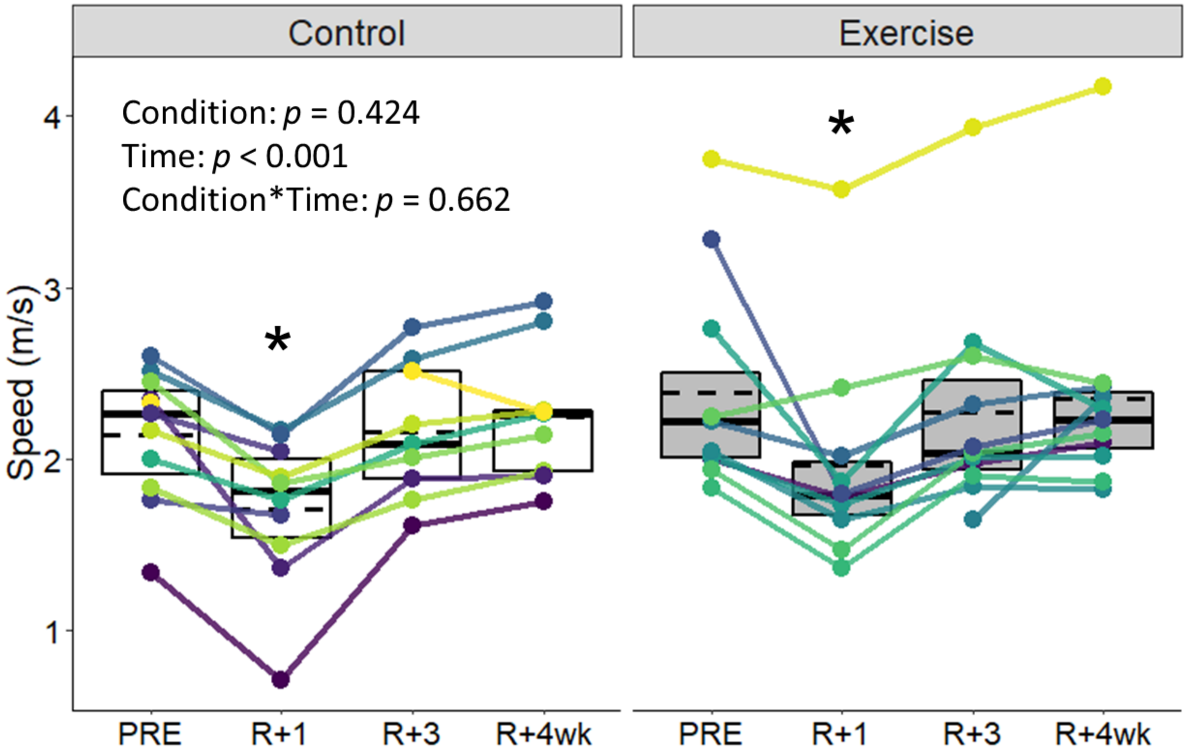

Figure 5.56. Comparison of walking speed at before bed rest (PRE), the first day (R+1), third day (R+3) and 4 weeks (R+4wk) after getting out of bed. A given colour represents a unique participant. *, different ($p<0.05$) from PRE.

Chapter 6
In-Home Gait Monitoring

6.1 Relevance

Studies on the application of radar technologies in human gait assessment have been conducted to (1) analyze and obtain gait parameters [14], [22], [24]–[27], [77] and (2) recognize humans from their gait patterns [57], [80], [103], [155]–[157]. For the first one, various radar signal processing methods have been proposed to extract gait characteristics such as speed, cadence, stride length, etc. Machine learning and artificial intelligence (AI) have been deployed for the latter. However, the focus of the work in this chapter is to integrate machine learning algorithms with radar signal processing to identify the type of in-home activity performed by a subject and to detect in-home walking periods to distinguish them from other in-home activities and then extract gait parameters.

Although the speed of random walking could be extracted using a MIMO FMCW radar, the position of a subject performing other in-home non-walking activities such as cleaning or working out also changes over time. Therefore, we need an algorithm to distinguish walking periods from other in-home activities and movements for an in-home gait monitoring assessment and activity recognition system. In this work, we propose a novel cloud-based in-home free-living activity recognition and gait monitoring system that integrates radar-based signal processing methods with a sequential deep learning algorithm (Autonomous In-home Gait Monitoring and Activity Recognition (AI-GM&AR) system. Our proposed AI-GM&AR system uses a sequential deep learning model to recognize the type of in-home activity, detect walking periods, and distinguish them from other in-home activities.

The primary purpose of this research is to perform in-home typical daily activity recognition (e.g., walking, sedentary, washing, vacuuming etc.) and gait period detection using radar to have a record of the subject’s activity level and gait patterns.

Most of the research on human gait analysis and activity recognition has been done in a simple, large, and low-clutter environment with a constrained range and limited activity (mainly in a straight line) [26], [29], [52], [77], [78], [80], [81], [158], [159]. However, when someone walks randomly or performs in-home activities in a cluttered environment such as a typical home, their patterns are different from that of straight-line activity in a large area [26], [29], [52], [80], [81]. As will be shown in this chapter, identifying walking periods and recognizing the type of activity a subject performs is complicated in such an environment using radar signal processing methods.

STFT has been widely used to train machine learning algorithms in many cases [158], [159]. STFT is a good solution for such a straight-line activity where it captures all micro-doppler which depends on relative angle. On a straight-line movement, the relative angle between the radar and the subject is constant, thus, the direction will not impact the extracted micro-Doppler. However, when it comes to random and non-straight-line in-home activities at various angles, STFT patterns may not be easily distinguishable. Since people have different walking patterns and other in-home activities, as shown in this chapter, models trained with STFT will not produce the best results. Furthermore, since STFT ignores the spatial information of subjects (e.g., range information), it does not have enough information to distinguish various in-home activities.

Unlike the work reported in [27] that used a complex radar system including four AWR1243 chips to create 192 channels to provide human point cloud information for 2D-CNN, we used only one AWR1443Boost radar sensor. Note that for a real-time everyday application, we need a fast and simple algorithm, whereas an expensive high-resolution radar and complex signal processing are required to prepare accurate point cloud information, as shown in [27]. In order to make the system affordable, it is preferred to have fewer and less expensive radar sensors. In this work, we show that, without the need for an expensive high-resolution radar leading to complicated and computational-costly algorithms for detection, clustering, and associations to extract point cloud information (x-y-z) [27], a Range-Doppler map (RDM) of a human body obtained from a low-cost radar is reliable and provides enough features for our purposes. RDMs are delivered to a sequential deep learning algorithm to be trained and predict in-home activities. In addition to the simplicity, compared to the point cloud method, another advantage of RDM is that only one single transmitter and a receiver can provide both the occupied position and all created micro-Doppler, leading to a less expensive system. Another advantage of using RDMs is that, compared to SFTF patterns, the RDM has both spatial and temporal features of subjects.

Assessing various deep learning models, we show that GRU [160] can extract temporal characteristics of the radar data and thus achieve sufficient recognition accuracy with relatively low complexity compared to the existing 2D-CNN and 2D-CNNLSTM methods [161]. Since RDM preprocessing is simple and fast, all signal processing pipelines are performed in a low-cost standalone

IoT Edge device without allocating an extra laptop or PC for signal processing. In this work, we utilize a Raspberry Pi to process radar raw data and perform all signal processing to be delivered to the GRU network. With simple and fast preprocessing to create RDMs performed by a Raspberry Pi, streamed data is sent to the cloud (Microsoft Azure), and the GRU network is applied to the streamed data to identify the type of activity a subject is performing in real-time.

Disclaimer: A major part of this chapter was reported in two journal papers:

- **Hajar Abedi**, Ahmad Ansariyan, Plinio P. Morita, Jennifer Boger, Alex Wong, and George Shaker "Contactless In-Home Cluttered-Environment Gait Analysis," (under preparation).
- **Hajar Abedi**, Ahmad Ansariyan, Plinio P. Morita, Jennifer Boger, Alex Wong, and George Shaker," AI-Powered Non-Contact In-Home Gait Monitoring and Activity Recognition System Based on mm-Wave FMCW Radar and Cloud Computing," *IEEE Internet of Things Journal*, 2023.

6.2 AI-GM&AR System Design

The diagram of our proposed AI-GM&AR system is presented in Figure **6**.**1**. The system's main components include the Client Side, the Cloud module, and the User Interface. To provide a detailed representation of the subject's daily activity, we focus our attention on the living room in this work as this is the central area of the house where the subjects spend most of their time and perform most of their activities, followed by the bedroom (to record sleeping time and duration), and the washroom (to record washroom frequency, enter, exit, and duration). Therefore, to enable tracking a subject in the three main living areas, we installed a standalone system (a radar integrated with a single board) in the subject's bedroom, living room, and washroom. Each system sends the radar configuration commands to run the radar, stores received raw signals, preprocesses the raw data, and then transfers it to the cloud. Each system in each room performs a signal processing chain to detect the presence or absence of the subject. To identify which space is currently occupied, a Presence-Absence Detection (PAD) algorithm is applied to the radar raw data [73]. We refer interested readers for more detail on the PAD algorithm to our previous papers published in [32], [73]. The PAD algorithm identifies the rooms as occupied or vacant. The data from the room occupied by the subject is sent to the cloud through the IoT Edge. Since our focus is on activity recognition and gait period identification in the living room in this work, if the living room is occupied, then the RDM will be sent to the cloud for further analysis. The pseudo-code of our proposed AI-GM&AR system is provided in Algorithm 6.1. The radar real-time raw data captured in each room is the system’s input to generate the subject’s activity report output. If the PAD

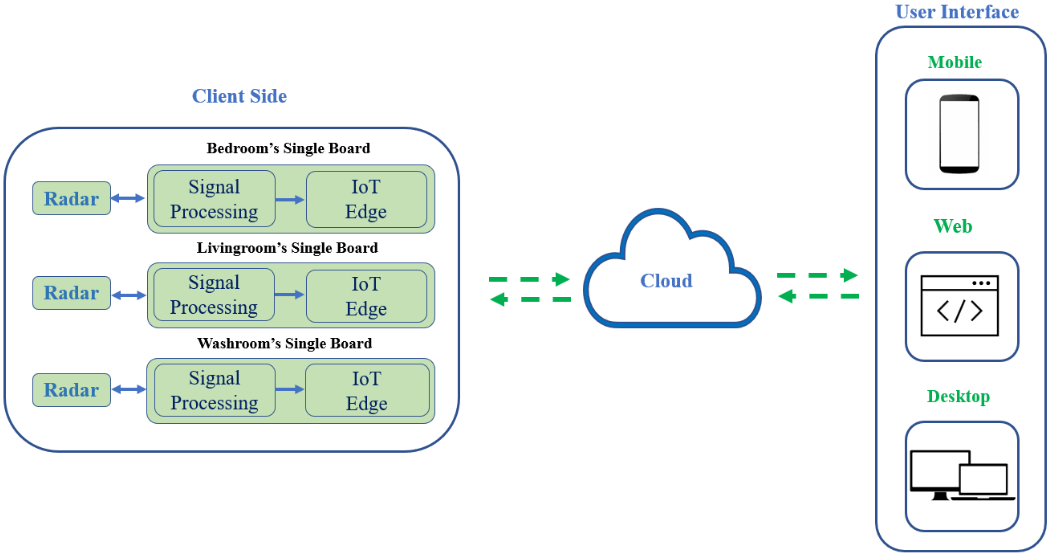

Figure 6.1. Diagram of the proposed AI-GM&AR system. Three standalone units are installed in the subject’s living environment collecting stream data and sending it to the cloud. In addition to gait parameters and the subject’s current status, the subject’s daily activity reports are recorded and shown using three different platforms: mobile, web and desktop apps.

Algorithm 6.1: In-Home Status Recognition Algorithm

Input: Radars Raw Data from each Single Board
Output: Activity Reports

```
while True:
  chirp=capture_raw_data ()
  room=PAD (chirp)
  if room == "in_bed"
        save_in_bed_date_and_time ()
  else if room="in_washroom"
        save_in_washroom_date_and_time ()
  else if room="out_of_home"
        save_out_of_home_date_time ()
  else if room== “Livingroom”
        status=check_status_of_livingroom (chirp)
        save_status_of_livingroom (status, date, time)
```

---

algorithm identifies the presence of a subject in the bed (occupied bed), the time duration of in-bed status will be stored in the cloud database to record the sleep or in-bed time. On the other hand, if the PAD algorithm identifies the subject's presence in the washroom, the entrance/exit time and the duration the subject spends in the washroom will be recorded. Deploying deep learning in the cloud, the type of activity performed by the subject will be predicted. If the PAD algorithm identifies the absence of the subject in all three areas, the status of the out-of-home will be determined (a vacant room). The amount of time the subject spends out of the home would also be recorded.

6.2.1 Deploying Machine Learning in the Cloud

There are two main steps in cloud computing to deploy real-time machine learning [162]: pre-runtime and run-time processes. As shown in Figure **6**.**2**, in the pre-runtime step, we collect data from the IoT device (the radar sensor) to train a deep learning network. The model is trained and optimized on a local machine. The model is then deployed into the cloud to be used in the run-time section. In the run-time step, radar sensors paired with Raspberry Pis (standalone sensors) are used to capture and preprocess streamed data from the environment and then send it to the cloud for further analysis. If the occupied room is the living room, the stream data is then transferred to the cloud and fed into the deep learning network to identify the type of in-home activity and gait periods [162].

It should be pointed out that if there is no connectivity to the cloud, the activity recognition system will not be able to operate in real-time. Based on the current scope of this thesis, which focuses on activity recognition and not fall detection, the lack of connectivity to the cloud would not pose a risk to the occupant. However, if the system were to be used for fall detection, there would be a risk as the system would not be able to communicate with the cloud for timely notification and emergency response. Therefore, it is important to consider the connectivity and reliability of the system in real-world applications to ensure the safety of the occupants. To mitigate this risk, the system could be designed to have a backup mode that operates locally (in a local server) on the device in the event of cloud connectivity loss. Additionally, the system could be designed with redundancies in place to ensure that connectivity loss is rare and quickly resolved, such as by using multiple internet connections or failover mechanisms.

6.3 Proposed AI-GM&AR Algorithm

The block diagram of our AI-GM&AR algorithm is illustrated in Figure **6.3**. The proposed algorithm consists of two processes: (1) walking period identification and activity recognition and (2) gait parameter extraction. In our proposed system, raw data from the radar is collected from a MIMO FMCW radar. As mentioned in a previous chapter, there are two types of clutter effects in received signals: (1) stationary clutter and (2) time-varying clutter (ghosts) [3]. The direct reflection from stationary or unanimated objects is called stationary clutter. The stationary clutter removal algorithm is applied to the range profile to remove signals reflected from stationary clutter [3]. However, the interaction between a subject and a stationary object creates multipath or ghosting effects [3]. The number and particular behaviour of the multiple paths depends on the room structure and the presence of moving subjects. After performing the stationary clutter removal algorithm, the remaining signals in the range profile are direct signals from the subject, caused by chest motions (breathing) and other motions created by performing in-home activities in addition to multipath effects [3]. In this chapter, it will be demonstrated that deep learning can classify in-home activities despite the existence of

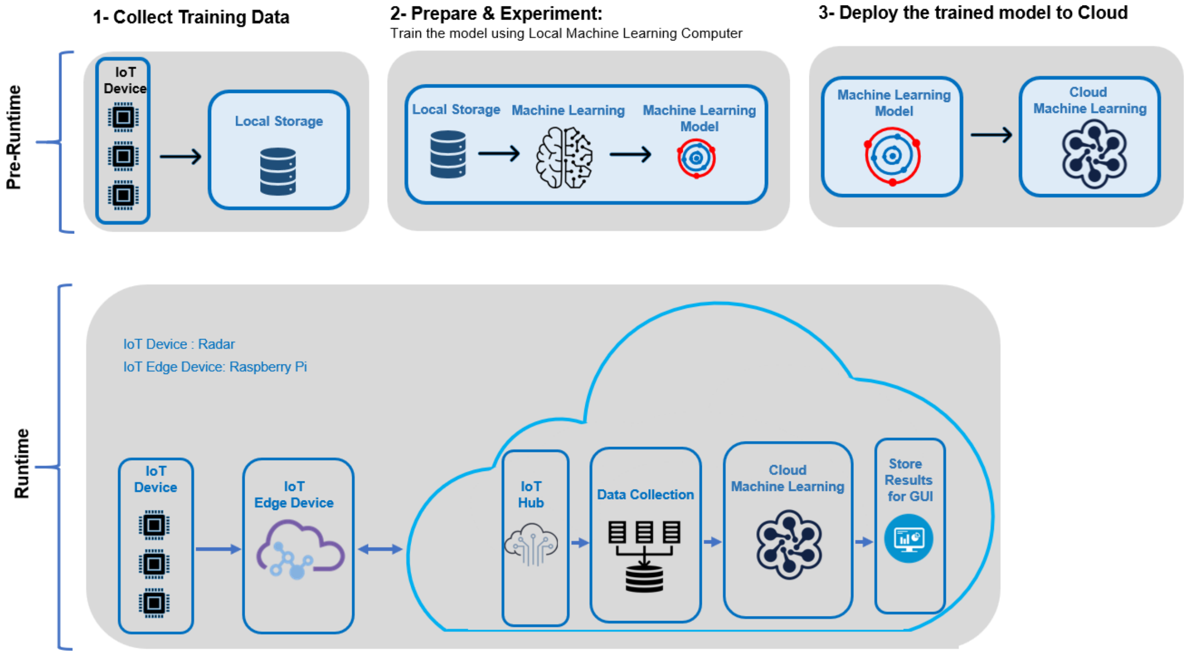

Figure 6.2. Flowchart of the IoT-based AI-GM&AR system showing the pre-run time and run-time processes in the cloud.

multipath effects or ghosts. Since the human body is non-rigid, reflections from a human body occupy multiple cells of range bins in the range profile. Human locomotion, including walking, is a complex motion, and the velocity of each segment of the human body performing different tasks varies over time [54], [57], [58], [64], producing various micro-Doppler shifts in scattered signals. Applying the second FFT on a series of radar chirps (i.e., frame), a range-Doppler map (RDM) is obtained. Therefore, using an FMCW radar, we simultaneously provide a range-Doppler map at each frame containing range and micro-Doppler signatures of a subject's in-home activities. As will be shown in this chapter, azimuth information is also needed to extract gait parameters.

Given that our target is a single subject, we use the entire RDM to train the model. This simplicity helps us avoid other signal processing such as detection (to capture occupied bins), clustering methods to cluster the detected bins, and then association algorithms to associate new bins to the previously occupied bins. We consider only one subject in this work because the main application of the AI-

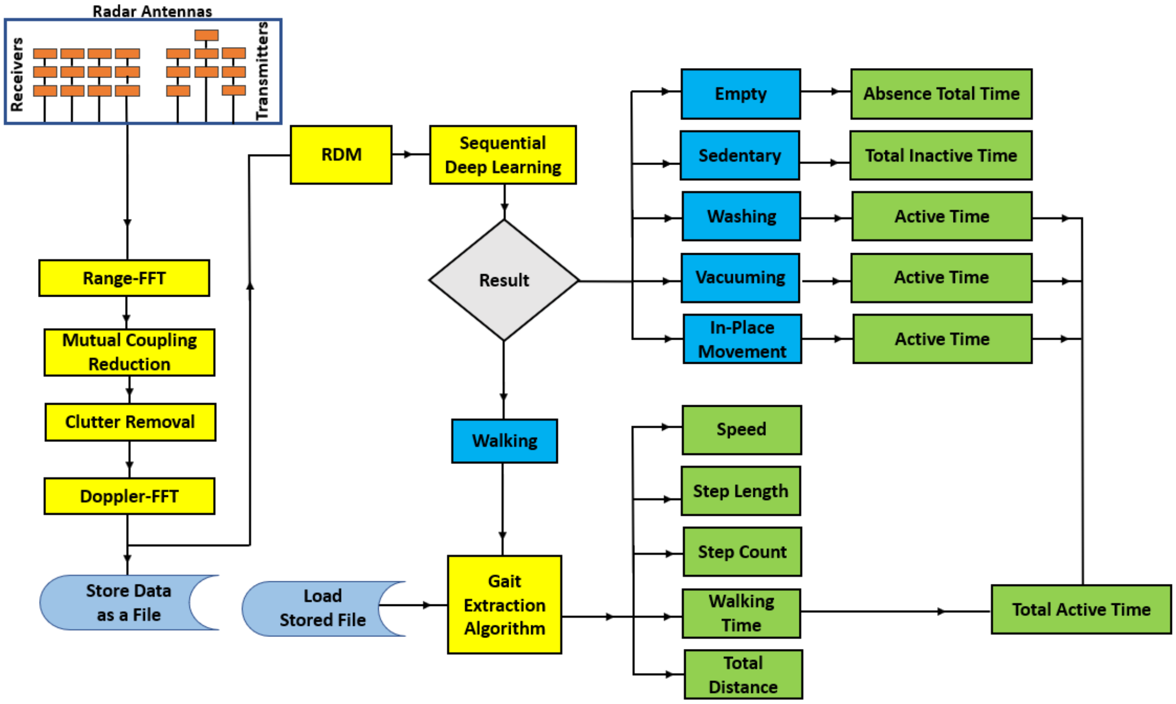

Figure 6.3. AI-GM&AR System Flowchart. Firstly, features for sequential deep learning will be provided and delivered to the network. If walking periods are identified, a gait extraction algorithm will be applied, and gait values will be provided.

GM&AR system is in long-term care facilities or retirement homes, where only one subject is monitored. Any in-home gait extraction method is prone to failure if the system is not intelligent enough to identify a human's in-home activities and differentiate between them. The system should provide precise and accurate gait data and be able to track a subject's in-home activities over long periods. The system should be able to identify the type of in-home activities a subject performs. Six classes are defined in this study: (1) "Empty", (2) "Sedentary", (3) "Washing", (4) "Vacuuming", (5) "In-place movement", and (6) "Walking". These are some of the activities a subject performs during a typical day. Another class as an "other" category was considered during the development of the activity recognition system. However, it was determined that including such a category would not be beneficial for the system's performance, as it could introduce ambiguity and reduce the accuracy of the classification. Instead, the six classes were carefully chosen based on their relevance to monitoring activities of daily living and the potential risks associated with them. If the occupant performs an activity that is not within the listed classes, it will be recognized and recorded as one of the recognized activities. However, based on the typical activity in a home, long-term care facility, or retirement home, the recognized activities could be modified. In addition, since the system is intended for monitoring activities of daily living and not for fall detection in this thesis, the six classes are considered adequate for the purpose of this research. However, if the system were to be used for fall detection, it may be necessary to include an "other" category to better capture unexpected events. In other words, the choice of classification approach, number of classes, etc., depends on the specific context and environment in which the system is used, as well as the goals and requirements of the application. In this study, we focused on a particular set of activities of daily living in a home environment. The number and types of classes were chosen based on their relevance to the intended application and the potential risks associated with them. However, for other contexts or applications, different sets of activities or classification approaches may be more appropriate. Our work provides a framework for further exploration and customization of the activity recognition system based on the specific needs and context of the application.

Algorithm 6.2 shows the pseudo-code of the proposed activity recognition algorithm. As shown, the deep learning network would predict the activity a subject performs and send out the result as the current status. For the case of detected walking periods, a gait extraction algorithm discussed in Section 6.5.1 will be applied to the stored RDM samples to obtain gait values.

6.3.1 Deep Learning for the AI-GM&AR System

Due to the complexity of human motion, complex signal processing is required to map the RDM patterns to a human's specific activity, which is mathematically not feasible [163]. For this reason, we have adopted machine learning as an effective tool for our AI-GM&AR system. During the development of the system, we considered several machine learning and deep learning approaches for activity recognition, such as support vector machines, random forests, and convolutional neural networks. We evaluated the performance of these approaches using various metrics such as accuracy, precision, and recall and compared them to determine the best approach for our specific application. Conventional machine learning algorithms are limited in their capacity to fully capture the rich information contained in complex data, particularly time-varying samples [163]. Our proposed system in this study leverages deep learning approaches [164] to use the resulting time-varying signatures of the subject being monitored. Using multiple deep layers in a single network enables the efficient extraction of a subject's features and the building of a classification boundary [163].

Many deep learning models have shown exceptional promise in radar-based human activity recognition systems [57], [80], [103], [155]–[157]. The raw data is commonly converted into a 2D spectrogram using the STFT method while being treated as an optical image. The corresponding architectures, such as 2D convolutional neural networks (2D-CNNs), are used in these systems. However, since a human body motion consists of a series of associated postures through time, ignoring these temporal characteristics could lead to a complex network with many parameters, which may not result in accurate recognition.

Deep recurrent neural networks (DRNN) have successfully addressed classification problems that feature temporal sequences [164]. DRNNs use a hidden node as memory, passing previous information to the next state for processing sequential inputs. Through this process, a DRNN can extract the temporal features of data. Long short-term memory (LSTM) and gated recurrent unit (GRU) are the two common models for sequential learning [163]. Due to the complex structure of a single LSTM unit, the LSTM network contains many parameters and so requires a larger sample size. LSTM contains three gates: the forget gate, the input gate, and the output gate [30]. On the contrary, a GRU network has a simpler structure and fewer parameters. A GRU network includes only the reset gate and the update gate. From a spatial complexity perspective, LSTM has more parameters than GRU, therefore, GRU has fewer computation costs than LSTM [160].

Algorithm 6.2: In-Home Activity Recognition Algorithm

```
check_status_of_livingroom (chirp):
Input: Radar Raw Data in Livingroom (Radar Unit #1)
Output: Type of Activity in the Living Room

  chirp=capture_radar_raw_data_from_livingroom ()
  fft=fast_fourier_transform (chirp)
  complex=fft [0:int (fft.size/2)]
  mcr=mutual_coupling_reduction(complex)
  cr=clutter_removal (mcr)
  R_P=save_in_database (cr)
  RDM=fft (R_P)
  result=GRU (RDM)
  if result== “empty”
          return “empty”
  if result== “sedentary”
          return “sedentary”
  if result== “washing”
          return “washing”
  if result== “vacuuming”
          return “vacuuming”
  if result=="in_place_movement"
          return “in_place_movement”
  if result== “walking”
          return gate_extraction (data)
```

In this work, we show that the RDM has enough features for a single subject in-home monitoring, and the GRU network is a promising model to be used for time-varying RDMs of human activity classification. We demonstrate that GRU achieves sufficient recognition accuracy with relatively low complexity without the need for the subject’s point cloud information [161]. The advantages of RDM, compared to point cloud information, are that such a system can provide valuable information using only one single transmitter and a receiver. Additionally, preprocessing is faster and simpler. An alternative approach using point cloud information would require an expensive high-resolution radar and complex signal processing.

6.4 Experimental Results

We use the same devices used to conduct the other parts of this thesis: the mm-wave FMCW radar systems from TI Co. Ltd. Our AI-GM&AR system uses only one AWR1443Boost radar for each room.

We selected this MIMO radar in this study, although a single transmitter and receiver are enough for in-home activity recognition and walking period identification. As will be sown, after detecting in-home random non-straight-line walking periods, azimuth information of the subject is required in addition to the subject's range to get the subject's accurate position over time (velocity = position/time).

6.4.1 Radar Configuration

In this experiment, we use the following parameters for configuring the radar: chirp duration - 380 μsec; chirp slope - 43.03 MHz/μsec; chirps per frame– 256; frame period– 98 msec; frequency bandwidth– 3602 MHz; operating frequency– 77 GHz, and A/D sampling rate– 4400 ksps. Using this configuration, the following parameters are obtained: maximum detachable range– 8.24 m, range resolution– 6. 49 cm, velocity resolution– 0.02 m/s, and maximum velocity– 2.54 m/s.

6.4.2 Dataset Construction for Deep Learning

As stated earlier, datasets collected by other researchers in this field were collected in controlled situations in a large environment with almost no clutter [26], [29], [52], [80], [81]. While this type of initial research is critical in developing practical systems, there needs to be research exploring how to computationally deal with subjects behaving naturally among everyday objects typically found in one's homes, as they would in a real home uncontrolled environment. Previous research reported in [27] explored a highly cluttered environment but in controlled scenarios using an expensive and complex high-resolution radar to create human point cloud information. However, no research has been reported on a single-sensor radar dealing with in-home gait and activity monitoring using RDMs. Since our goal is to provide an in-home activity recognition system, we collected data in a typical cluttered apartment. Figure **6**.**4** depicts the living room area of the apartment where we conducted our experiment and collected our in-home datasets. This apartment is located in the research area of the Schlegel-University of Waterloo Research Institute for Aging (Schlegel-UW RIA). The living room has a typical highly cluttered environment with many reflective objects, similar to what would be found in a living room in any modern apartment building, including a TV, a fridge, metal window frames, and concrete floors and ceilings.

To compile this dataset, we invited seven subjects (three females and four males with heights ranging from 156 cm to 187 cm) to randomly walk in the apartment at their selected speed and perform various in-home activities without any predefined path to follow. If we walk or move in a highly cluttered environment, we create various multipath effects that should be removed from the actual signals from the subject [3], [165]. This effect adds more complexity to the signal processing chain in addition to the required high-resolution and complex radar sensors. To compile datasets in a typical home, we installed the radar sensor in a living room of an apartment, shown in Figure **6.4**. We defined six classes: (1) "Empty", (2) "Sedentary", (3) "Washing", (4) "Vacuuming", (5) "In-place movement", and (6) "Walking". Our purpose for the "Empty" class was to identify the presence or absence of the subject in a living room. The result of the PAD algorithm and the deep learning will be combined to provide the final presence/ absence status. The purpose of the "Sedentary" class was to know how long the subject was sedentary (not active) during the day. This information could help the subject keep track of his/her daily activity and modify his/her future activities.

The "Washing", "Vacuuming", and "In-place movement" classes were defined in order to differentiate these activities from periods of walking and to track the subject's daily activities that involve movement other than walking. It is important to identify periods of walking, as defined by the "walking" class, to apply gait extraction algorithms accurately. Failure to properly identify walking periods can result in errors in gait data over time when applying gait extraction algorithms to non-walking activities. Any small error in gait parameters would cause misleading information in prediction and any subsequent proactive attempts (i.e., fall prevention) [18], [166], [167].

For dataset construction, seven young and healthy subjects performed their normal and natural daily life in the apartment. These are the protocols we followed for in-home dataset construction:

1. For the "Empty" class:

- No subject was in front of the radar, and no live body occupied the room.

2. For the "Sedentary" class:

- A subject was sitting still in different places on sofas/chairs.
- A subject was sitting at various locations on sofas while working with a cell phone.
- A subject was sitting at various locations on sofas while working with a laptop.
- A subject was sitting at various locations on sofas in the usual way (i.e., talking, moving his body, leg displacement, etc.).
- A subject was sitting at various locations on sofas facing back and toward the radar.

3. For the “Washing” class:

- A subject was washing dishes in the kitchen.
- A subject was drying the dishes.
- A subject was putting the dried dishes into the cabinets.
- A subject was cleaning the cabinets/ sink areas.

4. For the “Vacuuming” class:

- A subject was vacuuming the entire living room, even behind desks and coffee tables, in a typical way.

5. For the “In-place movement” class:

- A subject was working out.
- A subject was squatting.
- A subject was picking objects from tables/floors.
- A subject was sitting and standing from a chair.

6. For the “Walking” class:

- A subject was randomly walking in different directions in the entire living room, even behind desks and coffee tables, at his own selected speed.

In this study, datasets were collected with subjects moving naturally without being asked to move to a specific location. Therefore, it can be concluded that the data is not dependent on the radar’s relative position. However, it is possible that the “Washing” class may be dependent on the radar position due to the static nature of the activity in close proximity to the sink.

A total of 310357 range-Doppler maps were generated from data collected from seven participants, who each completed five different in-home activities for a total of 50 minutes of data. Each participant completed each task in approximately 10 minutes, resulting in approximately 7400 frames of data per class per subject. The labelling of the data is based on the order in which the tasks were completed, with some potential for minor labelling errors due to the subjects not perfectly following the requested activity for the full 10 minutes. These errors may include deviations from the requested activity, such

Figure 6.4. In-home environment experiment conducted in Schlegel-UW RIA. The radar is used to collect data for the local system to train and validate deep learning models.

as temporary pauses or walking while holding equipment. While efforts were made to minimize these errors, they were hard to control. For example, participants might have stopped vacuuming intermittently or walked while holding the vacuum instead of consistently vacuuming the floor. These variations were very difficult to control.

6.4.3 Results

In this subsection, we provide samples of RDMs and STFT patterns of in-home activities. We then provide and compare the results of various deep learning networks fed by RDMs and STFT.

6.4.3.1 Range-Doppler Maps

An example of the RDM of each in-home activity is provided in Figure **6.5** and Figure **6.7**. Each RDM is a matrix of 128 rows and 256 columns, normalized to its maximum. All RDMs shown here are the result of frame # 100. Note that frame #100 in Figure **6.5** and Figure **6.7** is just an example of each activity in this work, while other frames also show the details of each activity. The horizontal and vertical axes represent the subject's range (radial distance) and velocity, respectively. The RDM in Figure **6.5** (a) is for the empty room (when no subject was in the room). While there are several objects in the living room, as shown in Figure **6.4**, the RDM of the empty room shows some random noise after performing the clutter removal algorithm. Figure **6.5** (b) is the RDM of the environment when a subject was sitting on the sofa. The velocity shown is around -0.02 m/s to 0.02 m/s (mainly from the chest motion), with the occupied range bins from R=3.11 m to R=3.24 m. Comparing Figure **6.5** (a) and (b), the effectiveness of our stationary clutter removal algorithms is shown. It is demonstrated that subtracting the average signal value from the integrated signals eliminates the direct effects of the stationary objects (i.e., stationary clutter).

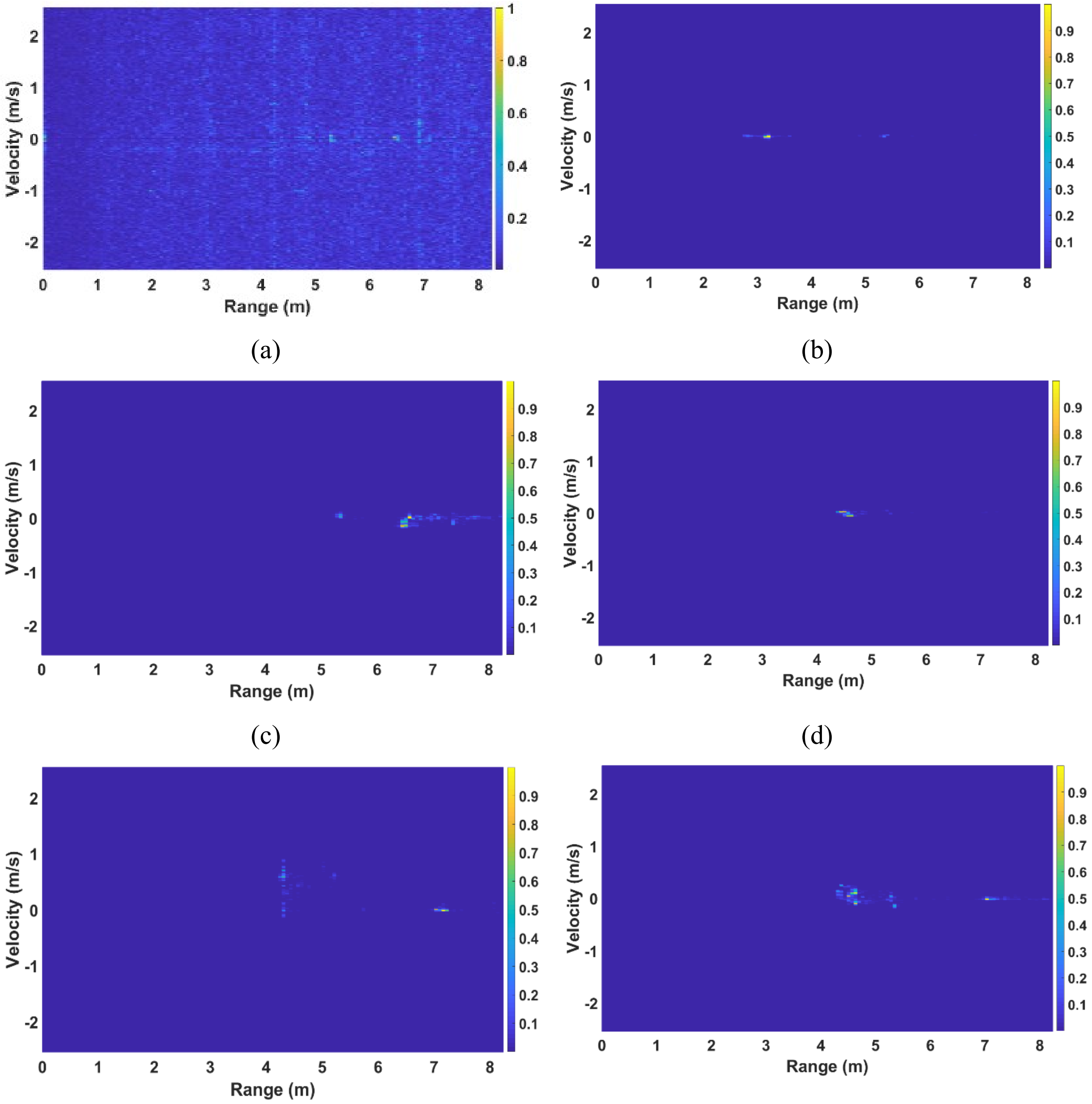

(a) (b)

(c) (d)

(e) (h)

Figure 6.5. Range-Doppler maps of (a) an empty room (frame #100), (b) a subject sitting on a sofa (frame #100), (c) a subject washing dishes (frame #100), (d) a subject picking up an object (frame #100), (e) a subject vacuuming (frame #100) (f) a subject vacuuming (frame #105).

Figure **6.5** (c) shows the RDM when the subject was standing by the sink washing dishes at an approximate R= 6.5 m. As shown, since the subject was at a close distance from a metallic object (the fridge in the kitchen), the interaction of the reflected signals from his body and the fridge created multipath effects (ghosts or time-varying clutter) [3], [165], observed at R=6.5 m extended to R=8 m. The multipath effect is more significant when the subject moves, particularly near reflective materials such as metals [3], [165]. Ghosts are visible for the case of vacuuming in Figure **6.5** (e) and (h) when the subject was at an approximate range of R= 4.5 m away from the radar, while ghosts are visible at R=7 m and further. One of the drawbacks of using point cloud information [27] to train machine learning is that ghosts' signals will be detected as a point cloud. Therefore, an even more sophisticated technique is needed to deal with ghosts and distinguish ghosts from the subject's direct reflections to be fed to machine learning. However, since the entire RDM is fed to our deep learning model without any handcrafted feature extraction method, the deep learning model handles ghost signals and predicts the classes based on what has been trained. The RDM of the environment with a subject picking up an object from the floor is provided in Figure **6.5** (d). The subject's body created velocity (micro-Doppler in radar received signals) ranging from -0.08 m/s to 0.02 m/s while range bins were occupied from R=4.34 m to R=4.67 m. For the case of vacuuming (Figure **6.5** (e)-(h)) and walking (Figure **6.6** (a)-(b)), since the subject had movement and the RDMs changed significantly frame by frame, we provided the RDMs at two different frames (#100 and #105) to provide more details. The subjects occupied multiple velocities and range bins for these two activities. For each of these activities, the RDMs are

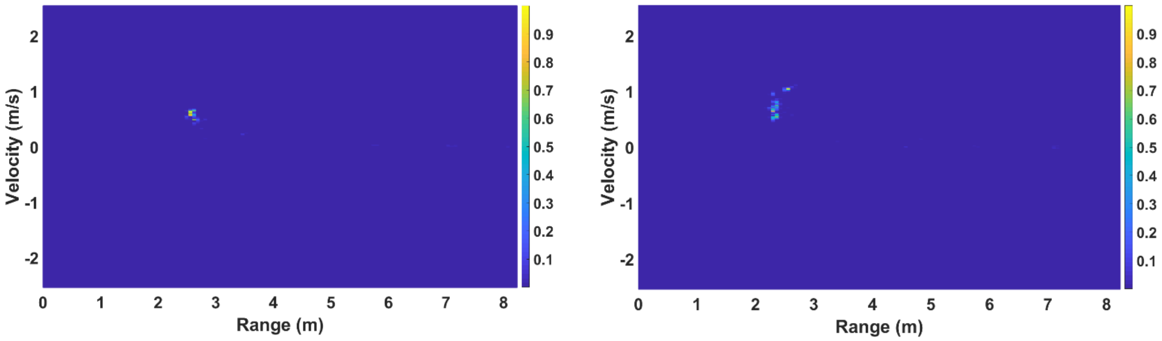

(a) (b)

Figure 6.6. Range-Doppler maps of (a) a subject walking (frame #100) (b) a subject walking (frame #105).

slightly different, so the deep learning model can extract sufficient features to distinguish them and identify the type of activity a subject is performing.

6.4.3.2 Deep Learning Results

To train and test machine learning algorithms, we followed two different validation approaches: First one was a K-fold validation method. In a 5-fold validation method, 80% of the whole data is used for training and 20% for testing. In the second method, we used data captured from a new subject for validation that was not part of the training dataset. To assess deep learning networks, it is essential to have a completely unseen subject for the test set to validate the network architecture and ensure the generalizability of the network in a real-life application. Although with the K-fold validation method, the samples are unseen in testing, the subjects are seen. With the second method, we intend to generalize our trained model to be functioning for any new subject. With the K-fold method, the activity patterns of all subjects are seen, while with the second method, the activity patterns of a new subject are unseen for the network.

To show the robustness and effectiveness of our proposed method for human activity recognition and gait period identification, we provided the outcomes of three procedures: 1. Train set based on RDM samples collected from six subjects performing various in-home activities at the apartment (living room), and the test set on samples collected from the seventh subject (Scenario #1), 2. The K-fold method, using RDM samples collected from all seven subjects performing various activities at the apartment (Scenario #2), 3. Train set based on STFT patterns collected from six subjects performing various in-home activities at the apartment (living room), and the test set on samples collected from the seventh subject (Scenario #3).

Since the performance of deep learning networks highly depends on their hyper-parameters to control how it learns the training dataset, optimizing the hyper-parameters utilized by each network is necessary. To find the best hyper-parameters for deep learning networks, a range of values was specified for five crucial hyper-parameters: learning rate, batch size, activation function, optimization algorithm and the number of layers. Several deep learning models were implemented to find the best model for our in-home activity recognition system. We implemented deep learning networks in TensorFlow (Keras) with a cross-entropy loss function in 50 epochs. Our criteria for choosing the best model were the performance in terms of accuracy and execution prediction time. The motivation to use accuracy as the performance metric in this work is that we have balanced datasets, so the models are not biased. Confusion matrices of four different deep learning models fed by RDMs, including 2D-

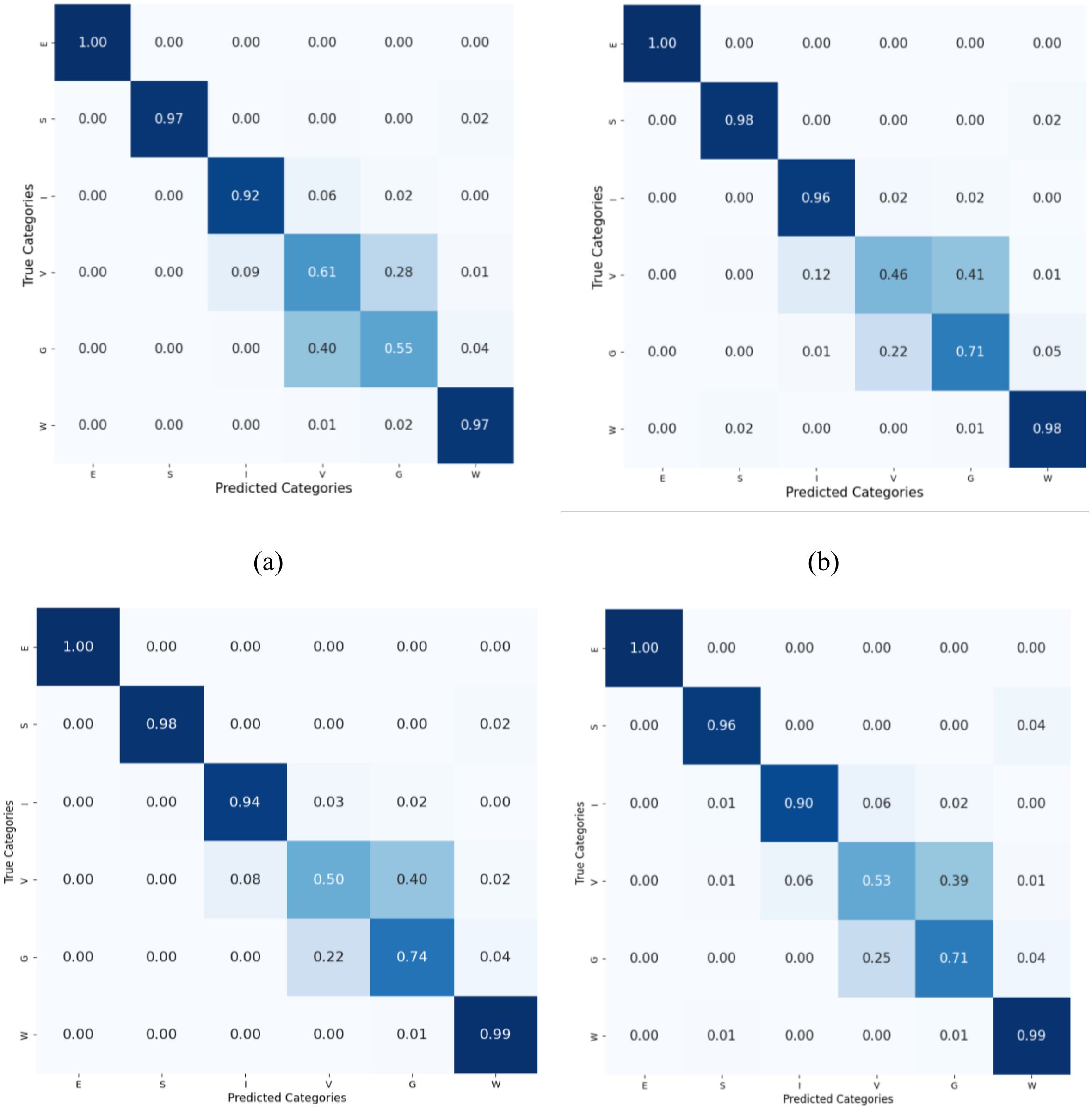

(a) (b)

(c) (d)

Figure 6.7. Confusion matrix yielded by the different networks, fed by RDMs, applied to test datasets (data collected from a complete new subject, Scenario #1) in the living room environment (a) 2-DCNN (b) 2-DCNNLSTM (c) LSTM and (d) GRU. Note that “E”, “S”, “I”, “V”, “G” and “W” stand for Empty, Sedentary, In-place movement, Vacuuming, Walking and Washing, respectively.

CNN, 2D-CNNLSTM, LSTM and GRU, are provided in Figure **6.7** for scenario #1. A summary of the performance of all four models is listed in Table **6.1**.

LSTM is the most accurate network in identifying the six in-home classes, while 2-DCNN is the least precise model. The total accuracy of 2-DCNN, 2-DCNNLSTM, LSTM and GRU models is 84%, 85%, 87% and 86%, respectively. All models identify the empty room 100% accurately, meaning that an occupied/ vacant room will be recognized without any error. 2-DCNNLSTM and LSTM models classify the "Sedentary", "In-place Movement" and "Washing" classes with less than 6% error. 2-DCNNLSTM, GRU and LSTM models can recognize walking periods and distinguish them from other activities with more than 70% accuracy. However, the CNN model performs poorly in identifying the walking periods. As seen, all recurrent neural networks performed better in predicting in-home activities, particularly "Walking". The most challenging class for all four networks is "Vacuuming" which is confused with "Walking" and "In-place movement". The reason for this poor performance will be further analyzed in this study. In addition to the accuracy, as shown in Table **6.1**, the execution prediction time of CNN and 2-DCNNLSTM is much longer than the other networks because of the complexity of the convolution-based neural networks. LSTM and GRU networks are more accurate and faster for in-home activity recognition. We deployed the GRU network for our real-time processing since it is faster in predicting a new class which is almost as accurate as the LSTM network in predicting the in-home activities of a new subject. Graphs of the performance of the accuracy and the loss function of the GRU network are plotted in Figure **6.8**.

The GRU network performance in predicting in-home activities of an unseen subject (Scenario #1) ensures generalizability. However, it is common to train a model based on a known subject to classify and monitor his future activities. Therefore, for Scenario #2, we analyze the GRU network in predicting

Table 6.1. Comparison of the result of different deep learning models (test data: a new participant)

Model	Inputs	Accuracy	Testing Time/Sample
GRU	STFT	75%	2.4 ms
LSTM	STFT	67%	6.9 ms
2-DCNN	STFT	69%	10.7 ms
1-DCNNLSTM	STFT	73%	4.7 ms
2-DCNN	RDM	84%	3.5 ms
GRU	RDM	86%	0.3 ms
LSTM	RDM	87%	1.2 ms
2-DCNNLSTM	RDM	85%	3.7 ms

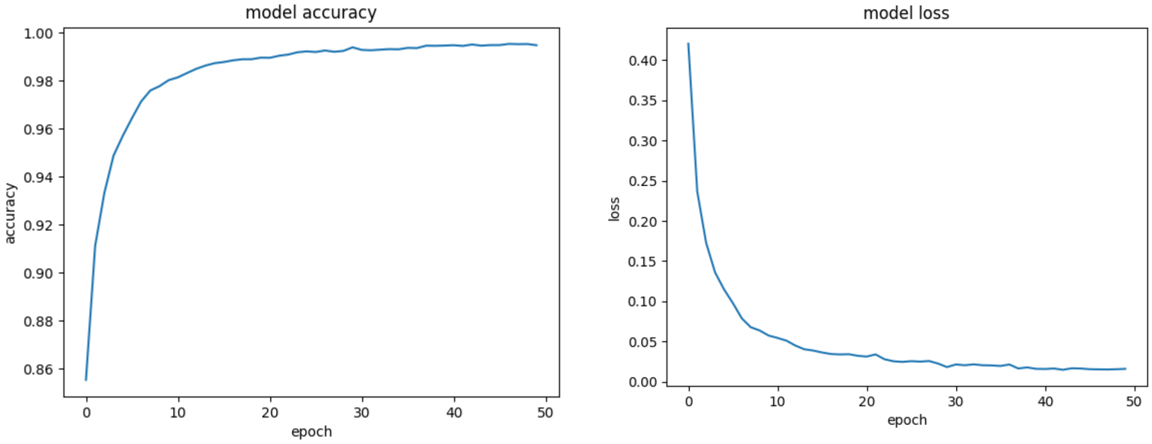

(a) (b)

Figure 6.8. Graphs of the performance of (a) the accuracy and (b) the loss function of the GRU network in each epoch.

new activities while the patterns of the subject's activities were previously trained. It should be pointed out that other networks were assessed for Scenario #2. We provide the outcome of GRU as it yields the best performance. The confusion matrix of the GRU network for Scenario #2 is provided in Figure **6.9**. The overall accuracy of this case is 93%. The network performance improved significantly because the network was trained based on all subjects' activity patterns. In this case, the GRU model predicts "Sedentary", "Washing" and "In-Place Movement" with more than 97% accuracy. The model can identify walking periods with 87% accuracy, while "Vacuuming" is still the least accurate class (75%). As seen in Figure **6.7** and Figure **6.9**, some of the RDMs of vacuuming were misclassified in the "Walking" class, leading to less accuracy in the "Vacuuming" class.

Although the model was tuned and various variables were assessed, the reason for this lower accuracy should be analyzed. Since the model was carefully analyzed and tuned, we referred to the datasets. We found that some participants did not follow our order for vacuuming perfectly. Instead of cleaning the floor, some of our participants were walking while holding the vacuum cleaner. This sanity check was done based on the result of all RDMs over the entire data and STFT patterns. Participants also confirmed this. Since our labelling method was to ask each participant to do each task for 10 minutes consistently, we stuck with this labelling method even though we found this flow in a small portion of our samples. To show the details of this flow, we provided the STFT patterns of two subjects in Figure **6.10**. Although non-straight-line STFT patterns might not be easily distinguishable, we provided the STFT results because it clearly shows the variation over time in one plot.

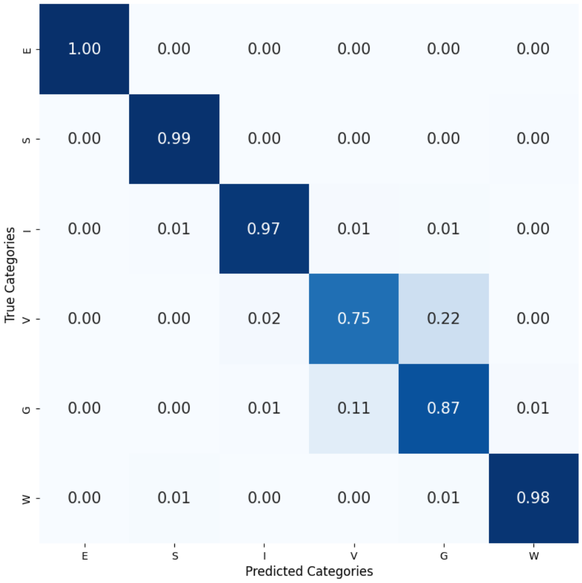

Figure 6.9. Confusion matrix yielded by the GRU network, fed by RDMs and applied to test datasets (Scenario #2) in the living room environment.

As shown, since subject “A” followed what he was asked to do perfectly, the STFT pattern of vacuuming (Figure **6.10** (a)) is entirely different from his walking pattern (Figure **6.10** (b)). However, subject “B” was not following our request and was not performing the actual vacuuming but holding the vacuum cleaner while walking. The STFT pattern of the vacuuming Figure **6.10** (c)) is very close to walking (Figure **6.10** (d). Therefore, we can conclude that the low accuracy of the “Vacuuming” class is because of the datasets, not the model. The model identifies some vacuuming samples as walking because the participants walked instead of vacuuming. It is important to note that the classification model was designed to detect specific patterns of movement associated with certain activities. While carrying a vacuum cleaner around the house may not fit into the vacuuming class, it may still be recognized as walking or another relevant activity class. It is important to consider the context of the activity and the patterns of movement associated with it when designing an activity recognition system. In this case, the low accuracy of the vacuuming class was due to the dataset rather than the model, and future work could involve collecting more diverse datasets and adding more classes to improve the model's performance.

Using STFT patterns as inputs for machine learning and deep learning models is a common approach in gait recognition studies. This approach has been shown to be effective in capturing the temporal and frequency characteristics of activity signals. However, it is important to note that the effectiveness of

STFT patterns as a feature extraction method may vary depending on the characteristics of the data being analyzed, and other feature extraction methods should also be considered and evaluated. Since many studies used STFT patterns as inputs for machine learning and deep learning models, we also train our deep learning models with STFT patterns. The purpose is to compare the results of deep learning networks fed by RDMs with the case of STFT inputs. To generate the STFT signature of each activity, we choose a small Hamming window for time-frequency analysis of the real-time radar human activities /gait signals. The length of the Hamming window is 128 samples. As shown in Figure **6.10**, STFT patterns show the time-varying velocity created by each subject without considering the occupied range bins. Figure **6.11** shows the network STFT inputs in detail. After optimizing the network parameters, the input is a vector of 1 × 256 consisting of 25 ms of a subject's micro-Doppler signature. The total number of time steps is set to 50. Note that for the time steps, we observed that when it is greater or less than 50, the performance of the networks degrades. Therefore, the dimension of the input of the networks is (1, 50, 256). In total, t=25×50=1250 ms of the subject's spectrogram is fed to

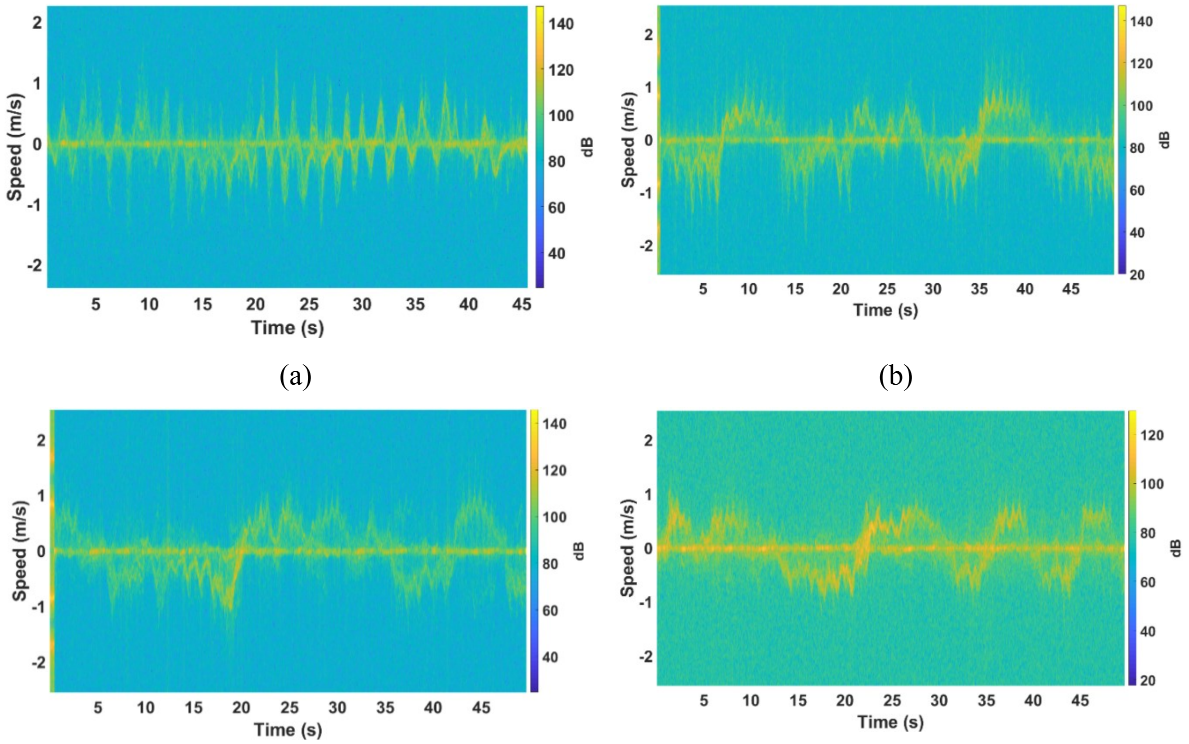

(a) (b)

(c) (d)

Figure 6.10. STFT patterns of (a) subject "A" vacuuming, (b) subject "A" walking, (c) subject "B" vacuuming, and (d) subject "B" walking.

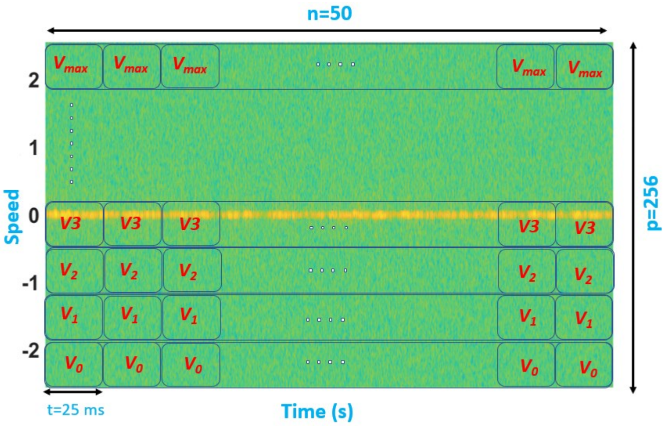

Figure 6.11. STFT patterns as inputs for deep learning models.

networks. Table **6.1** shows the summarized output of four networks fed by STFT patterns of Scenario #3.

As shown, GRU is the most accurate network in classifying activity patterns of a new subject. Comparing the performance of all four networks fed by RDMs, the network fed by STFT is less accurate. To detail the results, Figure **6.12** shows the confusion matrix yielded by the GRU network fed by STFT patterns. As seen, occupied versus empty rooms could be identified with 100% accuracy in this case as well. However, other classes are not predicted as accurately as the networks fed by the RDMs. For example, considering the RDMs as inputs for GRU, the "Sedentary" class was identified 96% accurately, while it is 83% accurate in this case. The pattern of "Washing" is also much less accurate in this case. One possible explanation could be that the network has not received enough information to distinguish several classes. For example, Figure **6.13** (a) and (b) show the STFT pattern of sitting on the sofa while working with a cell phone and washing dishes in the kitchen, respectively. The two patterns are not as distinguishable as the RDMs are in Figure **6.5** (b) and (c).

As mentioned, the GRU network is trained and optimized in a local machine. The tuned and optimized model with the parameters listed in Table **6.2** is then deployed into the cloud to be used in the run-time section. The network consists of multiple hidden layers, including the inputs, GRU cell layers, fully connected layers that combine all the features learned by GRU layers for classification, and the output layer. Therefore, the output size is equal to the number of classes. The SoftMax layer normalizes the output of the former layer to be used as classification probabilities.

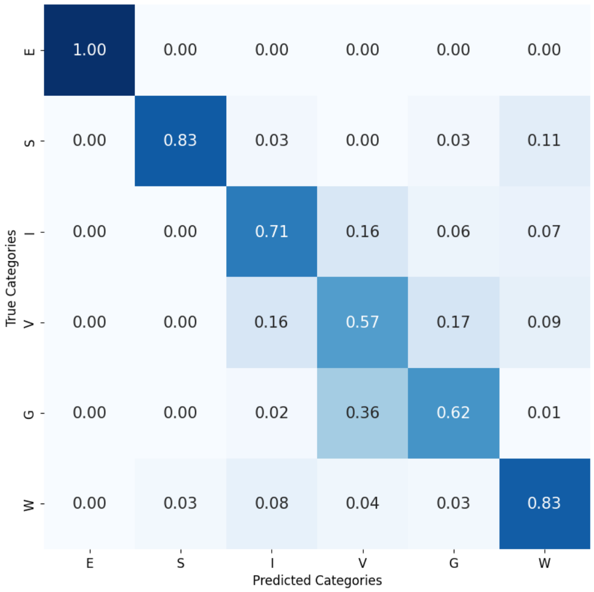

	E	S	I	V	G	W
E	1.00	0.00	0.00	0.00	0.00	0.00
S	0.00	0.83	0.03	0.00	0.03	0.11
I	0.00	0.00	0.71	0.16	0.06	0.07
V	0.00	0.00	0.16	0.57	0.17	0.09
G	0.00	0.00	0.02	0.36	0.62	0.01
W	0.00	0.03	0.08	0.04	0.03	0.83

Figure 6.12. Confusion matrix yielded by the GRU network, fed by STFT patterns, applied to test datasets (Scenario #3) in the living room environment.

Table 6.2. GRU networks hyper-parameters.

Hyper-parameters	Optimized values
Activation function	Rectified Linear Unit
Batch size	512
Number of layers	5
Learning rate	0.01
Optimization algorithm	Adam
Number of units for each layer	(256, 128, 64, 64, 6)

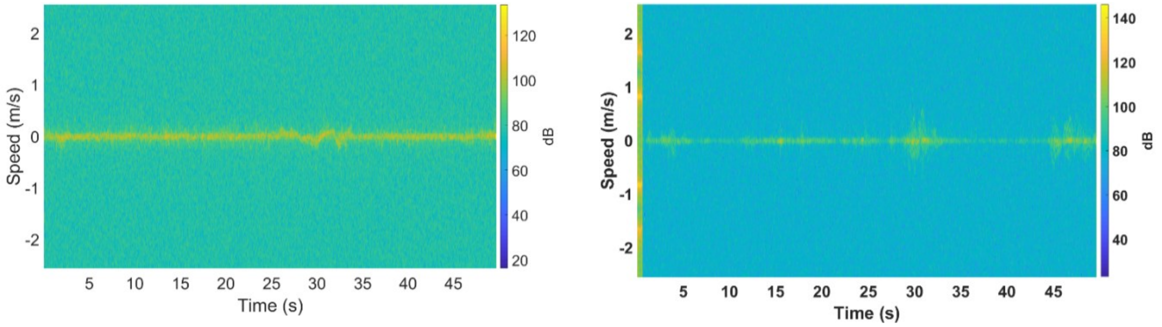

(a) (b)

Figure 6.13. Time series inputs: STFT patterns of a subject (a) sitting on the sofa (b) washing dishes.

6.5 In-Home Gait Monitoring

In this section, gait parameter extraction methods are discussed. To extract gait values of a subject walking in a non-straight line, firstly, signals after performing the clutter removal algorithm are analyzed for the case when a subject was walking inside cluttered rooms. Normalized range-azimuth maps (RAM) and RDM of a walking subject, along with their detected points after performing CFAR, are provided to support the analysis and illustrate remaining signals from a subject and multipath effects. All the tests were conducted in the RIA apartment, as shown in Figure **6.14**. Analyzing the RAMs and RDMs helps understand ghosts and the subject's signal characteristics. Several examples of consecutive frames of RAMs and RDMs after performing the stationary clutter removal algorithm before and after CFAR are provided. To discriminate between direct subjects' signals and indirect ones (ghosts or multipath effects), the amplitude, velocity, and frequency of the existence of these signals over time in RDMs and RAMs are analyzed. Figure **6.15** (a) and (b) show the RAMs and RDMs and detected points at frame #1 and frame #2 when a subject just started to walk. The results obtained from frames #3 and #4 are also illustrated in Figure **6.16**. Additionally, RAMs and RDMs at two more consecutive frames, # 30 and #31, during walking, when the subject was in the middle of the room, walking around 4 m away from the radar, are shown in Figure **6.17**. Note that black rectangles show the subject's position at each plot, so other detected points are noise or ghosts.

In terms of signal intensity, comparing the intensity of direct signals in RAMs in Figure **6.15**, Figure **6.16** and Figure **6.17**, the amplitude (brightness of the signals shown by black rectangles) of the target's signals and ghosts fluctuates significantly frame by frame. Ghosts' signals have amplitude levels similar to or stronger than the subject's signals in several frames, therefore, entail a severe problem of separating subject signals from ghosts and noise. For example, the red rectangles in Figure **6.16** (b)

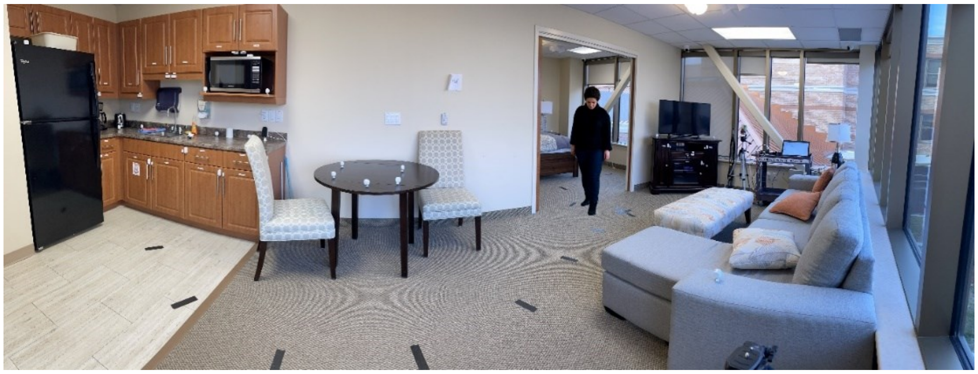

Figure 6.14. In-home environment walking tests conducted in the Schlegel-UW RIA.

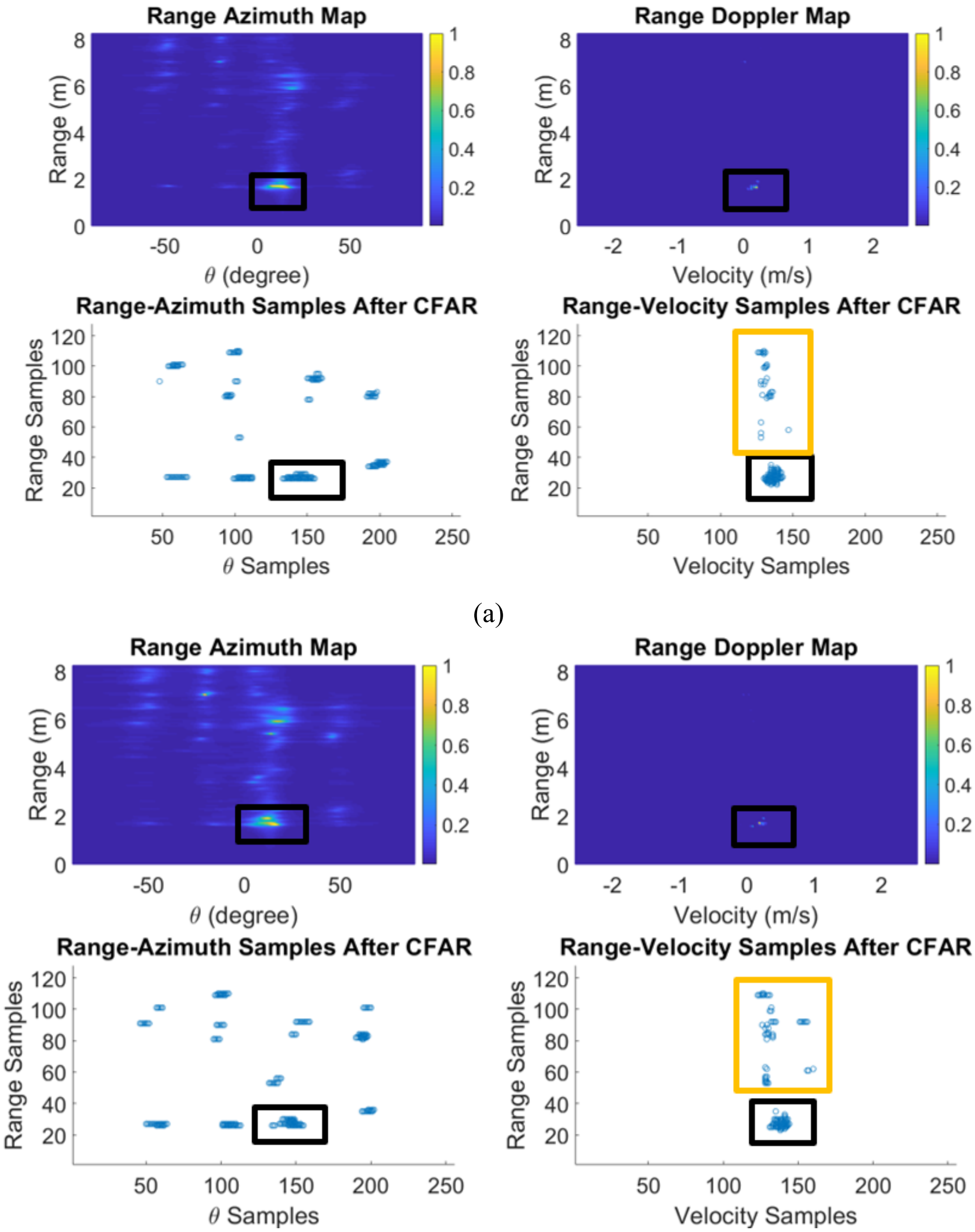

(a)

(b)

Figure 6.15. RDMs, RAMs of the environment when a subject was walking, along with the corresponding detected points after performing CFAR (a) Frame #1, (b) Frame #2. The black rectangles show the subject's direct signals while the orange rectangle shows the ghosts detected points in RDMs.

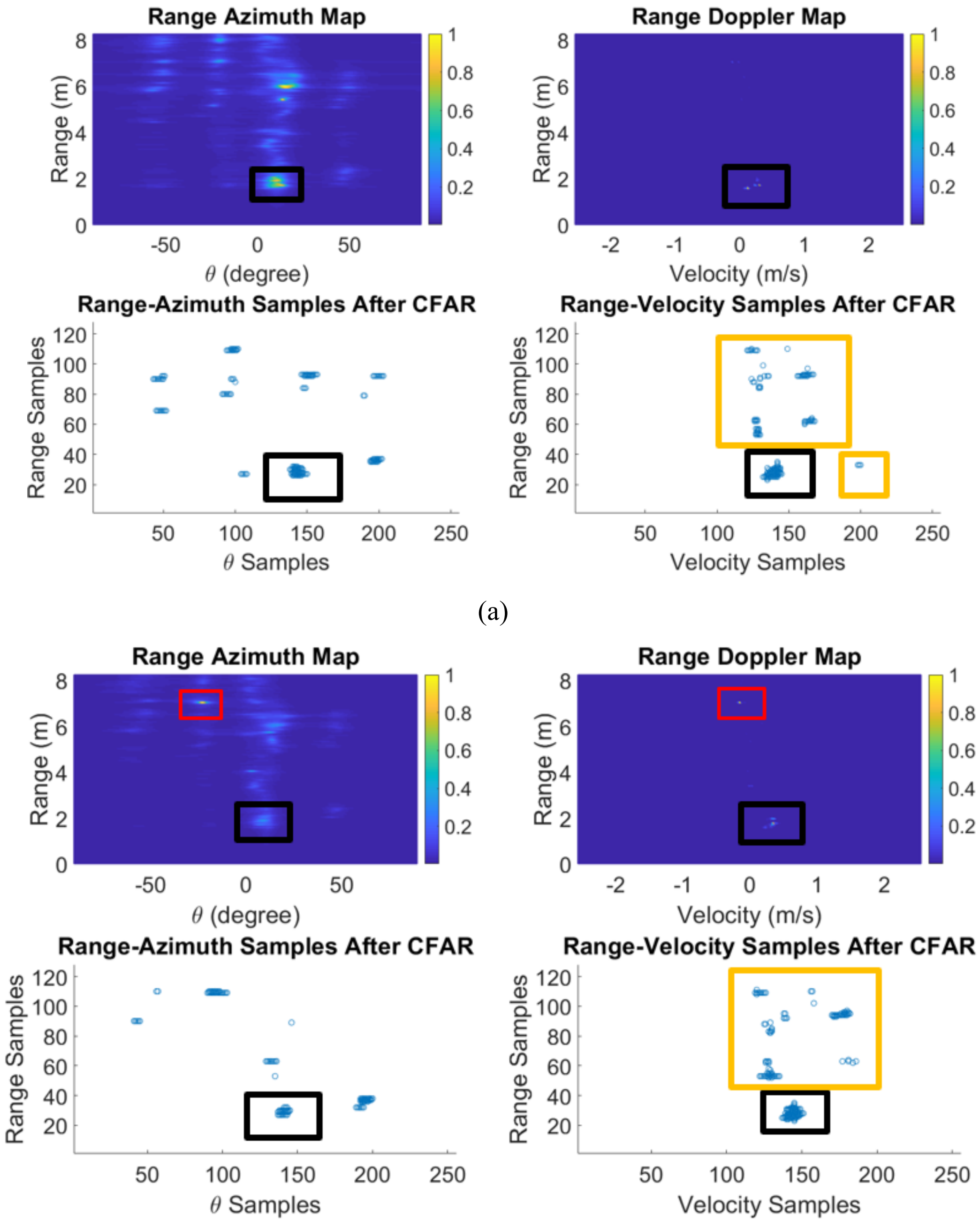

(a)

(b)

Figure 6.16. RDMs, RAMs of the environment when a subject was walking, along with the corresponding detected points after performing CFAR (a) Frame #3 and (b) Frame #4. The black rectangles show the subject's direct signals while the orange rectangle shows the ghosts detected points in RDMs.

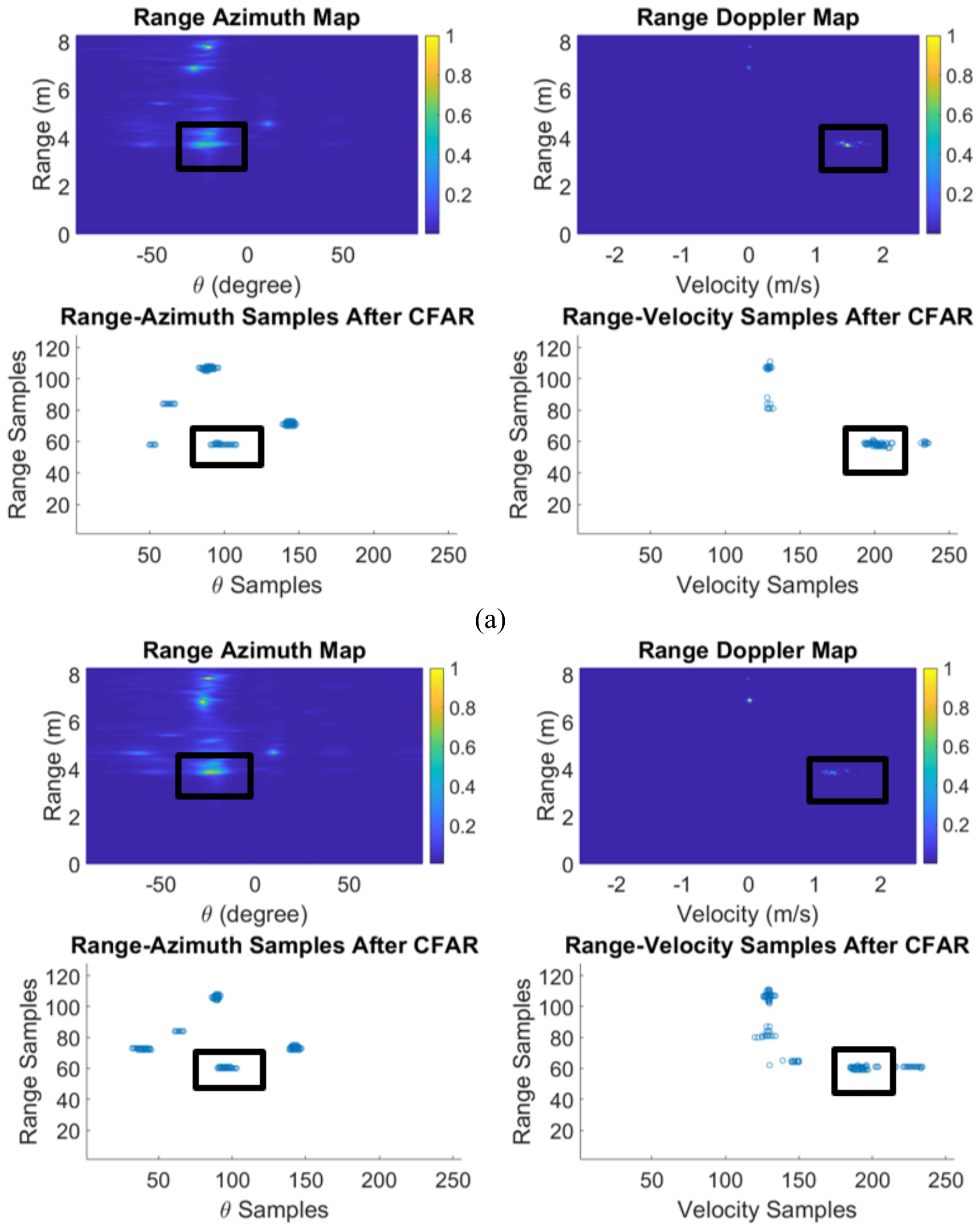

(a)

(b)

Figure 6.17. RDMs, RAMs of the environment when a subject was walking along with their corresponding detected points after performing CFAR (a) Frame #30 and (b) Frame #31. The black rectangles show the subject's direct signals.

demonstrate that the amplitude of the ghost's signal is brighter (stronger) than the subject's signal. Hence, we cannot distinguish the subject's signals from ghosts based on their amplitude at each frame.

There are two other parameters to consider: velocity and the frequency of the existence of these signals over time. Stationary objects create zero Doppler or velocity that could be removed by filtering (removing signals around zero Doppler). However, as shown in Figure **6.15** and Figure **6.16** (orange rectangles), in addition to the subject's direct signals, there are many other detected points with non-zero velocity, called time-varying clutter points in this thesis. As mentioned in the previous chapter, the existence of time-varying clutter is the main challenge for in-home gait monitoring or, generally, gait monitoring in a cluttered environment.

In terms of the frequency of the existence of detected signals, analyzing numerous data, we realized that subjects' direct signals are consistent over time and have velocity more than zero because the subject was walking, whereas ghosts or time-varying clutter appear and disappear frame by frame, so not consistent over time. This is demonstrated in Figure **6.18** after performing DBSCAN and removing clusters with zero velocity. Based on the performance of the different variables set for the DBSCAN parameters, epsilon neighbourhood, ε=2, and min_points=5 were selected as optimized values. As shown in black rectangles, the subject's cluster is consistent over these four frames, while ghost clusters are present in one frame while disappearing in another one. The same results could be obtained at other frames, but these plots are provided as examples to illustrate the details.

6.5.1 In-Home Gait Parameters Extraction Algorithm

The block diagram of our proposed in-home gait extraction algorithm is provided in Figure **6.19**. As shown, after removing detected points with zero-Doppler and performing DBSCAN on the remaining points, the same algorithm (STA) proposed in Section 5.3.3 is applied to track a walking subject over time. The parent with the maximum detected cluster is then selected over time as the target's tracked cluster. The outcome of the STA algorithm provides the 2D position of the walking subject over time from which walking speed can easily be calculated. To extract other gait parameters, such as step time, step length, cadence, etc., similar to the previous chapter, we based our gait extraction algorithm on the fluctuation of the torso's movement during the stance and swing phase, as it is one of the key factors impacted by other segments of body movements during walking cycles [168]. It should be mentioned that although our subject walks randomly but not in a straight line, we can still extract gait values based on the torso's motion. This is because, even though the actual value of speed is affected by the motion angles, the torso's fluctuation is detectable during swing and stance time, regardless of the angle of

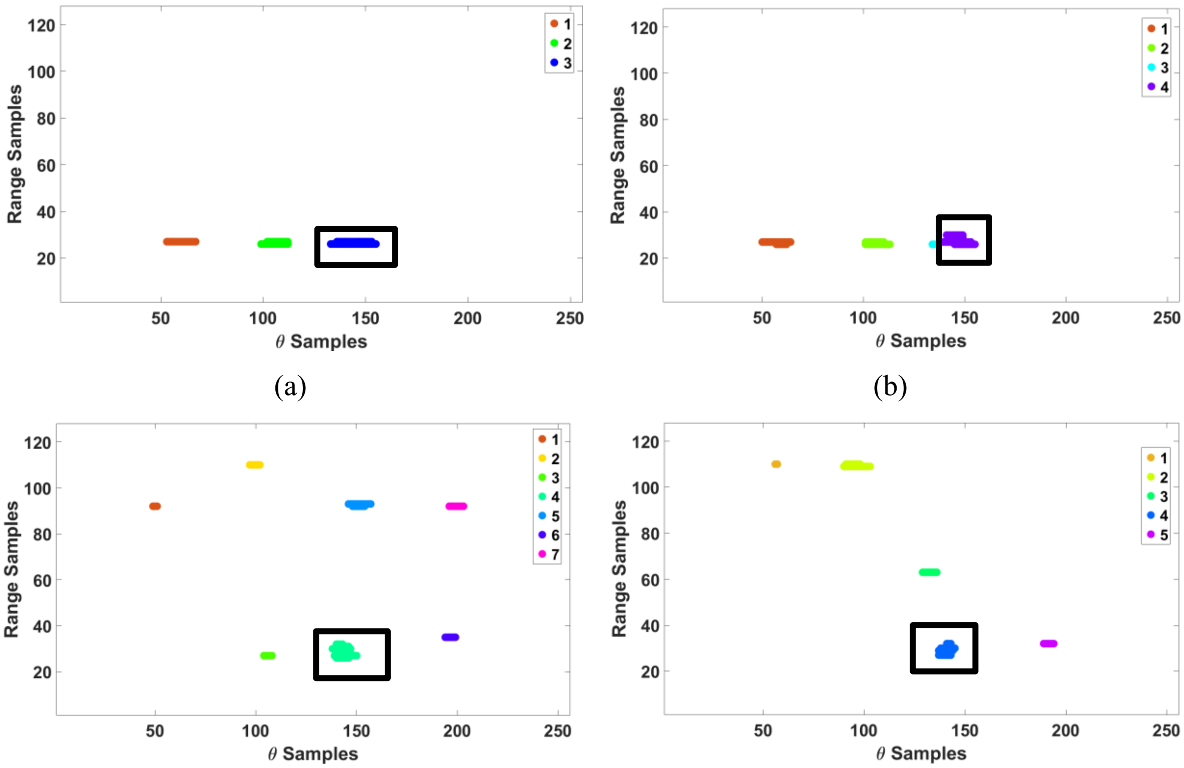

(a) (b)

(c) (d)

Figure 6.18. Identified clusters by DBSCAN in RAM maps after removing points with zero-velocity (a) Frame #1, (b) Frame #2, (c) Frame #3, (d) Frame #4. The black rectangles show the subject's direct signals.

motion. The basis of our algorithm is the fluctuation of the torso's velocity that speeds up and down during the stance and swing phase. The torso's movement is not only precise, but it provides very distinctive information from which a straightforward peak detection algorithm can provide several gait values [3], [53].

The STA obtains the subject's positions to extract and quantify gait parameters, as shown in Figure **6.19**. Walking speed is then calculated based on the change of the subject's position over time. The velocity of the torso is calculated by performing a second FFT (Doppler-FFT) over the torso's range bin. Since the maximum velocity of the torso is achieved when the foot touches the ground (step time), applying a peak detection algorithm to the results of the absolute value of Doppler-FFT over the torso's range bin, the torso's maximum speed is obtained [101]. The corresponding time of the torso's maximum speed shows the time when the foot touches the ground (contact position time/step time).

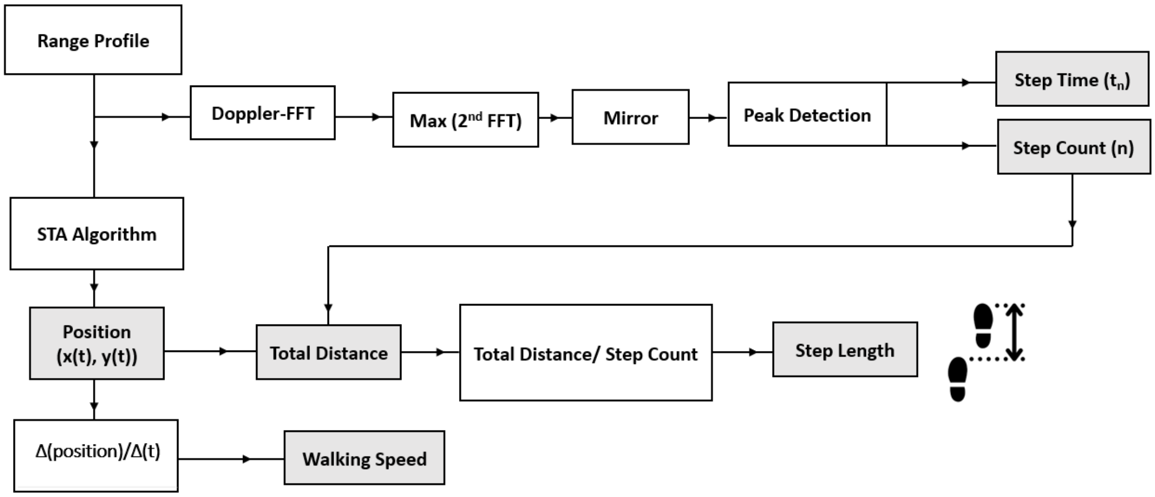

Figure 6.19. Proposed in-home gait parameter extraction algorithm.

Then, the contact position time can be obtained, which can be used to determine the number of steps or step counts. Consequently, the average step length is the total distance/step counts. Therefore, applying our fast and easy-to-implement gait extraction algorithm, we could extract spatiotemporal gait values (e.g., step time, step length, step counts, speed etc.) while a subject walks randomly in a cluttered room.

In summary, our proposed algorithms are based on these premises:

1. The velocity of stationary clutter is zero, which could be removed by subtracting the average of signals over time and filtering detected points with zero velocity.
2. The existence of time-varying clutter or ghost is not consistent over time but varies frame by frame
3. Signals from a walking subject are consistent over time (as long as detected by CFAR).
4. At each frame, the closest cluster to the subject's previous cluster is the subject's cluster.
5. The speed of the torso's range bin fluctuates during the stance and swing phase and affects the Doppler values accordingly, even if subjects walk in a non-straight path.

6.5.2 Measurement Results

The performance of the proposed in-home gait extraction algorithm was validated in two different living areas (1) the RIA apartment and (2) a living room in a small apartment. For both apartments, similar to previous chapters, since a ground truth such as GaitRite or a Vicon system was not available, we asked participants to step on the marked points to have reference/ true values for step length and step counts. For the tests in the RIA apartment, two participants (two male participants with a height of 185 cm and 164 cm) were asked to follow a curvy path, as shown in Figure **6.14**. Similar to the walking tests in previous chapters, the step length was set to 70 cm in the RIA building.

The results of the in-home subject tracker algorithm are presented in Figure **6.20**, demonstrating the effectiveness of the proposed methods in eliminating ghost signals and accurately tracking the walking subject over time. Figure **6.20** (a) shows all clusters detected by DBSCAN after removing clusters with zero velocity, while the black curve represents the walking path. Figure **6.20** (b) illustrates the subject clusters identified by the proposed method. The proposed method successfully tracked the subject and removed ghost detections. To evaluate the accuracy of the algorithm, the extracted gait values were compared to the actual values since the exact position of the subject was not known at each frame.

Table **6.3** summarizes the extracted gait values of two subjects during two walking tests in the RIA apartment. The speed error ranges from 0.0967 m/s to 0.0012 m/s, with an average speed error of 0.0515. The average error for step count and step length was 6 and 3.5 cm, respectively. In addition to the average value, the proposed method also shows the step time at each gait cycle, as shown in Figure **6.21**. Overall, the extracted gait parameters demonstrate that the proposed in-home gait monitoring method is almost as accurate as other methods where the subject walked in a straight line.

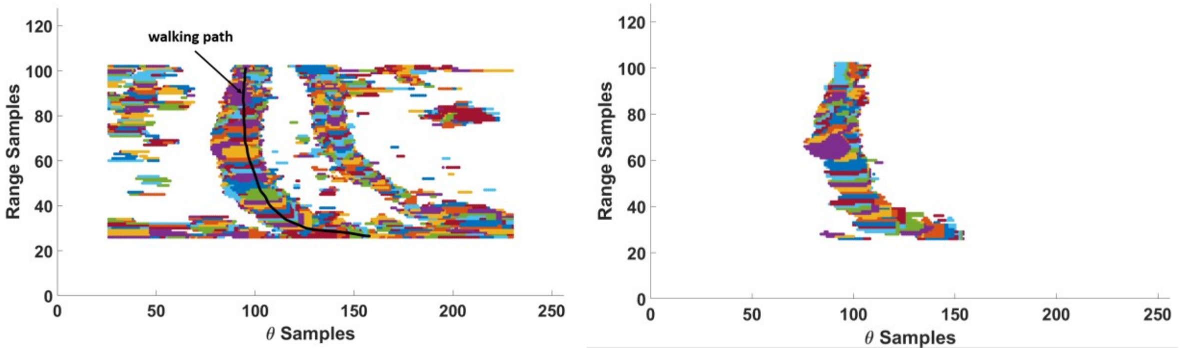

(a) (b)

Figure 6.20. Detected clusters (a) all clusters identified by DBSCAN after removing clusters with zero-velocity (b) subject’s detected clusters. The back curve shows the walking path.

Table 6.3. Extracted in-home gait parameters.

	Speed from radar (m/s)	Speed from stopwatch (m/s)	Number of steps Reference: 42	Step length (Reference value: 70 cm)
Subject 1-Trial 1	1.061	0. 99	Estimated: 45	74
Subject 1-Trial 2	1.08	1.06	Estimated: 49	70
Subject 2-Trial 1	0.96	0.87	Estimated: 48	72
Subject 2-Trial 2	0.96	0.96	Estimated: 49	71
Average error	0.05		+6	+ 3.5

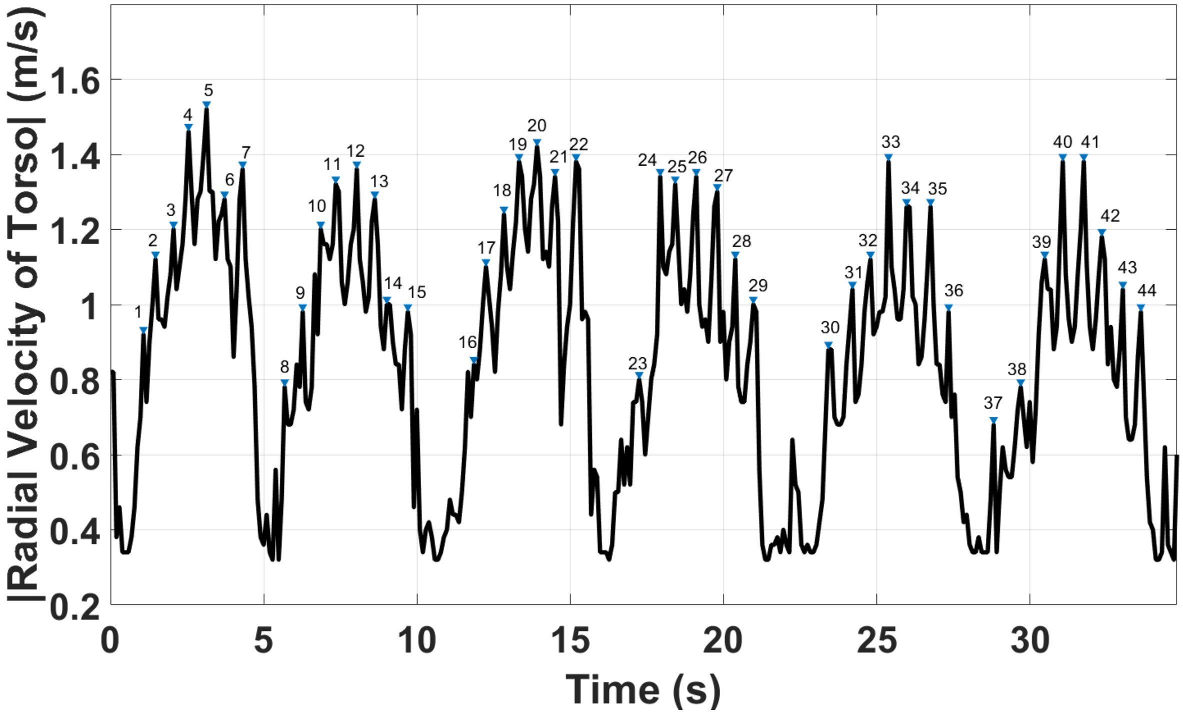

Figure 6.21. Peak detection algorithm applied to the absolute value of the torso’s radial velocity.

All previous walking tests in this thesis were based on step lengths of 70 cm for men and 60 cm for women. The following results present the performance of the proposed in-home gait extraction algorithm in a cluttered living room apartment, where the participants were asked to walk in marked paths with different step lengths (30 cm, 60 cm, and 80 cm). These experiments were designed to assess the algorithm's ability to handle step length variability since, with age, gait speed becomes slower and step lengths shorter [169].

Five subjects (two males and three females with heights ranging from 156 cm to 187 cm) participated in a walking experiment in a living room. The floor was marked with designated stepping positions, and a stopwatch was used to measure the walking speed. Each participant was required to perform the walking test four times, resulting in a total of 60 recorded walking tests. Figure **6.22** showcases the performance of the in-home subject tracker in following the subject's movement within a cluttered living room. Figure **6.22** (a) shows the detected target cluster as determined by the proposed algorithm while the subject was walking with a step length of 80 cm. Figure **6.22** (b) illustrates the subject's position, depicted by its trajectory, and the actual path, represented by a black curve. Note that the black curve represents an estimated, not exact, position of the subject as a reference path. Despite the subject's curvy walking path, the proposed algorithm accurately detects the subject's position, as seen by the close overlap of the actual and detected positions. Figure **6.22** is an example of the results obtained from the proposed method, showing its effectiveness while similar results were obtained in other tests. To evaluate the proposed gait extraction algorithm, the results of the peak detection algorithm applied to the absolute value of the torso's radial velocity are presented first. Figure **6.23**, Figure **6.24** and Figure **6.25** show the subject's torso's absolute radial velocity for step lengths of 30 cm, 60 cm and 80 cm, respectively. The significant differences in the value of the radial velocity of the torso are due to the subject's curved walking path, causing a change in the relative angle between the subject and the radar, affecting the Doppler value. These results indicate that CW radars are not accurate in estimating walking speed when the subject walks in a curved path since the value of the Doppler will be affected by the angle of motion. However, MIMO FMCW radars can resolve this issue by providing range,

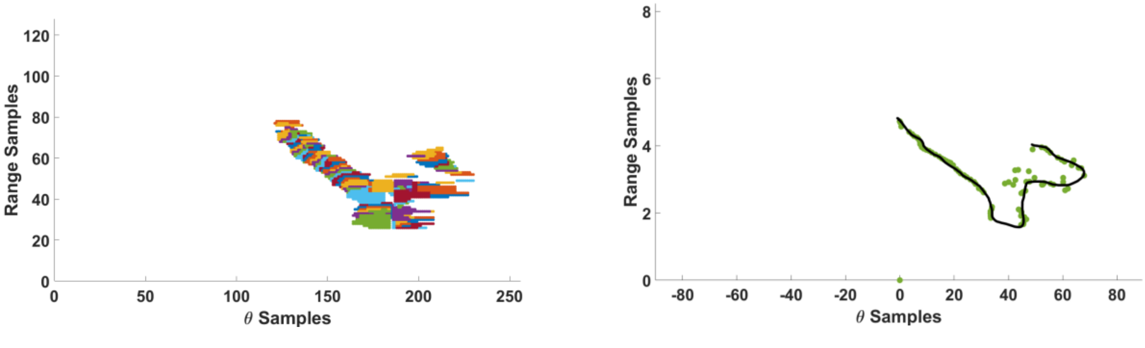

(a) (b)

Figure 6.22. Subjects walking paths identified by the proposed algorithm (a) detected clusters and (b) detected position. The back curve shows the approximate reference walking path.

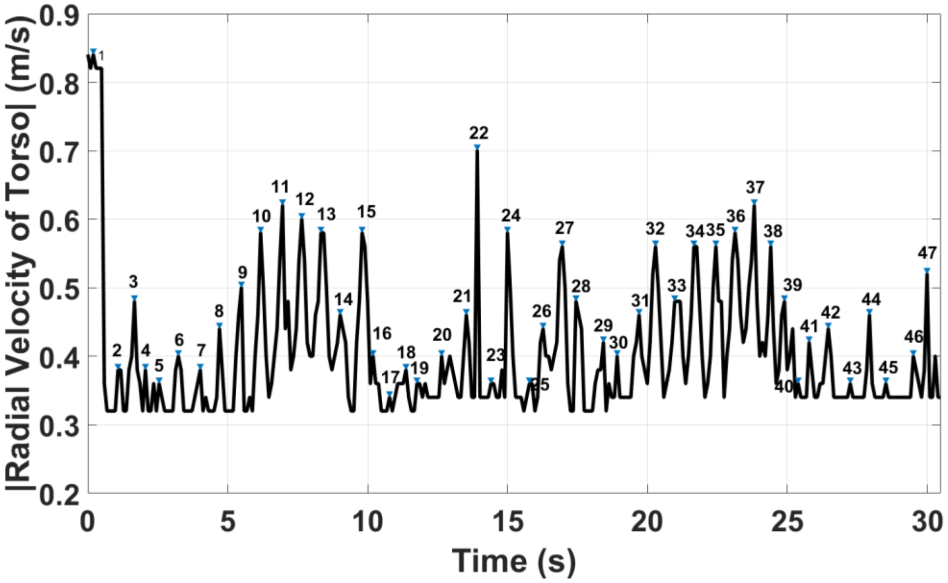

Figure 6.23. Peak detection algorithm applied to the absolute value of the torso's radial velocity while the subject was asked to step on the marks with 30 cm spacing. Step counts are shown by the small arrows and numbers above the plot line.

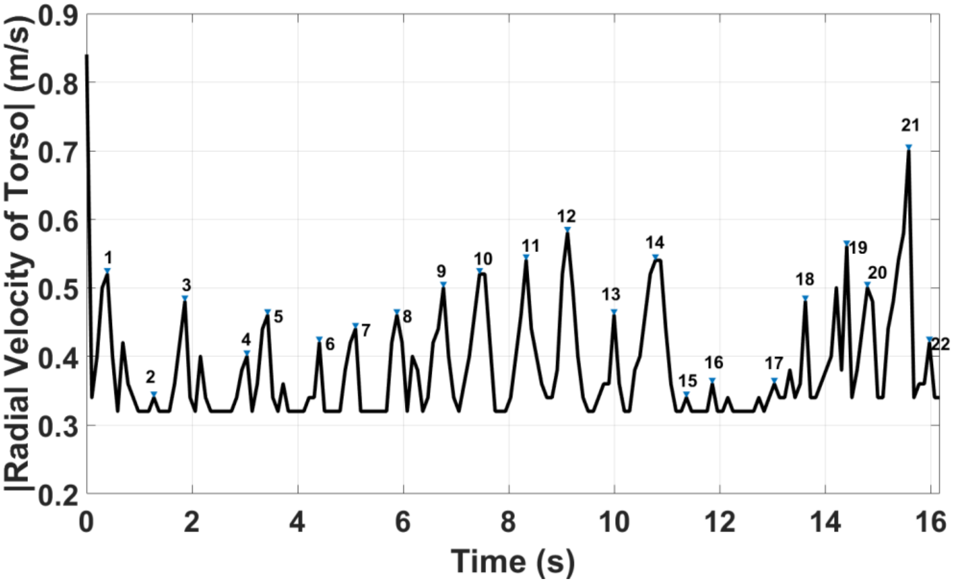

Figure 6.24. Peak detection algorithm applied to the absolute value of the torso's radial velocity while the subject was asked to step on the marks with 60 cm spacing. Step counts are shown by the small arrows and numbers above the plot line.

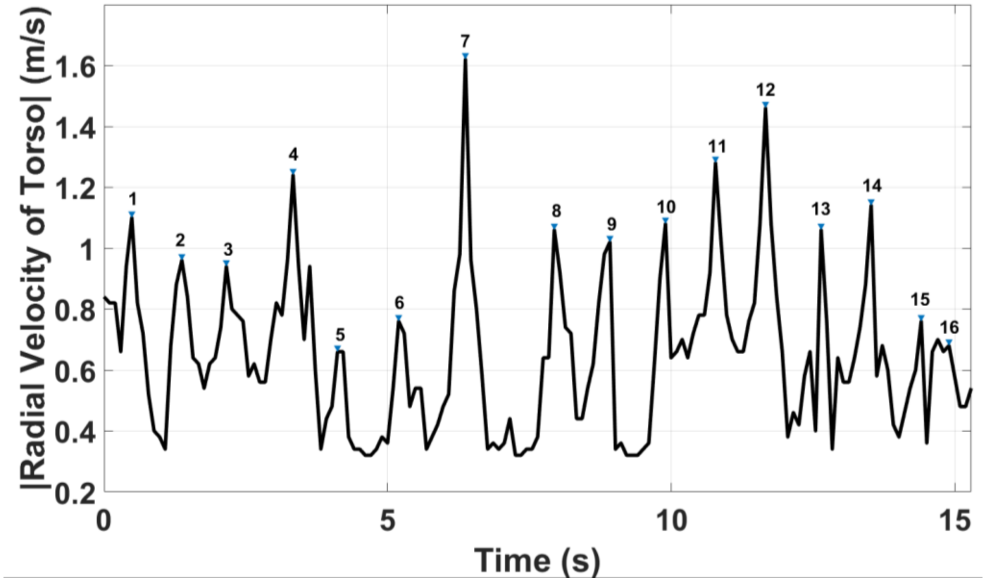

Figure 6.25. Peak detection algorithm applied to the absolute value of the torso's radial velocity while the subject was asked to step on the marks with 80 cm spacing. Step counts are shown by the small arrows and numbers above the plot line.

azimuth, and Doppler information on the environment. The results of the proposed gait extraction algorithm show that the fluctuations of the torso's velocity during stance and swing phases can be captured even though the value of the radial velocity is affected by the angle of motion, allowing for a reliable estimation of step time and step count. This is demonstrated in Figure 6.23, Figure 6.24 and Figure 6.25, which show the step time and step counts (the small arrows and numbers above the plot line show step counts). For example, Figure 6.23 illustrates that the algorithm detected 47 peaks in the plot, which represents the step time and number, while the true number of steps was 42 with a step length of 30 cm. The algorithm estimated the step length to be 36 cm. Despite the difficulty in maintaining a step length of 30 cm for the participant and its impact on the walking speed, the algorithm still provided quite accurate results regarding the step counts and step length. The results for step count and step length were more accurate in Figure 6.24 and Figure 6.25, where the step lengths of 60 cm and 80 cm were closer to normal walking patterns. The peak detection algorithm effectively identified the step counts with an error of only 1 step for 60 cm and 0 steps for 80 cm, with a step length error of 3 cm for 60 cm and 2 cm for 80 cm.

The accuracy of the proposed algorithm in determining the walking speed was evaluated by comparing the results of all 60 walking tests obtained from the algorithm with the values estimated using a stopwatch. The comparison is presented in a Bland-Altman plot in Figure **6.26**, which shows the difference between the simultaneous readings from the radar and stopwatch. The solid line at 0.0549 m/s represents the average difference between the two measurements, while the two dashed lines depict the 95% confidence interval, known as the limits of agreement. The different colours in the plot indicate the unique step lengths followed by participants. The difference between the two measures includes an error inherent in the stopwatch method (as it is based on a human pressing a button). However, the results of the Bland-Altman analysis indicate that there is a small difference (0.0549 m/s) between the two methods.

In order to assess the accuracy of our proposed method for gait speed estimation, it is essential to describe two common terms: minimal detectable change (MDC) and minimal clinically important change (MCIC). MDC, i.e., smallest detectable change or smallest real change, is defined as the smallest amount of change in the score detected by a method independent of measurement error [170]. In other words, MDC indicates the smallest change detected by a method that exceeds measurement

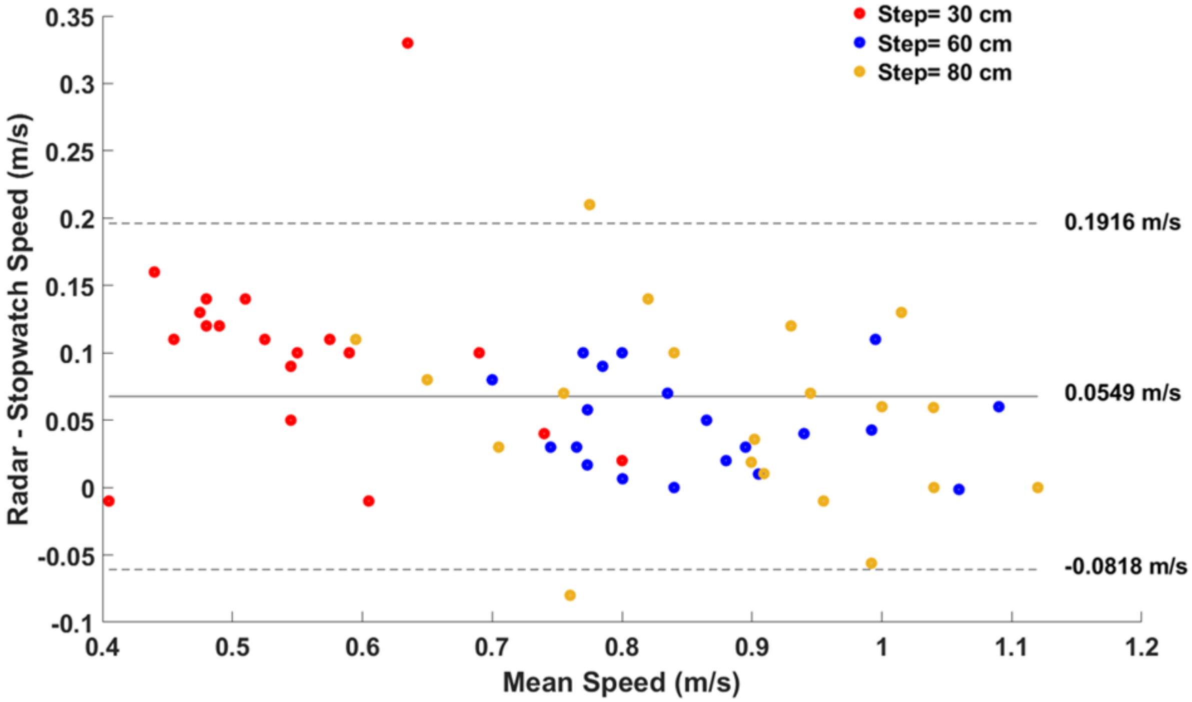

Figure 6.26. Repeated measures Bland-Altman plot comparing the walking speed calculated from the stopwatch and radar data. A given colour represents a unique step length. The solid and dashed horizontal lines represent the bias and 95% limits of agreement.

error. MDC is calculated as one-half the difference between the upper and lower agreement limits of the Bland–Altman plot, i.e., one-half of the Bland–Altman agreement width [170]. MCIC is the smallest change in the outcome measure considered important by investigators, clinicians, or other experts [170]. This value should be based on values reported in the literature or by experts and specified before conducting experiments. A proper method of measurement should have an MDC < MCIC.

A significant number of studies have been conducted to find MCID for changes in gait speed measurements for patients with various pathologies [115], [171]–[173]. The acceptable level of accuracy for walking speed varied depending on various factors, such as the patient population, the clinical condition being evaluated, and the purpose of the assessment.

The results of our study in Figure **6.26** shows that the MDC for gait speed estimation was determined to be 0.13 m/s, with [0.19 -0.08] as a confidence interval. This value was found to align with the MCID values reported in a systematic review [173], which showed that a change in comfortable gait speed between 0.1 m/s and 0.17 m/s could be considered clinically significant for different types of pathologies [173]. Previous studies also indicated that an improvement or decrease of 0.1 m/s is related to positive or negative health outcomes, respectively [171], [174], [175].

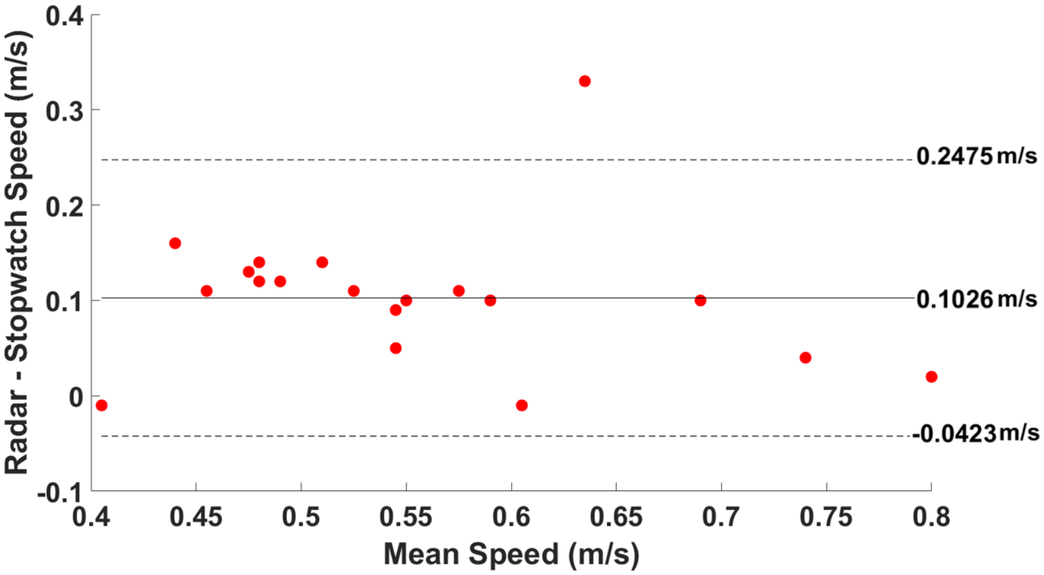

Figure 6.27. Repeated measures Bland-Altman plot comparing the walking speed calculated from the stopwatch and radar data for the case of step length of 30 cm. The solid and dashed horizontal lines represent the bias and 95% limits of agreement.

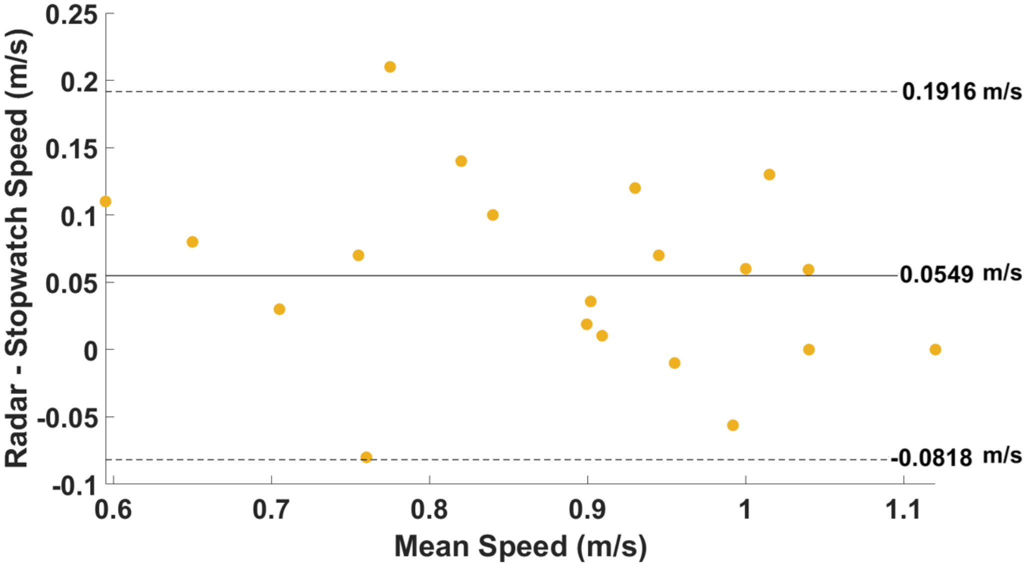

Figure 6.28. Repeated measures Bland-Altman plot comparing the walking speed calculated from the stopwatch and radar data for the case of step length of 80 cm. The solid and dashed horizontal lines represent the bias and 95% limits of agreement.

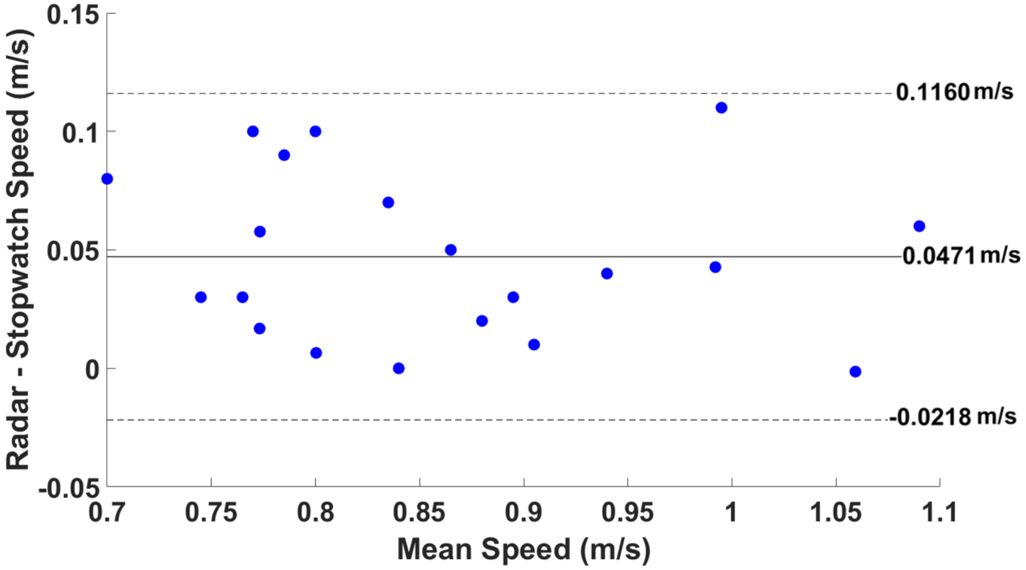

Figure 6.29. Repeated measures Bland-Altman plot comparing the walking speed calculated from the stopwatch and radar data for the case of step length of 60 cm. The solid and dashed horizontal lines represent the bias and 95% limits of agreement.

Further analysis was performed using the Bland-Altman method to evaluate the system's accuracy with varying step lengths. The results, presented in Figure **6.27**, indicate that the MDC for walking speed with a step length of 30 cm was determined to be 0.14 m/s, with a confidence interval of [0.24 - 0.04]. A separate analysis of the step length of 80 cm produced an MDC of 0.1367 m/s with a confidence interval of [0.19 - 0.08], as shown in Figure **6.28**. Furthermore, Figure **6.29** demonstrates that the MDC of 0.0689 m/s achieved from a step length of 60 cm is significantly better, being under the reported MCID range, with the whole confidence interval below the range. Therefore, the obtained MDC is in line with the reported MCID values, indicating a promising capability to identify a clinically meaningful change in walking speed. The results also showed that the MDC was significantly lower (as expected) when subjects walked in their normal walking patterns [176]. It should be pointed out that the results of the agreement analysis are in line with the ones obtained by [14], which used a lower-frequency RF sensor. Also, their algorithm was based on the fluctuation of the height of a walking subject to extract the average step length, while our method is based on the fluctuation of the torso’s velocity during the stance and swing phases. Our method is more reliable because the resolution of the radar might not be enough to detect all fluctuations in the height of a walking subject. Moreover, we integrated machine learning to identify walking periods while they proposed an iterative method to detect walking periods which is prone to failure under different conditions, for example, in a periodic motion while vacuuming the floor.

We also looked at errors that our algorithm made when estimating the step count in Figure **6.30**. To evaluate the performance of our algorithm in estimating the step count, we compared the estimated step count with the reference step count. The comparison results are provided in a box plot, where the y-axis represents the error in the step count compared to the reference step count. The box plot provides valuable information about the distribution of the error values, including the median (50th percentile), quartiles (25th and 75th percentiles), and outliers (minimum and maximum values). The median represents the center of the distribution and indicates the typical error value, while the quartiles give an idea of the spread of the error values. The minimum and maximum values show the presence of outliers and indicate the range of the error values.

When the reference step length was set to 30 cm, the median error in step count was found to be 2.5 steps. The maximum error was 10 steps, while the minimum error was 0 steps. The 50th percentile error in the step count when the reference step length was set to 60 cm was 1 step. The maximum error was 6 steps, and the minimum error was 0 steps. Similarly, for the step length of 80 cm, the median error was 0.5 steps, the maximum error was 4 steps, and the minimum error was 0 steps. These results indicate that the algorithm performs well in estimating the step count for reference step lengths of 60 cm and 80 cm, with a relatively low error, while the performance for the step length of 30 cm is relatively lower with a higher error.

Besides detecting the occurrence of steps or step counts, our algorithm also estimates the average step length. We compared the predicted step length to the reference values of 30 cm, 60 cm and 80 cm to evaluate its performance. Figure **6.31** presents the results in a box plot with the y-axis depicting the error in step length compared to the reference. For the error in step length of 30 cm, the median or the 50th percentile error was found to be 10 cm. The maximum error was 25 cm, while the minimum was 4 cm. For the error in step length with reference to 60 cm, the 50th percentile error was 4.5 cm. The maximum error was 19 cm, while the minimum error was 1 cm. Similarly, for the error in step length with reference to 80 cm, the 50th percentile error was 5 cm, the maximum error was 18 cm, and the minimum error was 0 cm. This indicates that the algorithm's performance was consistent, with the majority of errors being less than 5 cm and the maximum error being 18 cm.

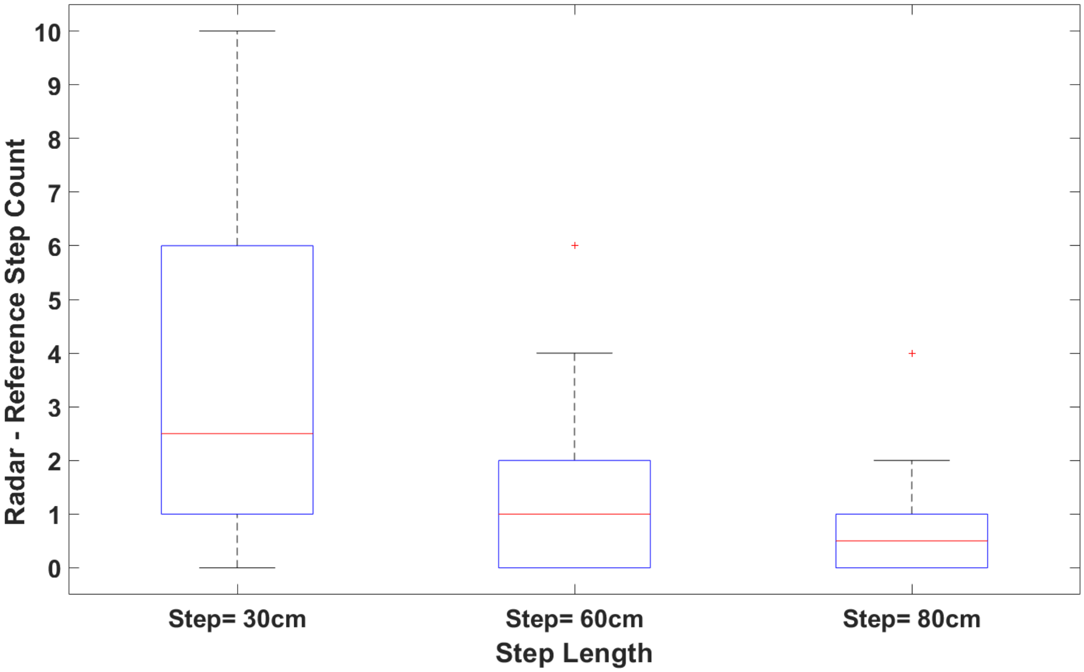

Figure 6.30. Comparison of step counts while the reference step length was set to 30 cm, 60 cm and 80 cm.

The results of our proposed gait extraction algorithm are highly promising, showcasing its effectiveness in accurately extracting gait parameters even in cluttered environments. The results indicate that the algorithm is capable of accurately capturing walking speed, step count and step length. The algorithm demonstrated minimal error in step count and acceptable error in walking speed and step length. However, the results suggest that the algorithm is sensitive to deviations from normal walking patterns, such as when the step length is set to 30 cm in this case. Despite this sensitivity, the algorithm's performance is still robust enough to accurately extract gait parameters in an in-home setting, where the walking path is not always a straight line. These results suggest that the proposed algorithm has the potential to make a significant impact in the field of gait analysis.

It should be mentioned that MCID values were not found in the literature to compare the MDC of the step length and step counts. However, in [177], the researchers compared the risk of death over the follow-up period among people who took fewer than 4,000, up to 8,000, or 12,000 or more steps a day. They also tested whether step intensity, measured by cadence, was associated with better health. It was shown that participants who took 8,000 steps per day had a 51% lower risk compared with those who took 4,000 per day. For general fitness, most adults should aim for 10,000 steps per day. This figure may rise or fall depending on age, current fitness level, and health goals [177]. However, in their study,

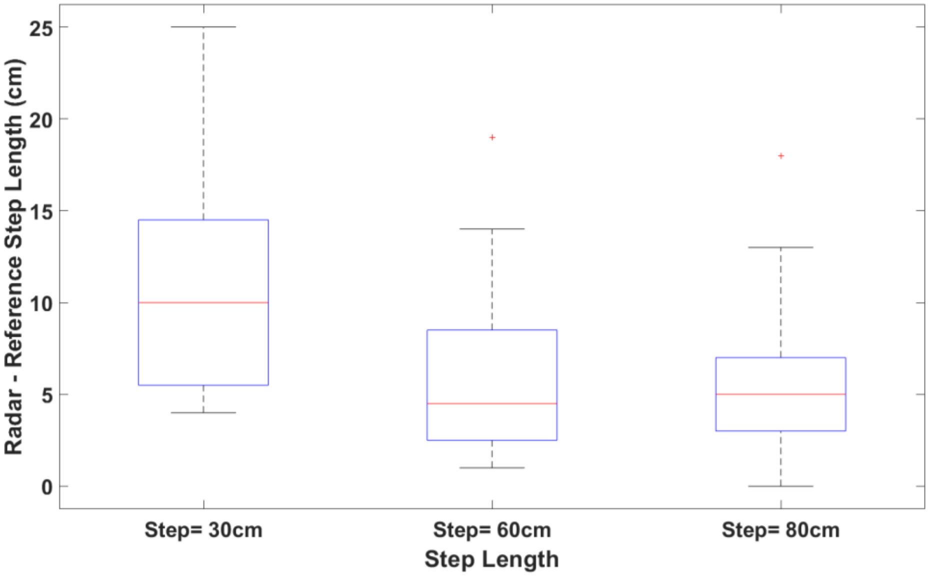

Figure 6.31. Comparison of step length while the reference step length was set to 30 cm, 60 cm and 80 cm.

step intensity did not seem to impact the mortality risk once the total number of steps per day was considered. Only an increased number of steps per day was associated with a reduced risk of death. Therefore, our proposed device could be used to flag a person's low number of steps taken over a day, especially for older adults. However, the cutpoints to send an alert should be determined by a specialist. Similarly, for step length, the value of change in step length to be flagged should be decided by a caregiver or a specialist.

As shown in this chapter, our proposed cloud-based AI-GM&AR system not only detects walking periods and captures gait values but also contains rich information about a subject's daily activity level, such as the time the subject started and stopped walking, the distance of walking, how long the subject was stationary, how long the subject was active during a day (all other movements in addition to walking), if the target left home, etc. Additionally, the proposed standalone AI-GM&AR system provides a record of the subject's activity level over time, washroom frequency and duration, and sleep/sedentary/active/out-of-home durations accessible in the designed business intelligence dashboard developed in Azure. These daily reports provide the level of activities of daily living used as an indicator of a subject's functional status [32]. The reports also could be used to collectively describe that the subject has the fundamental skills required to independently care for oneself [178].

It is important to note that the adequacy of the results for the intended use of in-home tracking and gauging walking speed from a clinical perspective depends on various factors such as the specific requirements of the application, the accuracy and precision needed, and the limitations of the sensor setup and data processing techniques used. While the results presented in the chapter demonstrate the potential of the proposed system to track walking parameters and recognize different activities in a home environment, further validation and testing would be necessary to establish the reliability and validity of the system for clinical applications. Additionally, it is important to consider the limitations of the sensor setup, such as the range and resolution of the radar sensor and potential sources of error in the data processing and analysis techniques used. Overall, while the results are promising, further research is needed to fully assess the suitability of the proposed system for clinical applications.

Despite the promising results of this study, there are several limitations that should be acknowledged. First, the dataset used in this study was collected in one environment and may not fully represent the complexities of real-world scenarios. Further testing in various real-world environments is necessary to validate the effectiveness of the proposed system. Second, the study only focused on a limited set of activities, and the proposed system may not be suitable for detecting other activities that are not included in the dataset. Additionally, the study only considered healthy individuals and may not generalize to individuals with different health conditions or mobility impairments. Finally, the proposed system relies on cloud computing, which may pose a risk to occupant safety if there is no connectivity to the cloud (especially for fall detection).

Despite these limitations, this study presented a promising approach for activity recognition and monitoring in home environments. The proposed system demonstrated high accuracy in detecting six common activities of daily living, which could have significant clinical applications in assessing and monitoring individuals' mobility and functional status. Furthermore, the system's ability to estimate walking speed and other parameters could provide valuable insights into an individual's gait patterns and help clinicians identify early signs of mobility decline.

In future work, the proposed system could be extended to include more activities and individuals with different health conditions. Additionally, the use of multiple sensors could improve the system's performance and enable the detection of more complex activities. Finally, the proposed system's reliance on cloud computing could be addressed by developing an offline mode or a local computing platform that ensures the system's reliability and safety even in the absence of internet connectivity.

Chapter 7

Conclusions

Technologies that detect changes in gait of older adults could support the detection, evaluation, and monitoring of parameters related to changes in mobility, cognition, and frailty, which could be used to support more effective biomedical applications. Before such systems are possible and technological developments can take place, we must be able to extract crucial gait parameters with high accuracy while maintaining ease of use for practical implementation. This thesis described the development of a low-cost mm-wave wave FMCW radar sensor that can measure walking parameters in a range of indoor environments. Since this approach uses noninvasive wireless technologies, people do not need to wear or carry a device on their body. Because there is no camera, feelings of privacy are more readily supported compared to video-based methods. Compared to other gait measurement technologies, such as GaitRite, radar technology is cost-effective and can be utilized in a home setting. In addition, there is no requirement for physician involvement, making radar-based gait monitoring a zero-effort technology.

7.1 Summary of Contributions

A fast and relatively easy-to-implement gait extraction algorithm was proposed to extract spatiotemporal gait values. The gait extraction algorithm was based on the fluctuation of the torso's movement during the stance and swing phase, as it is one of the critical factors impacted by other segments of body movements during walking cycles. The torso movement is not only precise, but it provides very distinctive information from which a straightforward peak detection algorithm can provide several gait values. Preliminary validation testing of the proposed system demonstrated that only one FMCW radar could be used to extract spatiotemporal gait parameters. It was shown that the torso's range bin could be easily obtained by isolating the maximum reflected signals in a clutter-free environment. However, the multipath signals might be stronger than the direct torso's signals in a cluttered environment. The challenges of gait assessment in a cluttered environment, such as a hallway lined with metal cabinets, were addressed. Two viable solutions were proposed to eliminate the multipath reflections: (1) radar antenna modification and (2) novel signal processing.

It was shown that an easy and low-cost method of radar antenna modification could focus the field of view of a commercially available radar board. The results suggest that a stand-alone gait assessment system could be achieved using an add-on hyperbola-based dielectric lens antenna and implementing the proposed gait extraction algorithm. The in-package lens antenna design supports relatively easy implementation with commercially available radars. Since the system is portable, relatively easy-to-use, and low-cost, it could be installed in a variety of living environments, including long-term care, hospitals, or individuals' homes, for day-to-day natural gait assessment in a way that requires no effort from the people being monitored.

The second method was a novel algorithm with a combination of radar signal processing and unsupervised machine learning to remove multipath effects that could be deployed for any radar type without the need for radar sensor alteration or modification. The proposed method used the MIMO features of an FMCW radar to find the range and azimuth heatmap of the environment along with the Doppler information of the walking subject. Preliminary validation testing of the system demonstrated unsupervised machine learning combined with the proposed tracking algorithm was able to track and monitor a walking subject in a cluttered environment such as a long hallway and extract spatiotemporal gait parameters. The relative simplicity and cost-effectiveness of this method make it a realistic approach to monitoring gait in real-world settings, including people's homes.

The MIMO FMCW radar was used for more complicated scenarios to address challenges in multiple people gait monitoring. In this thesis, we reported a MIMO radar-based sensor to monitor speed of participants' walking before and after BR that does not require any device to be worn on the body. A novel iterative framework based on unsupervised learning and advanced signal processing was proposed to analyze the reflected radio signals and extract walking movements and trajectories through a hallway. To achieve this, various advanced algorithms were developed to remove multipath effects or ghosts created due to the interaction between walking subjects and stationary objects, to identify and separate reflected signals of two subjects walking at a close distance from each other, and to track multiple subjects over time. The system functionality was assessed in a first-of-its-kind study conducted in Canada to identify how bedrest gives rise to physical deconditioning (i.e., Microgravity Research Analogue (MRA): Understanding the health impact of inactivity for the benefit of older adults and astronauts' initiative). In this study, the negative impact of 14-day HDBR on older adults' walking speed was shown. These measurements were analyzed to compute participants' gait speed and assess its changes before and after BR. The proposed method allows the extraction of walking speed in multiple closely-spaced subjects simultaneously, which is distinct from previous approaches in which speed of only one subject was obtained. The results show that BR promotes reductions in walking speed.

The same radar technology was then implemented for in-home applications. A cloud-based in-home activity recognition and walking period identification system was proposed that utilizes IoT-based mm-wave FMCW radar sensors and sequential deep learning to generate data streams of naturally occurring human activities within the home environment. By leveraging the abundance of continuous data, the proposed system was capable of accurately identifying the type of activity being performed by a subject. This system represented a significant advancement in the development of autonomous continuous human monitoring systems as it not only detects walking periods and recognizes the type of activity but also has the potential to report on the activity level of the subject (e.g., sedentary vs. active) and various other parameters such as washroom usage frequency and sleep duration.

To evaluate the performance of the proposed system, a dataset of millimeter-wave data was compiled from subjects performing various activities within their own homes, representing a unique and first-of-its-kind resource for this purpose. In contrast to existing datasets for human activity recognition and gait analysis that have been collected in constrained, artificially controlled environments and have focused on simple yet-realistic activities and straight-line walking periods, our dataset captured naturally occurring human activities in a familiar and commonly used living-space environment. Utilizing range-Doppler maps of a single subject performing various activities in their living environment as input, a deep GRU network was trained to classify in-home activities in the cloud. RDMs were considered as inputs for deep learning networks that resulted in more accurate outcomes compared with STFT inputs. This is because RDMs consist of time-varying information of both range and micro-Doppler, while STFT patterns only represent micro-Doppler features. Although the radar used in this study provides azimuth of the subject, azimuth information was not included as inputs for deep learning models. There were three reasons behind this: 1. The RDM method is fast and easy-to-implement that a Raspberry Pi can handle and generate. However, to calculate azimuth, a beamforming algorithm is a time-consuming process that is not fast enough for real-time application. 2. Adding more features would lead to more complex models; the execution prediction time of a complex model is longer than a simpler model. 3. RDMs provide enough features for our models to accurately predict new classes without needing more information. For real-time applications, simplicity and processing speed should be considered decisive and critical factors. Analyzing different deep learning models, GRU networks were found to be faster while obtaining a similar accuracy as other, more complex networks. Because of the complex structure of the LSTM and CNNLSTM networks, they contain many parameters and are slower comparatively.

For the more complex and comprehensive scenarios, although the system's accuracy slightly degrades for a new subject, it misidentified only a few non-walking samples as walking. Additionally, although micro-Doppler patterns depend on the radar sensor's relative angle with the subject, we showed that the GRU networks could overcome this issue. Regardless of the direction of walking or doing different activities, if the network is trained from the RDMs of various activities, it then predicts any new scenarios. Therefore, without any restriction, we can use the proposed system for a new subject. Moreover, a method of in-home gait extract was proposed to extract in-home spatiotemporal gait parameters. The preliminary results show that the radar can extract gait parameters while a subject walks in a non-straight line.

7.2 Impact of this Research

Although these results are preliminary (i.e., the small sample size in a constrained condition) and the 'ground truth' may have been flawed as it was recorded using a stopwatch, the results in this thesis suggest our radar system may be accurate enough to detect clinically meaningful changes. It is noted that findings in this thesis open new possibilities that could improve clinical practice across all people in addition to older adults. This work demonstrates the feasibility of continuously and passively monitoring activity at home. The monitoring device operates in the background, analyzing the reflection of radio signals without intervention from the subject being monitored. It could record activity levels, daily variations, and changes over time and could provide this information remotely to a professional caregiver in a timely manner. Thus, doctors and caregivers can achieve safe and frequent health monitoring without asking subjects to leave home or actively measure themselves and deliver more personalized care. Further research and development are needed to optimize the system's accuracy, reliability, and scalability in a real-world environment. This can be achieved by collecting more extensive and diverse datasets to train and validate the system and improving signal processing and machine learning algorithms to enhance the system's performance. In addition, the system's user interface and data visualization tools could be designed to be user-friendly, accessible, and understandable to both caregivers and residents. Finally, the system should undergo rigorous clinical validation and evaluation to demonstrate its effectiveness, safety, and usability in real-world settings.

The in-home gait monitoring system could be used as a tool to investigate behavioural symptoms and predict the risk of hospitalization. This technology might also have clinical utility for the assessment of individuals with Parkinson's Disease who have traditionally been underserved, including those who live in rural areas and those with difficulty leaving home due to limited mobility or cognitive impairment.

The major outcome of this research is an ambient assisted living system for monitoring people (especially older adults) at hospitals, long-term care facilities, and homes remotely. By leveraging the wealth of continuous sensing data, the system can detect variations in activity level and gait quality. This system is poised to be a significant achievement in the development of autonomous continuous patient monitoring systems. The system is safe, reliable, and affordable, which could reduce healthcare costs while also expanding medical services to hard-to-reach rural areas and increasing health equity across the underserved population. For example, for those who have less access to expensive gait assessment technologies, this system would provide day-to-day data on medical gait analysis, such as the detection of gait abnormalities.

Our work also has implications for other contexts beyond home environments, such as hospitals, rehabilitation centers, and long-term care facilities. The use of radar and machine learning could enable remote monitoring of patients and residents in these settings, allowing for more efficient use of resources and improved quality of care.

7.3 Limitations and Future Directions

The research presented in this thesis also has several limitations. The sample size for validation was small. Several walking tests were conducted in constrained conditions (e.g., participants were asked to step on a marked step). The 'ground truth' for walking speed may have lower accuracy as it was recorded using a stopwatch. To enhance the generalizability of our findings, it would be valuable to collect more diverse and extensive datasets that reflect a wider range of activities and living environments. Therefore, future works are needed to validate all the methods and results of gait parameters proposed in this thesis by more participants using a common standard measurement device such as GaitRite. In addition, it should be noted that most of the walking samples used in this thesis were collected in a controlled setting, which may not fully represent the complexities and challenges of real-world scenarios. Therefore, future work is needed to evaluate the system's performance in more diverse environments and with a larger and more diverse population, including those with various health conditions and mobility impairments. Furthermore, while our system shows promising results for gait analysis, it is not intended to replace clinical assessments or medical interventions. Rather, it could serve as a complementary tool to assist healthcare professionals in monitoring and assessing patients' functional status remotely and providing timely interventions when necessary.

Second, although the results presented in this thesis demonstrated the feasibility of using radar technology for in-home gait analysis, the testing was limited to fixed walking step lengths, which may not accurately reflect the variability in step lengths of individuals. To fully explore the capabilities of the radar and the proposed gait extraction algorithm, future work should include testing with a range of gait parameters, such as varying step lengths, stride lengths, stance/swing times etc. This will help to validate the algorithm's ability to capture gait spatiotemporal features in a dynamic and realistic scenario.

Third, all participants were healthy, which means that the generalizability of the results to populations with impaired gait patterns, such as older adults who walk slowly or have balance issues, remains uncertain. However, the main applications of this work would be for older adults who might not walk as fast as healthy people. Future research could explore the feasibility of using radar technology to track and analyze the gait patterns of people with impaired mobility, including those who have experienced falls or have difficulty walking. Such research could pave the way for the development of new technologies that use radar-based gait analysis to detect falls, gait freezing, and other gait impairments, potentially enhancing the safety and independence of older adults and others with mobility issues. Additionally, it would be valuable to investigate the various reasons for gait impairments and how they might affect radar-based gait analysis, as this could lead to the development of more accurate and personalized gait analysis systems for a wider range of individuals.

Fourth, although walking speed was captured for multiple-people scenarios and validated by several participants in the BR study, there are still several limitations to this study. In addition to the validation method, which might be flawed by the stopwatch, other gait spatiotemporal features were not obtained for multiple-people scenarios. Additionally, participants walked in a straight line. However, future works are needed to explore the radar capability in extracting other gait parameters as well as speed in a multiple-people scenario.

Fifth, the evaluation of the deep learning models was limited by the precision of the subject’s adherence to following the requested task and their self-reported label. Labelling was a challenging task. The label of each class could be affected by the subjects' activity at each frame, which could result in some flaws in the datasets. In this regard, future work could be done for in-home activity recognition where a camera recording is provided for a reliable labelling method. Moreover, different machine learning techniques and sensor modalities could be explored, such as incorporating wearable sensors or fusing data from multiple sensors.

Sixth, the in-home study was designed and tracked only one subject at a time, while in real-world scenarios, there could be multiple residents in a home. Therefore, future work should aim to implement multiple-person in-home activity recognition and gait monitoring systems to better reflect real-world situations.

Seventh, in this thesis, we focused on using a single radar with a single beam due to practical considerations such as cost and ease of implementation. But exploring the use of multiple radars or beams could be an interesting avenue for future research to improve the accuracy and robustness of the system.

Last, despite the promising results of using radar technology for in-home gait analysis, more extensive testing is needed to validate its clinical potential. The current study was performed in only two apartment buildings. Future work should aim to explore the capabilities of mm-wave-based human activity recognition and gait monitoring in various scenarios to determine its full potential as a clinical metric. Additionally, it would be beneficial to conduct longitudinal studies to evaluate the long-term performance of these systems in real-world settings.

In addition to improving the accuracy and robustness of the current system, one important direction for future work is the development of personalized activity recognition and gait analysis systems. This would involve adapting the system to individual differences in gait and activity patterns, such as variations in stride length, walking speed, and foot placement. By developing personalized models that can account for these differences, the system could improve its accuracy and provide more individualized insights into each person's gait and activity levels. One possible approach to developing personalized models is to incorporate additional sensor modalities, such as wearable sensors or cameras, which can capture more detailed information about gait and activity patterns. For example, wearable sensors can provide information about body position and orientation, while cameras can capture fine-grained details about walking style and foot placement. By fusing data from multiple sensors, it may be possible to develop more accurate and personalized models that can adapt to individual differences. Another approach is to explore the use of deep learning techniques, such as RNNs and CNNs, which are well-suited for learning complex temporal patterns in data. By training deep learning models on large datasets of gait and activity patterns, it may be possible to develop more accurate and personalized models that can capture subtle differences in gait and activity patterns. Overall, the development of personalized activity recognition and gait analysis systems has the potential to significantly improve the accuracy and usefulness of these systems, particularly in clinical settings where individual differences in gait and activity patterns are likely to be more pronounced.

Finally, it would be beneficial to conduct longitudinal studies to evaluate the long-term performance of these systems in real-world settings. This could involve deploying the system in a larger group of participants over an extended period and evaluating its accuracy, usability, and impact on health outcomes. Overall, while our work has made significant contributions to activity recognition and gait analysis in home environments, there is still much to be explored and optimized in this field.

7.4 Publications

The following provides a list of all the works published during the course of this thesis. These publications were either used directly in this thesis or aided in the development of the technology and served as reference materials.

Journal Articles

Under Preparation

1. Hajar Abedi, Eric Hedge, Carmelo Mastrandrea, Ahmad Ansariyan, Plinio P. Morita, Jennifer Boger, Alex Wong, Richard Hughson, and George Shaker “Non-Visual Contactless RF Sensor Shows 14-Day Head-Down Bedrest Promotes Reductions in Walking Speed”.
2. Hajar Abedi, Ahmad Ansariyan, Plinio P. Morita, Jennifer Boger, Alex Wong, and George Shaker “Contactless In-Home Cluttered Environments Gait Analysis”.
3. Mohammad Omid Bagheri, Hajar Abedi and George Shaker, “The Use of Dielectric Rod Superstrate for X-Band Radar Antenna Gain Improvement”.

Under Review

4. Hajar Abedi, Ala Eldin Omer, John Hanna, Steven Ding, Ahmad Ansariyan, Andrei Felipe Perez, Tom Paraschuk, Plinio P. Morita, Jennifer Boger, Alexander Wong, Safieddin Safavi-

Naeini, and George Shaker, “In-Package Integrated 3D-Printed Dielectric Lens for a Millimeter-Wave Radar,” *IEEE Transactions on Components, Packaging and Manufacturing Technology*.

Published/ Accepted

5. Hajar Abedi, Martin Ma, James He, Jennifer Yu, Ahmad Ansariyan and George Shaker, “Deep Learning-Based In-Cabin Monitoring and Vehicle Safety System Using a 4D Imaging Radar Sensor,” *IEEE Sensors Journal, 2023*.
6. Hajar Abedi, Ahmad Ansariyan, Plinio P. Morita, Jennifer Boger, Alex Wong, and George Shaker,” AI-Powered Non-Contact In-Home Gait Monitoring and Activity Recognition System Based on mm-Wave FMCW Radar and Cloud Computing,” *IEEE Internet of Things Journal*, 2023.
7. Hajar Abedi, Plinio P. Morita, Jennifer Boger, Alexander Wong, and George Shaker, “Hallway Gait Monitoring System Using an In-Package Integrated Dielectric Lens Paired with a mm-Wave Radar,” *Sensors–MDPI*, 2022.
8. Hajar Abedi, Plinio P. Morita, Jennifer Boger, Alexander Wong, and George Shaker, “Hallway Gait Monitoring Using Novel Radar Signal Processing and Unsupervised Learning,” *IEEE Sensors Journal*, 2022.
9. Hajar Abedi, Shenghang Luo, Vishvam Mazumdar, Michael MYR Riad, and George Shaker, “AI-Powered In-vehicle Passenger Monitoring using Low-Cost mm-Wave Radar”, *IEEE Access*, 2021.
10. Hajar Abedi, Clara Magnier, Vishvam Mazumdar and George Shaker, “Improving Passenger Safety in Cars Using Novel Radar Signal Processing,” *Engineering Reports*, 2021.
11. Hajar Abedi, George Shaker, Jennifer Boger, Plinio Morita and Alex Wong, “Use of Millimeter Wave FMCW Radar to Capture Gait Parameters,” *American Journal of Biomedical Science & Research*, 2019.

Conference Papers

1. Hajar Abedi, Ahmad Ansariyan, Plinio P. Morita, Jennifer Boger, Alexander Wong, and George Shaker, "Considerations for Antenna Design and Signal Processing in Radar-based Hallway Gait Monitoring", *International Symposium on Electromagnetic Theory (EMTS)*, 2023.

2. Hajar Abedi, Ahmad Ansariyan, Plinio P. Morita, Jennifer Boger, Alexander Wong, and George Shaker," In-Home Activity Monitoring Using Radars*", 8th Annual Conference on Vision and Intelligent Systems (CVIS 2022),* 2022.

3. Hajar Abedi, Ahmad Ansariyan, Christopher Lehman, Plinio P. Morita, Jennifer Boger, Alexander Wong, and George Shaker," Non-Visual and Contactless Wellness Monitoring for Long Term Care Facilities Using mm-Wave Radar Sensors" *IEEE Sensor Conference*, 2022.

4. Hajar Abedi and George Shaker, AI-Powered Radar Sensing for Non-Contact Health Monitoring, *Canadian Space Exploration Workshop*, 2022.

5. Hajar Abedi, Martin Ma, Jennifer Yu, James He, Ahmad Ansariyan, and George Shaker," On the Use of Machine Learning and Deep Learning for Radar- Based Passenger Monitoring" *IEEE International Symposium on Antennas and Propagation and USNC-URSI Radio Science Meeting*, 2022.

6. Hajar Abedi, Plinio P. Morita, Jennifer Boger, Alexander Wong, and George Shaker, "Unsupervised Learning for Hallway Gait Analysis using FMCW Radar," *IEEE International Symposium on Antennas and Propagation and USNC-URSI Radio Science Meeting (APS-URSI),* 2022.

7. Mohammad Omid Bagheri, Hajar Abedi, and George Shaker, "Radar Antenna Gain Improvement Using an Integrated In-Package Dielectric Rod Superstrate," *IEEE International Symposium on Antennas and Propagation and USNC-URSI Radio Science Meeting (APS-URSI)*, 2021.

8. Hajar Abedi, Plinio P. Morita, Jennifer Boger, Alexander Wong, and George Shaker, "In-Package Integrated Dielectric Lens Paired with a MIMO mm-Wave Radar for Corridor Gait Monitoring," *IEEE International Symposium on Antennas and Propagation and USNC-URSI Radio Science Meeting (APS-URSI)*, 2021.

9. Hajar Abedi, Ahmad Ansariyan, Plinio P. Morita, Jennifer Boger, Alexander Wong, and George Shaker, "Sequential Deep Learning for In-Home Activity Monitoring Using mm-Wave FMCW

Radar," IEEE International Symposium on Antennas and Propagation and USNC-URSI Radio Science Meeting *(APS-URSI)*, 2021.

10. Mohammad Omid Bagheri, Hajar Abedi, and George Shaker, "Radar Antenna Gain Improvement Using 3D Printed Dielectric Lens and Metamaterial-Inspired Superstrates," *International Symposium on Antenna Technology and Applied Electromagnetics* (*ANTEM)*, 2021.
11. Hajar Abedi, Clara Magnier, and George Shaker "Passenger Counting and Safety Improvement Using an AI-Powered Radar Technology," *International Symposium on Antenna Technology and Applied Electromagnetics* (*ANTEM)*, 2021.
12. Hajar Abedi, George Shaker, Jennifer Boger, Alexander Wong, and Plinio P. Morita, "Autonomous Human Monitoring and Activity Recognition for Safety and Health Improvement," *HFES International Symposium on Human Factors and Ergonomics in Health Care*, 2021.
13. Hajar Abedi and George Shaker, "Low-Cost 3D printed Dielectric Hyperbolic Lens Antenna for Beam Focusing and Steering of a 79 GHz MIMO Radar", *IEEE International Symposium on Antennas and Propagation and USNC-URSI Radio Science Meeting (APS-URSI)*, 2020.
14. Hajar Abedi, Shenghang Luo and George Shaker, "On the Use of Low-Cost Radars and Machine Learning for In-Vehicle Passenger Monitoring," *EEE 20th Topical Meeting on Silicon Monolithic Integrated Circuits in RF Systems (SiRF)*, 2020.
15. Hajar Abedi, Clara Magnier, Jennifer Boger, Plinio P. Morita, Alexander Wong, George Shaker, "Integration of Random Forests and MM-Wave FMCW Radar Technology for Gait Recognition," *6th Annual Conference on Vision and Intelligent Systems (CVIS 2019)*, 2019.
16. Chia Xujie Xavier, Hajar Abedi, Jennifer Boger, Plinio P. Morita, Alexander Wong, George Shaker, "2D-Multiple Signal Processing Approach to Human Orientation Monitoring Using Millimeter-wave FMCW Radar", *6th Annual Conference on Vision and Intelligent Systems (CVIS 2019)*, 2019.
17. Hajar Abedi, Shenghang Luo, Steven Ding, Clara Magnier, Michael Bacani, George Shaker "On the Use of Low-Cost Radars and Machine Learning for In-Vehicle Passenger Detection," *6th Annual Conference on Vision and Intelligent Systems (CVIS 2019),* 2019.
18. Mostafa Alizadeh, Hajar Abedi and George Shaker, "Low-Cost Low-Power In-Vehicle Occupant Detection with mm-wave FMCW Radar", *IEEE Sensor Conference,* 2019.

19. Hajar Abedi, George Shaker, Plinio P. Morita, Alex Wong, and Jennifer Boger, “Use of High-Frequency Radar to Capture Parameters of Gait”, *AGE-WELL’s 5th Annual Conference*, 2019.
20. Hajar Abedi, George Shaker, Plinio P. Morita, Alex Wong, and Jennifer Boger, “The use of radar in a smart bed for detecting gait-related physiological parameters”, *Symposium on Aging Research (SoAR)* 2019.

Patent

1. George Shaker, Mostafa Alizadeh, Safieddin Safavi-Naeini, Hajar Abedi, Xavier Chia, “System and Method for Sensing with Millimeter Waves for Sleep Position Detection, Vital Signs Monitoring and/or Driver Detection”, US Patent App. 17/139,212.

References

[1] J. Perry and J. M. Burnfield "Gait Analysis: Normal and Pathological Function." *Journal of Sports Science & Medicine*, vol.9, no. 2, 2010

[2] A. Middleton, S. L. Fritz, and M. Lusardi, "Walking Speed: The functional Vital Sign," *Journal of Aging and Physical Activity*, vol. 23, no. 2, pp. 314–322, 2015, doi: 10.1123/japa.2013-0236.

[3] H. Abedi, J. Boger, P. P. Morita, A. Wong, and G. Shaker, "Hallway Gait Monitoring Using Novel Radar Signal Processing and Unsupervised Learning," *IEEE Sensors Journal*, pp. 1–1, 2022, doi: 10.1109/JSEN.2022.3184188.

[4] N. M. Peel, S. S. Kuys, and K. Klein, "Gait Speed as a Measure in Geriatric Assessment in Clinical Settings: A Systematic Review," *Journals of Gerontology - Series A Biological Sciences and Medical Sciences*, vol. 68, no. 1, pp. 39–46, 2013, doi: 10.1093/gerona/gls174.

[5] H. Abedi, A. Ansariyan, P. P. Morita, J. Boger, A. Wong, and G. Shaker, "Sequential Deep Learning for In-Home Activity Monitoring Using mm-Wave FMCW Radar," *2021 IEEE International Symposium on Antennas and Propagation and North American Radio Science Meeting, APS/URSI 2021 - Proceedings*, pp. 1499–1500, 2021, doi: 10.1109/APS/URSI47566.2021.9704291.

[6] A. K. Seifert, M. Grimmer, and A. M. Zoubir, "Doppler Radar for the Extraction of Biomechanical Parameters in Gait Analysis," *IEEE Journal of Biomedical and Health Informatics*, vol. 25, no. 2, pp. 547–558, Feb. 2021, doi: 10.1109/JBHI.2020.2994471.

[7] A. L. McDonough, M. Batavia, F. C. Chen, S. Kwon, and J. Ziai, "The Validity and Reliability of the GAITRite System's Measurements: A Preliminary Evaluation," *Archives of Physical Medicine and Rehabilitation*, vol. 82, no. 3, pp. 419–425, 2001, doi: 10.1053/apmr.2001.19778.

[8] A. Muro-de-la-Herran, B. García-Zapirain, and A. Méndez-Zorrilla, "Gait Analysis Methods: An Overview of Wearable and Non-Wearable Systems, Highlighting Clinical Applications," *Sensors (Switzerland)*, vol. 14, no. 2, pp. 3362–3394, 2014, doi: 10.3390/s140203362.

[9] A. K. Welmer, D. Rizzuto, C. Qiu, B. Caracciolo, and E. J. Laukka, "Walking Speed, Processing Speed, and Dementia: A Population-Based Longitudinal Study," *Journals of Gerontology -*

Series A Biological Sciences and Medical Sciences, vol. 69, no. 12, pp. 1503–1510, 2014, doi: 10.1093/gerona/glu047.

[10] A. M. Sabatini, C. Martelloni, S. Scapellato, and F. Cavallo, "Assessment of Walking Features from Foot Inertial Sensing," *IEEE Transactions on Biomedical Engineering*, vol. 52, no. 3, pp. 486–494, Mar. 2005, doi: 10.1109/TBME.2004.840727.

[11] J. Verghese, C. Wang, R. B. Lipton, R. Holtzer, and X. Xue, "Quantitative Gait Dysfunction and Risk of Cognitive Decline and Dementia," *Journal of Neurology, Neurosurgery and Psychiatry*, vol. 78, no. 9, pp. 929–935, 2007, doi: 10.1136/jnnp.2006.106914.

[12] A. Alfaro-Acha, S. al Snih, M. A. Raji, K. S. Markides, and K. J. Ottenbacher, "Does 8-foot Walk Time Predict Cognitive Decline in Older Mexicans Americans?," *Journal of the American Geriatrics Society*, vol. 55, no. 2, pp. 245–251, 2007, doi: 10.1111/j.1532-5415.2007.01039.x.

[13] G. A. van Kan *et al.*, "Gait Speed, Body Composition, and Dementia. The EPIDOS-Toulouse Cohort," *Journals of Gerontology - Series A Biological Sciences and Medical Sciences*, vol. 67 A, no. 4, pp. 425–432, 2012, doi: 10.1093/gerona/glr177.

[14] C. Y. Hsu, Y. Liu, Z. Kabelac, R. Hristov, D. Katabi, and C. Liu, "Extracting gait Velocity and Stride Length from Surrounding Radio Signals," *Conference on Human Factors in Computing Systems - Proceedings*, vol. 2017-May, pp. 2116–2126, 2017, doi: 10.1145/3025453.3025937.

[15] R. Schniepp *et al.*, "Increased Gait Variability Is Associated with the History of Falls in Patients with Cerebellar Ataxia," *Journal of Neurology*, vol. 261, no. 1, pp. 213–223, 2014, doi: 10.1007/s00415-013-7189-3.

[16] M. L. Callisaya *et al.*, "Gait, Gait Variability and the Risk of Multiple Incident Falls in Older People: A Population-Based Study," *Age and Ageing*, vol. 40, no. 4, pp. 481–487, 2011, doi: 10.1093/ageing/afr055.

[17] R. A. Hackett, H. Davies-Kershaw, D. Cadar, M. Orrell, and A. Steptoe, "Walking Speed, Cognitive Function, and Dementia Risk in the English Longitudinal Study of Ageing," *Journal of the American Geriatrics Society*, vol. 66, no. 9, pp. 1670–1675, 2018, doi: 10.1111/jgs.15312.

[18] K. E. Webster, J. E. Wittwer, and J. A. Feller, "Validity of the GAITRite® walkway System for the Measurement of Averaged and Individual Step Parameters of Gait," *Gait & Posture*, vol. 22, no. 4, pp. 317–321, Dec. 2005, doi: 10.1016/j.gaitpost.2004.10.005.

[19] A. Pfister, A. M. West, S. Bronner, and J. A. Noah, "Comparative Abilities of Microsoft Kinect and Vicon 3D Motion Capture for Gait Analysis," *Journal of Medical Engineering & Technology*, vol. 38, no. 5, pp. 274–280, 2014, doi: 10.3109/03091902.2014.909540.

[20] B. G. Contini *et al.*, "A Wearable Gait Analysis Protocol to Support the Choice of the Appropriate Ankle-Foot Orthosis: A Comparative Assessment in Children with Cerebral Palsy," *Clinical Biomechanics*, vol. 70, no. October 2018, pp. 177–185, 2019, doi: 10.1016/j.clinbiomech.2019.08.009.

[21] "Physilog® | Inertial Measurement Sensor (IMU)." Accessed: Feb. 15, 2022. [Online]. Available: https://research.gaitup.com/physilog/.

[22] S. Z. Gurbuz, C. Clemente, A. Balleri, and J. J. Soraghan, "Micro-Doppler-based In-Home Aided and Unaided Walking Recognition with Multiple Radar and Sonar Systems," *IET Radar, Sonar and Navigation*, vol. 11, no. 1, pp. 107–115, 2017, doi: 10.1049/iet-rsn.2016.0055.

[23] X. Ma, R. Zhao, X. Liu, H. Kuang, and M. A. A. Al-Qaness, "Classification of Human Motions Using Micro-Doppler Radar in the Environments with Micro-Motion Interference," *Sensors (Switzerland)*, vol. 19, no. 11, 2019, doi: 10.3390/s19112598.

[24] D. Tahmoush and J. Silvious, "Gait Variations in Human Micro-Doppler," *International Journal of Electronics and Telecommunications*, vol. 57, no. 1, pp. 23–28, 2011, doi: 10.2478/v10177-011-0003-1.

[25] A. K. Seifert, M. G. Amin, and A. M. Zoubir, "Toward Unobtrusive In-Home Gait Analysis Based on Radar Micro-Doppler Signatures," *IEEE Transactions on Biomedical Engineering*, vol. 66, no. 9, pp. 2629–2640, Sep. 2019, doi: 10.1109/TBME.2019.2893528.

[26] K. Saho, K. Uemura, K. Sugano, and M. Matsumoto, "Using Micro-Doppler Radar to Measure Gait Features Associated with Cognitive Functions in Elderly Adults," *IEEE Access*, vol. 7, pp. 24122–24131, 2019, doi: 10.1109/ACCESS.2019.2900303.

[27] Y. Kim, I. Alnujaim, and D. Oh, "Human Activity Classification Based on Point Clouds Measured by Millimeter Wave MIMO Radar with Deep Recurrent Neural Networks," *IEEE Sensors Journal*, vol. 21, no. 12, 2021, doi: 10.1109/JSEN.2021.3068388.

[28] H. Abedi, C. Magnier, J. Boger, and A. Wong, “Integration of Random Forests and MM-Wave FMCW Radar Technology for Gait Recognition,” *Journal of Computational Vision and Imaging Systems*, vol. 5, no. 1, pp. 2–2, 2019, doi: 10.1109/bhi.2018.8333371.

[29] H. Abedi, G. Shaker, J. Boger, P. Morita, and A. Wong, “Use of Millimeter Wave FMCW Radar to Capture Gait Parameters,” *American Journal of Biomedical Science and Research*, no. 2, pp. 2019–2025, doi: 10.34297/AJBSR.2019.06.001009.

[30] H. Abedi, A. Ansariyan, P. P. Morita, A. Wong, J. Boger, and G. Shaker, “AI-Powered Non-Contact In-Home Gait Monitoring and Activity Recognition System Based on mm-Wave FMCW Radar and Cloud Computing,” *IEEE Internet of Things Journal*, 2023. doi: 10.1109/JIOT.2023.3235268.

[31] “Semiconductor & System Solutions - Infineon Technologies.” Accessed: Aug. 10, 2022. [Online]. Available: https://www.infineon.com/.

[32] H. Abedi, M. Ma, J. Yu, J. He, A. Ansariyan, and G. Shaker, “On the Use of Machine Learning and Deep Learning for Radar- Based Passenger Monitoring,” *2022 IEEE International Symposium on Antennas and Propagation and USNC-URSI Radio Science Meeting (AP-S/URSI)*, pp. 902–903, Sep. 2022, doi: 10.1109/AP-S/USNC-URSI47032.2022.9887034.

[33] “AWR1443, AWR1243 Evaluation Module (AWR1443BOOST, AWR1243BOOST) mmWave Sensing Solution User’s Guide,” 2017, Accessed: Jan. 05, 2023. [Online]. Available: www.ti.com.

[34] H. Abedi *et al.*, “Non-Visual and Contactless Wellness Monitoring for Long Term Care Facilities Using mm-Wave Radar Sensors,” *2022 IEEE Sensors*, pp. 1–4, Oct. 2022, doi: 10.1109/SENSORS52175.2022.9967327.

[35] D. Jarchi, J. Pope, T. K. M. Lee, L. Tamjidi, A. Mirzaei, and S. Sanei, “A Review on Accelerometry-Based Gait Analysis and Emerging Clinical Applications,” *IEEE Reviews in Biomedical Engineering*, vol. 11, pp. 177–194, 2018, doi: 10.1109/RBME.2018.2807182.

[36] G. A. Borelli, “On the Movement of Animals”, Springer-Verlag, 1989, doi: 10.1007/978-3-642-73812-8.

[37] W. Braune and O. (Otto) Fischer, “The Human Gait,” Springer-Verlag, 1987.

[38] R. Baker, “The history of Gait Analysis Before the Advent of Modern Computers,” *Gait & Posture*, vol. 26, no. 3, pp. 331–342, 2007, doi: 10.1016/j.gaitpost.2006.10.014.

[39] M. Nirenberg, W. Vernon, and I. Birch, “A Review of the Historical Use and Criticisms of Gait Analysis Evidence,” *Science and Justice*, vol. 58, no. 4, pp. 292–298, Jul. 2018, doi: 10.1016/j.scijus.2018.03.002.

[40] D. H. Sutherland, “The Evolution of Clinical Gait Analysis Part 1: Kinesiological EMG,” *Gait & Posture*, vol. 14, no. 1, pp. 61–70, 2001, doi: 10.1016/S0966-6362(01)00100-X.

[41] S. T. Pheasant, “A Review of: ‘Human Walking”, by V. T. Inman, H.J. Ralston, and F. Todd,” Ergonomics, vol. 24, no. 12, pp. 969–976, 1981, doi: 10.1080/00140138108924919.

[42] D. H. Sutherland, “The Evolution of Clinical Gait Analysis Part III - Kinetics and energy assessment,” *Gait & Posture*, vol. 21, no. 4, pp. 447–461, 2005, doi: 10.1016/j.gaitpost.2004.07.008.

[43] D. H. Sutherland, “The Evolution of Clinical Gait Analysis: Part II kinematics,” *Gait & Posture*, vol. 16, no. 2, pp. 159–179, 2002, doi: 10.1016/S0966-6362(02)00004-8.

[44] A. K. Seifert *et al.*, “Gait Analysis using Smartwatches,” *Gait & Posture*, vol. 12, no. 1, pp. 2434–2443, 2019, doi: 10.1109/PIMRCW.2019.8880821.

[45] J. E. Graham, G. v. Ostir, S. R. Fisher, and K. J. Ottenbacher, “Assessing Walking Speed in Clinical Research: A Systematic Review,” *Journal of Evaluation in Clinical Practice,* vol. 14, no. 4, pp. 552–562, 2008, doi: 10.1111/j.1365-2753.2007.00917.x.

[46] T. Buracchio, H. H. Dodge, D. Howieson, D. Wasserman, and J. Kaye, “The Trajectory of Gait Speed Preceding Mild Cognitive Impairment,” *Archives of Neurology*, vol. 67, no. 8, pp. 980–986, 2010, doi: 10.1001/archneurol.2010.159.

[47] M. A. Chen, “Frailty and Cardiovascular Disease: Potential Role of Gait Speed in Surgical Risk Stratification in Older Adults,” *Journal of Geriatric Cardiology*, vol. 12, no. 1, pp. 44–56, 2015, doi: 10.11909/j.issn.1671-5411.2015.01.006.

[48] M. Cesari *et al.*, “Prognostic Value of Usual Gait Speed in Well-Functioning Older People - Results from the Health, Aging and Body Composition Study,” *Journal of the American Geriatrics Society*, vol. 53, no. 10, pp. 1675–1680, 2005, doi: 10.1111/j.1532-5415.2005.53501.x.

[49] O. Beauchet *et al.*, "Guidelines for Assessment of Gait and Reference Values for Spatiotemporal Gait Parameters in Older Adults: The Biomathics and Canadian Gait Consortiums Initiative," *Frontiers in Human Neuroscience*, vol. 11, p. 353, Aug. 2017, doi: 10.3389/FNHUM.2017.00353/BIBTEX.

[50] B. Bilney, M. Morris, and K. Webster, "Concurrent Related Validity of the GAITRite® Walkway System for Quantification of the Spatial and Temporal Parameters of Gait," *Gait & Posture*, vol. 17, no. 1, pp. 68–74, Feb. 2003, doi: 10.1016/S0966-6362(02)00053-X.

[51] F. Yang, D. Espy, T. Bhatt, and Y. C. Pai, "Two Types of Slip-Induced Falls Among Community Dwelling Older Adults," *Journal of Biomechanics*, vol. 45, no. 7, pp. 1259–1264, 2012, doi: 10.1016/j.jbiomech.2012.01.036.

[52] A. Boroomand, G. Shaker, P. P. Morita, A. Wong, and J. Boger, "Autonomous Gait Speed Estimation Using 24 GHz FMCW Radar Technology," *2018 IEEE EMBS International Conference on Biomedical and Health Informatics, BHI 2018*, vol. 2018-Janua, no. March, pp. 66–69, 2018, doi: 10.1109/BHI.2018.8333371.

[53] H. Abedi, J. Boger, P. P. Morita, A. Wong, and G. Shaker, "Hallway Gait Monitoring System Using an In-Package Integrated Dielectric Lens Paired with a mm-Wave Radar," *Sensors 2023, Vol. 23, Page 71*, vol. 23, no. 1, p. 71, Dec. 2022, doi: 10.3390/S23010071.

[54] J. L. Geisheimer, W. S. Marshall, and E. Greneker, "A Continuous-Wave (CW) Radar for Gait Analysis," *Conference Record of the Asilomar Conference on Signals, Systems and Computers*, vol. 1, pp. 834–838, 2001, doi: 10.1109/acssc.2001.987041.

[55] B. Lau, S. Haider, A. Boroomand, G. Shaker, J. Boger, and P. Morita, "Gait Speed Tracking System using UWB Radar," *IET Conference Publications*, vol. 2018, no. CP741, pp. 4–7, 2018, doi: 10.1049/cp.2018.1258.

[56] J. L. Geisheimer, E. F. Greneker, and W. S. Marshall, "A High-Resolution Doppler Model of Human Gait," *International Society for Optics and Photonics, AeroSense 2002*, vol. 4744, no. 2002, pp. 8–18.

[57] M. Otero, "Application of a Continuous Wave Radar for Human Gait Recognition," *Signal Processing, Sensor Fusion, and Target Recognition XIV*, vol. 5809, no. May, p. 538, 2005, doi: 10.1117/12.607176.

[58] M. G. Anderson and R. L. Rogers, “Micro-Doppler Analysis of Multiple Frequency Continuous Wave Radar Signatures,” *Radar Sensor Technology XI*, vol. 6547, no. May 2007, p. 65470A, 2007, doi: 10.1117/12.719800.

[59] C. Hornsteiner and J. Detlefsen, “Characterisation of Human Gait Using a Continuous-Wave Radar at 24 GHz,” *Advances in Radio Science*, vol. 6, no. B.2, pp. 67–70, May 2008, doi: 10.5194/ARS-6-67-2008.

[60] D. Tahmoush and J. Silvious, “Radar Micro-Doppler for Long Range Front-View Gait Recognition,” *IEEE 3rd International Conference on Biometrics: Theory, Applications and Systems, BTAS 2009*, 2009, doi: 10.1109/BTAS.2009.5339049.

[61] 2-D median filtering - MATLAB medfilt2 – MathWorks, [Online]. Available: https://www.mathworks.com/help/images/ref/medfilt2.html

[62] D. Tahmoush and J. Silvious, “Stride Rate in Radar Micro-Doppler Images,” *Proceedings of IEEE International Conference on Systems, Man and Cybernetics*, no. October, pp. 4218–4223, 2009, doi: 10.1109/ICSMC.2009.5346830.

[63] M. R. D. Rodrigues and Y. C. Eldar, “Information-Theoretic Methods in Data Science”, 1st Edition, Cambridge University Press, 2020.

[64] J. Zhang, “Basic Gait Analysis Based on Continuous Wave Radar,” *Gait & Posture*, vol. 36, no. 4, pp. 667–671, 2012, doi: 10.1016/j.gaitpost.2012.04.020.

[65] B. Godana, G. Leus, and A. Barroso, “Estimating Indoor Walking Velocity Profile using a Software Radio-Based Radar,” *Proceedings - 1st International Conference on Sensor Device Technologies and Applications, 2010*, pp. 44–51, 2010, doi: 10.1109/SENSORDEVICES.2010.16.

[66] Merrill I. Skolnik, “Introduction to Radar Systems Second Edition.” 3rd Edition, McGraw-Hill, 2001.

[67] T. Yardibi *et al.*, “Gait Characterization via Pulse-Doppler Radar,” *2011 IEEE International Conference on Pervasive Computing and Communications Workshops, PERCOM Workshops 2011*, pp. 662–667, 2011, doi: 10.1109/PERCOMW.2011.5766971.

[68] P. E. Cuddihy *et al.*, "Radar Walking Speed Measurements of Seniors in Their Apartments: Technology for Fall Prevention," *Proceedings of the Annual International Conference of the IEEE Engineering in Medicine and Biology Society, EMBS*, pp. 260–263, 2012, doi: 10.1109/EMBC.2012.6345919.

[69] F. Wang, M. Skubic, M. Rantz, and P. E. Cuddihy, "Quantitative Gait Measurement with Pulse-Doppler Radar for Passive In-Home Gait Assessment," *IEEE Transactions on Biomedical Engineering*, vol. 61, no. 9, pp. 2434–2443, 2014, doi: 10.1109/TBME.2014.2319333.

[70] A. G. Stove, "Linear FMCW Radar Techniques," *IEE Proceedings, Part F: Radar and Signal Processing*, vol. 139, no. 5, pp. 343–350, 1992, doi: 10.1049/IP-F-2.1992.0048/CITE/REFWORKS.

[71] S. Rao, "Introduction to mm-wave Sensing: FMCW Radars," *Course*, 2017, [Online]. Available: https://training.ti.com/sites/default/files/docs/mmwaveSensing-FMCW-offlineviewing_3.pdf.

[72] H. Abedi, S. Luo, V. Mazumdar, and G. Shaker, "AI-Powered In-Vehicle Passenger Monitoring using Low-Cost mm-Wave Radar," *IEEE Access*, pp. 1–1, 2021, doi: 10.1109/ACCESS.2021.3138051.

[73] H. Abedi, C. Magnier, V. Mazumdar, and G. Shaker, "Improving Passenger Safety in Cars Using Novel Radar Signal Processing," *Engineering Reports*, May 2021, doi: 10.1002/eng2.12413.

[74] R. J. Javier and Y. Kim, "Application of Linear Predictive Coding for Human Activity Classification Based on Micro-Doppler Signatures," *IEEE Geoscience and Remote Sensing Letters*, vol. 11, no. 10, pp. 1831–1834, 2014, doi: 10.1109/LGRS.2014.2311819.

[75] D. Avrahami, M. Patel, Y. Yamaura, and S. Kratz, "Below the Surface: Unobtrusive Activity Recognition for Work Surfaces Using RF-Radar Sensing," *International Conference on Intelligent User Interfaces, Proceedings IUI*, pp. 439–451, 2018, doi: 10.1145/3172944.3172962.

[76] M. T. Mitchell, Machine Learning, Burr Ridge, IL, USA: McGraw Hill, vol. 45, 1997.

[77] D. P. Fairchild and R. M. Narayanan, "Classification of Human Motions Using Empirical Mode Decomposition of Human Micro-Doppler Signatures," *IET Radar, Sonar & Navigation*, vol. 8, no. 5, pp. 425–434, Jun. 2014, doi: 10.1049/IET-RSN.2013.0165.

[78] Y. Kim and T. Moon, "Human Detection and Activity Classification based on Micro-Doppler Signatures Using Deep Convolutional Neural Networks," *IEEE Geoscience and Remote Sensing Letters*, vol. 13, no. 1, pp. 8–12, Jan. 2016, doi: 10.1109/LGRS.2015.2491329.

[79] X. Li, Y. He, and X. Jing, "A Survey of Deep Learning-Based Human Activity Recognition in Radar," *Remote Sensing (Basel)*, vol. 11, no. 9, 2019, doi: 10.3390/rs11091068.

[80] P. Addabbo, M. L. Bernardi, F. Biondi, M. Cimitile, C. Clemente, and D. Orlando, "Temporal Convolutional Neural Networks for Radar Micro-Doppler Based Gait Recognition†," *Sensors (Switzerland)*, vol. 21, no. 2, pp. 1–15, 2021, doi: 10.3390/s21020381.

[81] F. Quaiyum, N. Tran, J. E. Piou, O. Kilic, and A. E. Fathy, "Noncontact Human Gait Analysis and Limb Joint Tracking Using Doppler Radar," *IEEE Journal of Electromagnetics, RF and Microwaves in Medicine and Biology*, vol. 3, no. 1, pp. 61–70, 2019, doi: 10.1109/JERM.2018.2881238.

[82] A. N. Aicha, G. Englebienne, and B. Kröse, "Continuous Measuring of the Indoor Walking Speed of Older Adults Living Alone," *Journal of Ambient Intelligence and Humanized Computing*, vol. 9, no. 3, pp. 589–599, 2018, doi: 10.1007/s12652-017-0456-x.

[83] "AWR1443 data sheet, product information and support | [Online]. Available: TI.com." https://www.ti.com/product/AWR1443 (accessed Aug. 12, 2021).

[84] "DCA1000EVM Evaluation board | [Online]. Available: TI.com." https://www.ti.com/tool/DCA1000EVM (accessed Aug. 16, 2021).

[85] H. Abedi and G. Shaker, "Low-Cost 3D printed Dielectric Hyperbolic Lens Antenna for Beam Focusing and Steering of a 79 GHz MIMO Radar," *2020 IEEE International Symposium on Antennas and Propagation and North American Radio Science Meeting, IEEECONF 2020 - Proceedings*, pp. 1543–1544, Jul. 2020, doi: 10.1109/IEEECONF35879.2020.9329969.

[86] H. Abedi, C. Magnier, and G. Shaker, "Passenger Monitoring Using AI-Powered Radar," *2021 IEEE 19th International Symposium on Antenna Technology and Applied Electromagnetics, ANTEM 2021*, Aug. 2021, doi: 10.1109/ANTEM51107.2021.9518503.

[87] M. Alizadeh, H. Abedi, and G. Shaker, “Low-Cost Low-Power In-Vehicle Occupant Detection with mm-Wave FMCW Radar,” *Proceedings of IEEE Sensors*, vol. 2019-October, Oct. 2019, doi: 10.1109/SENSORS43011.2019.8956880.

[88] H. Abedi, S. Luo, and G. Shaker, “On the use of Low-Cost Radars and Machine Learning for In-Vehicle Passenger Monitoring,” *2020 IEEE 20th Topical Meeting on Silicon Monolithic Integrated Circuits in RF Systems, SiRF 2020*, pp. 63–65, Jan. 2020, doi: 10.1109/SIRF46766.2020.9040191.

[89] C. Karabacak, S. Z. Gurbuz, A. C. Gurbuz, M. B. Guldogan, G. Hendeby, and F. Gustafsson, “Knowledge Exploitation for Human Micro-Doppler Classification,” *IEEE Geoscience and Remote Sensing Letters*, vol. 12, no. 10, pp. 2125–2129, 2015, doi: 10.1109/LGRS.2015.2452311.

[90] A. Murari and K. N. Singh, “Lund and Browder Chart—Modified versus Original: A Comparative Study,” *Acute and Critical Care*, vol. 34, no. 4, pp. 276–281, Nov. 2019, doi: 10.4266/ACC.2019.00647.

[91] “Ansys HFSS | 3D High Frequency Simulation Software.” [Online]. Available: https://www.ansys.com/products/electronics/ansys-hfss (accessed Aug. 16, 2021).

[92] B. Bogin and M. I. Varela-Silva, “Leg Length, Body Proportion, and Health: A Review with a Note on Beauty,” *International Journal of Environmental Research and Public Health*, vol. 7, no. 3, pp. 1047–1075, 2010, doi: 10.3390/IJERPH7031047.

[93] A. K. Seifert, A. M. Zoubir, and M. G. Amin, “Radar-based Human Gait Recognition in Cane-Assisted Walks,” *2017 IEEE Radar Conference, RadarConf 2017*, no. mD, pp. 1428–1433, 2017, doi: 10.1109/RADAR.2017.7944431.

[94] V. C. Chen, F. Li, S. S. Ho, and H. Wechsler, “Micro-Doppler Effect in Radar: Phenomenon, Model, and Simulation Study,” *IEEE Transactions on Aerospace and Electronic Systems*, vol. 42, no. 1, pp. 2–21, 2006, doi: 10.1109/TAES.2006.1603402.

[95] O. Postolache, J. M. D. Pereira, V. Viegas, and P. S. Girao, “Gait Rehabilitation Assessment Based on Microwave Doppler Radars Embedded in Walkers,” *2015 IEEE International Symposium on Medical Measurements and Applications, MeMeA 2015 - Proceedings*, pp. 208–213, 2015, doi: 10.1109/MeMeA.2015.7145200.

[96] D. Alshamaa, A. Chkeir, R. Soubra, and F. Mourad-Chehade, “Measurement of Gait Speed using a Doppler Radar: Influence of Acceleration and Deceleration Zones,” *SAS 2019 - 2019 IEEE Sensors Applications Symposium, Conference Proceedings*, 2019, doi: 10.1109/SAS.2019.8706123.

[97] P. P. Morita *et al.*, “Comparative Analysis of Gait Speed Estimation Using Wideband and Narrowband Radars, Thermal Camera, and Motion Tracking Suit Technologies,” *Journal of Healthcare Informatics Research,* vol. 4, no. 3, pp. 215–237, 2020, doi: 10.1007/s41666-020-00071-7.

[98] G. Diraco, A. Leone, and P. Siciliano, “A Radar-Based Smart Sensor for Unobtrusive Elderly Monitoring in Ambient Assisted Living Applications,” *Biosensors (Basel)*, vol. 7, no. 4, 2017, doi: 10.3390/bios7040055.

[99] Z. K. Qiu, D. Z. Li, and W. D. Jiang, “Study of Continuous Wave Radar for Human Motion Characteristics Measurement,” *International Conference on Signal Processing Proceedings, ICSP*, pp. 1078–1081, 2010, doi: 10.1109/ICOSP.2010.5655886.

[100] “The Average Walking Stride Length | livestrong”, [Online]. Available: https://www.livestrong.com/article/438170-the-average-walking-stride-length/ (accessed Sep. 13, 2022).

[101] “Peak Analysis - MATLAB & Simulink Example.” [Online]. Available: https://www.mathworks.com/help/signal/ug/peak-analysis.html;jsessionid=8073d5f14c99d3ea8a8919bee82c (accessed Jan. 03, 2022).

[102] A. K. Seifert, A. M. Zoubir, and M. G. Amin, “Detection of Gait Asymmetry Using Indoor Doppler Radar,” *2019 IEEE Radar Conference (RadarConf)*, 2019. doi: 10.1109/RADAR.2019.8835611

[103] L. Fei, H. Binke, Z. Hang, and D. Hao, “Human Gait Recognition using Micro-Doppler Features,” *Proceedings of 2012 5th Global Symposium on Millimeter-Waves, GSMM 2012*, no. Gsmm, pp. 326–329, 2012, doi: 10.1109/GSMM.2012.6314067.

[104] J. W. Palmer, K. F. Bing, A. C. Sharma, and J. B. Perkins, “Exploitation of Radar Doppler Signatures for Gait Analysis,” *The Asilomar Conference on Signals, Systems, and Computers*, vol. 30332, no. 1, pp. 629–632, 2012, doi: 10.1109/ACSSC.2012.6489085.

[105] V. C. Chen, “Detection and Analysis of Human Motion by Radar,” *2008 IEEE Radar Conference, RADAR 2008*, vol. 2, no. 1, pp. 2–5, 2008, doi: 10.1109/RADAR.2008.4721059.

[106] H. Abedi, P. P. Morita, J. Boger, A. Wong, and G. Shaker, “In-Package Integrated Dielectric Lens Paired with a MIMO mm-Wave Radar for Corridor Gait Monitoring,” *2021 IEEE International Symposium on Antennas and Propagation and North American Radio Science Meeting, APS/URSI 2021 - Proceedings*, pp. 1795–1796, 2021, doi: 10.1109/APS/URSI47566.2021.9704192.

[107] M. Mercuri *et al.*, “Enabling Robust Radar-Based Localization and Vital Signs Monitoring in Multipath Propagation Environments,” *IEEE Transactions on Biomedical Engineering*, vol. 68, no. 11, pp. 3228–3240, Nov. 2021, doi: 10.1109/TBME.2021.3066876.

[108] K. Saho, K. Shioiri, M. Fujimoto, and Y. Kobayashi, “Micro-Doppler Radar Gait Measurement to Detect Age- And Fall Risk-Related Differences in Gait: A Simulation Study on Comparison of Deep Learning and Gait Parameter-Based Approaches,” *IEEE Access*, vol. 9, pp. 18518–18526, 2021, doi: 10.1109/ACCESS.2021.3053298.

[109] “Constant False Alarm Rate (CFAR) Detection - MATLAB & Simulink.” [Online]. Available: https://www.mathworks.com/help/phased/ug/constant-false-alarm-rate-cfar-detection.html (accessed Sep. 13, 2022).

[110] E. Cortina, D. Otero, and C. E. D’Attellis, “Maneuvering Target Tracking Using Extended Kalman Filter,” *IEEE Transactions on Aerospace and Electronic Systems*, vol. 27, no. 1, pp. 155–158, 1991, doi: 10.1109/7.68158.

[111] S. H. Chang, N. Mitsumoto, and J. W. Burdick, “An Algorithm for UWB Radar-based Human Detection,” *IEEE National Radar Conference - Proceedings*, 2009, doi: 10.1109/RADAR.2009.4976999.

[112] J. Zhang, T. Jin, Y. He, L. Qiu, and Z. Zhou, “Human Tracking Using Range and Velocity Measurements by Multistatic Radar,” *2016 Progress In Electromagnetics Research Symposium, PIERS 2016 - Proceedings*, pp. 520–525, Nov. 2016, doi: 10.1109/PIERS.2016.7734384.

[113] C. Will, P. Vaishnav, A. Chakraborty, and A. Santra, “Human Target Detection, Tracking, and Classification using 24-Ghz FMCW Radar,” *IEEE Sensors Journal*, vol. 19, no. 17, pp. 7283–7299, Sep. 2019, doi: 10.1109/JSEN.2019.2914365.

[114] P. Vaishnav and A. Santra, “Continuous Human Activity Classification with Unscented Kalman Filter Tracking Using FMCW Radar,” *IEEE Sensors Letter*, vol. 4, no. 5, May 2020, doi: 10.1109/LSENS.2020.2991367.

[115] S. Perera, S. H. Mody, R. C. Woodman, and S. A. Studenski, “Meaningful Change and Responsiveness in Common Physical Performance Measures in Older Adults,” *Journal of the American Geriatrics Society*, vol. 54, no. 5, pp. 743–749, May 2006, doi: 10.1111/J.1532-5415.2006.00701.X.

[116] P. P. Morita *et al.*, “Comparison of Gait Speed Estimation of Multiple Sensor-Based Technologies,” *Proceedings of the International Symposium on Human Factors and Ergonomics in Health Care*, vol. 8, no. 1, pp. 135–139, Sep. 2019, doi: 10.1177/2327857919081032.

[117] M. Kamran Saleem, H. Vettikaladi, M. A. S. Alkanhal, and M. Himdi, “Lens Antenna for Wide Angle Beam Scanning at 79 GHz for Automotive Short Range Radar Applications,” *IEEE Transactions on Antennas and Propagation*, vol. 65, no. 4, pp. 2041–2046, Apr. 2017, doi: 10.1109/TAP.2017.2669726.

[118] M. A. Belen and P. Mahouti, “Design of Nonuniform Substrate Dielectric Lens Antennas using 3D Printing Technology,” *Microwave and Optical Technology Letters*, vol. 62, no. 2, pp. 756–762, Feb. 2020, doi: 10.1002/MOP.32065.

[119] R. J. Mailloux, “Phased Array Antenna Handbook,” Artech, 2017.

[120] P. Hallbjörner, Z. He, S. Bruce, and S. Cheng, “Low-profile 77-GHz Lens Antenna with Array Feeder,” *IEEE Antennas and Wireless Propagation Letters*, vol. 11, pp. 205–207, 2012, doi: 10.1109/LAWP.2012.2188265.

[121] C. A. Fernandes, E. B. Lima, and J. R. Costa, “Dielectric Lens Antennas”, Springer Science+Business Media, 2015. DOI: 10.1007/978-981-4560-75-7_40-1.

[122] K. X. Wang and H. Wong, “A Wideband Millimeter-Wave Circularly Polarized Antenna with 3-D Printed Polarizer,” *IEEE Transactions on Antennas and Propagation*, vol. 65, no. 3, pp. 1038–1046, Mar. 2017, doi: 10.1109/TAP.2016.2647693.

[123] Y. X. Zhang, Y. C. Jiao, and S. bin Liu, “3-D-Printed Comb Mushroom-Like Dielectric Lens for Stable Gain Enhancement of Printed Log-Periodic Dipole Array,” *IEEE Antennas and*

Wireless Propagation Letters, vol. 17, no. 11, pp. 2099–2103, Nov. 2018, doi: 10.1109/LAWP.2018.2851298.

[124] B. Tariq Malik *et al.*, "Antenna Gain Enhancement by Using Low-Infill 3D-Printed Dielectric Lens Antennas", *IEEE Access*, vol. 7, pp. 102467–102476, 2019. doi: 10.1109/ACCESS.2019.2931772.

[125] M. Al-Tikriti, S. Koch, and M. Uno, "A Compact Broadband Stacked Microstrip Array Antenna Using Eggcup-Type of Lens," *IEEE Microwave and Wireless Components Letters*, vol. 16, no. 4, pp. 230–232, Apr. 2006, doi: 10.1109/LMWC.2006.872099.

[126] Y. Tajima and Y. Yamada, "Design of Shaped Dielectric Lens Antenna for Wide Angle Beam Steering," *Electronics and Communications in Japan, Part III: Fundamental Electronic Science* vol. 89, no. 2, pp. 1–12, Feb. 2006, doi: 10.1002/ECJC.20185.

[127] A. Artemenko, A. Mozharovskiy, A. Maltsev, R. Maslennikov, A. Sevastyanov, and V. Ssorin, "2D Electronically Beam Steerable Integrated Lens Antennas for mmWave Applications," *European Microwave Week 2012: "Space for Microwaves", EuMW 2012, Conference Proceedings - 42nd European Microwave Conference, EuMC 2012*, pp. 213–216, 2012, doi: 10.23919/EUMC.2012.6459155.

[128] A. Artemenko, A. Maltsev, A. Mozharovskiy, A. Sevastyanov, V. Ssorin, and R. Maslennikov, "Millimeter-Wave Electronically Steerable Integrated Lens Antennas for WLAN/WPAN Applications," *IEEE Transactions on Antennas and Propagation*, vol. 61, no. 4, pp. 1665–1671, 2013, doi: 10.1109/TAP.2012.2232266.

[129] J. R. Costa, M. G. Silveirinha, and C. A. Fernandes, "Evaluation of a Double-Shell Integrated Scanning Lens Antenna," *IEEE Antennas and Wireless Propagation Letters*, vol. 7, pp. 781–784, 2008, doi: 10.1109/LAWP.2008.2008403.

[130] R. Sauleau, C. A. Fernandes, and J. R. Costa, "Review of Lens Antenna Design and Technologies for mm-Wave Shaped-Beam Applications," *ANTEM 2005 - 11th International Symposium on Antenna Technology and Applied Electromagnetics, Conference Proceedings*, 2005, doi: 10.1109/ANTEM.2005.7852157.

[131] T. Jaschke, B. Rohrdantz, H. K. Mitto, and A. F. Jacob, “Ultrawideband SIW-Fed Lens Antenna,” *IEEE Antennas and Wireless Propagation Letters*, vol. 16, pp. 2010–2013, 2017, doi: 10.1109/LAWP.2017.2693179.

[132] N. Chudpooti, N. Duangrit, P. Akkaraekthalin, I. D. Robertson, and N. Somjit, “220-320 GHz Hemispherical Lens Antennas Using Digital Light Processed Photopolymers,” *IEEE Access*, vol. 7, pp. 12283–12290, 2019, doi: 10.1109/ACCESS.2019.2893230.

[133] A. Dhouibi, S. N. Burokur, A. de Lustrac, and A. Priou, “Compact Metamaterial-Based Substrate-Integrated Luneburg Lens Antenna,” *IEEE Antennas and Wireless Propagation Letters*, vol. 11, pp. 1504–1507, 2012, doi: 10.1109/LAWP.2012.2233191.

[134] A. Mozharovskiy, A. Artemenko, V. Ssorin, R. Maslennikov, A. Sevastyano, “High Gain Millimeter-Wave Lens Antennas with Improved Aperture Efficiency,” *9th European Conference on Antennas and Propagation (EuCAP)*, 2015.

[135] R. J. Friel, M. Gerling-Gerdin, E. Nilsson, and B. P. Andreasson, “3D Printed Radar Lenses with Anti-Reflective Structures,” *Designs, Vol. 3, Page 28*, vol. 3, no. 2, p. 28, 2019, doi: 10.3390/DESIGNS3020028.

[136] R. Ernst, E. Nilsson, and P. A. Viberg, “60GHz Vital Sign Radar using 3D-Printed Lens,” *Proceedings of IEEE Sensors*, Jan. 2017, doi: 10.1109/ICSENS.2016.7808774.

[137] A. L. Hagström *et al.*, “An Iterative Approach to Determine the Refractive Index of 3D Printed 60GHz PLA Lenses,” *IET Conference Publications*, vol. 2018, no. CP746, 2018, doi: 10.1049/CP.2018.1480.

[138] P. Piksa, S. Zvanovec, and P. Cerny, “Elliptic and Hyperbolic Dielectric Lens Antennas in mm-Waves” *Radioengineering*, vol. 20, no. 1, 2011.

[139] B. Fuchs, O. Lafond, S. Rondineau, M. Himdi, and L. le Coq, “Off-Axis Performances of Half Maxwell Fish-Eye Lens Antennas at 77 GHz,” *IEEE Transactions on Antennas and Propagation*, vol. 55, no. 2, pp. 479–482, Feb. 2007, doi: 10.1109/TAP.2006.886576.

[140] Constantine A. Balanis, “Antenna Theory: Analysis and Design, 4th Edition | Wiley,” p. 1104, 2016.

[141] “Antenna Design & Modeling Software | Ansys.” [Online]: Available: https://www.ansys.com/applications/antenna-design-and-placement (accessed Aug. 16, 2021).

[142] A. E. Omer, S. Gigoyan, G. Shaker, and S. Safavi-Naeini, “WGM-Based Sensing of Characterized Glucose- Aqueous Solutions at mm-Waves,” *IEEE Access*, vol. 8, pp. 38809–38825, 2020, doi: 10.1109/ACCESS.2020.2975805.

[143] “E. Schubert, M. Kunert, W. Menzel, J. Fortuny-Guasch, J. Chareau “Human RCS Measurements and Dummy Requirements for the Assessment of Radar Based Active Pedestrian Safety Systems,” *14th International Radar Symposium (IRS),* 2013.

[144] Brower P Hicks D, “Maintaining Muscle Function in Patients on Bed Rest”, *The American Journal of Nursing*, 1972.

[145] R H Cress, F Burrell, W C Fleming, “A Review of the Dangers of Prolonged Bed Rest”, *The American Journal of the Medical Sciences*, 1968.

[146] M. C. Creditor, “Hazards of Hospitalization of the Elderly,” *Annals of Internal Medicine*, vol. 118, no. 3, pp. 219–223, 1993, doi: 10.7326/0003-4819-118-3-199302010-00011.

[147] A. A. Ferrando, H. W. Lane, C. A. Stuart, J. Davis-Street, and R. R. Wolfe, “Prolonged Bed Rest Decreases Skeletal Muscle and Whole Body Protein Synthesis,” *American Physiological Society Journal*, vol. 270, no. 4 Pt 1, 1996, doi: 10.1152/AJPENDO.1996.270.4. E627.

[148] R. L. Hughson *et al.*, “Increased Postflight Carotid Artery Stiffness and Inflight Insulin Resistance Resulting From 6-Mo Spaceflight in Male and Female Astronauts,” *The American Journal of Physiology-Heart and Circulatory Physiology*, vol. 310, no. 5, pp. H628–H638, Mar. 2016, doi: 10.1152/AJPHEART.00802.2015/SUPPL_FILE/PODCAST.MP3.

[149] E. T. Hedge *et al.*, “Implementation of Exercise Countermeasures During Spaceflight and Microgravity Analogue Studies: Developing Countermeasure Protocols for Bedrest in Older Adults (BROA),” *Frontiers in Physiology*, vol. 13, Aug. 2022, doi: 10.3389/FPHYS.2022.928313.

[150] F. G. di Girolamo *et al.*, “The Aging Muscle in Experimental Bed Rest: A Systematic Review and Meta-Analysis,” *Frontiers in Nutrition*, vol. 8, p. 204, Aug. 2021, doi: 10.3389/FNUT.2021.633987/BIBTEX.

[151] A. S. Monaghan, J. M. Huisinga, and D. S. Peterson, “The Application of Principal Component Analysis to Characterize Gait and Its Association with Falls in Multiple Sclerosis,” *Scientific Reports*, vol. 11, no. 1, pp. 1–10, 2021, doi: 10.1038/s41598-021-92353-2.

[152] P. Kortebein, A. Ferrando, J. Lombeida, R. Wolfe, and W. J. Evans, “Effect of 10 Days of Bed Rest on Skeletal Muscle in Healthy Older Adults,” *The Journal of the American Medical Association*, vol. 297, no. 16, pp. 1772–1774, Apr. 2007, doi: 10.1001/JAMA.297.16.1772-B.

[153] A. A. Ferrando *et al.*, “EAA Supplementation to Increase Nitrogen Intake Improves Muscle Function During Bed Rest in the Elderly,” *Clinical Nutrition*, vol. 29, no. 1, pp. 18–23, Feb. 2010, doi: 10.1016/J.CLNU.2009.03.009.

[154] R. H. Coker, N. P. Hays, R. H. Williams, R. R. Wolfe, and W. J. Evans, “Bed Rest Promotes Reductions in Walking Speed, Functional Parameters, and Aerobic Fitness in Older, Healthy Adults,” *The Journals of Gerontology. Series A, Biological Sciences and Medical Sciences*, vol. 70, no. 1, p. 91, Jan. 2015, doi: 10.1093/GERONA/GLU123.

[155] P. Janakaraj, K. Jakkala, A. Bhuyan, Z. Sun, P. Wang, and M. Lee, “STAR: Simultaneous Tracking and Recognition through Millimeter Waves and Deep Learning,” *Proceedings of the 12th IFIP Wireless and Mobile Networking Conference, WMNC 2019*, pp. 211–218, 2019, doi: 10.23919/WMNC.2019.8881354.

[156] Q. Zou, Y. Wang, Q. Wang, Y. Zhao, and Q. Li, “Deep Learning-Based Gait Recognition Using Smartphones in the Wild,” *IEEE Transactions on Information Forensics and Security*, vol. 15, pp. 3197–3212, 2020, doi: 10.1109/TIFS.2020.2985628.

[157] P. Addabbo, M. L. Bernardi, F. Biondi, M. Cimitile, C. Clemente, and D. Orlando, “Gait recognition using FMCW Radar and Temporal Convolutional Deep Neural Networks,” in *2020 IEEE International Workshop on Metrology for AeroSpace, MetroAeroSpace 2020 - Proceedings*, Jun. 2020, pp. 171–175. doi: 10.1109/MetroAeroSpace48742.2020.9160199.

[158] H. Chen and W. Ye, “Classification of Human Activity Based on Radar Signal Using 1-D Convolutional Neural Network,” *IEEE Geoscience and Remote Sensing Letters*, vol. 17, no. 7, pp. 1178–1182, Jul. 2020, doi: 10.1109/LGRS.2019.2942097.

[159] J. P. Zhu, H. Q. Chen, and W. bin Ye, “Classification of human activities based on radar signals using 1D-CNN and LSTM,” *Proceedings - IEEE International Symposium on Circuits and Systems*, vol. 2020-October, 2020, doi: 10.1109/ISCAS45731.2020.9181233/VIDEO.

[160] X. Yang, P. Chen, M. Wang, S. Guo, C. Jia, and G. Cui, “Human Motion Serialization Recognition with Through-The-Wall Radar,” *IEEE Access*, vol. 8, pp. 186879–186889, 2020, doi: 10.1109/ACCESS.2020.3029247.

[161] M. Wang, G. Cui, X. Yang, and L. Kong, “Human Body and Limb Motion Recognition via Stacked Gated Recurrent Units Network,” *IET Radar, Sonar and Navigation*, vol. 12, no. 9, pp. 1046–1051, Sep. 2018, doi: 10.1049/iet-rsn.2018.5054.

[162] Microsoft Docs, “Azure Machine Learning Documentation”, 2021. [Online]. Available: Https://Docs.Microsoft.Com/En-Us/Azure/Machine-Learning.

[163] I. Nirmal, A. Khamis, M. Hassan, W. Hu, and X. Zhu, “Deep Learning for Radio-based Human Sensing: Recent Advances and Future Directions,” *IEEE Communications Surveys and Tutorials*, Oct. 2020, Accessed: Apr. 22, 2021. [Online]. Available: http://arxiv.org/abs/2010.12717

[164] L. Deng and D. Yu, “Deep learning: Methods and applications,” *Foundations and Trends in Signal Processing*, vol. 7, no. 3–4. Now Publishers Inc, pp. 197–387, Jun. 30, 2013. doi: 10.1561/2000000039.

[165] M. Mercuri, I. R. Lorato, Y. H. Liu, F. Wieringa, C. van Hoof, and T. Torfs, “Vital-Sign Monitoring and Spatial Tracking of Multiple People Using a Contactless Radar-Based Sensor,” *Nature Electronics 2019 2:6*, vol. 2, no. 6, pp. 252–262, Jun. 2019, doi: 10.1038/s41928-019-0258-6.

[166] C. Ammann-Reiffer, C. H. G. Bastiaenen, R. A. de Bie, and H. J. A. van Hedel, “Measurement Properties of Gait-Related Outcomes in Youth with Neuromuscular Diagnoses: A Systematic Review,” *Physical Therapy,* vol. 94, no. 8, pp. 1067–1082, 2014, doi: 10.2522/ptj.20130299.

[167] D. N. Martini, G. C. Goulet, D. H. Gates, and S. P. Broglio, “Long-Term Effects of Adolescent Concussion History on Gait, Across Age,” *Gait & Posture*, vol. 49, pp. 264–270, 2016, doi: 10.1016/j.gaitpost.2016.06.028.

[168] C. S. Mendes, I. Bartos, Z. Márka, T. Akay, S. Márka, and R. S. Mann, “Quantification of Gait Parameters in Freely Walking Rodents,” *BMC Biology*, vol. 13, no. 1, pp. 1–11, 2015, doi: 10.1186/s12915-015-0154-0.

[169] D. D. Espy, F. Yang, T. Bhatt, and Y. C. Pai, “Independent Influence of Gait Speed and Step Length on Stability and Fall Risk,” *Gait & Posture*, vol. 32, no. 3, pp. 378–382, Jul. 2010, doi: 10.1016/J.GAITPOST.2010.06.013.

[170] S. Haghayegh, H. A. Kang, S. Khoshnevis, M. H. Smolensky, M. H. Smolensky, and K. R. Diller, “A Comprehensive Guideline for Bland–Altman and Intra Class Correlation Calculations to Properly Compare Two Methods of Measurement and Interpret Findings,” *Physiological Measurement*, vol. 41, no. 5, p. 055012, Jun. 2020, doi: 10.1088/1361-6579/AB86D6.

[171] S. Studenski *et al.*, “Gait Speed and Survival in Older Adults,” *The Journal of the American Medical Association*, vol. 305, no. 1, pp. 50–58, Jan. 2011, doi: 10.1001/JAMA.2010.1923.

[172] J. K. Tilson *et al.*, “Meaningful Gait Speed Improvement During the First 60 Days Poststroke: Minimal Clinically Important Difference,” *Physical Therapy*, vol. 90, no. 2, pp. 196–208, Feb. 2010, doi: 10.2522/PTJ.20090079.

[173] R. W. Bohannon and S. S. Glenney, “Minimal Clinically Important Difference for Change in Comfortable Gait Speed of Adults with Pathology: A Systematic Review,” *Journal of Evaluation in Clinical Practice*, vol. 20, no. 4, pp. 295–300, 2014, doi: 10.1111/JEP.12158.

[174] S. E. Hardy, S. Perera, Y. F. Roumani, J. M. Chandler, and S. A. Studenski, “Improvement in Usual Gait Speed Predicts Better Survival in Older Adults,” *Journal of the American Geriatrics Society*, vol. 55, no. 11, pp. 1727–1734, Nov. 2007, doi: 10.1111/J.1532-5415.2007.01413.X.

[175] J. L. Purser *et al.*, “Walking Speed Predicts Health Status and Hospital Costs for Frail Elderly Male Veterans,” *Journal of Rehabilitation Research & Development*, vol. 42, no. 4, pp. 535–545, Jul. 2005, doi: 10.1682/JRRD.2004.07.0087.

[176] L. Reggi, L. Palmerini, L. Chiari, and S. Mellone, “Real-World Walking Speed Assessment Using a Mass-Market RTK-GNSS Receiver,” *Frontiers in Bioengineering and Biotechnology,* vol. 10, p. 501, Mar. 2022, doi: 10.3389/FBIOE.2022.873202/XML/NLM.

[177] P. F. Saint-Maurice *et al.*, “Association of Daily Step Count and Step Intensity with Mortality Among US Adults,” *The Journal of the American Medical Association*, vol. 323, no. 12, pp. 1151–1160, Mar. 2020, doi: 10.1001/JAMA.2020.1382.

[178] P. F. Edemekong, D. L. Bomgaars, S. Sukumaran, and S. B. Levy, “Activities of Daily Living,” *Encyclopedia of the Neurological Sciences*, pp. 47–48, Jul. 2021, Accessed: Sep. 30, 2021. [Online]. Available: https://www.ncbi.nlm.nih.gov/books/NBK470404/

Appendix A

FMCW Radar Fundamentals

Radar stands for radio detection and ranging and basically describes a method of distance measurement between the radar device itself and objects in its field of view. In all radar systems, as shown in Figure **1**, an electromagnetic signal is emitted by a transmitter, and the signal is reflected off targets of interest at a certain range from the transmitter. Then, a receiver scans for these echoes of the transmitted signal and identifies characteristics of the target, such as distance or position. In addition to the distance, the received signal contains targets' radial velocity information. Furthermore, targets' azimuth and elevation angles can be obtained using various antenna arrangements.

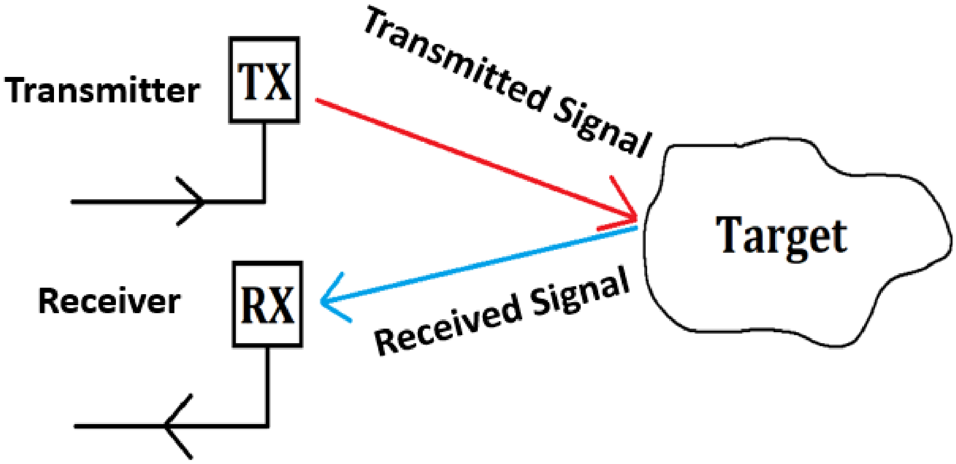

Figure 1. Principle of a radar system (EM signals are transmitted by transmitter antennas and received by receiver antennas).

The distance of a target can be calculated by measuring the time between transmitted and received waves and knowing their speed. Conventional pulse radars periodically emit a monochromatic pulse [72]. The target's distance from the radar is determined based on the time delay between the transmission of the signal and the reception of the echoed pulse. These systems, however, are unsuitable for short-range measurements as a device with an extremely fast clock speed would be required to discriminate the time delay of signals even at magnitudes of 1 meter [72].

As one of the most promising among other radar techniques, an FMCW radar could be used to avoid the above problem by using transmitting sinusoidal signals with a linearly increasing frequency over time, known as chirps (compressed high-intensity radar pulse) [72]. A linear combination of sinusoid signals with low frequencies could be achieved by multiplying the received signal by the transmitted signal. FMCW radar systems can enable simpler hardware and architecture types and provide information about the range and radial velocity of multiple targets by processing the observations of beat signals [72]. Moreover, to obtain the exact position of a subject, the azimuth information of the subject is also required. A multiple inputs multiple outputs (MIMO) FMCW radar system can provide 2D (x-y) or 3D (x-y-z) point cloud information of a subject in addition to the velocity [72].

Figure **2** is a block diagram of an FMCW radar showing a single representative Tx chain and Rx chain (although, in practice, multiple chains are present to support multiple Tx and Rx antennas). The local oscillator (LO) generates a linear frequency ramp (also called a chirp) transmitted on the Tx antenna. The received signal (reflected from the scene in front of the radar) on the Rx antenna mixes with the transmit signal to create an intermediate frequency (IF) signal. An analog-to-digital converter (ADC) then digitizes the received IF signal for subsequent processing.

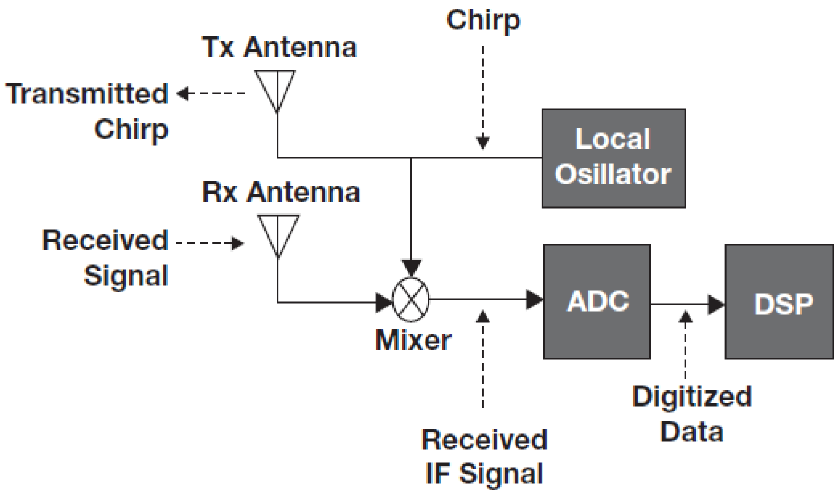

Figure 2. Block diagram of an FMCW radar reproduced from [77].

In a Time Division Multiplexed (TDM) MIMO FMCW radar, a sequence of chirps is sent in a frame from different transmit antennas. Each chirp consisting of a sinusoid signal with swept frequency from (carrier frequency) f_c to $f_c + B$ with the bandwidth of $B = f_{max} - f_{min}$ determines the capability of a radar system to resolve separate targets that are close together in range. The received signal is then correlated with the transmit signal creating a beat signal with a frequency of f_b containing information about the illuminated scene. In Figure **3**, the transmitted and received signals of an FMCW radar and the corresponding beat frequency are shown [73].

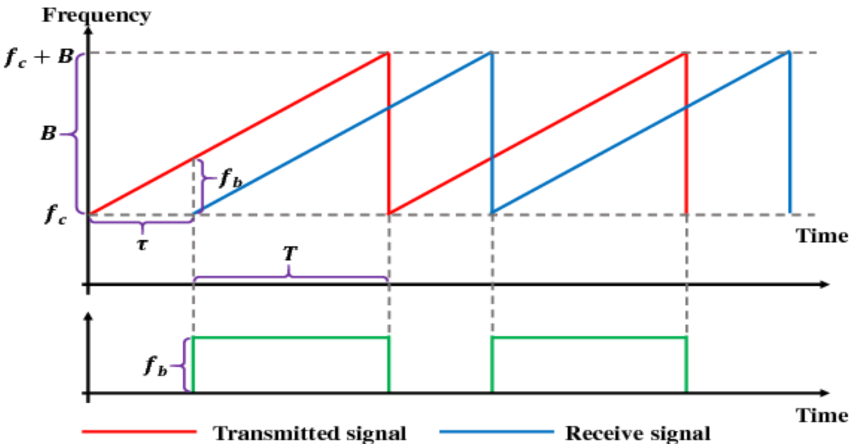

Figure 3. Transmitted, received, and beat signals in an FMCW radar.

In an FMCW radar, having “up chirps” (i.e., only positive-slope chirps) for a transmitted signal *s(t)*, the received signal at l^{st} antenna element reflected by the target $x_l(t)$ can be modelled as (assuming that the target is a single point target) [73]:

$$x_l(t_f,t_s)=b_l\exp[-j(2\pi f_b t_f+2\frac{vt_s}{\lambda_{\max}}+\tau_l+\alpha_l+\Delta\psi_l(t_f,t_s)]+e_l(t_f,t_s). \tag{1}$$

where t_f and t_s are fast and slow time indexes, b_l and α_l are the channel’s mismatched magnitude and phase, and f_b is the beat frequency. The beat frequency is the frequency of an (IF) signal produced by an object in front of the radar located at the range of R calculated by

$$f_b = S\frac{2R}{c} \tag{2}$$

where S is the rate of increase in the frequency of the sinusoid, and c is the speed of light in free space. Moreover, v, λ_{max}, τ_l, $\Delta\psi_l(t_f,t_s)$, and $e_l(t_f,t_s)$ in. (1) are the target’s radial velocity, the wavelength corresponding to the start frequency of the FMCW ramp, the phase shift at l^{st} receiver due to the angle of arrival (AoA), the residual phase noise and the additive noise, respectively.

The range of an object is limited by IF bandwidth supported by the radar device written as:

$$R_{\max} = c\frac{f_{b\max}}{2S} \tag{3}$$

where f_{bmax} is the maximum supported IF bandwidth. Since the f_{bmax} is also dependent on the ADC sampling frequency, an ADC sampling rate of F_s limits the maximum range of the radar to

$$R_{\max} = c\frac{F_S}{4S}. \tag{4}$$

Since the range estimation of a detected target in the FMCW radar is primarily dependent on the frequency resolution of the Discrete Fourier Transform (DFT) performed on the base-band signals, the new range resolution of the radar is given by

$$\Delta R = \frac{c}{2B}. \tag{5}$$

In an FMCW radar, to resolve objects in range, the Fast Fourier Transform (FFT) is performed on the beat signal (range-FFT) that provides the relative radial distances (i.e., range) of various objects scanned by the radar. Fourier Transform converts a time domain signal into the frequency domain. Fast Fourier transform (FFT) processing on the digitized samples resolves objects in a range such that the frequency of the peaks in the range FFT directly corresponds to the ranges of various objects in the scene. As illustrated in Figure **4**, multiple objects in front of the radar will create multiple reflected chirps at the Rx antenna and multiple IF tones, which result in multiple strikes in the IF frequency spectrum. Therefore, range information of targets could be obtained by applying range-FFT to the received signals.

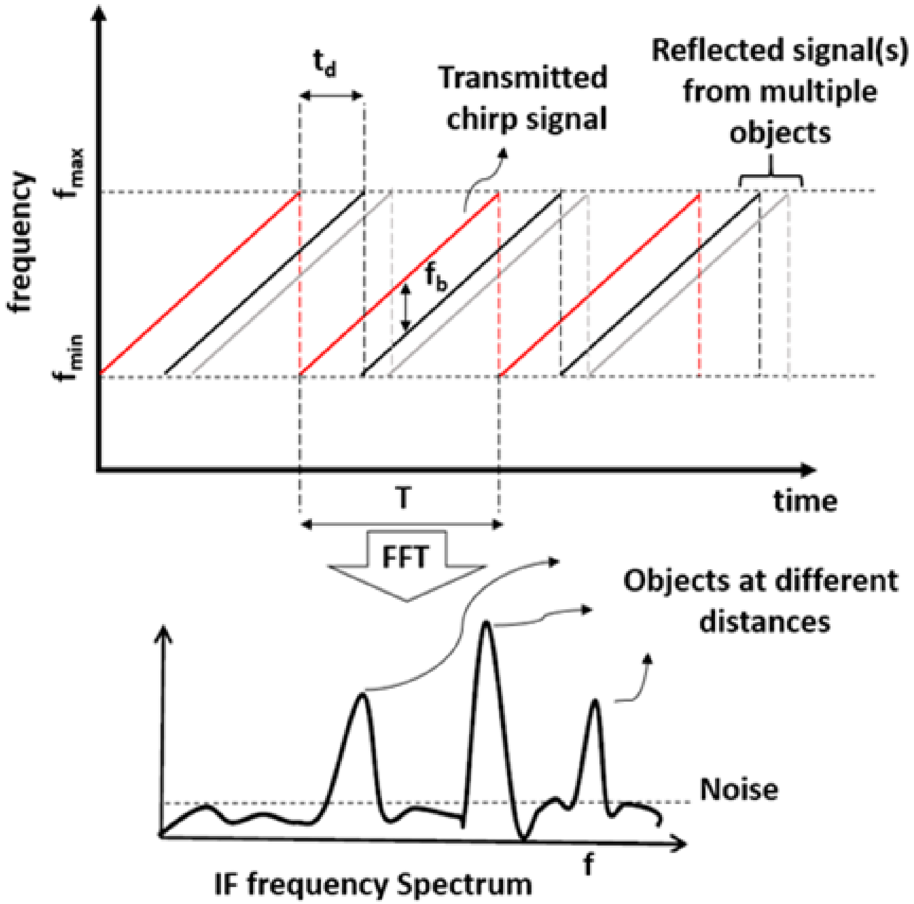

Figure 4. Range processing of consecutive chirps. The range of multiple targets is obtained in the frequency domain by applying range-FFT.

Moreover, to obtain the velocity information of an object, a sequence of chirps separated by T_c ($T_c = \tau + T$), called a frame, is required. The frame structure in an FMCW radar is depicted in Figure **5**. The range-FFTs corresponding to each chirp will have peaks in the same location but different

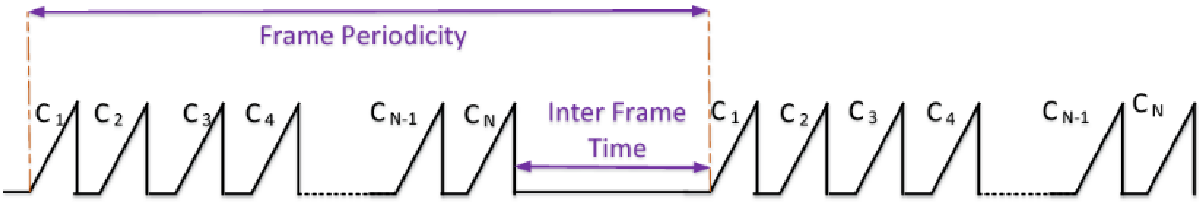

Figure 5. Frame structure in an FMCW radar system.

phases. The measured phase difference (ω) corresponds to the motion of the object of $v \cdot T_c$. Therefore, performing the second series of FFTs (Doppler-FFT) across the chirps, the velocity of objects can be calculated by [73]

$$\omega = \frac{4\pi v T_c}{\lambda} \Rightarrow v = \frac{\lambda \omega}{4\pi T_c}. \tag{6}$$

To calculate the unambiguous range of velocity, the phase of the signal should be less than π, which is written as:

$$|\,\omega\,| \; < \; \pi \Rightarrow v < \frac{\lambda}{4T_c}. \tag{7}$$

Thus, we require closely spaced chirps (shorter Tc) to detect higher velocities. The velocity resolution (v_{res}) is inversely proportional to the frame time (T_f) or the number of chirps (N) per frame given by

There are several defining characteristics of a chirp affecting the operating conditions of an FMCW radar in specific ways. A chirp structure in an FMCW radar is illustrated in Figure **6**, along with defining parameters. Note that the characteristics used to configure a chirp, as well as their effects on the operation of the radar, are outlined in Table **4.1**.

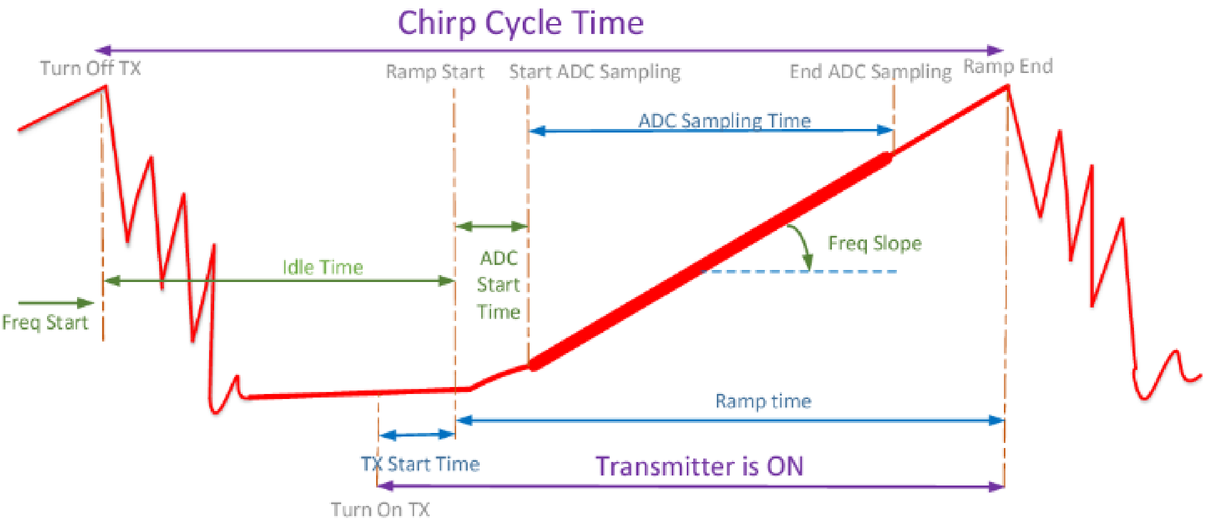

Figure 6. Chirp configuration in FMCW radar systems.

Appendix B

Short-Time Fourier Transform

Short-Time Fourier Transform (STFT) is as written by [73]

$$\mathrm{STFT}(\mathrm{t},\mathrm{f}) = \left|\sum_{n=0}^{P} w(n)x(t-n)e^{-j2\pi f n}\right|^2 \tag{1}$$

where *w(n)* is the window function and *x(t)* is the signal to be transformed.

In this thesis, we used a Hamming window centered around zero with a P length set to 256.

Appendix C
Capon Beamformer

To locate an object in a 2D space, the angle of the object is required along with its range. Estimating the angle of arrival of an object requires at least two receiver antennas. To calculate the AoA (angle of arrival) of an object, at least two receivers, separated by a distance of *d*, are required. As shown in Figure **7**, the reflected signals from an object (at an angle θ with respect to the radar) arriving at each successive receiver are delayed by $dsin(\theta)$. This delay causes a phase shift of $\omega = (2\pi/\lambda)\times dsin(\theta)$ between the signals received at the two receivers. Because the phase difference, ω, can be uniquely estimated only in the range (–π, π), it follows by substituting ω = π that the unambiguous field of view of the radar is achieved with an inter-antenna distance of d = λ/2.

To estimate the AoA of a target, several algorithms have been proposed and analyzed thoroughly. The Capon approach has been among many well-known algorithms for the AoA determination of incident signals using an array antenna structure. The Capon beamformer is a spatial filtering technique that can estimate the AoA of signals in the presence of noise and interference. It works by forming a set of weights for the array elements that maximizes the signal-to-interference-plus-noise ratio (SINR) of the received signal. The basic idea of the Capon beamformer is to find the optimal set of weights for the array elements that minimizes the output power while satisfying a constraint on the desired signal power. The optimal weights are obtained by solving an optimization problem that involves the inversion of a covariance matrix of the received signals. The Capon approach estimates the AoA by reordering terms in (1) and stacking the received signal from all receiver channels in a column vector. It can be expressed as [72]:

$$x_l(t_f, t_s) = e_l(t_f, t_s) + \bar{\bar{\Gamma}} \cdot \bar{a}\,(\theta) \cdot y(v, f_b, t_f, t_s) \cdot s(t_f, t_s) \tag{1}$$

where Γ, *a*, and *y* are defined as follows:

$$\bar{\bar{\Gamma}} = \begin{pmatrix} b_1 \cdot e^{-j\xi_1} & 0 & 0 \\ 0 & \ddots & 0 \\ 0 & 0 & b_L \cdot e^{-j\xi_L} \end{pmatrix}, \bar{a}\,(\theta) = \begin{pmatrix} e^{-j\tau_1} \\ \vdots \\ e^{-j\tau_L} \end{pmatrix}, \tag{2}$$

and

$$y\,(v, f_b, t_f, t_s) = e^{-j\left[2\pi f_b \cdot t_s + \frac{2v \cdot t_s}{\lambda_{max}} + \Delta\psi(t_f, t_s)\right]} \tag{3}$$

Here, θ is the angle of arrival (AoA) of the target, Γ depends on the channel gain/phase mismatches, and a depends on AoA, which is called the steering vector. If there is more than one target at different ranges, i.e., with different f_b, then the received vector is the summation of all the vectors received from each target given by

$$x_l(t_f, t_s) = e_l(t_f, t_s) + \bar{\bar{\Gamma}} \cdot \bar{\bar{A}}\,(\theta) \cdot Y(v, f_b, t_f, t_s) \tag{4}$$

where $\bar{\bar{A}}$ is a matrix with K number of targets that has columns corresponding to the steering vector of each target. Y is a diagonal matrix with the elements of $y\ (v, f_b, t_f, t_s,)$. In (4), the vectors $\bar{\bar{A}}$, v, and f_b are the unknown parameters of the target; however, only elements of $\bar{\bar{A}}$ are functions of receiver channel indexes. Hence, matrix Y does not contribute to the covariance of x. In fact, the covariance matrix of x can be computed in the following manner when the additive noise is uncorrelated to Y:

$$R = E(x \cdot x^H) = P_S \cdot \bar{\bar{\Gamma}} \cdot \bar{\bar{A}}(\theta) \cdot \bar{\bar{A}}^H(\theta) \cdot \bar{\bar{\Gamma}}^H + R_n \tag{5}$$

where P_S is the power of signals, and R_n is the noise covariance, which is a positive definite matrix by assuming that the noise at each receiver is independent of the others. Moreover, the first term in the covariance of (5) is positive definite since $A(\theta)$ is a Vandermonde matrix with positive kernels [72]. Therefore, R is a positive definite, which is invertible. The Capon output filter spectrum is computed as

$$\Phi(\hat{\theta}) = \frac{a}{a^H(\hat{\theta}) \cdot R^{-1} \cdot a(\hat{\theta})} \tag{6}$$

With the azimuth information of the target obtained from the capon beamformer and the range calculated from the range-FFT, a range-azimuth heat map of the subject is obtained. The range-azimuth heat map represents the density of reflected signals in the environment.

The Capon beamformer has several advantages over other beamforming techniques. It can handle multiple signals with different DOAs and frequencies, and it can adapt to changes in the environment and signal statistics. It also provides high spatial resolution and accuracy, and it can suppress interference and noise sources that are closely spaced to the desired signal. However, the Capon beamformer has some limitations and challenges, such as its sensitivity to errors in the covariance matrix estimation, its high computational complexity, and its poor performance in the presence of non-Gaussian noise and distortion.

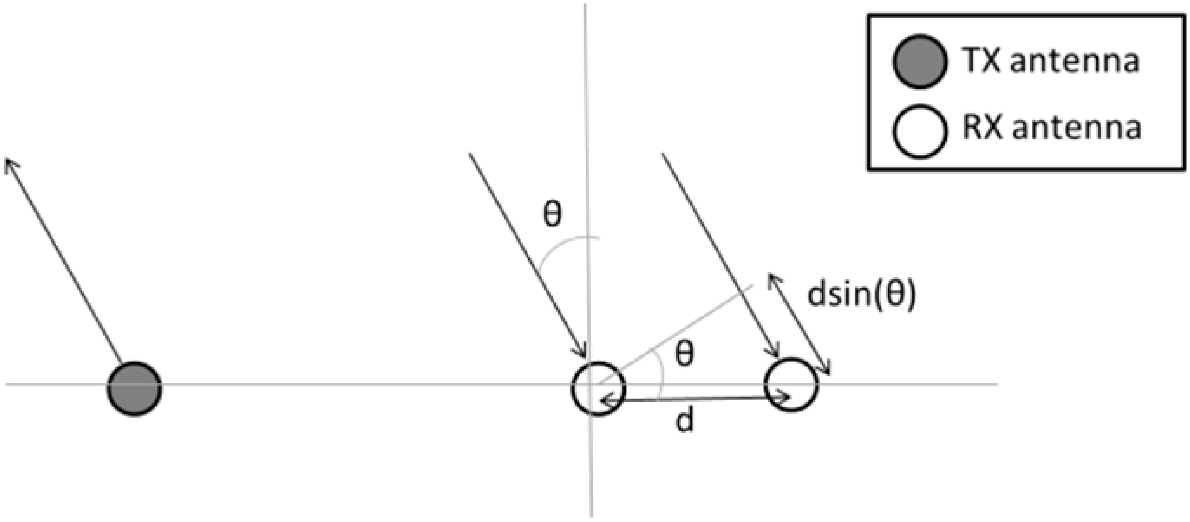

Figure 7. Angle estimation using two receiver Antennas.

Appendix D
MIMO Radars

Single-input-multiple-output (SIMO) radar refers to a radar device with a single Tx and multiple Rx antennas. The angle resolution of a SIMO radar depends on the number of Rx antennas. For example, a device with four Rx antennas has an angle resolution of about 30º, while a device with eight Rx antennas has an angle resolution of about 15º. Therefore, a direct approach to improving the angle resolution requires increasing the number of Rx antennas. This approach has its limits because each additional Rx antenna requires a separate Rx processing chain on the device (each with an LNA, mixer, IF filter, and ADC).

State-of-the-art radars have a low angular resolution determined by the antenna aperture [32], [34], [72]. The resolution attained through conventional beamforming cannot break this physical limitation. Therefore, these radars adopt a MIMO radar approach to achieve higher angular resolution at a smaller aperture and a feasible number of channels. MIMO refers to a radar with multiple Tx and multiple Rx antennas. Superresolution methods that are successfully used in military applications, such as MVDR (Minimum Variance Distortionless Response) and MUSIC (Multiple Signal Classification), are implemented in these radar systems. MUSIC is a spectral analysis technique used to estimate the AOA of radar signals, while MVDR is a beamforming technique used to improve the quality of radar measurements in the presence of interference and noise. Both techniques can be used to estimate the AOA of radar signals, but they are based on different principles and are used in different applications.

The angle resolution of a MIMO radar with N_{Tx} Tx antennas and N_{Rx} Rx antennas (with proper antenna placement) can be equivalent to that of a SIMO radar with $N_{Tx} \times N_{Rx}$ Rx antennas. The MIMO radar, therefore, provides a cost-effective way to improve the angular resolution of the radar. The principle of MIMO radar is illustrated in Figure **8**. By transmitting a sequence of pulses with different frequencies and phase offsets from each antenna and then using the received signals to form a virtual array of antennas with a larger aperture than the physical antennas, the radar can achieve spatial multiplexing or beamforming. For example, to separate two targets at the same range and velocity but with different angles of arrival, the radar uses spatial filtering to separate the signals from the two targets. Spatial filtering is a signal processing technique that uses spatial information from multiple antennas to separate the signals from different sources. In the case of the MIMO FMCW radar, the

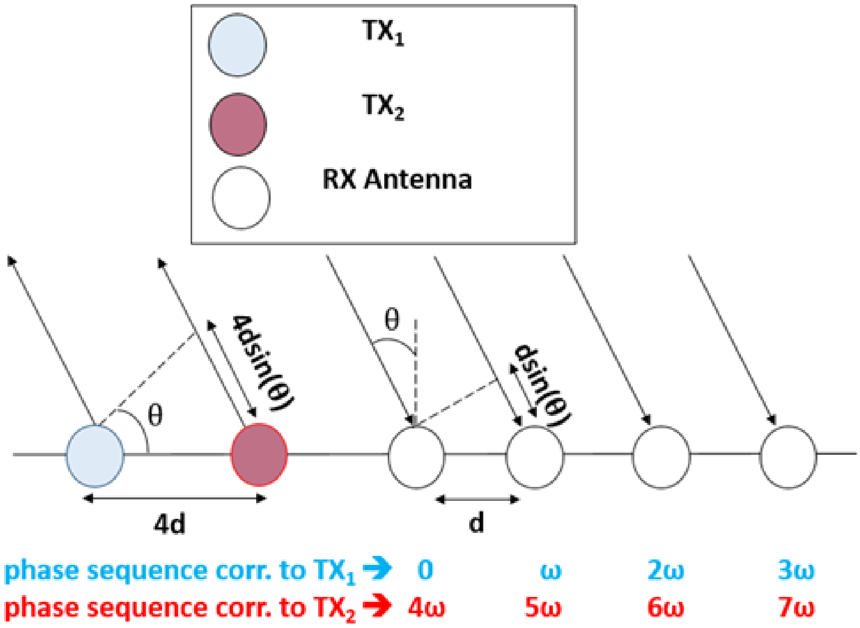

Figure 8. Principle of MIMO Radars. Using MIMO radar, we can create a virtual channel to increase the angular resolution.

received signals from each antenna are combined to form a virtual antenna array. The spatial filtering is then applied to the received signals to separate the signals from the two targets. Spatial filtering can be done using various techniques such as matched filtering, least-squares estimation, or compressive sensing. Another possible approach is to use a waveform diversity technique, such as frequency-hopping or phase-coded waveforms, to separate the signals from the two targets. In this case, the radar transmits a sequence of pulses with different waveform characteristics from each antenna and then uses the received signals to estimate the range, velocity, and angle of arrival of each target.

Waveform diversity techniques use different waveforms with varying frequency or phase characteristics to separate the signals from different targets. This technique requires careful design of the waveforms and signal processing algorithms to ensure that the waveforms are distinguishable and do not interfere with each other. However, it offers the advantage of being able to use a simpler antenna layout and potentially better separation of targets with similar range and velocity but a different angle of arrival.

In general, the choice of technique depends on various trade-offs such as performance, complexity, and cost. A detailed analysis of the system requirements, constraints, and available resources can help select the most appropriate technique for a given scenario.

For example, in the scenario pictured in Figure **5.48**, the angular resolution of the MIMO FMCW radar after forming the virtual array is around 15º. This means that the radar can only distinguish two targets that are separated by at least 15º. At a range of 15 m away from the radar, the minimum separation distance between the two targets that can be discriminated is more than 3 m, which is larger than the actual distance between the walking subjects of 50 cm.

This suggests that additional techniques are needed to separate the two targets. One possible approach is to use more advanced signal processing techniques such as super-resolution algorithms such as Capon's method, MUSIC and ESPRIT (Estimation of Signal Parameters via Rotational Invariance Techniques), which can improve the angular resolution of the radar beyond the physical limit of the antenna array. Another approach is to use multiple radar systems with different antenna layouts or operating frequencies and then combine the received signals to achieve better separation of targets.

In addition, to signal processing techniques, it is also important to consider the design of the radar system itself. Factors such as the antenna layout, the waveform characteristics, and the power levels of the transmitted signals can all affect the performance of the radar in separating closely-spaced targets. Therefore, a careful design of the radar system and a thorough analysis of the system requirements and constraints are essential for achieving the desired performance in such scenarios.

While various techniques have been proposed to discriminate closely-spaced targets in radar systems, the effectiveness of these methods depends on the specific scenario and radar sensor being used. In our case, we used an FMCW MIMO radar, but even with a Capon beamformer, the achievable angular resolution was not sufficient to separate two closely-spaced walking subjects. To address this limitation, we developed an advanced signal processing and association method to successfully separate the two walking subjects that were less than 50 cm apart and extract their respective walking speeds.